Technische Universität München
TUM School of Engineering and Design

Systems Engineering Based Crashworthiness Design for the Small Overlap Load Case

Iván Cuevas Salazar

Complete reprint of the dissertation approved by the TUM School of Engineering and Design of the Technical University of Munich for the award of the Doktor der Ingenieurwissenschaften (Dr.-Ing.).

Chair: Prof. Dr.-Ing. Kai-Uwe Bletzinger

Dissertation Examiners:

1. Prof. Dr.-Ing. habil. Fabian Duddeck
2. Assoc. Prof. Dr. Christophe Bastien

The dissertation was submitted to the Technical University of Munich on 30.05.2023 and accepted by the TUM School of Engineering and Design on 05.09.2023

Abstract

The Insurance Institute for Highway Safety (IIHS) introduced the Small Overlap frontal (SOF) crash test in 2012 to assess the crashworthiness of vehicles during a collision scenario where only 25% of the vehicle's width is in initial contact with a rigid barrier. This load case proved challenging to the automakers since less than 8% of the tested vehicles obtained a Good structural rating during its first year of implementation. As a result, automakers developed different strategies to improve the structural response. By 2019, Good structural ratings accounted for more than 90% of the tested vehicles. However, automakers now face the challenge of designing efficient, lightweight, and robust solutions that can be effectively integrated into the product development process. Hence, the aim of this work is to develop a framework for the crashworthiness design for the SOF load case that takes advantage of the well-established process of systems engineering and enhances it with novel physics- and statistics-based methodologies to accelerate the product development cycles while producing robust structural solutions.

In this work, the global vehicle characteristics and targeted structural rating are systematically decomposed to create load-path and component requirements. These requirements are expressed as intervals of the so-called resistance-to-deformation characteristics represented by force-displacement curves. The calculation of the intervals leading to feasible designs is conducted following a data-driven solution space definition. For this purpose, the SOF crash test dataset from the IIHS is analyzed by means of an automatized object recognition procedure applied to the high-speed video footage. Then, the vehicle kinematics are analyzed and correlated to the occupant compartment deformations. Next, ranges of kinematic parameters that lead to optimal structural performance are identified. These ranges are used as constraints for a hierarchical solution spaces calculation with the resistance-to-deformation characteristics as design variables. A low-fidelity model, developed for the early-design phase mapping the vehicle kinematics to the structural performance, is used as feasibility evaluator in the calculation of the solution spaces. Afterwards, a solution space-based iterative simulation scheme, developed for the implementation of the requirements, is applied to a full-vehicle finite element model. Here, the fulfillment of the low-level requirements is used as an objective function to determine the optimal functional properties of the components. Additionally, the robustness of the design is considered by quantifying and modeling the relevant sources of uncertainty present in the SOF load case. Efficient sampling algorithms are implemented to reduce the amount of samples needed to cover the uncertainty space. Furthermore, a novel robustness index is introduced to describe the scatter of the system's response and to obtain a robust achievement of the primary structural targets. Subsequently, the component's functional properties are reconstructed in the hardware evaluation phase by means of a dedicated crash event analysis using the acceleration and force signals. These functional properties are compared against the load-path requirements. The proposed design framework is validated with a SOF hardware test and is applied to a full-vehicle finite element model where the robustness of the design is improved. Finally, the outlook and limitations of the developed methodologies are discussed.

Zusammenfassung

Das Insurance Institute for Highway Safety (IIHS) führte im Jahr 2012 den Small Overlap Frontal Crashtest (SOF) ein, um die Aufpralltüchtigkeit von Fahrzeugen bei einem Aufprallszenario zu bewerten, bei dem nur 25% der Fahrzeugbreite in Erstkontakt mit einer starren Barriere stehen. Dieser Lastfall erwies sich für die Automobilhersteller als Herausforderung, da im ersten Jahr der Durchführung weniger als 8% der getesteten Fahrzeuge eine gute Strukturbewertung erhielten. Infolgedessen entwickelten die Automobilhersteller verschiedene Strategien zur Verbesserung des Strukturverhaltens. Bis 2019 erreichten mehr als 90% der geprüften Fahrzeuge eine Struktur-Rating "Gut". Allerdings stehen die Automobilhersteller nun vor der Herausforderung, effiziente, leichte und robuste Lösungen zu entwickeln, die sich effektiv in den Produktentwicklungsprozess integrieren lassen. Ziel dieser Arbeit ist es daher, einen Rahmen für die Auslegung der Crashsicherheit für den SOF-Lastfall zu entwickeln, der die Vorteile des etablierten Prozesses der Systemtechnik nutzt und diesen mit neuartigen, auf Physik und Statistik basierenden Methoden erweitert, um die Produktentwicklungszyklen zu beschleunigen und gleichzeitig robuste strukturelle Lösungen zu entwickeln.

In dieser Arbeit werden die globalen Fahrzeugeigenschaften und das angestrebte Struktur-Rating systematisch herunter gebrochen, um Lastpfad- und Komponentenanforderungen zu erstellen. Diese Anforderungen werden als Intervalle der sogenannten Verformungswiderstandskennwerte ausgedrückt, die durch Kraft-Weg-Kurven dargestellt werden. Die Berechnung der Intervalle, die zu realisierbaren Entwürfen führen, erfolgt nach einer datengesteuerten Lösungsraumdefinition. Zu diesem Zweck wird der SOF-Crashtest-Datensatz des IIHS mit Hilfe eines automatisierten Objekterkennungsverfahrens analysiert, das auf die Hochgeschwindigkeits-Videoaufnahmen angewendet wird. Anschließend wird die Fahrzeugkinematik analysiert und mit den Verformungen der Insassenzelle korreliert. Dann werden die Bereiche der kinematischen Parameter ermittelt, die zu einer optimalen Strukturleistung führen. Diese Bereiche werden als Randbedingungen für eine hierarchische Lösungsraumberechnung mit den Widerstands-/Verformungseigenschaften als Entwurfsvariablen verwendet. Ein Low-Fidelity-Modell, das für die frühe Entwicklungsphase entwickelt wurde und die Fahrzeugkinematik auf die strukturelle Leistung abbildet, wird bei der Berechnung der Lösungsräume als Machbarkeitsbewertungsinstrument verwendet. Anschließend wird ein lösungsraumbasiertes iteratives Simulationsschema, das für die Umsetzung der Anforderungen entwickelt wurde, auf ein Finite-Elemente-Modell des Gesamtfahrzeugs angewendet. Dabei wird die Erfüllung der Low-Level-Anforderungen als Zielfunktion verwendet, um die optimalen Funktionseigenschaften der Komponenten zu bestimmen. Zusätzlich wird die Robustheit des Entwurfs durch Quantifizierung und Modellierung der relevanten Unsicherheitsquellen im SOF-Lastfall berücksichtigt. Effiziente Sampling-Algorithmen werden implementiert, um die Anzahl der Stichproben zu reduzieren, die zur Abdeckung des Unsicherheitsraums erforderlich sind. Darüber hinaus wird ein neuartiger Robustheitsindex eingeführt, um die Streuung der Systemleistung zu beschreiben und eine robuste Erreichung der primären Strukturziele zu gewährleisten.

Schließlich werden in der Hardware-Evaluierungsphase die funktionalen Eigenschaften der Komponente mit Hilfe einer speziellen Crash-Ereignis-Analyse anhand der Beschleunigungs- und Kraftsignale rekonstruiert. Diese funktionalen Eigenschaften werden mit den Lastpfadanforderungen verglichen. Der vorgeschlagene Entwurfsrahmen wird mit einem SOF-Hardwaretest validiert und auf ein Finite-Elemente-Modell des Gesamtfahrzeugs angewendet, wodurch die Robustheit des Entwurfs verbessert wird. Abschließend werden die möglichen Weiterentwicklungen und Grenzen der entwickelten Methoden diskutiert.

Acknowledgements

Thanks to the Passive Safety Department of the BMW Group for all the interesting discussions, encouragement and support while conducting this research. Thanks to Professor Fabian Duddeck for the guidance during the development of this project. Thanks to my parents Diana and Iván for giving me the tools to be able to face the great challenges of life. Thanks to my sister Alejandra for inspiring me with her resilience and strength. Thanks to my partner in crime Anahi for all her support and patience in this endeavor, all this would not have been possible without her.

Contents

Chapter 1

Introduction

The crashworthiness assessment of vehicle structures is a key component in automotive design. Crashworthiness design focuses on the development of energy absorbing structures with the main objective of reducing occupant injuries and consequently producing safer vehicles. The performance of the vehicle structure during a crash, namely, the deceleration and structural integrity of the occupant compartment, is essential for the effective operation of the restraint system. The overall performance of a vehicle is regulated and assessed by the correspondent authorities of each country. This assessment or homologation process is a requirement for the vehicle's availability in a certain market and ensures that all new vehicles fulfill a minimum technical standard. Complementary to these regulations, consumer test ratings offer to the general public a means to compare the performance in a crash test among vehicles of a given class. Granting that the crashworthiness can often be too abstract to the average car owner, the compelling communication of the test ratings can translate directly into changes in consumer vehicle purchases (Cicchino, 2015). Additionally, the consumer test can act more quickly into adjusting the test parameters in order to reflect in a closer manner the real world crash scenarios. In order to test the crashworthiness performance of vehicles, several institutions have developed a series of test scenarios that represent real-life crash events. The increase in traffic accidents during the 1960s and 1970s initiated the creation of organizations such as the American Transportation Agency and the European Enhanced Vehicle Safety Committee, which accelerated the development of the crashworthiness design techniques from the automotive manufacturers. Currently, the National Highway Traffic Safety Administration (NHTSA) is the agency responsible for the definition and implementation of the Federal Motor Vehicle Safety Standards (FMVSS) in the USA. In addition, the Insurance Institute for Highway Safety (IIHS) evaluates the crashworthiness and crash avoidance and mitigation capabilities of vehicles and assigns them ratings by using complementary tests to the FMVSS.

The IIHS introduced in 2012 the Small Overlap Frontal (SOF) crash test case to

represent the collision of the front corner of the vehicle with only 25% overlap with respect to the frontal structure (Insurance Institute for Highway Safety, 2021). This test scenario became one of the most challenging cases encouraging manufacturers to redesign the structure of their vehicles. The SOF crash test considers three aspects: the integrity of the structure by measuring the intrusions at the occupant compartment, the dummy kinematics, and injury criteria (see Insurance Institute for Highway Safety (2021)). During the first year of evaluation, only 7.4% of the vehicles tested obtained a Good structural rating. By 2015 this percentage increased to 50%. In 2019, almost 92% obtained a Good structural rating (see Section 3.3.2). The strategies to minimize the intrusions in the occupant compartment include the reinforcement and integration of energy-absorbing components in the outboards of the front rails of the vehicle (Thomas, 2011). Each countermeasure influences the vehicle kinematics, namely, the trajectory of the vehicle and the maximum rotation exhibited at the end of the crash. Moreover, the vehicle kinematics determine the movement of the occupants and therefore influences the dummy kinematics and injury values.

The increase of vehicles obtaining a Good structural rating shows that the automakers have developed crash structures that effectively decrease the deformations at the occupant compartment. The implementation of these design strategies is carried out during the simulation-driven design phase. However, a considerable amount of design iterations and simulation evaluations are needed to develop a structure that reaches its intrusion targets. In some cases, optimization procedures have been developed as an attempt to reduce the time needed for the design (see Section 2.7.2). Nonetheless, these approaches require a full-vehicle finite element model (FE model), which implies that the design can only start after the first geometries of the structure are available, resulting in a relatively high computational cost. These and other gaps in the integration of these design strategies in the product development process have been identified in this work (see Chapter 2). Two methodological voids are present in the current design strategies for the SOF load case. Firstly, the benefits of a systems engineering (SE) approach are not exploited, since the high-level requirements, i.e. obtaining a Good structural rating, are not decomposed into component requirements, that if fulfilled, guarantee that the system targets are achieved. Secondly, even when defined in the virtual development phase, where simulations are used to drive the crashworthiness design, the evaluation of the fulfillment of these component requirements in the hardware tests is not practical. Consequently, the influence of the individual components' behavior cannot be traced down in the full-vehicle's structural response. To close this gap, physical and mathematical methods to map the functional properties at the component level to the system level performance and to find the appropriate set of functional properties that allow the fulfillment of the high-level requirements are needed. Moreover, such methods should be easy to integrate into the current product development process used in the automotive industry.

In the following paragraphs, an introduction on the topics relevant to the development of a design strategy for the SOF load case is given. First, the basic concepts of SE and their application in the automotive development process are presented. Second, a view on

crashworthiness design is described from the requirement definition and decomposition perspective. Third, the solution spaces approach is introduced as a mechanism to define the ranges in which the functional properties of the structure produce designs that fulfill the crashworthiness requirements. Finally, the aspect of robustness is framed in the context of the sources of uncertainty that are implicit to the crashworthiness evaluation and their impact in the performance of the vehicle during a crash.

Systems Engineering. A successful implementation of any design framework should consider the formal aspects of the current methodologies used in product development such as the V-model for SE (see Section 2.1) as well as the cultural aspects and changes that the automotive industry has suffered in the last decades. Weber (2009) stated the following during the shift of paradigm caused by the introduction of more complex electric and electronic systems in the automotive industry the 1980s:

> "Automotive development unquestionably has its roots in traditional engineering, and the prevailing culture in development centers is dominated by 'car guys'– mostly with a background in mechanical, electrical or control engineering – and their idea of how product development should work. But with the rapid increase of electronically controlled functions in cars over the last decade, a different breed of experts have almost unnoticedly populated development centers: computer scientists and software engineers, who mostly came from non-automotive and even non-industry companies, and apart from wearing different clothes and living different lifestyles – which actually made integration on a personal level difficult – had different ideas of (and needs for) product development, complete vehicle integration or quality and reliability." (Weber, 2009, p. 56)

Generally speaking, automakers have implemented efficient development processes that lead to optimal designs for most of their design areas. However, potential synergies regarding the applicability of methods intended for different areas go often unnoticed. Crashworthiness design strategies where the high level targets are decomposed and defined at the component level are available for a number of load cases (see Section 2.5). However, to the author's knowledge, no methodology is currently available for the specification, implementation, and load-path level evaluation for the SOF load case. Such methodology should follow the V-model starting with the requirement and target setting, continuing to the implementation and ending with the testing procedures. A high level of clarity right from the initial design stages can be achieved when the formulation of the requirements is carried out in parallel to the definition of the strategy to fulfill them and measure them at all the relevant design phases.

Additionally to the increase in complexity of the automotive systems, the competition with other automakers has driven the development of more effective product development projects. With the need to improve their development processes and remain competitive in the domestic and global markets, several studies were conducted in order to understand the difference in productivity between the automakers of the USA, Europe, and

Japan. Table 1.1 summarizes the results of one of such studies reported by Percivall (1992). Vehicle development programs with model introductions between 1981 and 1987 were studied and analyzed considering three aspects: the engineering hours needed to complete the program, the total product quality index, and the lead time of the project. The Japanese automakers needed ca. one-third of the engineering hours needed by the automakers of the USA and Europe. At the same time, the product quality index of the USA and Europe projects was 30% less compared to the Japanese, while also requiring 10 months of additional lead times. This implies that the reduction in the development time was not achieved by sacrificing the quality of the product. Two main factors were identified as causes for these differences between automakers. First, the Japanese OEMs relied more on the work of the suppliers than the automakers from the USA. Two-thirds of the components used in Japanese vehicles were black-box procurements, while only one-fifth were black-box in the USA case. A black-box procurement allows the automobile manufacture to focus on defining the performance and specifications of a component, while leaving the supplier with the freedom and responsibility of designing the component. An additional benefit of the use of specifications and a black-box approach is the parallelization of activities from the program engineers, which reduces the lead time and engineering hours.

The focus on specifications makes the definition of their correctness crucial for the success of the program. If the automaker is not capable of defining a set of specifications of the components, it is then forced to test the entirety of the system to verify that the high-level targets are achieved, which decreases the development speed. The specification of requirements divides the complex problem into more manageable and parallelizable tasks. The second factor identified to have an influence on the project performance was the loyalty to the department rather than to the product that is being developed. This is understandable since design specialists optimize the aspect of the system that, from their perspective, is best understood and valued. This point reinforces the need for well-defined systems specifications that design specialists can use to optimize their components, allowing the parallelization of the product development. Approaches such as the so-called solution spaces facilitate the definition of system and component-level specifications and targets.

Table 1.1 Product development performance (Percivall, 1992)

Performance Measure	**US**	**Europe**	**Japan**
Engineering hours (millions)	3.5	3.4	1.2
Total product quality index	41	41	58
Lead time (months)	61.9	57.6	42.6

Automotive OEMs from the USA and Japan followed two different work-planning strategies. Percivall (1992) stated that in the 1980s, Japanese manufacturers allocated resources and set the priorities at the beginning of the development process in contrast to manufacturers in the USA, which increased the number of design changes towards the end of the development process closer to the product launch. The cost implementing

design changes in a later phase is relatively higher than in the early phase. Weber (2009) estimates that the resolution cost per problem is ca. 10X during the concept design phase, 100X during the detail design phase, and 1000X in the prototyping and evaluation phases. The so-called up-front engineering concentrates on solving as many issues as possible in the concept design phase, while the conventional design-build-test approach is shifted towards the production ramp-up phase.

SE dictates that the correct specification at the component level can only be achieved after defining high-level requirements and cascading them into the lower levels. The high-level requirements are defined by governmental regulations and consumer needs. In the early stages of product development, these requirements guide the selection of several solution concepts. Choosing the best solution concept early on in the development process allows for more time to be invested in the optimization and integration of the vehicle system. As mentioned by Bhise (2017), the redesign of any product in the later phases involves higher costs and engineering time that could be avoided by "designing right the first time". Designing right the first time involves making key decisions about the technologies used for the solution concept and creating a set of assumptions to drive the complete development process. Subsequent decisions will depend on the selected technologies and design configurations. If these early assumptions lose their validity in later stages, the changes required to achieve the vehicle targets may involve substantially higher development costs and the discarding of the early design work in virtual or in hardware form.

Crashworthiness Requirements The requirements of any vehicle are twofold: the legal requirements for its legal registration in a given market and the customer requirements that affect an individual user's perception of the vehicle's functions. On one hand, the legal requirements are stipulated in governmental directives and regulations and are well-defined and objectively measured. On the other hand, customer requirements can be subjective (Weber, 2009). Considering this, the process of formulating, coordinating, and tracking a coherent set of product targets is called targets management.

In the case of crashworthiness, the legal requirements in the USA are defined in the Federal Motor Vehicles Safety Standards (FMVSS). Additionally, organizations such as the Insurance Institute for Highway Safety (IIHS) and the National Highway Traffic Safety Administration (NHTSA) also test the crashworthiness of the vehicles and report the results in the form of ratings. The New Car Assessment Program (NCAP), used by the NHTSA, assigns a five stars rating to vehicles presenting 10% probability or less of severe injury to its occupants during the crash tests representing frontal collisions (Hershman, 2001). In this case, the achievement of five starts in the frontal crash test of NHTSA can be seen as a high-level requirement defined by the car manufacturer. This abstract high-level requirement translates to a more concrete objective, namely, a 10% probability or less of severe injury. The probability of severe injury is defined by the NCAP protocol (see Hershman (2001)) as a subspace of two quantities: the Head Injury Criterion (HIC) and the chest acceleration of the driver. The regions corresponding to the probability of severe injury as a function of the HIC and chest acceleration are available

in Hershman (2001). The maximum resultant chest acceleration is measured in the crash test using the information collected by the acceleration sensor located in the chest region of the test dummy. In a similar way, the HIC is calculated using the three-dimensional acceleration measured at the head's center of gravity and the HIC equation stated in, e.g., Christensen and Bastien (2016). Both the HIC and chest acceleration are objective measurements of the vehicle performance and serve as an example of decomposition of the high-level requirement. Consequently, for a consistent and traceable design, maximum thresholds for the HIC and chest accelerations are defined.

Occupant kinematics, and specifically, HIC and chest acceleration, are a result of the restraint system performance and occupant compartment behavior during the crash test. Therefore, targets defined for the dummy kinematics are translated into targets for the restraint system and the vehicle structure. Airbag and seat belt parameters are optimized so that the dummy kinematics and consequently, the HIC and chest acceleration do not exceed the target values. However, the occupant compartment deceleration and stability dictate the maximum performance that can be extracted from restraint systems. Accordingly, targets are also defined with regards to the maximum acceleration as well as to the maximum deformation of the occupant compartment itself.

The deformation of the occupant compartment is a direct function of the stiffness of structures such as the firewall and A-Pillar. Similarly, the maximum acceleration of the vehicle is a function of the mass of the vehicle, initial test velocity, i.e. initial kinetic energy, the energy absorption characteristics of the frontal structure, and the available deformation space. Since the mass is usually a parameter dictated by other factors in the vehicle development rather than crashworthiness, the energy absorption characteristics and the available deformation space remain as the only properties that influence the performance of the frontal structure and that depend on the crashworthiness design. Both, energy absorption characteristics and deformation space can be interpreted as force-displacement characteristics of the components of the front structure, which in consequence means that targets defined upon the force and deformation levels of the components are also defined to produce the desired structural performance.

By using the relationships between mechanical quantities such as dummy kinematics, initial kinetic energy, acceleration, and energy absorption, it is possible to decompose the high-level targets into component-level requirements. The so-called functional properties of the components, i.e. force-displacement characteristics, are designed in order to achieve the energy absorption and deceleration levels required to allow for an optimal performance of the restraints systems and subsequently dummy kinematics, i.e. HIC and chest acceleration, that lead to a lower probability of severe injury and finally the desired rating. An analogous application example of the use of SE in crashworthiness design and the definition of multi-level requirements is documented in the work of Hong et al. (2006), where the frontal structure of a vehicle subjected to a frontal crash load case is designed using an aluminum material concept.

The HIC and chest acceleration are well-defined by means of a mathematical function describing the regions of probability of severe injury. However, additional methods are required to define a range of values for the functional properties that allow the fulfillment

of the acceleration and occupant compartment deformation requirements. This fact highlights the need for two concrete methodologies. The first methodology should be capable of coupling the high-level mechanical behavior of the dummy and occupant compartment to the functional properties of the components. The second methodology should provide the information to indicate the ranges in which the values of the functional properties yield the acceleration and deformation values that fulfill the structural targets. Both points are addressed in this work; the first one in the form of the so-called low-fidelity model (see Chapter 4) and the second one in the form of the so-called solution spaces approach (see Chapter 5).

Solution Spaces With the increasing complexity of the systems designed in the product development process, the cooperation among different engineering areas and teams becomes essential. This collaborative design increases the need for intensive communication as well as negotiation among the different areas concerning the implementation of design solutions. However, the best solution for a particular engineering area may not represent the optimum for another. As Lottaz (2000) states, conflict occurs in the negotiations when only a single solution is proposed and no common ground can be found so that the component and high-level requirements are satisfied. The underlying principle of the solution spaces approach is to generate independent intervals for every functional property of the system, so that a design within these intervals fulfills the low and high-level requirements. Under the consideration that all design variables representing the functional properties stay inside the intervals defined in the solution space, deviations of a particular parameter do not imply adjustments to other parameters. This approach creates the desired flexibility in the development process and facilitates the interactions with the areas involved in the design. Intervals in solution spaces are selected so that when the functional properties lie within these ranges, the system's requirements are achieved. Additionally to the increased flexibility in the interaction with different engineering areas, the solution spaces approach has the benefit of being able to define such intervals as low-level requirements and use them to drive the design during the early design phase. Yet, it is possible that during later phases, design variables take different values than the ones specified in the early phase either due to changes inherent in the design maturity or changes due to uncontrollable sources of uncertainty. Solution spaces ensure that, as long as these deviations lie within the specified interval, the uncertainty related to the fulfillment of the high-level requirements is eliminated.

The solution spaces approach requires an efficient and relatively cheap evaluation of the feasibility of the design. Therefore, the model to be used as evaluator should have the following main characteristics. On one hand, the functional properties of the system, upon which the component requirements are being defined, should be directly mapped to the system level response to evaluate if the high-level requirements are fulfilled. Since the definition and decomposition of the requirements are carried out during the early design phase, the evaluator model should use as input only the information available at this design phase. On the other hand, the evaluation of the feasibility should allow for a large number of iterations to determine the largest solution space possible. A physics-

based low-fidelity model used as evaluator model facilitates the implementation of the solution spaces approach. The kinematic model proposed in Chapter 4, that estimates the vehicle trajectory during the SOF crash test based in the vehicles properties, fulfills these conditions.

Three potential benefits are identified when including the solution spaces approach in the development process. The first one consists on the parallelization of the design tasks. If the intervals that guarantee the fulfillment of the system requirements are independent, the detailed engineering of the components can be done in parallel without the explicit need of evaluating a model of the complete system to assess the feasibility of the design. The second benefit is that the interval itself can be used as a constraint during the detailed engineering phase and other relevant objectives, such as weight and production cost, can be optimized at the component level. The use of intervals in the optimization process improves the chances of obtaining lightweight designs that do not impose deviations to the functional properties jeopardizing thus the fulfillment of the high-level requirements. The third benefit is that, even if the functional properties vary in a later design phase due to the influence of manufacturing or other sources of uncertainty, the system will still be able to reach its targets as long as such variations do not surpass the defined intervals. For these reasons, the use of solution spaces improves the robustness of the system.

Robustness "Real-world crashes often occur in scenarios dissimilar to laboratory barrier crash set-ups" (Wagstrom et al., 2013, p. 385). Dissimilarities between the evaluation conditions specified in the crash test protocols and the real-world environments are considered in the work of Wagstrom et al. (2013). They quantify the influence of parameters such as initial velocities, and vehicle relative orientations on the structural response in frontal car-to-car crash scenarios. Using finite element models of two identical vehicles, Wagstrom et al. (2013) identify collision scenarios that produce a significantly different structural response between the two vehicles. In other words, the robustness of the structure is assessed by varying the test conditions. A robust structural design is expected to offer protection to its occupants despite the uncertain real-world crash conditions. This implies that the probability of meeting the high-level structural requirement should remain acceptable even when considering uncertain test conditions.

Regardless of the fact that the majority of the models used to design systems and components is deterministic, in real-life there are several sources of uncertainties concerning the test conditions and functional properties of the components that cause a scattered system's response. In the automotive industry and specially for crashworthiness design, authors such as Eichmueller and Meywerk (2020) claim that relevant factors such as the material properties, e.g. the plastic flow curve, may present variabilities of ± 20 MPa; wall-thickness variations of ± 0.01 mm; relative position deviations of the longitudinal members of ± 1 mm and orientation deviations of ± 0.5 degrees. Although, the uncertainties may be reduced by avoiding imprecise interface requirements and poorly defined test environments, real-life applications of systems engineering demand the quantification of the effect these uncertainties have on the system's response and particularly, on the ability of the system to fulfill the high-level requirements (Kossiakoff et al., 2020). In

the particular case of the SOF crash test, the suspension subsystem adds to the already known sources of uncertainty present in crashworthiness. The mechanical properties of the linkages and their connections to the knuckle and sub-frame, the rupture behavior of the wheel as well as the interaction of the tire with the rest of the structure and the barrier can significantly influence the system's response. The study of the effect of these uncertainty sources and their classification in the context of crashworthiness design is the focus of Section 6.2.

1.1. Aims and objectives

The aim of this work is to develop a framework for the crashworthiness design for the SOF load case. Combining the best components of the legacy processes, as well as innovative, physics- and statistics-based methodologies, this work uses the systems engineering framework to develop a design strategy that accelerates the crashworthiness design while producing robust structures capable of efficiently fulfilling the requirements of the SOF load case. The complex design process, starting from the early design phase and finishing with the official crash test of the series production vehicles, can be standardized in order to accelerate it. Figure 1.1 presents the design framework proposed in this work.

This process is triggered by the introduction a new vehicle concept with a given set of vehicle characteristics such as vehicle type and proportions. From early on, the target structural ratings for each load case, including the SOF load case, are defined. Taking this full-vehicle primary structural target as a base, this work proposes a systematic decomposition into load-path and component requirements. The requirement decomposition demands the definition of the functional properties for each level of abstraction. For this purpose, this methodology introduces a selection of abstract physical quantities, i.e. component functional properties, in the form of force-displacement curves or resistance-to-deformation characteristics. These characteristics are used as design variables first at the full-vehicle level and then at the load-path level, where the decomposed requirements are used. The properties are mapped to the structural response via a low-fidelity kinematic model that efficiently calculates the trajectory of the vehicle during the crash using only the information available at the early-phase design as input.

The selection of intervals or ranges, within which these design variables should lie to guarantee the fulfillment of the high-level requirements, is found through the development of an enhanced solution spaces approach. The identification of such ranges is carried out in a Data-driven Solution Space Definition framework. Here, the relationship between the kinematic behavior at the full-vehicle level and the resulting structure rating, determined in a correlation analysis using the available crash tests by the IIHS, is used along with physical and mathematical models to find a set of feasible designs and their correspondent functional properties. Once these sets of feasible designs or solution spaces have been defined, the simulation-based design cycle starts. In this cycle, the functional properties of the initial design are measured in a FE model of the vehicle by means of a dedicated post-processing routine. Design changes are implemented so that the low-level requirements are fulfilled following a Solution Space-based Iterative Simu-

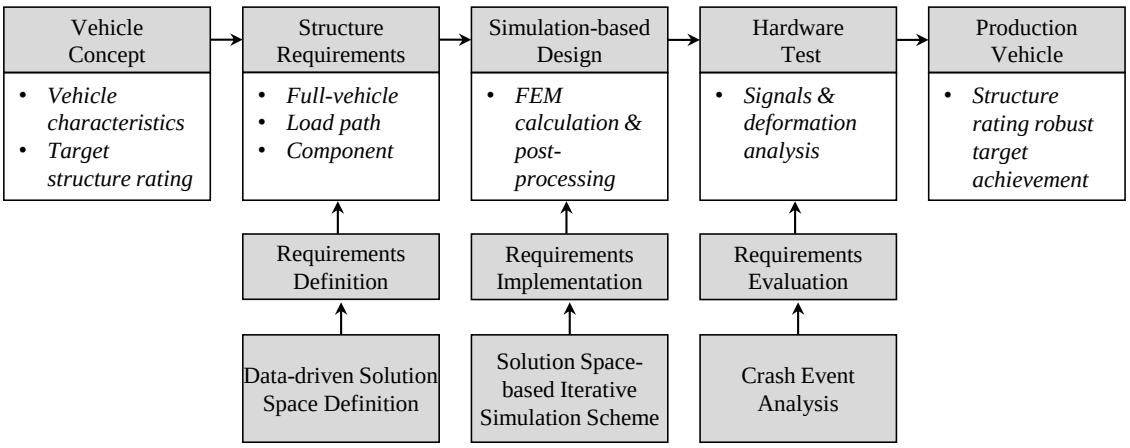

Figure 1.1 Proposed crashworthiness design for the SOF Load Case

lation Scheme, where the fulfillment of the constraints defined by the solution space is used as the objective function of an optimization procedure.

The robustness of the design is explicitly considered by characterizing and modeling the relevant sources of uncertainty that affect the structural response in this specific load case. Efficient sampling algorithms are implemented to maximize the coverage of the uncertainty space and, at the same time, minimize the necessary number of samples. Additionally, a novel Robustness Index is introduced to describe the scatter of the response of the system and to define objective targets that produce a robust achievement of the primary structural targets.

When the virtual design cycle has converged to a mature design, hardware tests are conducted to validate the performance of the vehicle. In order to measure the functional properties and be able to compare them against the requirements in the hardware phase, a specialized Crash Event Analysis is here carried out. The Crash Event Analysis is performed through the use of a dedicated force-measurement barrier in combination with a trajectory reconstruction tool. With this approach, functional properties of individual components can be recreated enabling the assessment of the fulfillment of the low-level requirements in the hardware phase. This serves as a tracking mechanism for the performance of the components in case the primary structural targets are not achieved. Ultimately, when the design process is concluded, the evaluation of the series production vehicle conducted in the official test by the IIHS serves as definitive validation of the structural performance of the vehicle.

The present work is structured as follows. An overview of the current design methodologies used in the automotive product development, is given in Chapter 2. First, the well-established Systems Engineering (SE) process is introduced with focus on the cur-

rent strategies for the implementation of the V-model used for the definition, verification and validation of requirements. Then, the process of defining high-level requirements and their decomposition into low-level component requirements is analyzed. Next, the design phases in the automotive product development process are studied, while establishing the gaps and areas of improvement of such processes oriented for crashworthiness design. Additionally, the use of the low-fidelity models in the context of crashworthiness design is analyzed in parallel to the current techniques available for the calculation of solution spaces. Afterwards, an examination of the techniques for uncertainty quantification and robustness analysis is presented. The state of the art chapter finalizes with the current methods to analyze and design the structural response of vehicles subjected to the SOF load case. In Chapter 3, a characterization of the kinematic and structural behavior of the vehicle is introduced with the objective of establishing the relationships between selected kinematic parameters and the resulting deformations of the occupant compartment. Next, Chapter 4 presents a low-fidelity kinematic model, defined for the full-vehicle and load-path levels, capable of describing the trajectory of the vehicle by using input parameters such as its mass and proportions. This is followed by the development of a SOF specific solution spaces method in Chapter 5. Then, in Chapter 6, the Solution Space-based Iterative Simulation Scheme has the objective of integrating the solution space into the virtual design cycle in parallel with the explicit consideration of the sources of uncertainty. A robustness index is introduced to characterize the response of the system under the scatter of the relevant input parameters. The kinematic model and solution spaces are validated by the comparison to the results of a hardware crash test in Chapter 7. Afterwards, the presented methodologies are applied in a design exercise with the objective of improving the robustness of the response of a vehicle evaluated with a full-vehicle FE model. Finally, the limitations and outlook of these methodologies are discussed in Chapters 8 and 9.

Research questions The following questions are established as starting point for this research and are answered in the following chapters.

- How to accelerate the structural design of vehicles subjected to the SOF crash test?
- How to characterize the kinematic response of vehicles during the SOF crash test?
- How to characterize the structural response of vehicles during the SOF crash test?
- How to represent the SOF crash test with a model suitable for the early design phase?
- How to calculate solution spaces for the selected functional properties in combination with a kinematic model?
- How to include the sources of uncertainty in the structural design?
- How to define the robustness of a design?
- How to validate SOF low-fidelity models?
- How to validate solution spaces?
- How to improve the robustness of an existing structural design?

Innovations presented in this work

- Characterization of the kinematic response of a vehicle subjected to the SOF load case
- Summarization of the SOF structure rating in a single scalar value
- Identification of kinematic behavior that leads to the robust achievement of a Good SOF structure rating
- Development of a SOF low-fidelity kinematic model that predicts the vehicle trajectory using high-level properties at full-vehicle and load-path levels
- Further development of the solution spaces method for SOF kinematic model applications
- Characterization of the sources of uncertainty affecting the SOF load-case
- Definition of a robustness index to characterize the vehicle performance in the SOF load case
- Development of a crashworthiness design framework for the SOF load case

Chapter 2

State of the Art

2.1. Systems Engineering

The automotive product development has the objective of creating a system, i.e. a vehicle, through a series of steps, tasks and operations that use several inputs, such as information, raw materials and energy sources. This series of steps is called a process (Bhise, 2017). In the context of product development and Systems Engineering (SE), the definitions of a system available in the literature (Kuykendall, 2001; Blanchard and Fabrycky, 2011; Winner, 2013; Bach et al., 2017; Bhise, 2017; Kossiakoff et al., 2020), coincide in the following points:

- A system contains a set of components or elements that perform together to execute one or more functions.
- These elements are different to one another and are connected to perform a greater function not individually achievable by themselves.
- The effect of each component in the system's response is traceable.
- The decomposition of the system facilitates the definition of low-level requirements such that, if fulfilled, a high-level target is achieved.
- A system has predefined boundaries and interactions among its elements.
- These boundaries are defined according to the allocation of the system's functions.
- A system is considered complex if it incorporates a collection of interacting and diverse elements with intricate relationships with one another.
- The hierarchical structure of a system is populated in the upper levels by the subsystems which perform a subset of the high-level functions. The lower levels are reserved for subdivided elements that perform primary functions only when organized and in coordination with other elements.

SE is a goal-independent and process-oriented methodology for developing complex systems. The International Council on Systems Engineering, INCOSE, defines SE as an interdisciplinary means to enable the realization of successful systems by early focus on

customer needs, documenting requirements, design synthesis, and system validation (INCOSE, 2015). SE is a core competence to cope with complex systems in the automotive world and to ensure that an objectively verifiable methodological framework is put into place to facilitate the development of optimal solutions for automotive systems (Winner, 2013). The goal of SE is to guide the engineering development of the system as a whole by selecting the path to follow out of the multiple possible paths (Kossiakoff et al., 2020). This guidance also considers the uncertainty of two factors that affect the system performance: the operating environments and the future requirements. The system as a whole must have an effective performance even under operational environments that are variable and in continuous evolution, without increased costs or increased complexity.

SE can be understood as a multidisciplinary decision-making engineering process, whose objective is to design and verify that vehicles fulfill their high-level requirements by defining component-level specifications. The hierarchical nature of the system is characterized by Bhise (2017) by means of a top-down approach, which interprets the product, i.e. the vehicle, as a whole system and then decomposes it into lower levels, i.e. subsystems and components. By means of suitably defined specifications, the lower levels are designed to meet the requirements of the higher levels. Ultimately, systems engineering, together with other engineering disciplines, has the objective of establishing the vehicle high-level requirements, allocate the functions to the subsystems in the vehicle and define the appropriate set of specifications to the low-level entities or components. This process of formulating requirements, designing and validating the design is formalized in the so-called V-model.

There are different interpretations of the V-model which are fine-tuned to suit the needs of specific applications (Fisher, 1998; National Highway Traffic Safety Administration, 2007; INCOSE, 2015; Bhise, 2017; D'Ambrosio and Soremekun, 2017). However, a consensus exists on the V-model having these four steps: 1) definition of high-level requirements and concept, 2) decomposition of systems and definition of requirements for each design level, 3) design and engineering implementation, and 4) verification and validation. Figure 2.1 presents an interpretation of the V-model in the context of crashworthiness design. The following provides the perspective of different authors on the aforementioned steps.

1) Definition of high-level requirements and concept. The first decisions regarding concept solutions and technologies are taken with the support of feasibility studies carried out through a concept exploration stage, which is subsequently based on the scope of the project and overall configuration. In the automotive product development, it is during this step that high-level vehicle characteristics, e.g. vehicle type, intended markets, power-train location and technology, are defined.

2) Decomposition of systems and definition of requirements for each design level. Transition from a general overview of the system to a detailed perspective of the system's specifications. Several layers of decomposition take place so that the system is divided into subsystems and components. This decomposition also takes place from the requirements' point of view. High-level requirements are divided into more detailed specifications that are allocated at the subsystem and component levels. Besides the specification of the

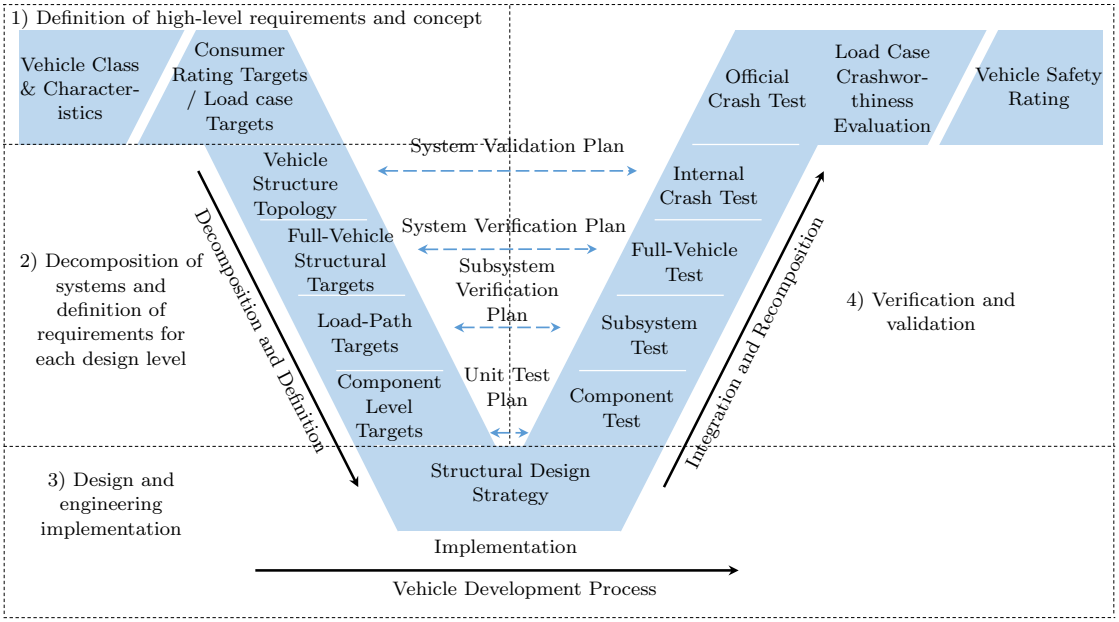

Figure 2.1 Systems engineering V-diagram for crashworthiness design (Illustration based on National Highway Traffic Safety Administration (2007))

functional properties of the components themselves, supplementary requirements on the interfaces of such components are also needed. During this specification process, it is ensured that every requirement can be measured and confirmed, otherwise the requirement is considered invalid. This aspect implies an increased difficulty in the cascading and definition of the requirements. However, being able to track down the performance of every component to understand the root cause in case of a malfunction is specially advantageous in the system-level validation step. This point also highlights the fact that a relatively high number of low-level requirements does not necessarily guarantee the achievement of the high-level objectives. It is actually the quality of the requirements at the lower level the key for a successful system development.

3) Design and engineering implementation. The core of the V-model is the implementation of the concept solutions at the component-level, namely the component engineering and development. Here, the previously defined specifications are transformed into engineering solutions for the lower-level entities of the system. The benefits of a suitable component specification are relevant during this step. The parallelization of the engineering of the components is only possible if the development is independent and conducted without the need to test the complete system in every design iteration.

4) Verification and validation. After the component design, the verification of the specifications takes place. The verification implies the measurement of the relevant characteristic and the comparison of the value of such characteristic to the upper and lower limits of the specification. Hardware and virtual tests are performed first at the lowest

level, i.e. component, and then a sequential integration of components is carried out with its respective verification test. The objective is to determine if each component and subsystem meet their requirements, and then in the final step, validate the performance of the complete system. In order to systematize the documentation of the verification process, a verification event should be recorded by the responsible individual with the correspondent test procedure and system configuration, i.e. which combination of components is tested. The so-called verification test can be done virtually to simulate a considerably larger set of test and manufacturing conditions to show that the component is able to fulfill its requirements despite of variations. The verification is only possible at the component and subsystem level. Therefore, the validation takes place at the system level. Through the use of a validation plan to establish the most critical configurations, the system-level performance and the fulfillment of the high-level requirements is confirmed. The official crash test, conducted either by the governmental institution or by the independent organization, is the final performance validation step in the context of crashworthiness design.

These four steps are schematically represented in the V-model in Figure 2.1. The left side defines the system, its components and requirements, the bottom part addresses the design of the components, and the right side verifies the design specifications and validates the system performance. The symmetrical nature of the V-model is a reflection of the relationship between the steps on both sides. During the system requirements analysis, the verification plan is developed in parallel so that the system engineers explicitly consider how to verify each requirement as they are being defined (National Highway Traffic Safety Administration, 2007).

Additionally to the traditional V-model, enhanced techniques that tackle some of the model's limitations are available in the literature and presented as follows:

5 Loops V-model. Introduced in the work of Bhise (2017), this enhancement defines the V-model in five loops: requirement loop, design loop, control loops, verification loop, and validation loop. The loops represent that several iterations are needed to define the high-level requirements as well as the decomposition of the lower-levels design specifications. The iterations ensure that high-level requirements are reached when the low-level requirements are fulfilled and that low-level requirements are achievable with the selected technologies.

Decomposition tree. In order to make the system decomposition process in a structured manner, Bhise (2017) proposes the use of a hierarchical diagram or decomposition tree, where the subsystems, and components are graphically organized below the system level. The decomposition tree allows for an efficient traceability of the components.

Onion model. This model is proposed by Fisher (1998) as an alternative to define the system's hierarchy and is constructed using the following steps. First, high-level requirements are defined along with a high-level model. Second, a high-level physical design, verification and validation plans are developed. Third, the requirements are traced to the model, to the design and to the verification plan to confirm that all requirements were addressed. Fourth, the first three steps are conducted iteratively until every requirement and every level are considered. This technique iterates over the design levels and offers

a method to confirm that no requirement is left behind. However, it can become costly for systems with a relatively high degree of complexity.

Matrix diagram. The use of models as mapping functions between low-level characteristics and system response enhances the understanding of the system. However, if the use of models is not possible, Bhise (2017) suggests to use matrix diagrams to document the input-output relationships by sorting the vehicle characteristics as rows and vehicle systems in columns and expressing the strength of the relationship with an integer number starting with 0 representing no relationship and ending with 9 representing a strong relationship. This matrix diagram provides a basis for the requirement decomposition but does not help in the definition of the design specifications.

Concurrent design. As documented in the work of Mario et al. (2013), this approach focuses on the design and engineering step of the V-model and proposes to systematically decompose the complex design tasks into various subtasks that are conducted in parallel. This collaborative technique based on an intensive communication exchange also offers mechanisms to establish clear communication channels. The information exchange is intensified at the beginning of the design process and clear interfaces between the components and subsystems as well as ranges for the specifications are established, so that as long as the component performance is within specification range, the high-level targets are achieved. A wide specification range provides more flexibility to the designers and also reduces the need for increased information exchange.

Simultaneous Engineering. Similarly to concurrent design, this technique prioritizes the parallelization of the development tasks over serializing them (Mario et al., 2013). However, this parallelization occurs within the design level of a component itself and not among components or subsystems. This technique offers the possibility of early identification of issues with the selected design concept. With this approach, an accelerated design cycle is made possible at the expense of increased resources and manpower.

Front-loading. This approach presented by Mario et al. (2013) is used to define as many multi-level requirements as possible during the definition of the high-level targets. The shift of the resources to the concept step of the V-model as well as the utilization of knowledge from previous projects has the intention of reducing the development time. The availability of knowledge, either from experts or previous projects, is essential. However, the universe of possible concept solutions is constrained to the previous implementations, which may lead to stagnation.

Agile SE. The design iterations at the low-level result in an implicit bottom-up approach contrary to the top-down approach intended by the V-model. The Agile systems engineering proposed by Kossiakoff et al. (2020) prioritizes the search of alternatives and their integration solutions. These activities are expected to be done in parallel to the traditional system engineering activities to avoid the discarding of potential solutions due to the rework needed to integrate them in the system in the later stages.

Model-based SE. The need of a mapping function between the system response and the functional properties of the components is addressed by the so-called model-based Systems Engineering. Friedman and Ghidella (2006) define a model-based design as an approach that uses a representation of the system, i.e. a model, as a form of an exe-

cutable specification that designers can rapidly evaluate, modify and integrate into larger systems. D'Ambrosio and Soremekun (2017) interpret the model-based systems engineering as a systematically-constructed information repository that uses models instead of documents as a central element to capture information. In order to avoid a document-intensive SE approach based on document searches, a model-based is preferred so that rich queries yield relevant, compact and meaningful information (Kossiakoff et al., 2020). This strategy is formalized by the use of modeling languages, such as the Unified Modeling Language (UML), and the Systems Modeling Language (SysML). These models and meta-models or low-fidelity models are used in the early stages of development and become a central tool for the mapping of system responses and low-level functional properties. To exploit the potential of the low-fidelity models, the amount of information needed for the model to work should be minimized to be compatible with the lack of information present in the early stages of development.

2.2. Definition of Requirements

As described previously, the definition of requirements and their decomposition into the lower levels is one of the key steps when using the V-model in SE. A requirement specifies a characteristic of the product that, when evaluated in the test environment, results in the accomplishment of a given objective (Bhise, 2017). The types of requirements can be classified according to the hierarchical level in which they are defined and what type of aspects of the system they evaluate. Kossiakoff et al. (2020) presents in his work the following classification:

- Functional requirements: refer to the capability of the system to perform a specific action under a certain operation condition and is defined at the system level.
- Performance requirements: provide details on how the action defined by the functional requirements should be executed.
- Physical requirements: refer to the physical characteristics and attributes of the system, e.g. weight, volume, material.
- Operational requirements: description of the execution in terms of the operational outcome.
- System-level requirements: quantitative metrics to specify system performance.
- Component-level requirements: technical details of the functional properties of the components.

The main benefit of defining requirements across the hierarchical levels of the system is the parallelization of the design tasks and the traceability of the influence factors of the system performance. Additionally, the cross-functional interactions are made visible across the different engineering teams and the transparency regarding the priority of the system's performance is increased (Bhise, 2017). The design responsibilities are also clearly divided among the different areas. Enabling the confirmation of the completeness of high-level requirements in the early phase. In this way, quick assessments of design changes and their impact in the vehicle performance are made possible and early verification procedures can be put into place.

The requirement development process is costly and time consuming. Considerable amounts of data may be gathered, together with test results and evaluations, before a requirement is developed. For this reason, Bhise (2017) states that requirements may be derived in the first instance from standards, design guidelines, evaluation procedures and experience from past failures and successes. Independent of the source, the quality of the requirements should also be evaluated to maximize the chances of project success. Characteristics of good requirements according to Bhise (2017) are: unambiguity and completeness, consistent terminology and traceability across the hierarchical structure, clearness of the conditions of applicability, verifiability (the relevant characteristic can be measured and compared against its specification), feasibility, and independence of other requirements at the low level. In contrast, the validation of the requirements implies that it has been determined that the fulfillment of the requirements at the low-level assures the achievement of the high-level targets.

In the automotive development process, Bhise (2017) expresses that the definition of vehicle-level requirements is the focus of the initial phase. These product-level requirements define the basic attributes of the vehicle, e.g. cost, size, weight, body-style, safety, and vehicle dynamics. Even if the details of the implementation are still unknown at this stage, the information derived from the product-level requirements can be used to trigger the requirement decomposition of the subsystem levels. In the next sections the phases of the product development process are examined in detail.

2.3. Product Development Process

As presented in Chapter 1, the cost of implementing design changes in a later phase is relatively higher than implementing them in the early phase. The definition of high-level requirements and their decomposition to the component level allows for the maximization of design changes to take place in the early phases. However, the availability of information on the system and components is limited in the design phase. For this reason, considering the information that is actually available in each development phase is crucial for the effective definition and implementation of the requirements.

The definitions of the product development phases available in the literature (see for example, Dowlatshahi (1992); Makkonen (1999); Sellgren (1999); Shephard et al. (2004); Wall (2007); Weber (2009); Mario et al. (2013); Sandberg et al. (2013); Yadav and Pradhan (2014); Ulrich and Eppinger (2015); Bhise (2017); Kossiakoff et al. (2020)) offer already detailed descriptions of the main deliverables and tasks performed in each phase. The identified product development phases are: 1) product class definition, 2) early phase design, 3) simulation-driven design, and 4) hardware-based validation. The characterization of the development phases is here re-formulated in terms of the availability of information at each phase and framed in the crashworthiness design context to reveal potential gaps in the current task decomposition approaches.

2.3.1. Product Class Definition

In the first phase, called product class definition or definition phase, the idea of creating a new product is generated together with a time-horizon towards the release of the product. The initial characteristics as well as the high-level requirements definition are based on market research and regulations of target markets, including crashworthiness assessments. These characteristics are expressed as the type of vehicle to be developed in terms of shape, size and styling. As stated by Weber (2009), the optics of a vehicle's body and proportions are the features that are first perceived by the buyer. The product class definition phase is where the raw-vehicle properties are defined together with the product profile and strategy. Such strategy should converge to a consistent set of high-level requirements for the selected vehicle class. The raw-vehicle properties refer to the vehicle style and proportions such as the wheel base, wheel size, track, overhangs, pillars' shape and belt line. This geometrical features trigger other conceptual dimensions such as the wheel house size, front rail transversal position, and pillar positions and dimensions. As a result of these geometrical definitions, the exterior and the interior structural components of the vehicle's body are roughly positioned in a preliminary 2-D packaging process, in which geometrical conflicts are identified and resolved. According to Bhise (2017), the high-level vehicle specifications defined in this phase are:

- vehicle type, body-style and size;
- exterior dimensions, e.g. length, width, height, cowl position, windshield slope angle, wheelbase, overhangs, track, ground clearance and approach angles;
- interior dimensions, e.g. seating reference point, pedal position, head, leg, knee and hip room for all occupants;
- longitudinal and lateral motion performance, e.g. acceleration times, maximum speed, stopping distance, turning radius and lateral acceleration while turning;
- energy efficiency and range.

With vehicle characteristics such as the overall dimensions, longitudinal and lateral motion performance, together with the energy efficiency and range, full vehicles properties such as total mass and rotational inertia are derived. This phase also includes the evaluation of economic feasibility and development of a framework for the evaluation of the component and system properties. Additionally to the overall vehicle shape and size, Bhise (2017) includes in this first phase the so-called pre-program planning. This planning involves the definition of the mission statement of the vehicle program based on the consumer needs and set of primary specifications for this particular vehicle class.

2.3.2. Early-phase Design

The information set derived in the product class definition phase enables the subsequent early-phase design to develop the system properties and requirements with a higher level of detail. The main purpose of the early-phase design is to get to a level of detail that is enough to determine if the design can meet all the high-level requirements and component targets. Therefore, the target agreement represents a central milestone of this design phase. The main derivable of the early-phase design, often called concept

phase, is a product and production concept that is technically and financially feasible indicating that the production and project targets are within reach by using the selected technologies.

In the early-phase design different solution concepts, that may also involve different technologies, are proposed and evaluated technically and accordingly to the business plan (Bhise, 2017). The solution concepts are conceived in the form of coarse CAD models of the interior and exterior of the vehicle. The tools to evaluate the alternative concepts are market research clinics, technical reviews and early-phase simulations. Low-fidelity models can be used to analyze the feasibility of the high-level requirements and its implementation at the component level. Even if these low-fidelity models do not provide the same level of detail of a later-phase simulation, they are useful tools to predict if the targets are achievable even if the industrialization of the product has not been yet detailed, particularly when considering the economic commitment implied by the concept selection.

2.3.3. Simulation-driven Design

The simulation-based design is a process where the primary means to evaluate the performance and verify requirements is the simulation. It takes place at two different stages of design: the first one immediately after the target definition where simulations serve as evaluations of the feasibility of the targets; the second one when the continuation of the project to mass production is confirmed and simulations are used to consider the design changes due to the industrialization and manufacturing processes. The virtual product design phase, also called engineering design phase or detailed engineering, focuses in the design, testing and analysis of the system's components and the system as a whole. This detailed design converges to the release of the interior and exterior surfaces of the vehicle's structure up to the lowest level, where the component design triggers the manufacturing process for tooling and the supply chain. To efficiently reach this level of detail, e.g. geometry, material specification, surface properties, considering the restricted time-frames, virtual tools are used in a simulation-driven product development framework. The main goal is to predict the behavior of the components without the need of physical prototypes with acceptable accuracy. After several design iterations, simulations ensure that the components meet their requirements.

The benefits of a simulation-driven design are particularly evident in the early stages, where the ability to choose the optimal solution far outweigh the cost of implementing the necessary design changes to integrate them. This approach not only allows for the efficient verification of the solutions but also enables an open dialog with the other stakeholders involved in the product design to generate optimized solutions. The work units of the simulation-driven design are the system and component models. Different models are used for different purposes: economic models are used to evaluate market-relevant or business-case-relevant data; process models are used to design the information workforce; functional and geometrical models are used to predict, analyze and evaluate the influence that technical characteristics of the components have on the fulfillment of the high-level requirements.

Being the geometrical integration one of the key components of this virtual product design phase, Computer Aided Design (CAD) models serve not only to identify static interferences, clearances and collisions, but also to analyze operational movements. The wheel envelope, which accommodates all of the possible steering and suspension-travel movements, exemplifies a relevant geometric integration and operational movement analysis that directly affects the available space for the front structure of the vehicle and potentially influences the crash performance. The detailed crash behavior of the vehicle is evaluated using specialized virtual design tools such as FE models.

These models use discretized geometries derived from the 3-D CAD models with material characteristics and boundary conditions assigned with the objective of predicting the relevant mechanical responses of the vehicle when subjected to a particular load case. The use of the FEM involves three main steps: pre-processing, solution, and post-processing. During the pre-processing step, the discretization and simplification of the physical system is conducted; next, the solution process involves a numerical solution of the governing equations over the modeled space; finally, during the post-processing step the relevant output quantities are extracted from the simulation. Given that the cost of performing a full-vehicle crash test using physical prototypes lies in the range of millions of euros, the most elaborated simulation methods, e.g. explicit finite element models (EFEM), are used during the vehicle development framework (Weber, 2009). In these models the accuracy of the simulations should be such that the result of the hardware test confirms the observations obtained from the simulations (Weber, 2009). Even if the monetary costs of the evaluation of physical prototypes are magnitudes greater than the computational costs associated to virtual crash testing, the creation of models and further evaluation is an intricate process. A state-of-the-art EFEM of a full vehicle contains ca. 10 million shell elements, with an edge length between 3 to 10mm, and requires up to 30h using 400 CPUs (Jergeus, 2018). At the early-phase design, the lack of information about the secondary subsystems, i.e. interior and exterior trims, leads to the use of reduced models, where only the structural components and other relevant subsystems, such as the power-train, are explicitly represented. The primary information extracted from the EFEM corresponds to the nodal displacements, i.e. structure deformation, acceleration and force measurements of the virtual test dummy. The secondary information set corresponds to the section and contact forces, internal energy values, plastic deformation, damage and failure values of the sheet metal and solid components, as well as the state of the joining elements such as structural adhesives, spot- and seam welds. Herewith, the component and system level requirements are virtually verified.

Considering the benefits of the use of a simulation-driven design, this approach has become predominant in the automotive industry as the primary tool for decision-making. However, as Youn et al. (2011) states, issues related to the uncertainty and scatter on the component properties and test conditions that affect the systems response should be studied. A calibration plan is often implemented for this purpose. Here, the design engineers start from the system-level and select key performance indicators and then trace the influence of each component-level property. Additionally, a calibrated execution identifies the predictive models, where both known and unknown input variables co-

exist. Finally, through the use of a statistical calibration technique the results of the simulations are compared with physical tests. An improved level of accuracy is reached after optimizing the response of the simulation, taking the unknown inputs as design variables and minimizing the statistical deviation to the physical results.

The analysis of the influence of uncertainty on the system performance and the subsequent design improvements leads to a more robust system. The characterization of these uncertainties as well as the efficient evaluation and analysis of their influence are the main facilitators when explicitly considering uncertainty in the design process. Methodologies such as the use of low-fidelity models and the solution spaces approach for the early-phase design, as well as the robustness analysis for the simulation-driven design phase can be used to address this topic. They have however not been applied together in a crashworthiness application for the Small Overlap load case. This work addresses this gap.

2.3.4. Hardware-based Design Verification and Validation

It is the objective of this phase to evaluate the performance of the individual system components and the whole assembly as well as their integration into a complete working system. It includes developing a test environment to analyze the performance of the full vehicle (Kossiakoff et al., 2020). A so-called test and evaluation master plan (TEMP) is used to define the critical configurations to be tested in hardware form.

The need for hardware tests becomes especially relevant during two different development phases. The first phase corresponds to the early prototypes. Here, the need to confirm the simulation results is key to continue towards the design freeze of the tooling required for the series production. These prototypes have a relatively high cost and the information extracted from the real crash tests is essential to identify any deviation from the investigations using the virtual prototypes. The second phase is the pre-series evaluation. At this later phase, the structural design of the vehicle is evaluated and the series manufacturing processes are assessed. Any changes required at this phase involve a relatively high cost due to the implicit design change needed in the tooling.

In contrast to the virtual design phase, a considerable allocation of resources may be needed to implement output analyzers that convert the physical measures obtained from the tests into quantities that are used to determine if the multi-level requirements were fulfilled. The three main sources of information in a crash test are: a) the acceleration, force, and rotational velocity signals from sensors in the test dummy, vehicle and barrier, b) the high-speed video footage and c) the post-crash static deformation measurements. According to Weber (2009), up to 20 high speed cameras capture the three-dimensional motion during the crash and ca. 35,000 data items are recorded per dummy. Considering the frontal impact and rating requirement example of Chapter 1, the Head Injury Criteria (HIC) and chest acceleration can be directly obtained from the analysis of the signals captured by the sensors of the test dummy along with the deceleration and deformation of the occupant compartment. However, the functional properties such as force-displacement curves and energy absorption at the component level can only be estimated by analyzing their deformation. The lack of hardware options to measure

force-displacement characteristics at the component level represents a setback in the verification of the requirements process during the hardware test phases. To fill this gap, this work introduces a methodology to extract all of the information required for the verification of the requirements from the system to component level, based on the use of a dedicated force-measurement barrier for the Small Overlap load case, presented by Silva and Parera (2016).

2.4. Low-fidelity Models for Crashworthiness Design

The development of low-level requirements in the context of SE requires the mapping of the functional properties at the component level to the system-level response. The models used for this mapping, on one hand, have to provide an acceptable level of accuracy, while on the other hand, must be able to operate without detailed information on the system and its components. This potentially contradictory condition is tackled by developing models that are based on first principles simplifying thus the physics of the phenomenon. In this way, global properties such as masses and approximated geometries, which are available at the early phase, are sufficient to generate the necessary output to drive the design in the early phase. One of the first registered examples of the use of low-fidelity models in the context of automotive product development is documented in the work of Mario et al. (2013). It consists of a simplified single track model for the calculation of driving characteristics and was introduced by Riekert and Schunck (1940). In the context of crashworthiness, one of the first low-fidelity models is presented by Kamal (1970). This model consists of a system of spring and mass elements representing the structure of a vehicle and its response during a frontal impact. Nowadays, the approach of using simplified and low-fidelity models for crashworthiness is an extended practice in the automotive industry, considering that they enable a decision-making process without the need of detailed information about the system to be developed. However, a variety of low-fidelity approaches exists, each providing its own set of limitations and benefits. Therefore, an examination of the methods to determine their suitability and applicability to the design phase in question is crucial. In this section, different types of low-fidelity models are studied, in particular with regards to their potential to be used in the early design phase, the load cases they can represent as well as their use in the context of robustness analysis and the solution spaces methodology.

A comprehensive classification of low-fidelity models used for crashworthiness design according the methodology used for their creation is provided in the works of Duddeck and Wehrle (2015); Fang et al. (2016); Vangi (2020); Noorsumar et al. (2021). The classification used in this work, presented in Table 2.1, incorporates the distinctions made by these authors and offers a global perspective on the methods available. The model classes identified are: crash pulse models, analytic and semi-analytic models, multi-body models, reduced order dynamic models or lumped-mass models, non-linear finite element models and response surface models.

Table 2.1 Low-fidelity models for crashworthiness design

Crash Pulse models	The pulse of the vehicle experimented during a crash event is modeled by using mathematical functions that represent the acceleration of the passenger compartment.
Sub-categories:	• Halfsine pulse shape: A sine function with the pulse duration and maximum acceleration as parameters is used for the approximation of the pulse. • Haversine pulse shape: A quadratic sine function is used to represent better the initial phase of the pulse curve. It uses the same parameters as the halfsine pulse shape model. • Triangular pulse shape: The pulse is characterized by a maximum value of acceleration and the time at which this maximum value occurs. • Macmillan model: A polynomial is used for pulse characterization. The formulation of the polynomial must ensure that the acceleration at t_0 equals to 0, a single maximum value is reached and that the slope of the acceleration curve tends to zero towards the end of the crash. • Direct integration of the force-displacement curves: The force-displacement curves of the spring elements can be arbitrarily defined, e.g. piecewise linear, and are integrated numerically to obtain the acceleration, velocities and displacement time-series.
Relevant authors:	Cheng (2002); Varat and Husher (2003); Gu et al. (2005); Woolley (2008); Huang (2002); Wei et al. (2015); Wei (2017)
Analytic & semi-analytic models	Collapse theory and limit analysis are used to characterize the behavior of components. The macro-element and super folding methods are used for applications with beam-like components subjected to axial and bending loads.
Relevant authors:	Wierzbicki and Abramowicz (1983); Abramowicz and Jones (1984); Kim et al. (1996); Liu (2005); Halgrin et al. (2008); Tran et al. (2014); Georgiou and Zeguer (2018); Gui et al. (2018)

Table 2.1 (continue) Low-fidelity models for crashworthiness design

Multi-body models	The relative motion of the components is dictated by a structure of rigid bodies connected by joints. These models typically based in the Lagrangian method and the governing equations of the system are solved numerically.
Relevant authors:	Coulomb (1785); Denavit and Hartenberg (1955); Pars and Lagrange (1966); Dopker (1988); King et al. (1972); Barley and Cripps (1992); Kortüm (1993); Ambrósio and Dias (2007); Sousa et al. (2008); Larsson (2001); Hegazy et al. (2000); Rahnejat (2000); Portal and Dias (2006); Carvalho et al. (2010); Carvalho and Ambrósio (2010); Elkady et al. (2012b); Nikravesh (2012); Hassan et al. (2019); Shi et al. (2019)
Reduced order dynamic models	The degrees of freedom of the system are reduced by representing the rigid components as concentrated masses and the deformable components are linear and non-linear springs and dampers. The energy conservation laws are used to setup the governing equations and calculate the motion of the relevant portions of the structure. These models are often referred to as lumped-parameter models or lumped-mass models (LPM). For structural applications, the passenger compartment is represented as a single lumped mass.
Sub-categories:	• Campbell model: The force-displacement curve takes its most elemental representation by utilizing a constant stiffness. A minimum force value defines the point beyond no further deformations are allowed. • McHenry model: Using the Campbell model as a base, a restitution phase, with an additional slope, is introduced for unloading conditions. • Kelvin model: A damper parallel to the spring is added to the system. • Impulsive models: Neither the duration of the impact nor the deformation of the vehicles are explicitly considered. The velocities of the bodies after the impact are calculated assuming rigid body motions and using the conservation of energy and linear and angular momentum.
Relevant authors:	Sharp and Goodall (1969); Kamal (1970); Tomassoni (1984); Trella and Kanianthra (1985); Mentzer et al. (1992); Cheva et al. (1996); Brach and Brach (1998); Kim et al. (2001); Kim and Arora (2003a,b); Dias and Pereira (2004); Elmarakbi and Zu (2005); Marler et al. (2006); Dong et al. (2007); Jonsén et al. (2009); Elkady et al. (2011, 2012b,a); Marzbanrad and Pahlavani (2011); Elkady and Elmarakbi (2012); Elmarakbi et al. (2013); Fender et al. (2013); Graff (2013); Pahlavani and Marzbanrad (2015); Graff et al. (2016); Ionut et al. (2017); Jazar (2017); Munyazikwiye et al. (2018); Prochowski et al. (2018); Lange et al. (2018b)

Table 2.1 (continue) Low-fidelity models for crashworthiness design

Non-linear finite element models	Boundary value problems for partial differential equations are solved using the explicit finite element method. The vehicle is discretized using the CAD geometries as base, and therefore, the level of detail required is relatively high. These models are used intensively during the simulation-driven design phase. The non-linear mechanisms present in this type of models include: contact, large plastic deformations and rotations, and failure. Different simplification techniques are applied to these type of models to allow their application during the early phases. Components originally represented by shell or solid elements, that are not the main focus of the study, are replaced by less detailed representations, i.e. beam, springs, rigid, and mass elements. Fidelity is lost in the areas of lower relevance, while the main focus areas maintain their detailed representation.
Sub-categories:	• Sub-structure modeling: A section of the vehicle's structure is cut so that the relevant portion remains. The interface is modeled through the introduction of prescribed boundary conditions. • Hybrid Nonlinear FE–rigid body: Less relevant parts of the structure are replaced by rigid bodies and concentrated mass elements. • Hybrid Nonlinear FE–elastic FE: Components with only elastic deformations are assigned elastic-only materials and computed with implicit methods. • Hybrid fine–rough FE mesh: regions of less interest are discretized using a coarser mesh. Space mapping techniques are also utilized to map relevant results from the coarser mesh to the finer discretized regions following a multi-fidelity approach.
Relevant authors:	Hrennikoff (1941); Courant (1943); Clough (1960); Pifko and Winter (1981); Benson et al. (1986); Howard et al. (2000); Kirkpatrick et al. (2003); Kiefer et al. (2004); Redhe (2004); Böttcher et al. (2005); Redhe and Nilsson (2005); Spethmann et al. (2006); Jonsén et al. (2009); Singh (2009); Chen et al. (2012); Gutermuth et al. (2013); Rayamajhi (2014); Ramaswamy et al. (2016); Meng et al. (2017); Schäffer et al. (2017); Schäffer et al. (2018); Numata et al. (2018); Pak et al. (2019); Xueyan et al. (2019); Noorsumar et al. (2020); Yu et al. (2020); Putra et al. (2021)

Response surface models	The input and output relationships of the system are established by a statistical approximation model. The main steps for the creation of these models are: design of experiments, data collection and data fitting. These models are relatively cheap to evaluate but require a base model, usually a finite element model, to generate the samples to be used in the reconstruction of the input-output behavior.
Sub-categories:	• Polynomial response surface: Works well in the problems with <10 variables and problems with random errors. Adequate for predicting energy absorption. • Radial basis function: Relatively insensitive to sample size in terms of accuracy and robustness. Adequate for predicting maximum acceleration. • Kriging: Suitable for problems with <50 variables. Relatively sensitive to the noise due to the interpolation of the sample data. • Artificial neural network: Adequate for very large design problems with ca. 10,000 parameters. • Successive surrogate modeling: Iterative and sequential sampling of regions of interest to improve accuracy.
Relevant authors:	Box and Wilson (1951); Free et al. (1976); Cox and Baybutt (1981); Myers et al. (1989); Omar et al. (1998); Gu et al. (2005); Ghannam et al. (2011); Shi et al. (2012); Munyazikwiye et al. (2013); Shahidi and Pakzad (2013); Zuolong et al. (2015); Munyazikwiye et al. (2017); Usta et al. (2018); Şenaras (2019); Anselma et al. (2020); Yu et al. (2020)

The level of detail of the information required for the previously described models for the crashworthiness design significantly varies from one model to another. On one end, the non-linear finite element models require detailed information about the geometry to be discretized, as well as the material characteristics and contact conditions. These models are used to represent a wide range of load cases, including rigid, deformable, moving and stationary barriers. On the other end, the crash pulse models are able to characterize the structure's acceleration response to the impact without the explicit consideration of detailed vehicle characteristics. However, they provide no information regarding the deformation of the structural components. In the case of the response surface models, the accuracy of the model is implicitly defined by the type of model used to create the input-output relationships. Therefore, this type of models cannot be used in the early phase if the intended design deviates from the available high-fidelity models that could be used to train the response surface. Considering the analytical and semi-analytical models, the current collapse and limit theories are only available for a limited number of cross-sections and loading conditions. Moreover, these models need as input detailed information such as the cross-section and material characteristics. This suggests

that multi-body models and lumped-mass models are the best candidates for intensive use during the early design phase. The LPM offer a sufficient level of abstraction to represent the energy absorption, force levels and vehicle kinematics needed to guide the design in the early phase. Additionally, they can be defined at the component and system levels. Since the force-deformation characteristics are consequences of the combination of material, cross-section and deformation behavior, the level of detail needed to define these models is minimum. Only a coarse approximation of the topology of the structure is sufficient to define such models. Vehicle components in these models are represented by springs, beams, damper and mass elements. Beam elements are able to represent more complex deformation behaviors and loading conditions than the spring elements. However, considerably more effort is necessary for the definition and measurement of their functional properties, e.g. moment-angle and torsion-twist characteristics. Several methodologies are available that define efficient system identification procedures for the lumped-mass models using linear and non-linear spring elements (Kim et al., 2001; Kim and Arora, 2003a,b; Marler et al., 2006; Marzbanrad and Pahlavani, 2011; Fender et al., 2013; Pahlavani and Marzbanrad, 2015; Munyazikwiye et al., 2018). The relatively low computational costs of these models allow their use in solution space methodologies as well as in robustness and uncertainty analysis. As long as the output response can be used to guide the crashworthiness design, the simpler the model and the cheaper its design feasibility evaluation, the more successful is its implementation in the early phase.

Despite the methodology to develop the aforementioned low-fidelity models, their applicability has been limited to the following load cases including the full-frontal impact with a rigid barrier, frontal oblique and offset impact with deformable barrier, side impact with rigid and deformable barrier as well as rear impact and roof crush (Vangi, 2020). The Small Overlap load case has been underrepresented in the context of low-fidelity modeling. The works of Thomas (2011); Brach et al. (2014); Mueller et al. (2014) in the context of planar impact mechanics, and Schäffer et al. (2018) for sub-structure modeling are efforts to represent this load case using low-fidelity models. However, these models have not been used in the early design phase, considering that, on one hand, the level of detail of the input data is not suitable for this particular design phase and on the other hand, the functional properties at the low-level are not directly mapped to the high-level requirements. This gap is recognized in this work. Moreover, the current available models are studied in detail in Section 2.7 with the objective of developing a suitable low-fidelity model for the early design phase for the Small Overlap load case.

2.5. Solution Spaces

The basic principle of the solution space approach is to create independent intervals for each functional property of the system at the lower levels. Following this approach, it is ensured that the high-level targets are achieved as long as the functional properties lie within these intervals. Methods following these set-based design principle have been proposed by multiple authors (Ward and Seering, 1993; Ward et al., 1995; McKenney et al., 2011; Kennedy et al., 2014). Other approaches, such as the ones from Milanese

et al. (1996); Rocco et al. (2003); Naujoks et al. (2005); Harwood and Barton (2017), have formalized the solution spaces methodology for general applications. However, the solution spaces approach has been further developed for automotive applications in the works of Lehar and Zimmermann (2012); Zimmermann and von Hoessle (2013); Fender (2014); Fender et al. (2014); Song et al. (2015, 2018); Graff et al. (2016); Fender et al. (2016); Lange et al. (2018a); Vogt et al. (2018); Erschen et al. (2018); Harbrecht et al. (2019); Daub et al. (2020); Roetzer et al. (2020); Kundla et al. (2020); Harbrecht et al. (2021). The following summary of the concepts and specificities of the solution spaces methodologies in the context of crashworthiness aims to identify which crash load cases have been represented so far and what are the limitations of the currently available approaches.

A robust structural design for crashworthiness is expected to reach all predefined targets and fulfill all of the high-level requirements even if the functional properties of a certain component in the vehicle's structure present a deviation from the specific design value. This is not true in optimized designs that do not explicitly consider sources of uncertainty, as they tend to be sensitive to parameter changes and thus, do not offer a robust response. Tolerance to variations of the functional properties is essential in crashworthiness applications. As Zimmermann and von Hoessle (2013) state, the tolerance to these variations is measured by the size of the solution space that guarantees that the system's response is acceptable.

Considering a list of design parameters to represent the functional properties of each component in question, Zimmermann and von Hoessle (2013) define the solution space as a multi-dimensional box or hyper-cuboid with permissible intervals. Their proposed method aims to find the largest solution space possible that ensures that if all design variables lie within the permissible interval, the vehicle as a whole achieves its targets. At the same time they aim to define the permissible range of each component independent of the behavior of other components. Moreover, their algorithm uses interval boundaries, rather than the design parameters themselves, as degrees of freedom. It uses the following essential steps for the calculation of the solution space. First, an iterative sampling of a candidate box-shaped region of the design space is conducted. Second, a readjustment of the regions boundaries is executed to increase the percentage of feasible designs inside the multi-dimensional box. These two steps are carried out during two distinct phases called exploration and consolidation. In the exploration phase, sample designs are generated using a Monte Carlo scheme assuming a uniform distribution over a candidate box. Afterwards, the feasibility of the samples is evaluated. Then, a subset inside the candidate box with the maximum volume with feasible designs is identified. This phase is repeated until the position of the multi-dimensional box does not change. During the consolidation phase, a subset containing a specified minimum of feasible designs is identified by moving the boundaries of the box. This calculation is called indirect because the boundaries of the solution space are indirectly detected by evaluating all the sample points. In contrast, a direct evaluation only evaluates the feasibility of the design at the corners of the sample space, as it is later introduced by Fender et al. (2016).

The method proposed in the work of Zimmermann and von Hoessle (2013) is applied

to a lumped-mass model representing a simplified version of a vehicle's frontal structure subjected to the US New Car Assessment Program (USNCAP) frontal crash load case. The lumped-mass model contains two ideally plastic unidimensional deformable elements, with constant force levels and located in series with a mass element connected to the second element, representing the total mass of the vehicle. The first element contacts a rigid barrier and an initial velocity is applied to the mass to excite the system. The requirements of the systems are: the deceleration of the mass should not exceed a maximum value, the deformation should start in the first element, and the initial kinetic energy of the system should be absorbed by the deformation elements before reaching a maximum deformation value. After applying the proposed solution space algorithm, permissible intervals, fulfilling the aforementioned constraints, in the form of upper and lower boundaries for the forces of the two deformation elements are identified. Zimmermann and von Hoessle (2013) state that specially during the early design phases a larger solution space, with an acceptable probability of containing unfeasible designs, should be chosen in favor of a smaller one containing only feasible samples in order to maximize the flexibility of the design process.

Despite the benefits of the solution space approach, Zimmermann and von Hoessle (2013) acknowledge the following limitations of the method. On one side, the convergence of the algorithm tends to be slower for high-dimensional problems since more intervals need to be moved to find the multi-dimensional box. On the other side, the optimal shape of the box is not guaranteed since local optima may produce an earlier convergence of its position and consequent shape. The repeatability of the method is affected by the non-deterministic nature of the sampling. Also, unfeasible designs may coexist in the same space but may go undetected by the sampling scheme. The method proposed by Zimmermann and von Hoessle (2013) was further analyzed in the work of Graff et al. (2016) and tested against benchmarks with analytical solutions. They find that for problems with disconnected regions, i.e. not only convex feasible domains, the solution may converge to a local optimum because the algorithm is only able to move the candidate box inside regions that produce large enough growth rates of the feasible solutions. Additionally, it was found that the volume of the solution box increases with an increased number of samples, and at the same time the convergence speed decreases. This last point confirms that this method is computationally expensive when calculating large solution spaces for high-dimensional problems.

The method of Zimmermann and von Hoessle (2013) is extended by Fender et al. (2014) with the goal of identifying the parameters that an adjustment to their permissible intervals highly increases the share of feasible designs and reduces the effort to change a bad design into a good design. Fender et al. (2014) claim that by formulating appropriate constraints upon the design parameters themselves, a relatively small displacement of the interval boundaries suffices in some cases to achieve the feasibility of the complete system. The USNCAP front crash setup and constraints introduced by Zimmermann and von Hoessle (2013) are used to exemplify that if a design lies close enough to the acceleration, energy absorption and order of deformation constraints, and one of the force levels of the deformation elements is fixed, further displacement of the second

force level results in a relatively larger solution space. Such key parameters, which significantly contribute to having a feasible system by undergoing minimum changes, can be identified in the solutions space's algorithm if slightly modified. This modification consists of calculating the distance of a certain parameter to the constraint characterized by a constraint-violation error, in addition to calculating the share of feasible designs.

Measurements to reduce the highly computational costs involved in the indirect solution space calculation are presented in the work of Fender et al. (2016). They propose describing the inequality constraints and objective function with a linear formulation. This allows the use of efficient techniques for linear programming such as the interior point method presented in Nocedal and Wright (2006). In the previous approach, a model is evaluated at each sample point and iteration to assess the feasibility of a design. This direct method only evaluates the constraint violation at the corners of the multi-dimensional box, which results in a decrease of the calculation time. Using the simplified front crash load case presented by Zimmermann and von Hoessle (2013), Fender et al. (2016) use the direct method to calculate a solution space that proves to lie within the boundaries computed with the indirect method. However, the reduction in computational costs come with the disadvantage that the solution space is smaller in size when compared to the results of the indirect approach because the direct approach ensures that all the corners of the box do not violate their constraints. This situation is aggravated in the case of high-dimensional problems.

In order to increase the size of the solution spaces obtained with the direct method, a relaxation scheme is proposed by Lange et al. (2018a). The constraints of the analyzed problem, i.e. the simplified front crash load case, are linear; therefore, it is sufficient to evaluate the vertices of the solution space to obtain a convex feasible solution. Designs with some parameters in the middle of their intervals, i.e. outperforming the constraints, may have enabled other parameters to have a larger interval if these parameters were located closer to the constraints but still in the feasible space. To allow the search for a larger solution space, Lange et al. (2018a) propose a manipulation of the constraints by replacing the box-shaped spaces to an ellipsoidal uncertainty set that is evaluated at an interior point around the center of the ellipsoid. Additionally, the possibility to fix $a - priori$ some predetermined segments of the solution space is presented in this relaxation approach offering an increased flexibility in the design process.

The solution space approach is further enhanced in the work of Vogt et al. (2018) by introducing a distinction between early-decision variables and late-decision variables in context of the so-called solution-compensation spaces. On one hand, the early-decision variables correspond to parameters that present a relatively high uncertainty and must be treated as intervals during the early design phase. The sensitivity of the system's response to these variables is relatively high in comparison to the rest of the parameter set. On the other hand, the late-decision variables can be adjusted to take any specific value inside a predetermined design interval and are therefore more controllable. During the component design phase a value is assigned to the early-decision variables. Then, this approach adds a compensation phase for the late-decision variables, where their values are selected ensuring that these, along with the early-decision variables, produce a feasible

design. This is achieved by projecting the design interval of late-decision variables into the solution space of early-decision variables and then evaluating the constraints to find the solution space for the late-decision variables. This approach is applied in Vogt et al. (2018) to a driving dynamics setup, where a quasi-steady state cornering, ramp steering, and sine with dwell load case are evaluated.

The geometrical mismatch of the feasible design space and the axis-parallel solution spaces often leads to solution spaces that are impractical for real engineering applications. The work of Erschen et al. (2018) proposes an alternative to deal with this issue where pairs of variables are coupled in so-called 2-D spaces which are, in turn, confined by polygons. In this way, the solution space is formed by the Cartesian product of all the 2-D spaces of each pair of design variables. The maximization of the size of the solution spaces is carried out by using an interior-point algorithm and is tested effectively in a chassis design problem.

Another approach to tackle the issue of often small and impractical solution spaces is presented by Harbrecht et al. (2019). In some cases, the size of the solution space may be restricted by the axis-parallel orientation of the solution space box. Harbrecht et al. (2019) increases the size of the solution space by coupling design variables and allowing two-dimensional box-rotations. The size is considerably increased for cases when the design variables are strongly correlated. Some variables may be left unpaired when a large-enough solution space is expected. To identify the best pairs of variables, the covariance matrix of the feasible design points is calculated in a pre-optimization step. The benefits of the box-rotation are evident if the correlation analysis can be leveraged. However, if the paired variables are designed by different engineering teams, a more intensive communication is needed than in the case of using the uncoupled solution spaces methodology. This approach is tested in a 6-D vehicle dynamics problem where the force-velocity, force-displacement, and stiffness characteristics of a set of suspension components are used as design variables as well as in a 8-D nonlinear acoustics problem where nine noise transfer paths are designed by having a total noise level as critical value.

Daub et al. (2020) optimizes the shape of the solution space with the objective of increasing its size. The optimization is accomplished by the decomposition of the performance of the system into the sum of the component performance functions which are optimized individually. The decomposition does not imply decoupling all the design variables, which means that a minimum level of coordination with other designers that have influence over the given component is needed. However, this potential drawback is compensated by a flexibility increase associated with the larger size of the solution space. This method is applied to the USNCAP frontal load case problem used by Zimmermann and von Hoessle (2013) yielding a larger solution space compared to the results obtained by Zimmermann and von Hoessle (2013).

The work of Harbrecht et al. (2019) and Daub et al. (2020) is expanded by Harbrecht et al. (2021) by defining the solution spaces as a product of polygons. This polytope (higher-dimensional polygon) optimization proposed by Harbrecht et al. (2021) yields much larger solution spaces than the axis-parallel hyperbox originally proposed by Zimmermann and von Hoessle (2013). Nonetheless, a loss of flexibility is expected while

coupling the design variables. Therefore, Harbrecht et al. (2021) suggests that the coupled design variables should lie within the influence of one designer. Otherwise, the higher level of communication and coordination needed may hinder the benefits of the larger solution space. The algorithm is based on Monte Carlo sampling iterations that follow the exploration and consolidation phases as in Harbrecht et al. (2019), and on evaluations of the size and quality of the polytope. The quality of the polytope is evaluated by considering the number of self-intersections, presence of spikes, and minimum and maximum size of angles. This algorithm is tested on 2-D, 3-D and 10-D problems producing satisfactory results.

The previous approaches offer suitable techniques for the identification of solution spaces for the design of a single vehicle with a particular set of characteristics. However, in the automotive product development, it is often the case that a platform is designed to accommodate several vehicle styles with different mass and deformation space characteristics.

The work of Song et al. (2015), on the extension of the solution spaces method for vehicle architectures, offers the possibility to identify common components among these vehicles to facilitate the design process. Using the USNCAP frontal impact model from the previous works, candidate components for common usage are identified by examining their mass, length and position in the frontal structure. To evaluate the feasibility of the designs simultaneously, the sections of the deformation elements are synchronized by adding artificial force-deformation sections to ensure that the components that are candidates for common usage are discretized equally in all of the vehicles to be evaluated. Consequently, this synchronization of sections leads to a finer discretization of the deformable elements and an increased number of degrees of freedom. Additional equality constraints are also introduced that ensure identical solution spaces for common components. Moreover, the objective function defining the size of the solution space is formulated as the sum of squares of each individual interval to ensure convexity. Inside this function, a weighting factor is used to prioritize the maximization of a particular interval. Finally, the smooth nature of the force-deformation behavior is also mathematically enforced by introducing a constraint that minimizes the variation of the interval widths.

In the same line of commonality optimization, Roetzer et al. (2020) states the question of weather a maximum commonality approach also equals to a cost-optimal scenario when dealing with product families. In order to use interchangeable components, these components should be standardized, which in turn may lead to the over-dimensioning of such components. Roetzer et al. (2020) proposes three main steps to find the cost-optimal commonality for product families. First, calculating axis-parallel solution spaces for each variant of the product family. Second, identifying overlaps of the calculated solution spaces. Third, using an objective function to minimize the total cost of the product family (i.e. manufacturing costs, costs related to the complexity of introducing a new variant, and costs changes related to the economies of scale) to optimize the design variables. Roetzer et al. (2020) concludes that the selection of the biggest solution space for each component does not automatically produce a higher commonality between the

products and that the number of products produced, production/purchasing costs and cost of a new variant are dominant factors specific to the product and company in question that determine the cost-optimal commonality.

Even when the presented expansions of the solution spaces methodology increase the applicability of this technique for crashworthiness scenarios, the main limitation for the applicability of the method still is the efficient evaluation of the constraints. The feasibility assessment is available when using the USNCAP frontal load case low-fidelity model as evaluator or a mathematical formulation of the constraints. However, the broad spectrum of load cases in crashworthiness design increases the need for low-fidelity models for other load cases.

The applicability of the solution spaces approach is expanded with the inclusion of the rear impact load case, defined in the Federal Motor Vehicle Safety Standard 301 (FMVSS), in the work of Song et al. (2018). This load case involves a moving deformable barrier (MDB), with an initial velocity contacting the vehicle along its longitudinal axis with only 70% overlap to the rear structure. Three constraints are considered to evaluate the feasibility of the design. The first one concerns the maximum force level in the load-paths. The second one limits the intrusion and deformation of the structure to protect critical components. This constraint can be interpreted as the absorption of the barrier's kinetic energy until the point when both vehicle and barrier have reached the same velocity and the corresponding maximum deformation that results up to this point. The third constraint is similar to the order of deformation constraint defined in the frontal load case. It ensures that due to reparability requirements, the structure deforms from the rear to the front. Any rotation of the vehicle and barrier are neglected assuming a one-dimensional load and deformation. Since a MDB is considered, the absorption of energy takes place not only at the vehicle's structure but also on the barriers side. An extraction of the force-deformation characteristics of the barrier is also carried out by using quasi-static simulations and formulated as a function of the impact location, impactor shape and deformation level. This results in a resistance to deformation per unit length. The simplified version of the structure in the work of Song et al. (2018), is represented by deformation elements showing the available deformation length. Several parallel load-paths are considered, each with its own deformation level. The contact surface of the vehicle and the barrier is approximated by square spaces and the barrier's force-deformation properties are interpolated from the general characterization obtained previously. The deformation elements are discretized into sections with assumed constant force levels. Finally, the evaluation of the non-linear constraints and identification of the solution space is carried out by using a sequential linear programming technique.

As an effort to expand the application of solution spaces to other engineering disciplines related to automotive design, Kundla et al. (2020) proposes the usage of artificial neural networks for subframe design considering the requirements for stiffness, acoustics, crash, durability, package, manufacturing, assembly, service, mass and costs. The mapping of the fulfillment of the criteria to the characteristic values of the subframe are captured in its CAD and FEM representation. In order to accelerate the evaluation of design changes, a large number of design samples are evaluated and a substitute model is created using

a neural network. Then, the neural network is used to calculate the solution space.

The study of the available literature makes evident that the development of the solution spaces approach in the context of crashworthiness has been greatly influenced by the challenges and specific nature of the models and constraints that represent the different load cases. This development has produced efficient methods for the representation of the USNCAP frontal crash and FMVSS 301 rear impact load cases. A need to further develop this methodology is identified with the aim of calculating solution spaces for other load cases during the early design phase and defining component level requirements that streamline the development of the vehicle structures.

2.6. Robustness Analysis

2.6.1. Uncertainty Quantification & Classification

A classification of the uncertainties from the perspective system design is proposed by Daub and Duddeck (2020). They identify three sources of uncertainty: design variables, uncontrollable parameters and constraints. The uncertainty affecting the design variables comes from the lack of detailed information of the design, e.g. geometrical details or undefined manufacturing processes. The uncontrollable parameters are defined as the variation in the operating conditions and test environments. Lastly, the constraints uncertainty (a certain type of model uncertainty) arises from the simplification and approximation of the real physical objects and their abstraction used for their modeling.

An alternative classification of uncertainties that focuses on their fundamental causes, rather than only on the system's perspective, distinguishes two classes: epistemic and aleatoric uncertainty. On one side, Daub and Duddeck (2020) state that epistemic or lack-of-knowledge uncertainties define the range in which controllable design variables may exist. On the other side, aleatoric uncertainties are considered random and irreducible and are reserved for uncontrollable parameters that fluctuate around known nominal values.

In real-life applications, both aleatoric and epistemic uncertainties affect the system's response at the same time. Kamariotis et al. (2019) introduce techniques for numerical uncertainty quantification and uncertainty-based sensitivity analysis based on two different approaches. The first approach is the so-called interval valued probability method (IVP), which calculates ranges around the statistical quantity of interest (QOI) and uses these intervals to compute the effect of uncertainty. In contrast, the second approach, called Bayesian probabilistic (BP) method obtains a full distribution of the QOI based on epistemic statistics of the input variables. These two approaches use a double loop where the two types of uncertainty are separated to propagate their effects within the model.

To reduce the additional computational cost of evaluating the uncertainty effects in a double loop, Papaioannou et al. (2019) propose a unified framework for polymorphic uncertainty quantification for aleatory and epistemic uncertainties. This framework focuses on the evaluation of the capacity of the method to support engineering decisions regarding safety assessments and reliability-based design. Aleatory variables are treated

using probability theory, while epistemic variables are addressed with methods such as Probabilistic-interval, Fuzzy, Fuzzy-Interval, Fuzzy-probabilistic and Bayesian probabilistic. Papaioannou et al. (2019) conclude that the results on the safety assessment strongly depend on the behavior of the tails of the distributions used to characterize uncertainties. They identify that the approach selected to model epistemic uncertainties as well as the approach to characterize the probability of failure of the system have a relatively large effect on the decision making process. Both approaches are used in all design stages of the product development process.

In the context of crashworthiness design, uncertainties appear already in the early design stages and continue through the design stages, and arise from the simplification of the definition of the crash load-case to be tested, the structural response of the vehicle and the definition of the structure itself (Hunkeler et al., 2013). Due to the fact that crashworthiness is already a complex engineering discipline, these uncertainties are often neglected during the development process. Consequently, this results in significant deviation between the idealized design and the real manufactured product. Hunkeler et al. (2013) suggest classifying uncertainty sources that affect the crashworthiness response into uncertainties related to: geometry, material properties, impactor properties, and environment. Geometry uncertainties include physical aspects such as the shape and location of the components and their interfaces to the rest of the structure as well as the wall-thickness. Material uncertainties consist of variations in the Young's modulus, Poisson's ratio, mass density, plastic behavior, porosity, and failure and damage characteristics. Uncertainties due to features comprise for example, the position and mechanical properties of spot-welds and other joining technologies. The aforementioned sources of uncertainty can, to a certain degree, be influenced by the designers by the specification of nominal values and tolerances. However, aspects related to the impactor properties (e.g. initial speed, mass, orientation), to the environment (e.g. temperature, surface properties), and to the dummy (e.g. position and orientation) are random. During the simulation-driven design phase, additional sources of uncertainty such as the FEM-solver numerics (e.g. model partitioning, time-step mass scaling, and mesh discretization) as well as uncertainties related to the modeling approximations (e.g., material laws and geometrical simplifications) also affect the repeatability of the simulations (Hunkeler et al., 2013).

As a next step and once the uncertainty parameters are selected, Hunkeler et al. (2013) propose to select a stochastic model for each parameter. This selection is constrained by the availability of data to reconstruct the probability distributions. Nominal values and ranges are specified in the crash test protocols. Even though these are the primary source of information to define the range of variability, protocols' ranges may not necessarily represent the real-life conditions of the test (Hunkeler et al., 2013). A uniform distribution or a normal distribution with a maximum of two standard deviations is advised by the authors if no additional data is available. However, the use of empirical data or statistical methods to create probability distributions (such as maximum-entropy principle) can better represent the phenomena. The final step in the uncertainty characterization is to investigate the distribution of the response of the system, i.e. the output parameters.

For this goal, (Hunkeler et al., 2013) recommend to create a representative population, taking as a base the distribution of the input parameters, and evaluate the system response through simulations. Methods such as, D-Optimal, full-factorial, Monte-Carlo and Latin Hypercube sampling are typically used when generating a representative population efficiently. Further aspects to be considered such as the ideal number of samples according to the number of uncertain parameters are presented in Section 2.6.3.

The works of Paz et al. (2020) and Ren and Xiang (2014) present two practical applications of uncertainty analysis. On one side, Paz et al. (2020) study the effect of diverse sources of uncertainties in the progressive collapse of components under axial loads. In this application, the monitored output parameter is the peak crushing force. Three models are used for the system response evaluation, namely analytical formulas, numerical simulations and surrogate modeling. The results are compared to physical tests and Paz et al. (2020) conclude that the surrogate models, i.e. multivariate adaptive regression splines, result in the smallest deviation of the output scatter. On the other side, Ren and Xiang (2014) use a simplified FE model of an aircraft fuselage to evaluate the effect of initial conditions, structural dimensions and material properties on the deformation of the structure. Ren and Xiang (2014) propose the following four-step uncertainty analysis method. The first step consists of the parameter selection, each with three levels, i.e. upper, lower and mean. In the second step, the Box-Behnken method is used to sample a normalized and representative parameter space. The third step includes the definition of probability functions for the relevant output quantities obtained by the model evaluation. Finally, a gradient analysis with respect to each input parameter is performed, concluding that the dominant uncertainties are the frame thickness, yield strength, impact velocity, and angle of impact.

2.6.2. Uncertainties, Optimization and Solution Spaces

Additionally to the uncertainty sources and examples mentioned above, the nature of the explicit FEM and the numerical solvers can account to up to 10% of the variation obtained when simulating the different crash load cases (Duddeck, 2007a). The study performed by Hunkeler et al. (2013) indicates that when simulating the same model of a front rail of a standard passenger vehicle for ten times, a coefficient of variation of 0.15% for the specific energy absorption is produced. Although, the exact variation may be different for each particular output variable and highly depends on the modeling techniques and solver configuration, the numerical aspects of the simulation that may influence the decision making process should be analyzed. As Qiu et al. (2018) stated, crash simulations are not necessarily repeatable and can become a significant source of uncertainty due to instability of structures and contact bifurcations. Rounding and parallel computing errors combined with the highly non-linear nature of the crash simulations create the need to apply an uncertainty quantification process during the virtual design stages. Qiu et al. (2018) propose the steps presented below to explicitly consider the numerical uncertainty in an optimization procedure. Using this methodology, they conclude that for the front rail design application, a 4-sigma interval is enough when the optimization does not require re-meshing and 8-sigma when re-meshing is required.

1. Optimization problem definition
2. Sample creation using Optimized Latin Hypercube
3. Surrogate model selection: Polynomial Response Surface
4. Quantification of numerical noise
5. Definition of a confidence interval for the numerical noise and surrogate model error
6. Perform uncertainty-based quantification method for optimization
7. Optimization response using Particle Swarm algorithm

Analogously, Fang et al. (2014) express that the result of a purely deterministic optimization procedure may degrade when the solution is tested in a uncertain environment with relatively small deviations from the nominal conditions. They propose a so-called multi-objective sequential robust design optimization (MOSRDO) based on the particle swarm algorithm. The MOSRDO is applied to a foam-filled thin-walled structures optimization process and uses adaptive Kriging models to reduce the computational effort. Fang et al. (2014) apply a descriptive sampling procedure that consists of two steps: first, generate a descriptive set of variables for each design variable, and second, perform a random permutation over the generate set. Following this approach, the inner walls of the optimized structure become thicker when uncertainties are considered relative to the wall-thickness obtained in the simple optimization procedure.

Another subject of crashworthiness design that is also directly affected by the consideration of the uncertainties is the calculation of solution spaces as described in Section 2.5. Daub (2020) frames solution spaces in the context of the decision-making process, where designers have to define ranges for design variables, so that the low-level and high-level requirements are fulfilled.

These ranges or solution spaces should be as large as possible and, as Daub (2020) states, the selection of each design variable should be decoupled from each other to offer the maximum possible flexibility to the designer. Daub and Duddeck (2020) present a methodology for the calculation of solution spaces with controllable and uncontrollable variables directly modeled as intervals. Their work focuses on epistemic uncertainties. They argue that the lack of a detailed description of design features, i.e. the coarse representation of the system, during the early design phase may have a relatively larger effect on the system's response during the later design phases than the aleatoric uncertainties. Therefore, the size of the box-shaped solution spaces, i.e. a one-dimensional range defined by an upper and lower limit for each variable, may become smaller while explicitly considering the epistemic uncertainty of the variable in question. This phenomenon is exemplified in a model composed of two deformation elements and a lumped mass with an initial velocity as initial condition, representing a front crash load case. To calculate the solution space, presented by Daub and Duddeck (2020) define three constraints: energy absorption, maximum acceleration, and order of deformation of the components. Assuming a constant load level for the deformation elements, a base solution space is calculated without any consideration of uncertainties. Then, the uncontrollable parameters, namely mass, initial velocity, and allowable maximum acceleration are varied. Finally, both uncontrollable parameters and controllable variables are considered by including uncertainties in the load levels of both deformation elements. The solution space size is

reduced by ca. 50% in comparison to the baseline. The methodology described by Daub and Duddeck (2018), where ellipsoid-shaped and general-shaped solution spaces are proposed, provides an alternative formulation to overcome this reduction in size when using the solution spaces approach in the context of uncertainty quantification.

2.6.3. Robustness Quantification

Several definitions of robustness concerning the structural response of a system are available in the literature. Hunkeler et al. (2013) define a robust design as a design that matches the objectives and constraints of the system with at least a minimum target probability. Bagloee et al. (2017) express that robustness is a characteristic that describes to which degree the system is capable of completing its functions while being exposed to disturbances. Sørensen (2011) adds that the robustness of a system can be expressed in terms of the consequences of local damage of its components or exposure to conditions different to the nominal used for its design. Abdollahzadeh and Faghihmaleki (2017) state that robustness is dependent on two factors; one, the internal features of the structure such as redundancy and collapse characteristics, and two, the unexpected critical events to which the system is subjected. Furthermore, Andricevic et al. (2016) define two aspects for the evaluation of robustness under the consideration of aleatoric uncertainty. The first assessment concerns the feasibility in terms of the design targets, i.e. for a given number of samples representative of the uncertainty parameters, what is the percentage of samples that meet the target. The second assessment is made in terms of variability of the response, i.e. how big is the deviation from the response of the system under a nominal test environment. Other authors, present specialized probabilistic methods for assessing robustness (Lin et al., 2001; David et al., 2003; Avalle et al., 2007; Will and Frank, 2008; Will and Stelzmann, 2008).

A similar concept, often used interchangeably with robustness, is the system's reliability. It is defined by Duddeck (2007b) as the estimation of probability of failure of the system, namely the behavior of the tails of the output distribution. Additionally, the same author defines robustness as the degree of variance around the mean response of the system under the consideration of the previously described sources of uncertainty. Faber et al. (2006) introduce a quantification of the robustness based on the capability of the system to withstand damage to its components. Authors such as Andricevic et al. (2016) propose a combined reliability-based robust design optimization. Meanwhile, the work of Mourelatos and Liang (2005) specify a 90% success threshold of the probabilistic density function of the relevant output parameter to evaluate the robustness of the system. In contrast, Schumacher and Olschinka (2007) propose a success threshold based on the quantiles, e.g. 95%. The 95% probability approach is also described in the work of Hunkeler et al. (2013). However, these authors indicate that assuming a normally distributed output with a feasible interval existing in a range of ± 2 standard deviations around the mean value is a common practice in crashworthiness design. They also state that the typical six-sigma approach, i.e. ± 3 standard deviations and 99.73 %, used in other engineering disciplines, is not recommended due to the highly non-linear nature of the crash phenomena.

As a quantitative and simple way to measure the robustness of a particular design, Hunkeler et al. (2013) propose the examination of the output distributions and further calculation of statistical values such as mean, standard deviation, skewness and kurtosis. Moreover, the output distribution can be fitted to a known probability density function, facilitating the analytical computation of the probability of fulfillment of the requirements. These authors also suggest to study the correlation of the input parameters to the output distributions by the use of correlation matrices and Principal Components Analysis to identify coupled influences and reduce the dimensionality of the system. Likewise, optimization procedures, such as Robust Design Optimization, benefit from an explicit robustness evaluation by introducing a double loop where explicit uncertainties are considered by the evaluation of designs in the vicinity after each optimization iteration. Nevertheless, Hunkeler et al. (2013) state that robustness analyses are limited to a relatively low number of parameters due to the costly evaluation of the designs and high number of combination of parameters. For this reason, Bhise (2017) proposes to perform a combined sensitivity and robustness analysis to discard the parameters that have a relatively low effect on the output and concentrate the sampling and evaluation effort in the most relevant input parameters.

The work of Hunkeler et al. (2013) uses the Latin Hypercube Sampling (LHS) instead of the Monte-Carlo method to generate the sampling population more efficiently and reduce the evaluation costs. The LHS method divides the design spaces into subspaces of equal probability and generates a random value within each subspace minimizing the linear correlation between each variable an optimization subroutine. The number of sample points to evaluate is typically limited to the available time and computational resources available.

Hunkeler et al. (2013) propose that in order to produce meaningful results, the number of samples should be twice the sum of the number of output variables plus the number of total input parameters including noise parameters (e.g. time-step for numerical effects consideration). However, the ideal number of samples is also dependent on the type of probability distribution of the inputs, system non-linearities and desired confidence interval for the study of the output parameters. This highlights the need for a methodology to estimate the minimum number of samples to characterize a crashworthiness design problem. The robustness evaluation presented in this work includes a methodology for the determination of the ideal number of parameters based on the aforementioned factors and is presented in Section 6.2.3.

2.6.4. Robustness Indices

Characterizing the robustness of a particular system response by a single scalar value or index is convenient when assessing different designs as well as their sensitivity to a certain set of uncertainty sources. A number of robustness indices, RB_I, that offer a way to quantify the structural robustness of mechanical systems are available in the literature and are tailored to their specific applications. A general classification proposed by Chen et al. (2016) makes a distinction between deterministic performance-based, reliability-based and risk-based indices. Deterministic RB_I are defined by Abdollahzadeh and

Faghihmaleki (2017) as the capacity of the structures to tolerate loads, in damaged and undamaged conditions, that deviate from the nominal load. In the work of Sørensen (2011), this type of RB_I is based on a so-called residual influence factor (RIF) which is in turn based on the reserve strength ratio (RSR) or maximum capacity of the structure divided by the design load. The damaged strength ratio is then a function of the RSR of a damaged and the RSR of an undamaged structure that has suffered the failure of a single component.

With regards to probabilistic RB_I, Abdollahzadeh and Faghihmaleki (2017) state that the probability of failure of the structural system is calculated considering damaged and undamaged conditions. Complementary to this definition Sørensen (2011) describes that this type of RB_I is related to structural redundancy and can be interpreted as a redundancy index. This property of the system is characterized using a convenient range of values from 0 to 1.

For risk-based RB_I, Abdollahzadeh and Faghihmaleki (2017) and Baker et al. (2008) state that the calculation of this RB_I includes a complete risk analysis that distinguishes between consequences caused by direct and indirect risk. Direct risks result from a local damage of the structure during a critical event, i.e. consequences of damaging the structure. Indirect risks consider the probability of local damage during a critical event, i.e. probability of damaging the structure. The robustness index proposed by Abdollahzadeh and Faghihmaleki (2017) is obtained by calculating the risk as a consequence of a single critical event. Sørensen (2011) considers that the risk calculation is a function of the following parameters: cost of damage or local failure, cost of indirect damages, probability of exposure to a critical event, probability of damage given an exposure, and probability of indirect damages given a local damage due to exposure.

More general RB_I, based on well-established methodologies such as the Taguchi method, are also available. Dehnad (1988) expresses that in essence, the Taguchi method defines robustness as the quadratic quality loss function. To increase the robustness, this author focuses first into putting the mean of the output distribution on target and then minimizes the variation around this mean value. An alternative definition is offered by Streilein and Hillmann (2002), where the RB_I is defined as the coefficient of variation, COV, in terms of the standard deviation and mean. The author classifies the system as robust if the COV of the output parameters is smaller or equal to the COV of the input. An extension of this method is presented in the work of Lee and Park (2002), where the signal-to-noise ratio is discarded in favor of a characteristic function that defines the robustness of the objectives and constraints. Furthermore, Hwang and Park (2005) introduce a RB_I based on the output variation and the probability of achieving the target by means of a robustness weighting function. Along this line, Watai et al. (2009) expand its usage to non-normal distributions based on the assessment of the feasibility of a design within a prescribed tolerance range. Ultimately, the work of Lomario et al. (2007) considers output distributions with multi-modal behavior and uses the Kolmogorov-Smirnov test to compare these output distributions to predefined ideal normal distributions.

Considering the specific case of the robustness characterization through the RB_I for structural members, Sippel and Marczyk (2009) state that for a structure to be robust, its

topology should not change even when it is subjected to disturbances. In this approach, robustness is measured by the complexity of the structure, i.e. the number of alternate load-paths, and disturbances are characterized by entropy. In the work of Chen et al. (2016), it is mentioned that the two key aspects to be solved in structural robustness are the uncertainty of abnormal events and the capacity that the structure has to resist collapse or failure when locally damaged; being this latter characteristic a property of the connectivity of the structure. Moreover, Chen et al. (2016) claim that the use of a single robustness index is unpractical for engineering applications as it does not capture all possible critical events. Therefore, these authors define robustness as the opposite of structural vulnerability, i.e. how far is the current loading state of a component relative to its failure state. The vulnerability of each component in the structure is weighted by a so-called importance coefficient. This coefficient is defined as the initial bearing capacity of the structure after failure of the component in question. Then, the overall robustness index of the structure can be calculated as 1-vul, being vul the weighted sum of all of the vulnerability values of each member in the structure. Similar robustness indices, such as the one proposed by Sørensen (2011) define the residual influence factor to measure the effect of a member failure on the total load-carrying capacity of a structure. Other displacement-based or stiffness-based RB_I approaches are proposed in the works of Biondini et al. (2008) and Starossek and Haberland (2009) respectively.

Dedicated RB_I, with specific characteristics tailored to crashworthiness applications have also been developed in the works of Andricevic et al. (2016) and Cuevas-Salazar and Song (2018). The robustness of the behavior of the axially loaded extrusion profiles analyzed by Andricevic et al. (2016) is characterized by a RB_I calculated as a weighted sum of the following four factors:

- achievement of targets defined as the ratio of number of samples meeting the upper and lower limits considered in the design requirements;
- standard deviation around the mean value;
- minimum and maximum values of the output response;
- weighted distance of non-feasible samples from the design target.

When the RB_I takes values from negative infinite to 0, the robustness of the design is considered unacceptably low. For values between 0 and 0.5 the robustness is considered low and major design improvements are recommended, while the robustness of the output is considered acceptable for values larger than 0.5. Apart from using an arbitrary robustness scale, the RB_I in Andricevic et al. (2016) depends on the selection of the weighting coefficients for each factor. Additional limitations are that it can only characterize a single output parameter at a time and that additional transformations are needed for mean responses and targets close to zero. The robustness index proposed by Cuevas-Salazar and Song (2018) is based on the calculation of the coefficient of variation of relevant output quantities and is tested using a full-vehicle FE model simulating the Small Overlap load case. The limitations of this approach include a codomain of negative infinite to positive infinite, i.e. $RB_I>0$ robust design and $RB_I<0$ not a robust design, which impedes an effective comparison among output parameters with extreme responses.

The ideal robustness index for crashworthiness applications should facilitate the comparison of the robustness of different output quantities and should be mathematically well-defined. Additionally, it should be as independent as possible from subjective interpretations and should not be characterized by an arbitrary scale. The issues identified are addressed in this work and a novel robustness index is proposed in Section 6.2.5.

2.7. The Small Overlap Frontal Crashworthiness Evaluation

Unlike other vehicle features that can be evaluated prior to purchase, the passive safety of a vehicle cannot be personally evaluated by the customer (Weber, 2009). Moreover, even after purchase, crashworthiness can only be tested in the undesirable situation of an accident. Therefore, the list of vehicle safety features and the results of standardized crash tests are the only clues the customer has to perceive the vehicle's passive safety. To test the crashworthiness of vehicles, several institutions have developed a series of test scenarios that represent real-world accidents. For example, the Insurance Institute for Highway Safety (IIHS) introduced the Small Overlap Frontal Crash (SOF) test case in 2012 to represent the collision of the vehicle's front corner with the corner of another vehicle, a tree, or a utility pole (Insurance Institute for Highway Safety, 2021). This test scenario has become one of the most challenging load cases, causing manufacturers to redesign their vehicles. In this crash test, the integrity of the structure is tested by measuring the intrusions into the occupant compartment, as well as the kinematics of the dummy and the injury criteria (Insurance Institute for Highway Safety, 2021). Strategies to minimize the deformation of the occupant compartment include bracing and installation of energy-absorbing elements on the outer areas of the vehicle's front rails (Thomas, 2011). Each countermeasure affects the kinematics of the vehicle, i.e. its trajectory and the maximum rotation occurring at the end of the impact. In addition, the vehicle kinematics determine the occupant motion and thus influences the dummy kinematics and injury values. The IIHS currently conducts the test on the driver and passenger sides. However, the analysis of this work focuses only on the test conducted on the driver side.

In the SOF crash test conducted by IIHS, the vehicle reaches its initial velocity of 64.4 km/h with a tolerance of ± 1 km/h and an average acceleration of 0.3 g. Approximately 25 cm before the barrier, the vehicle disengages from the propulsion system. The vehicle then strikes the barrier with a 25% ($\pm$ 1%) overlap with respect to its total width. The shape of the barrier consists of a constant radius arc of 150 mm connected to a flat surface with a width of 1000 mm. The barrier is attached to a base unit which is 1840 mm high, 3660 mm wide and 5420 mm deep as stated in Insurance Institute for Highway Safety (2021). The base unit is made out of laminated steel and reinforced concrete, has a total mass of 145,150 kg and is considered non deformable. Figure 2.2 shows a schematic diagram of the SOF crash test.

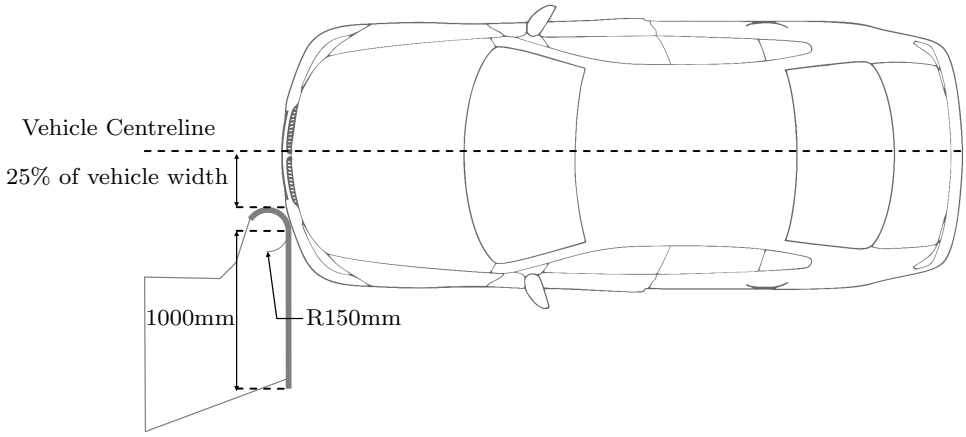

Figure 2.2 Vehicle position and barrier overlap at the moment of contact (Cuevas-Salazar et al., 2019)

The IIHS protocol defines six locations for measuring intrusions at the upper occupant compartment (UOC) and four locations at the lower occupant compartment (LOC) as presented in Figure 2.3. The intrusions are used by the IIHS to determine the structural rating if the vehicle. The upper limits of the intrusion values for each structural rating, $SR_{u_{lim}}$, are presented in Table 2.2.

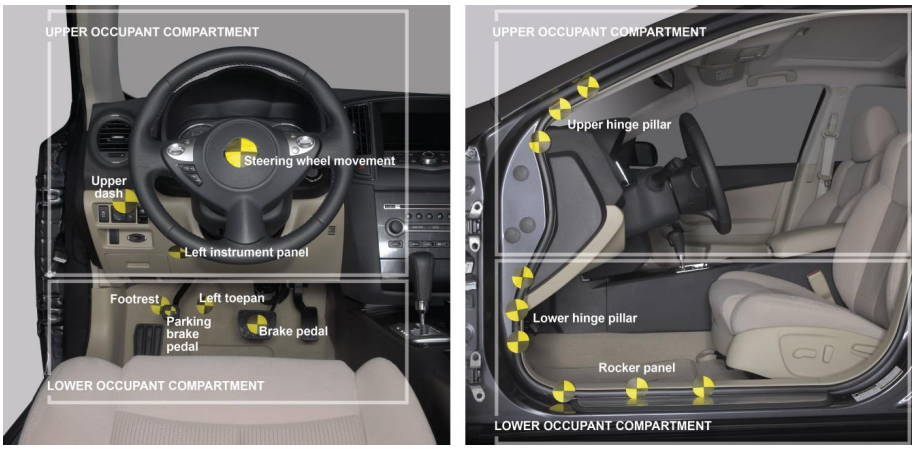

Figure 2.3 Locations for measuring vehicle intrusions. The maximum of the three measurements is taken for the upper and lower hinge pillar while the average value is taken for the rocker panel (Insurance Institute for Highway Safety (2021)).

The dummy kinematics and vehicle trajectory are captured by high-speed video cameras recording at 500 frames per second; six off-board (overhead, rear oblique, left side, front, front oblique, and right side) as well as four on-board (passenger door (front), inside roof passenger side, inside roof driver side, and passenger door (rear)). The off-

board video footage, i.e. the top-view, is used in this study to evaluate the kinematic performance of the vehicles. Even though the vehicle acceleration itself is not considered by the IIHS to calculate the vehicle rating, the longitudinal, lateral, and vertical accelerations of the occupant compartment are measured and recorded during the official tests (Insurance Institute for Highway Safety, 2021). During the development tests carried out by the automakers, additional tri-axial accelerometers and rotational velocity sensors are placed at various locations of the vehicle. Furthermore, a barrier capable of measuring the contact forces containing load cells at the frontal flat surface and at the rounded corner of the barrier, (five in the transversal direction and eight along the barrier's height) is used in development tests. The full instrumentation of the barrier can offer new data about the structural behavior during the test (Silva and Parera, 2016).

Table 2.2 Upper limit intrusion values in mm to earn a given Structural Rating ($SR_{u_{lim}}$) (Insurance Institute for Highway Safety (2021))

Intrusion	*Good*	*Acceptable*	*Marginal*
Lower occupant compartment			
Lower hinge pillar max, HP_l	150	225	300
Footrest, F_r	150	225	300
Left toepan, Tp_l	150	225	300
Brake pedal, B_p	150	225	300
Parking brake, P_b	150	225	300
Upper occupant compartment			
Rocker panel, R_p	50	100	150
Steering column, S_c	50	100	150
Upper hinge pillar, HP_u	75	125	175
Upper Dash, D_u	75	125	175
Left Instrument Panel, IP_l	75	125	175

2.7.1. Kinematic Characterization

An optimal classification of the SOF kinematic modes should cover the complete spectrum of kinematic behaviors independently of the vehicle architecture. Furthermore, the parameters and thresholds defined must be direct functions of the vehicle kinematics with a clear and precise definition of the points in time at which the measurements should be taken. Ultimately, the characterization of the vehicle kinematics should support the crashworthiness design of the vehicle by identifying kinematic behaviors that are of particular benefit to the dummy response and structural performance. Several authors have proposed approaches to classify the vehicles' kinematics when subjected to the SOF crash test. Based on the work of Cuevas-Salazar et al. (2019), Table 2.3 presents the main characteristics and limitations of the approaches available in the literature.

Table 2.3 Classifications of the kinematic response of vehicles subjected to the SOF load case

Lateral translation & rotation	Characterized by the post-impact lateral translation, u_y, and maximum rotation, θ_z, around the vertical axis of the vehicle.
Classification:	• Primarily lateral translation: Lateral movement away from the barrier: $u_y(t \approx 150\text{ms}) > 35\text{cm}$. • Primarily rotation: Higher longitudinal change in velocity and larger rotation around the barrier: $\max(\theta_z(t < 200\text{ms})) > 10°$, $u_y(t \approx 150\text{ms})$.
Remarks:	Lateral translations larger than 35 cm combined with rotations larger than 10° are not classified. Missing validation of the thresholds and the points in time at which the kinematic quantities are measured.
Relevant authors:	Mueller et al. (2014); Thomas (2011)
Sideswipe	The ratio $\mu = P_T/P_N$ relates the tangential, P_T, and normal impulses, P_N, applied to the vehicle during the crash. An optimization process using a planar impact mechanics model is conducted, with μ, the coefficient of restitution, and the crush-surface angle as design variables. The cost function is defined as the difference between the measured post-impact translational and rotational velocities. The final velocities are obtained using a video analysis of 41 crash tests. A statistical difference is identified between the values obtained for the impulse ratio and the coefficient of restitution while varying the barrier's geometry. A critical value was established for the ratio between the impulse ratio at the beginning of the crash, μ_0, and at the end of the crash, μ.
Classification:	• Sideswipe: Larger than zero final tangential velocity: $\mu/\mu_0 \leq 97\%$. • Non-Sideswipe: Negligible final tangential velocity: $\mu/\mu_0 > 97\%$.
Remarks:	Clear threshold for the kinematic modes. The parameter used for the differentiation of the modes is a variable directly related to the ratio between the tangential and longitudinal impulses. The optimization process may decrease the practical applicability of the method. Moreover, since the proposed threshold was obtained from testing a reduced variety of vehicle structures (mainly sedans), it could be challenging to extrapolate its use for other vehicle architectures.
Relevant authors:	Brach et al. (2014)

The current classifications are based on a reduced number of crash tests and their definitions are highly dependent on the vehicles available for the analysis. In some cases, the classification does not offer clear thresholds to distinguish the kinematic modes. With these limitations recognized, a well-defined classification based on the geometrical relationships and the vehicle's relative location at the end of the crash is proposed in Section 3.2.

2.7.2. Methodologies for Crashworthiness Design for the SOF Load Case

The classification of the kinematic modes of the SOF crash test enhances the derivation of structural design strategies that are implemented in the vehicle in the detailed engineering phase. These design strategies are studied in the work of Mueller et al. (2014). The two distinguishable kinematic responses, transversal displacement away from the barrier and vehicle longitudinal deceleration, are achieved by following either a maximization of the lateral impulse or the maximization of energy absorption. Optimization procedures for both strategies have been developed, where the profile and wall thickness of components such as the A-Pillar, front rails, Hinge-Pillar, and Rocker are used as design variables (Nguyen et al., 2015b,a; Kim, 2017; Luu and Anh, 2021; Liu et al., 2021b). Full-vehicle finite element models are used to evaluate the objective function of such optimization procedures that aim for a combination of minimization of the occupant compartment intrusions as well as the minimization of the total mass of the vehicle. In addition to these studies, Sen et al. (2013) and Nguyen (2017) propose to conduct sensitivity analyses in parallel to the optimization procedures to achieve a more robust response. In order to reduce the computational cost associated to the optimization procedures, Liu et al. (2021a) use a response surface to evaluate the fitness of the designs obtaining acceptable results.

The usage of full-vehicle models implies that the vehicle is already in a design phase where enough information is available to perform such an analysis. However, this approach does not enable the study of the vehicle's response during the early design phase. Moreover, it only evaluates the high-level requirement of structural rating. The lack of component requirements makes it impossible to parallelize the design and accelerate the development process. A multi-phase and requirement-oriented methodology for the design of vehicle structures subjected to the SOF load case is proposed in this work with the aim to tackle these limitations.

Chapter 3

Characterization of the SOF Load Case

The analysis of the vehicle kinematics at every instant of the SOF crash test allows the identification of the position of the occupant compartment relative to the barrier. Furthermore, the resulting intrusions, caused by the direct contact of the A-Pillar with the barrier or the forces transmitted by adjacent components, can be defined as a function of the vehicle kinematics. The importance of this force transfer to the vehicle during the crash has been stated in Silva and Parera (2016). As shown in Section 2.7, this aspect of this load case is incompletely investigated in the literature. Hence, this thesis proposes (i) to establish a precise distinction between the two possible kinematic modes and (ii) to exploit the strong correlation between the vehicle kinematics and the structural intrusion during the SOF crash test. The second point implies the estimation of the intrusions caused by the contact of the A-Pillar with the barrier by tracking the position of the occupant compartment relative to the barrier at every instant of the SOF crash test. This methodology, which, to the authors' knowledge, has only been discussed in a prior publication of the author, see (Cuevas-Salazar et al., 2019), is here refined and further developed as well as described and discussed in this chapter in detail.

3.1. Crash Event Analysis

The crash testing of series vehicles or prototypes is usually the last validation step conducted in the crashworthiness design. Once the virtual stages of design converge to a certain structure and the performance of the vehicle has been completely assessed through the use of simulations and component testing, the OEMs proceed with the full-vehicle hardware tests. The cost of evaluating the performance of a certain design in hardware is magnitudes higher than evaluating the design virtually. For this reason, the extraction and analysis of the information produced by the hardware tests are of essence when verifying requirements at the load-path level and validating the full-vehicle performance either with the intent to sign off the design or to improve it. In both cases, a clear,

repeatable and automated crash event analysis scheme is fundamental to streamline the data analysis and evaluate the performance of a single vehicle and at the same time have the capability to create a database of a large set of vehicles that enable more complex analysis. With a database already built, correlation and cluster analysis can be performed to find relationships between the input and output variables involved in the crash that ultimately help first to improve the understanding of the physics involved and secondly find the patterns that lead to a robust fulfillment of the structural targets. Figure 3.1 presents the crash event analysis scheme that provides a solid base for the study of the hardware tests used in this work.

The raw data available from the crash test that is relevant for this thesis is threefold: the high-speed video footage, the motion sensor data, i.e. acceleration and rotational velocity signals, and force signals from the measurement equipment in the barrier. The high-speed video footage and the motion sensor data are used either complementarily or separately when only one is available to reconstruct the trajectory of the vehicle during the crash. When the video of the crash is available, a video analysis routine is capable of recognizing the relevant features of the vehicle in time zero, i.e. the point in time where the first contact between the vehicle and the barrier occurs. The relevant features enable the contextualization of the position of the vehicle and the barrier. Through the use of pixel color identification and edge detection, features such as the barrier and vehicle edges, vehicle centerline and the several targets positioned over the vehicle, help to locate the vehicle and barrier in the video frame and relative to each other. Then, this features are tracked in each frame following the motion, i.e. translation and rotation of the vehicle. In a post-processing step, the pixel motion and distances are translated into a standard unit of measurement by means of a reference length and a spatial mapping procedure.

When motion sensor data is available, the acceleration and rotational velocities are used to reconstruct the trajectory of the vehicle. Usually, $3-D$ acceleration and rotational velocity sensors are placed near the center of gravity of the vehicle. In the majority of the cases, this part of the vehicle does not suffer deformations and the signals acquired by the sensors can be used to characterize the motion of the complete vehicle. To express the sensor signals in a global coordinate system that is independent of the vehicle orientation, a transformation of the acceleration and rotational velocities is applied. Given that the position and orientation of the sensors at the initial time, t_0, are known, a global and a local coordinate system are defined, in which the sensor data is expressed. This local coordinate system is rotated in each time step according to the rotational velocity signal and through the use of the simultaneous orthogonal rotation theorem, see (Tomazic and Stancin, 2011). Having calculated the orientation of the local coordinate system of the sensor with respect to the global coordinate system, the acceleration signal is also rotated to obtain it expressed in global terms. These $3-D$ acceleration and rotation signals expressed in the global coordinate system are used to calculate the trajectory of the center of gravity and through the use of the assumption of rigid body motion the position of any point in the structure can be obtained.

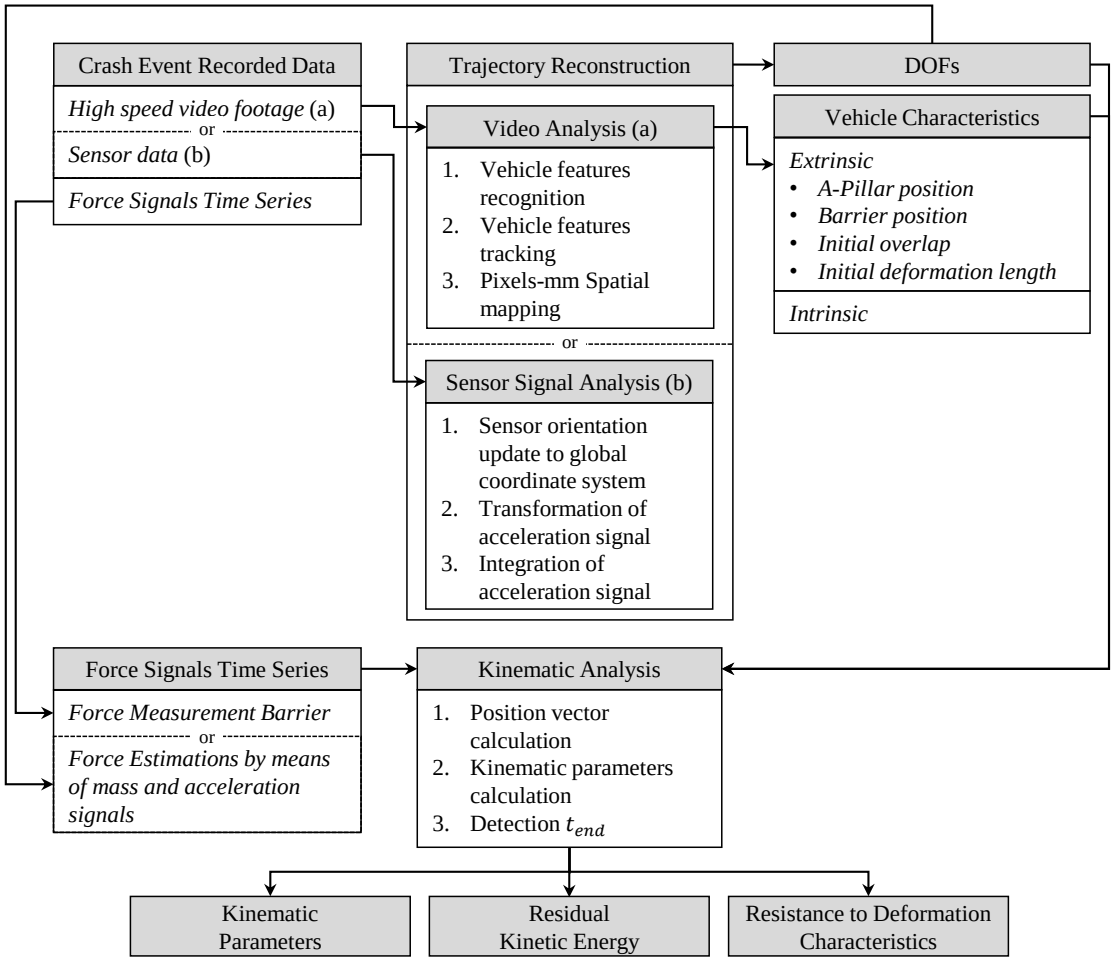

Figure 3.1 Crash event analysis framework

The third set of input data is the signals obtained from the force-measuring equipment integrated in the Small Overlap barrier. A number of force-measuring devices along and across the surface of the barrier provides force-time series that can be correlated to a certain spatial location and can be mapped also to the structure of the vehicle once its trajectory has been reconstructed. Being able to measure the forces acting on the vehicle is relevant because these are the functional properties that can be adjusted through design changes in the structure so that the deformations in the occupant compartment are minimized. In the case that a force-measuring barrier is not used during the crash test, the total forces can be estimated by using the acceleration signals and the mass of the vehicle.

Having collected and produced these three sets of crash event data, and together with the vehicle characteristics, the kinematic analysis of the Small Overlap load case can be carried out. The trajectory of the center of gravity of the vehicle, CG, can be expressed as the longitudinal translation, u_x, the transversal translation, u_y and the rotation around the vertical axis, θ_z. These three motion quantities are stored in the degree of freedom vector, DOF. Even if the crash phenomenon is a complex $3-D$ motion, the planar movement in the xy plane has the highest relevance. This assumption is assessed in the subsequent sections, where an example of this crash event analysis is presented. The kinematic analysis, through the definition and calculation of the kinematic parameters helps to characterize the overall motion of the vehicle and enables the study of the relationship between the vehicle kinematics and its crashworthiness performance. The next sections will provide an insight on this procedure and its application for crashworthiness design.

3.1.1. Hardware Experiment Evaluation

An object recognition algorithm was implemented to recognize the static, i.e. barrier-related, features and the dynamic features related to the vehicle and its trajectory. The main steps are summarized in the work-flow in Figure 3.3. Table 3.1 presents the variables and definitions used for the object recognition and extraction of kinematic quantities. The first step consists of the extraction of the static features, i.e. the edges of the barrier, represented by B_x and B_y. The edges of the SOF barrier are painted orange by the IIHS. Therefore, the three-dimensional array $\mathbf{F}$, containing the RGB values for each pixel in the frame, is color filtered to identify B_x and B_y, (see Figure 3.2). Next, the frame where the vehicle contacts the barrier is recognized in two sub-steps. First, $\mathbf{F}$ is transformed into a grey scale image obtaining the two-dimensional array $\mathbf{F_g}$. By comparing $\mathbf{F_g}$ in two consecutive frames, the pixels representing the moving vehicle are identified. Second, the distance between the pixels representing the moving vehicle and B_x is monitored. The first frame of contact between the barrier and the vehicle is identified when this distance is zero.

Once the frame of initial contact vehicle-barrier is determined, the dynamic features are identified at this same frame. First, the vehicle's centerline is identified by means of a color and spatial filter. The yellow pixels corresponding to the bonnet inch-tape are discarded and the pixels corresponding to the roof inch-tape are stored in the array

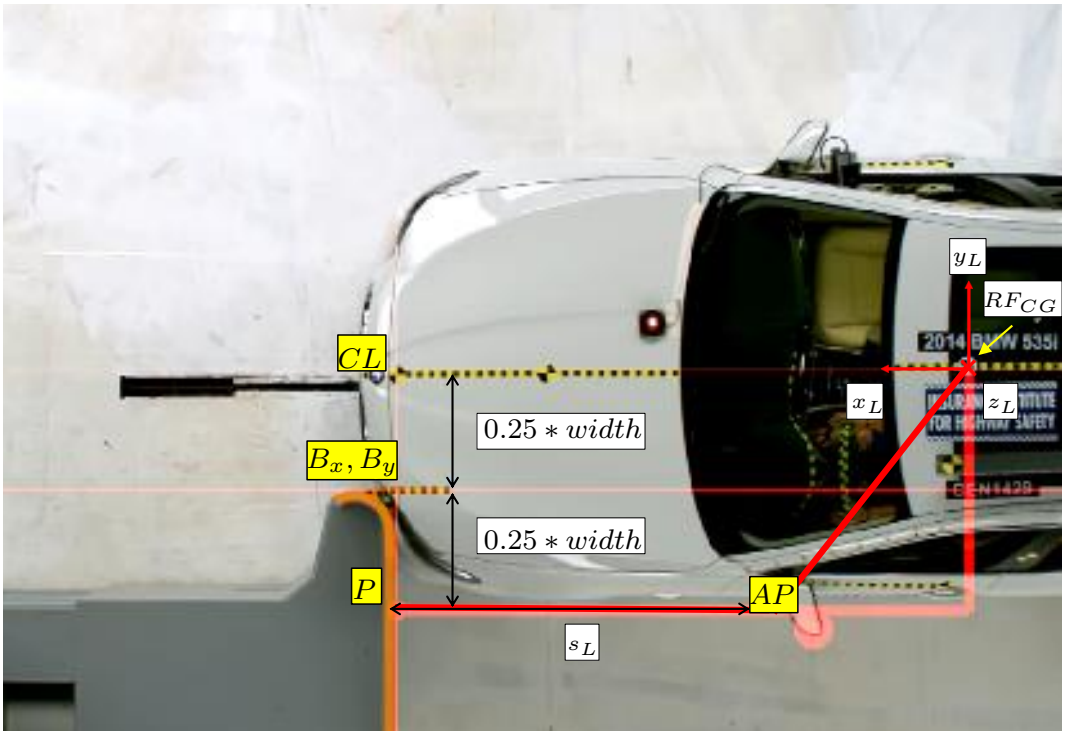

Figure 3.2 Identification of vehicle characteristics at the first frame of contact of the top view of the IIHS's SOF test (Cuevas-Salazar et al., 2019)

$\mathbf{F_{CL}}$. Then, the black-and-white photographic target representing the center of gravity is identified in the rectangular space containing the pixels corresponding to the roof. A pixel pattern depicting a reference target, T_{ref}, is compared against the photographic target. Next, the point AP, representing the location of A-Pillar, is defined by locating a point in the most outwards position of the structure using the centerline and the edge of the barrier B_y as reference points to calculate the 25% of the vehicles width. Having located these reference points in the frame representing the first vehicle-barrier contact, the dynamic features, the position of the center of gravity and the rotation of the vehicle are identified. The dynamic position of the center of gravity is located by iteratively comparing the reference of the photographic target against a subspace defined by a buffer zone around the location of the target in the previous frame. The dynamic rotation is identified by calculating the angle between the centerline and the horizontal axis of the frame. These two procedures are repeated at each available frame. In a last step, the pixel and frame values are converted to meters and seconds, on one hand, by using the distance between the two yellow targets at the roof representing the seat centerline as spatial reference (see (Insurance Institute for Highway Safety, 2021)), and on the other hand, by comparing the initial velocity measured in the video analysis to the stipulated initial velocity.

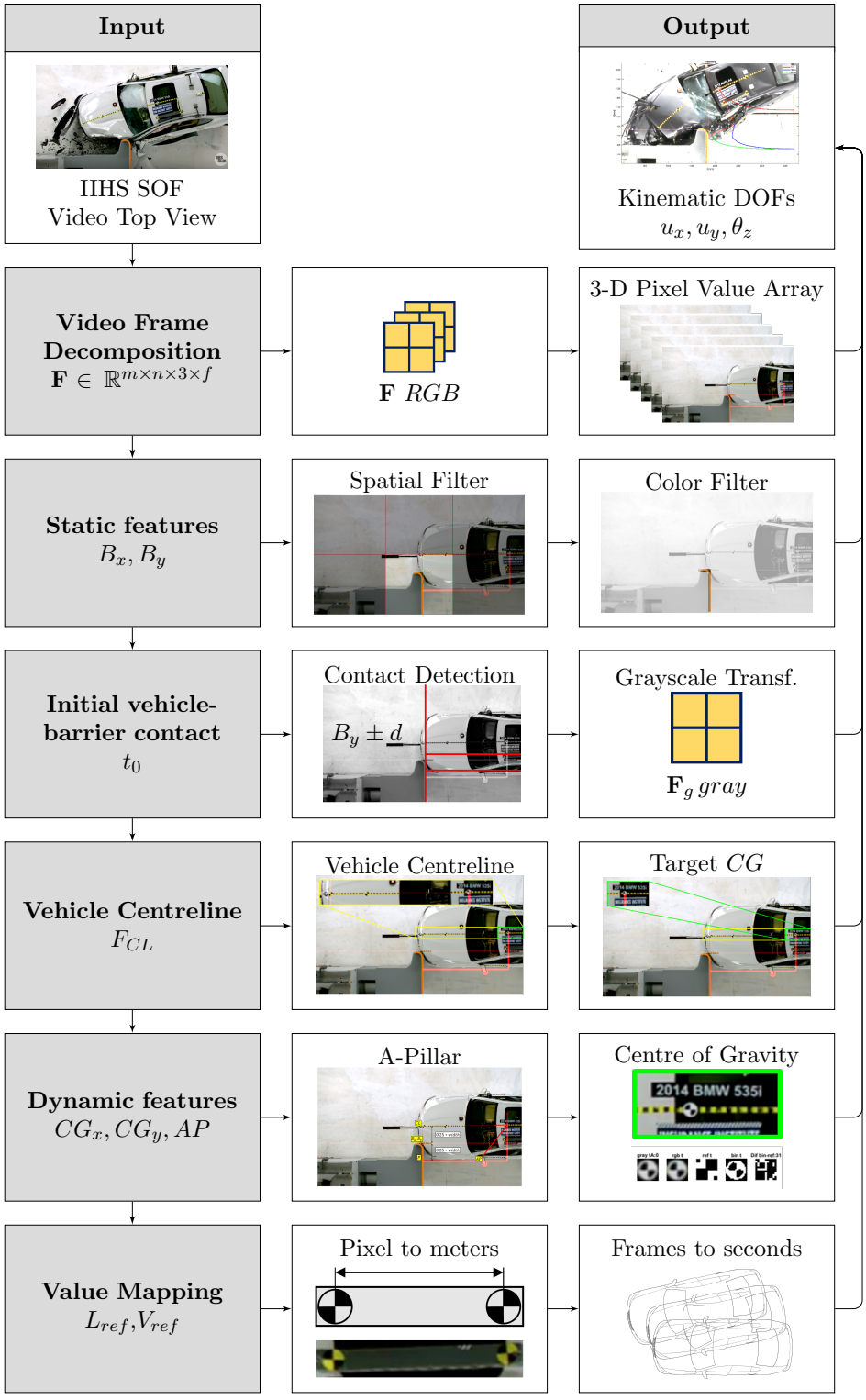

Figure 3.3 Algorithm for object recognition and extraction of kinematic quantities (Cuevas-Salazar et al., 2019)

Table 3.1 Variables and definitions used for the object recognition and extraction of kinematic quantities

Definition	Variable
Array with RGB values of each frame	$\mathbf{F} \in \mathbb{R}^{m \times n \times 3 \times f}$
Total number of frames	f
Vertical size of frame in pixels	m
Horizontal size of frame in pixels	n
Array with grey scale values of each frame	$\mathbf{F_g}$
Binary array with pixels of the vehicle centerline	$\mathbf{F_{CL}}$
Array with black-and-white reference target	T_{ref}
Reference length in mm for pixels-to-mm mapping	L_{ref}
Reference length in pixels for pixels-to-mm mapping	V_{ref}
Initial vehicle-barrier contact time point	t_0
Vertical position of vehicle centerline at first frame of contact	CL
Vehicle's local-x axis	x_L
Vehicle's local-y axis	y_L
Vehicle's local-z axis	z_L
Vehicle's local reference frame	RF_{CG}
Static global-x axis	x_G
Static global-y axis	y_G
Static global-z axis	z_G
Static global reference frame	RF_G
Horizontal edge of barrier	B_x
Vertical edge of barrier	B_y
Vertical position of vehicle's center of gravity	CG_x
Horizontal position of vehicle's center of gravity	CG_y
Vertical position A-Pillar	AP_x
Horizontal position A-Pillar	AP_y
Projection of A-Pillar onto the barrier	P
Distance between A-Pillar and projection P	s_L
25% of the vehicle's width	$w_{0.25}$

3.2. Characterization of the vehicle kinematics

The objective of the different crash tests is to investigate the response of the vehicle at the area of impact, where the large deformations are confined. Therefore, for the characterization of the vehicle's response, a combination of rigid and deformable body

mechanics is convenient to exploit the advantages of both approaches. This offers sufficient accuracy and efficiency for early phase development. Cuevas-Salazar et al. (2017) propose a kinematic model that considers the impact area as a deformable body and the rest of the vehicle as a rigid body. This model is used for the subsequent analysis presented in this work.

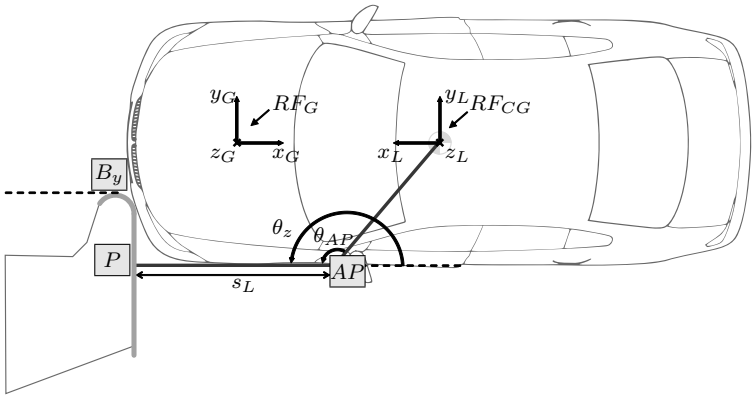

Figure 3.4 Vehicle reference frame. The point AP is the location of the A-Pillar while P represents the projection of the A-Pillar onto the barrier's surface. The coordinate B_y represents the barrier's edge closest to the vehicle's centerline (Cuevas-Salazar et al., 2019).

The center of gravity of the vehicle, CG, is used as reference point, to measure the rigid body motion. This reference point can be easily located on vehicles with different styles and is located outside the deformation zone. As described in Section 3.1, the kinematic model employs three degrees of freedom (DOFs): the displacements of the vehicle's CG, u_x and u_y, and the rotation, θ_z, around the vertical axis. The examination of high-speed video footage of the SOF test led to the simplification of the kinematics by assuming a planar motion in a horizontal 2-D plane. The DOFs are measured with respect to the global reference frame, RF_G, located at the vehicle's centerline at the front axle depicted in Figure 3.4. A supplementary co-rotational coordinate system, RF_{CG}, is located at the CG. In the model, the frontal structure is the only area considered deformable implying that the structure located after the A-Pillar is assumed to be rigid.

Besides the DOFs, additional parameters are introduced to characterize the kinematic response. The parameter s_L represents the length of the vector between the points AP and P. This vector rotates together with the vehicle's centerline. The points AP, P, B and CG are computed using RF_G as reference frame. The position of the A-Pillar is the point in the longitudinal direction that typically defines the starting point of the occupant compartment as well as the most outboards point of the vehicle structure. The parameter s_L is an indicator of the deformation length available before a hard contact between the A-Pillar and the barrier takes place. Table 3.2 presents auxiliary parameters conveniently derived as dimensionless quantities in order to facilitate a straightforward comparison among vehicle architectures.

Table 3.2 Kinematic parameters

Definition	Variable
Reduction of the distance relative to the initial available deformation length	$s = s_{L_{t_0}} - s_L$
Normalized version of s to take out the effect of vehicles with different front ends	$s_{\%} = s/s_{L_{t_0}}$
Normalized global longitudinal displacement wrt. initial available deformation length	$T_x = u_x/s_{L_{t_0}}$
Normalized global transversal displacement wrt. initial available deformation length	$T_y = u_y/s_{L_{t_0}}$
Normalized global longitudinal velocity wrt. initial velocity	$V_{x_{end_{\%}}} = V_{x_{end}}/V_{x_0}$
Normalized global longitudinal velocity wrt. initial velocity	$V_{y_{end_{\%}}} = V_{y_{end}}/V_{x_0}$
Ratio between the displacement of the point P along the y-axis and the initial overlap between the structure and the barrier defined by the distance from P to B_y.	$GV_P = \frac{P_{y_t} - P_{y_{t_0}}}{B_y - P_{y_{t_0}}}$

The glance-off value, GV_P, depicted in Figure 3.5, takes the value of zero at $t = t_0$. If the y-coordinate of P is greater than B_y, GV_P is larger than one. By calculating GV_P at each point in time, it can be determined if the vector $\mathbf{s_L}$ - and subsequently, the vehicle - is heading towards the barrier as well as the extent of the overlap between the structure and the barrier. Since this value is normalized by the initial overlap, the GV_P of vehicles with different widths and architectures can be conveniently compared.

The end of the crash, t_{end} is defined as the instant when either (a) the projection point P is located at a larger y-coordinate than the barrier's edge B_y or (b) the length s_L is no longer decreasing. It is first assumed that the end of the crash is triggered by event (a). The GV_P is calculated for all of the points in time and the first occurrence of $GV_P \geq 1$ is selected as $t_{end}^{GV_P}$. If during the crash $GV_P < 1$, $t_{end}^{GV_P}$ takes the last data point and therefore, it is assumed that the end of the crash is triggered by event (b). The value of s_L is then calculated for the available data along with its change rate, ds_L/dt. This derivative is inspected for values equal or smaller than zero. The first occurrence of $ds_L/dt \leq 0$ is set as $t_{end}^{s_L}$. The occurrence of this event indicates the start of the rebound. If no occurrence is found, the last point available is selected as $t_{end}^{s_L}$. Finally, the minimum of $t_{end}^{GV_P}$ and $t_{end}^{s_L}$ is chosen as the end of the crash. It is assumed that the end of the crash happens before the end of the available data points. The parameters, s_L, s, $s_{\%}$, $ds_{\%}/dt$, T_x, T_y, $V_{x_{end_{\%}}}$, $V_{y_{end_{\%}}}$, GV_P and t_{end} are direct functions of the kinematic DOFs (u_x, u_y, θ_z). Each parameter is precisely defined in the spatial and temporal dimensions.

3.2.1. Definition of Kinematic Modes

As described in the literature presented in Section 2.7.1, the use of the *primarily lateral translation* and *primarily rotation* definitions could lead to ambiguous results (Mueller

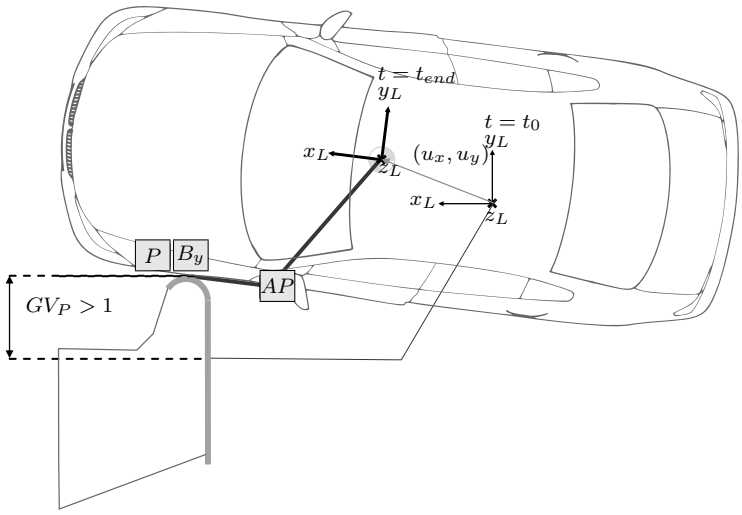

(a) $Glance - off$ kinematic mode.

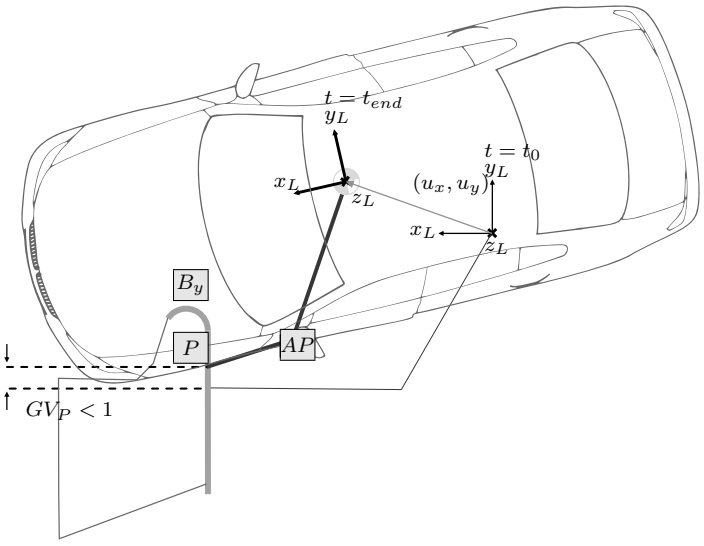

(b) $Deformation$ kinematic mode.

Figure 3.5 Kinematic modes and parameters ((a) *Glance-off*, (b) *Deformation*). The instant of the first contact between the vehicle and the barrier is defined as t_0. (Cuevas-Salazar et al., 2019)

et al., 2014). It is then convenient to make a clear and categorical distinction of the two kinematic modes. Furthermore, making such definition independent of the vehicle architecture and any empirical values is favorable for the comparison of different designs. A distinction between *deformation* and *glance-off* modes is proposed. A depiction of the two modes is presented in Figure 3.5 and formal definitions are given in Eqs. (3.1) and (3.2).

$$\begin{aligned} &Deformation \text{ mode}: \\ &\qquad GV_{P_{t_{end}}} < 1 \text{ and } \frac{ds_{\%}}{dt}\Big|_{t_{end}} \leq 0; \qquad (3.1) \\ &Glance-off \text{ mode}: \\ &\qquad GV_{P_{t_{end}}} \geq 1 \text{ and } \frac{ds_{\%}}{dt}\Big|_{t_{end}} > 0. \qquad (3.2) \end{aligned}$$

Both modes are mutually exclusive by the definition offered in Section 3.2 to calculate t_{end}. This distinction is neither directly linked to a particular vehicle architecture nor it is obtained empirically. Both $ds_{\%}/dt$ and GV_P come as results of a direct analysis of the vehicle kinematics. In addition, each kinematic mode results from different frontal structure configurations. On one hand, vehicles observing a *deformation* mode most likely carry energy-absorbing components in the longitudinal direction causing mainly longitudinal forces that stop the vehicle provoking $\frac{ds_{\%}}{dt}_{t_{end}} \leq 0$. On the other hand, vehicles observing *glance-off* mode contain transversal oriented structures causing enough force in the transversal direction to cause $GV_{P_{t_{end}}} \geq 1$.

3.2.2. Analysis of the Kinematic Response

The characterization and definition of the kinematic response is now used for the evaluation of real crash data. In Figure 3.6, an exemplary result of the video-analysis algorithm for a BMW 5 Series 2014 is presented. The primary kinematic variables u_x, u_y, and θ_z are used to calculate the kinematic parameters presented in Section 3.2. In this crash event, the minimum value of $s_{\%}$ and subsequently $\frac{ds_{\%}}{dt} \leq 0$ is achieved at $t_{end} \approx 100$ms. At this point in time a positive rotation is observed together with a GV_P<1. Therefore, this kinematic response is classified as deformation mode. The frame corresponding to this state is presented in Figure 3.7, which resembles the deformation mode presented in Figure 3.5b.

The IIHS small-overlap videos from 184 vehicles from model year 2012 to 2017 are analyzed and their kinematic quantities are calculated. The weight of the vehicles varies from 1.0 to 2.5 tonnes, the wheelbase ranges from 2.3 m to 3.8 m, and the width of the vehicle from 1.6 m to 2.0 m. The vehicle specifications, test videos, ratings and intrusion values are obtained from the IIHS TechData website (Insurance Institute for Highway Safety, 2017). In Figures 3.8 and 3.9, the dimensionless kinematic parameters ($s_{\%}$, $ds_{\%}/dt$, T_x, T_y, $V_{x_{end_{\%}}}$, $V_{y_{end_{\%}}}$, GV_P) and the rotation θ_z are plotted for all analyzed vehicles. The end point of the time-series of the kinematic parameters corresponds to

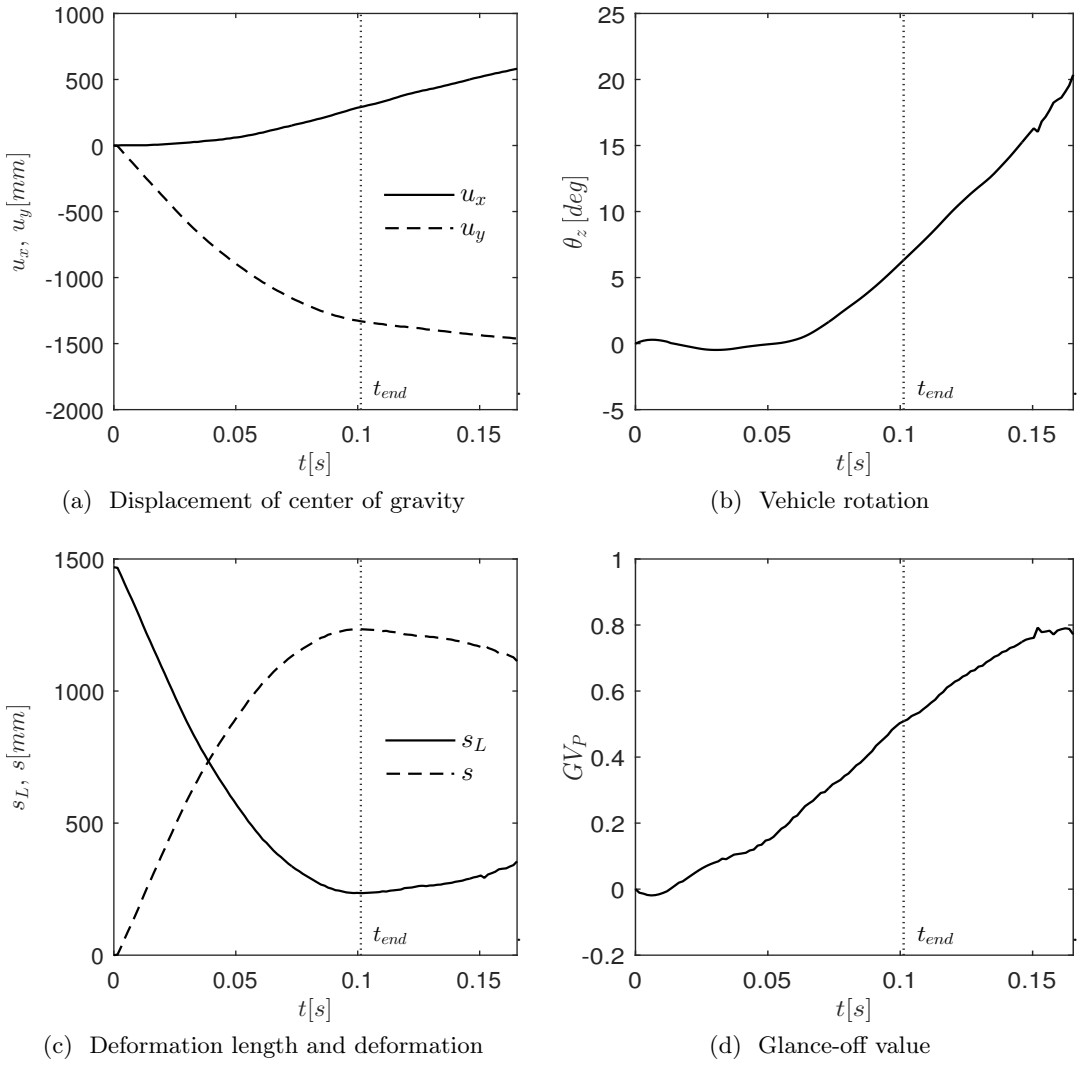

(a) Displacement of center of gravity

(b) Vehicle rotation

(c) Deformation length and deformation

(d) Glance-off value

Figure 3.6 Trajectory and kinematic DOFs (u_x, u_y, θ_z, GV_P, s_L, s) obtained by video analysis of the BMW 5 series 2014 (Cuevas-Salazar et al., 2019)

the t_{end} calculated for each case. The two defined kinematic modes, *glance-off* and *deformation*, are differentiated by line color and symbol.

The two kinematic modes present noticeable differences when comparing $ds_{\%}/dt$ and GV_P in Figure 3.8. These parameters are first plotted against time and are afterwards combined into one plot. In Figure 3.8(c), two distinguishable clusters are observed. The first cluster, corresponding to the *glance-off* mode, is located at the top of the sub-plot with $GV_{P_{t_{end}}} \geq 1$ and $ds_{\%}/dt_{t_{end}} > 0$. The second cluster (*deformation* mode), presents a $GV_{P_{t_{end}}} < 1$ and $ds_{\%}/dt_{t_{end}} \leq 0$. This means that the vehicles in the *glance-off* cluster have lost contact with the barrier and a positive velocity in the longitudinal direction

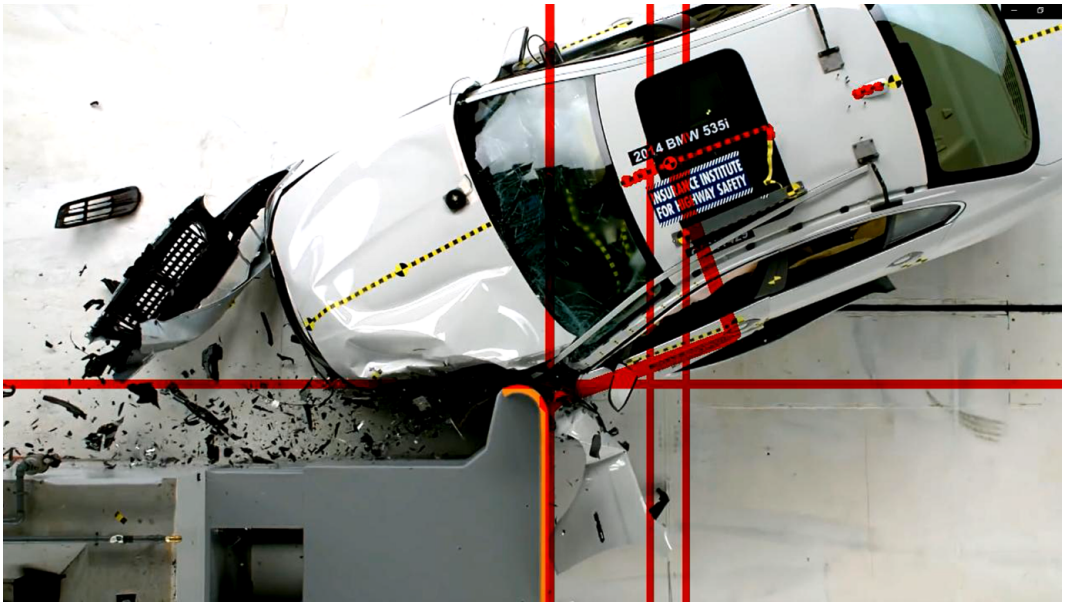

Figure 3.7 Video analysis of the BMW 5 series 2014; frame corresponding to t_{end}

of the vehicle still exists at t_{end}. On the contrary, for the vehicles in the *deformation* cluster, the projection point P is still on the barrier at t_{end} and no velocity exists in the longitudinal direction. Two vehicles, 2014 Mazda CX-9 and 2014 Nissan Juke, marked as a and b in Figure 3.8(c) cannot be classified since there were not enough video frames available to determine t_{end}.

In Figure 3.9(a), an overlapping range of rotation angles can be observed for the two kinematic modes. Positive and negative angles from $-5°$ to $15°$ are observed independently of the kinematic mode. In general, vehicles whose kinematic response fits the *glance-off* mode use relatively more deformation length as the ones in *deformation* mode. However, no clear limit can be detected to distinguish between the two modes as observed in Figure 3.9(b) $s_{\%}$ plot. The normalized trajectory represented by T_x and T_y is plotted in Figure 3.9(c) and, similarly, it can be observed that *glance-off* vehicles exhibit larger displacements in the y_G-direction. This behavior is also visible in Figure 3.9(d), where the vehicles with the *glance-off* mode have in most of the cases a larger $V_{x_{end_{\%}}}$ than the vehicles with the *deformation* mode. Although some ranges can be selected for the T_x, T_y, and $V_{x_{end_{\%}}}, V_{y_{end_{\%}}}$ parameters to characterize the two modes, these ranges can only be defined a posteriori. With this analysis the existence of two distinct kinematic modes is confirmed. A categorical definition for the two kinematic modes is possible by using the three main kinematic quantities u_x, u_y, θ_z and the auxiliary parameters.

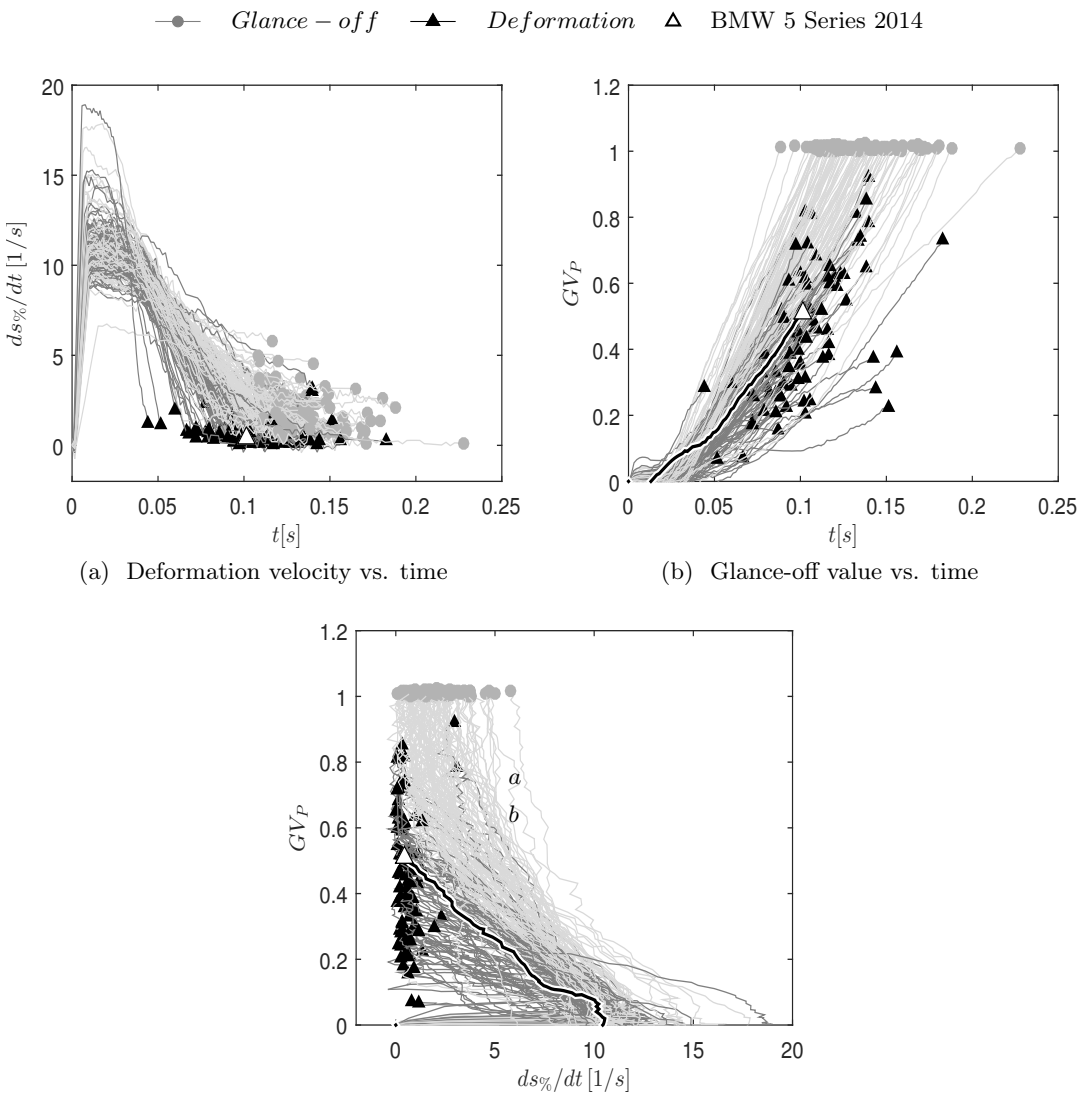

(a) Deformation velocity vs. time

(b) Glance-off value vs. time

(c) Glance-off value vs. Deformation velocity

Figure 3.8 Clustering of the kinematic modes (Cuevas-Salazar et al., 2019)

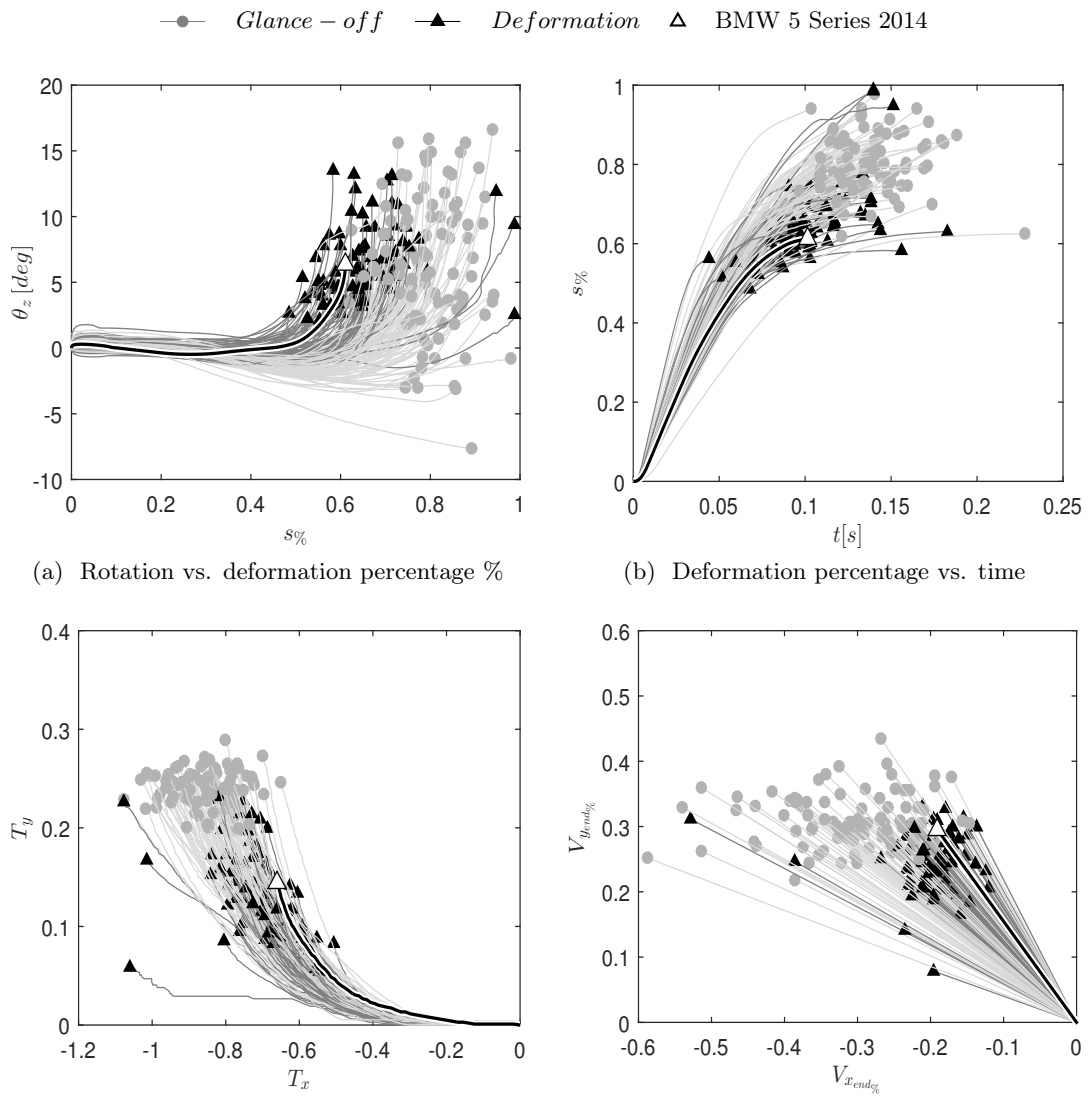

(a) Rotation vs. deformation percentage %

(b) Deformation percentage vs. time

(c) Normalized trajectory

(d) Normalized final velocity

Figure 3.9 Kinematic parameters (Cuevas-Salazar et al., 2019)

3.3. Characterization of Structural Rating and Crashworthiness

The IIHS ranges for rating the occupant compartment intrusion in millimeters (y-axis) and at different locations (x-axis) is presented in Figure 3.10. This figure shows the intrusion measurements for the 2016 BMW X1 with test number CEN1608 as an example. It is observed that for every location, there are four possible ratings which are defined as a piecewise constant function of the intrusion measurements at this location. The overall SOF structural rating, depicted in the pie chart, is calculated by the weighted combination of the location-specific ratings (see IIHS guidelines in (Insurance Institute for Highway Safety, 2017)). As a result, different vehicle characteristics could lead to similar structure performance and therefore, structural ratings. In the case of the exemplary vehicle, it obtained an Acceptable structural rating since two measurement points of the upper occupant compartment exceeded the limit defined for a Good structural rating.

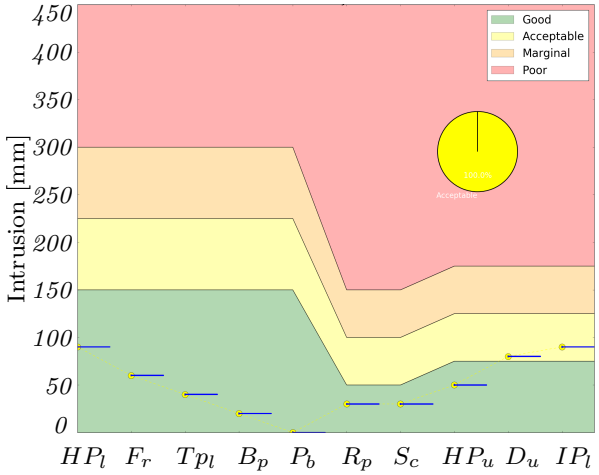

Figure 3.10 IIHS structural rating for the 2016 BMW X1 CEN1608

The IIHS scheme is efficient for communicating the crashworthiness of a vehicle to the general public. However, it is not suitable for comparing the performance of vehicles that have the same structural rating. Moreover, with this scheme, it is not possible to quantify how far is a vehicle from moving to the next worse rating or how much it should improve to obtain a better one. The following section proposes the definition of a variable called safety distance, D_S, which summarizes the structural rating into a single continuous scalar value and simplifies the correlation with the previously defined kinematic parameters, thus allowing the inter-vehicle structural performance comparison, within or outside the same structural rating.

3.3.1. Safety Distance to Target Structural Rating

The safety distance, D_S, to a given structural rating is defined as the distance in percent that the ranges to the associated structural rating must increase or decrease for a vehicle

with a given intrusion profile to move to the next or previous rating. Table 2.2 presents the upper limits for obtaining a Good, Acceptable and Marginal structural rating. Using these values, it can be calculated that the upper limits of Figure 3.10 should decrease altogether by 6.7% in order for the 2016 BMW X1 to obtain a Good structural rating. Therefore, its safety distance to a Good structural rating, D_{SG} is equal to -6.7% as observed in Figure 3.11(a). The safety distance can also be understood contrariwise. For example, how much distance is still available for the 2016 BMW X1 to obtain a Marginal structural rating, or what safety distance buffer there is to remain at Acceptable. As shown in Figure 3.11(b), the safety distance to an Acceptable structural rating, D_{SA} is 35.9%, i.e., the intrusions in the 2016 BMW X1 still have an overall buffer of 35.9% before worsening the structural rating to Marginal. For simplification purposes, in this work, the safety distance of all the vehicles is calculated using the Good structural rating as target, D_{SG}. This implies that vehicles with a positive D_{SG} have reached a Good structural rating and negative D_{SG} have either Acceptable, Marginal or Poor ratings. Table 3.3 summarizes the equivalences between D_{SG} and the four structural ratings.

Table 3.3 Equivalence of structural rating and safety distance to Good structural rating D_{SG} as percentage

Structural rating	**Safety distance**
Good	$\mathbf{0\% \leq D_{SG} \leq 100\%}$
Acceptable	$\mathbf{-60\% \leq D_{SG} < 0\%}$
Marginal	$\mathbf{-130\% \leq D_{SG} < -60\%}$
Poor	$D_{SG} < \mathbf{-130\%}$

The safety distance to a Good structural rating, D_{SG}, is computed using Algorithm 1. Starting with the intrusion measurements from the upper and lower occupant compartments collected in vector $\mathbf{I}$=$[HP_l, F_r, Tp_l, B_p, P_b, R_p, S_c, HP_u, D_u, IP_l]$, as presented in Table 2.2, the structural rating is calculated using the IIHS scheme. If these intrusions result in a Good structural rating, then the upper limits for an Acceptable rating are multiplied by a factor f_{SD}=(1-df), being df a small delta to decrease the magnitude of the upper limit. Afterwards, the intrusions in $\mathbf{I}$ are compared against this reduced upper limit and the updated rating is calculated. This is done iteratively until the upper limit is small enough so that the structural rating is no longer Good but Acceptable. The last value of df is reported and taken as D_{SG}. Alternatively, if the structural rating is not Good but Acceptable, the factor f_{SD} is redefined as f_{SD}=(1+df). The upper limit of the Good rating is multiplied by this factor, allowing for larger intrusions to still be associated with a Good structural rating. This is done iteratively until the rating transitions to Good. The last value of df is taken and reported as D_{SG}.

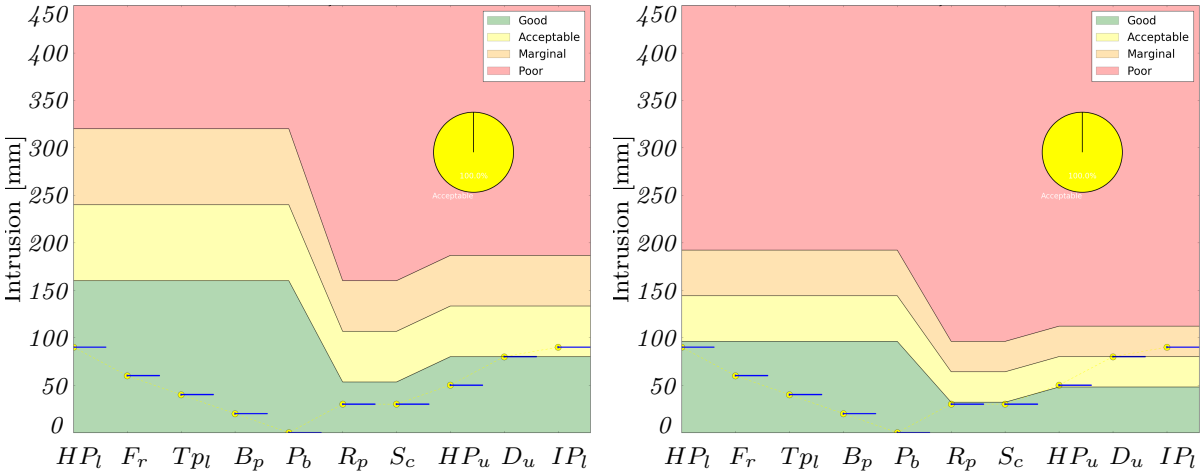

(a) Structural rating with safety distance D_{SG}=-6.7% to Good structural rating

(b) Structural rating with safety distance D_{SA}=35.9% to Acceptable structural rating

Figure 3.11 IIHS structural rating and safety distance to (a) Good and (b) Acceptable ratings for the 2016 BMW X1 CEN1608

Data: Intrusions vector **I** and upper limits defining structural ratings $SR_{u_{lim}}$
Result: D_{SG}, safety distance to Good structural rating
Calculate structural rating SR using **I**;
df = 1e-3 ;
if SR = *Good* **then**
  while SR = *Good* **do**
    f_{SD}=(1-df) ;
    Calculate new SR considering: $Updated_{SR_{u_{lim}}} = SR_{u_{lim}}\ f_{SD}$;
    if SR = *Acceptable* **then**
      $D_{SG} = df$
    else
      df +=1e-3
    end
  end
else
  while *not*(SR = *Good*) **do**
    f_{SD}=(1+df) ;
    Calculate new SR considering: $Updated_{SR_{u_{lim}}} = SR_{u_{lim}}\ f_{SD}$;
    if SR = *Good* **then**
      D_{SG} = -df
    else
      df +=1e-3
    end
  end
end

Algorithm 1: Calculation of safety distance to Good structural rating, D_SG

3.3.2. Evolution of Structural Rating and Safety Distance across Automobile Manufactures

The IIHS introduced the SOF crash test in 2012. Since its introduction, automobile manufactures have developed strategies to design a frontal structure capable of withstanding the loads of this type of crash scenario. Figure 3.12 shows the intrusion measurements and structural rating for the tested vehicles in four different years: 2012, 2014, 2016 and 2019. In the plots, intrusion measurements at different locations for a single vehicle are linked by a colored dotted line, whose color is in accordance to the vehicle overall rating. The blue area in every location represents the distribution of the intrusion measurements for all tested vehicles. It is clearly visible in Figure 3.12(a) that the first year of the SOF meant a challenge for most of the tested vehicles, since only 7.4% obtained a Good structural rating. A couple of years later, in 2014, the amount of vehicles with a Good structural rating increased to 21.6%. Even when the average industry rating improved, concentrated poor measurements at the Upper and Lower Hinge Pillar, Upper Dash and Left Instrument Panel are observed for these two years. The inflection point was 2016 where most of the vehicles, namely 65%, obtained a Good rating, more than the vehicles with Acceptable, Marginal and Poor ratings combined. In 2019, 91.3% of the vehicles obtained a Good structural rating. A generalized decreasing trend in the intrusion measurements at all locations is evident.

Table 3.4 displays the percentage of vehicles obtaining each rating at each year of testing as well as the average safety distance, D_{SG} for all tested vehicles from 2012 to 2019. Figure 3.13 displays the distribution of the D_{SG} for each test year. D_{SG} shows an increasing trend from D_{SG}, from -110%, implying an average Marginal structural rating for the industry in 2012, to 33% in 2016, implying an average Good structural rating for the industry. This trend shows that frontal structure design strategies are, in most of the cases, successful, thus placing the industry standard at D_{SG}>30%. The three vehicles with the highest D_{SG} are the 2018 BMW X3 (CEN1801) with D_{SG}=77%, the 2017 Volvo S90 (CEN1633) with D_{SG}=80% and the 2020 Ford Escape (CEN11910) with D_{SG}=87%. Such high D_{SG} values suggest that the strategies to reach a Good structural rating are already known. Therefore, the current challenge lies in defining the system, subsystem and component targets to achieve a competitive structural rating in the most efficient way possible. By defining the safety distance to a Good structural rating, it is possible to effectively and efficiently correlate the kinematic quantities with the definition of structural crashworthiness, and the resulting structural rating. In the following section, these interdependencies between vehicle kinematics and structural performance are studied with the objective of defining targets for the kinematic quantities to ensure that the designed vehicle achieves its desired rating.

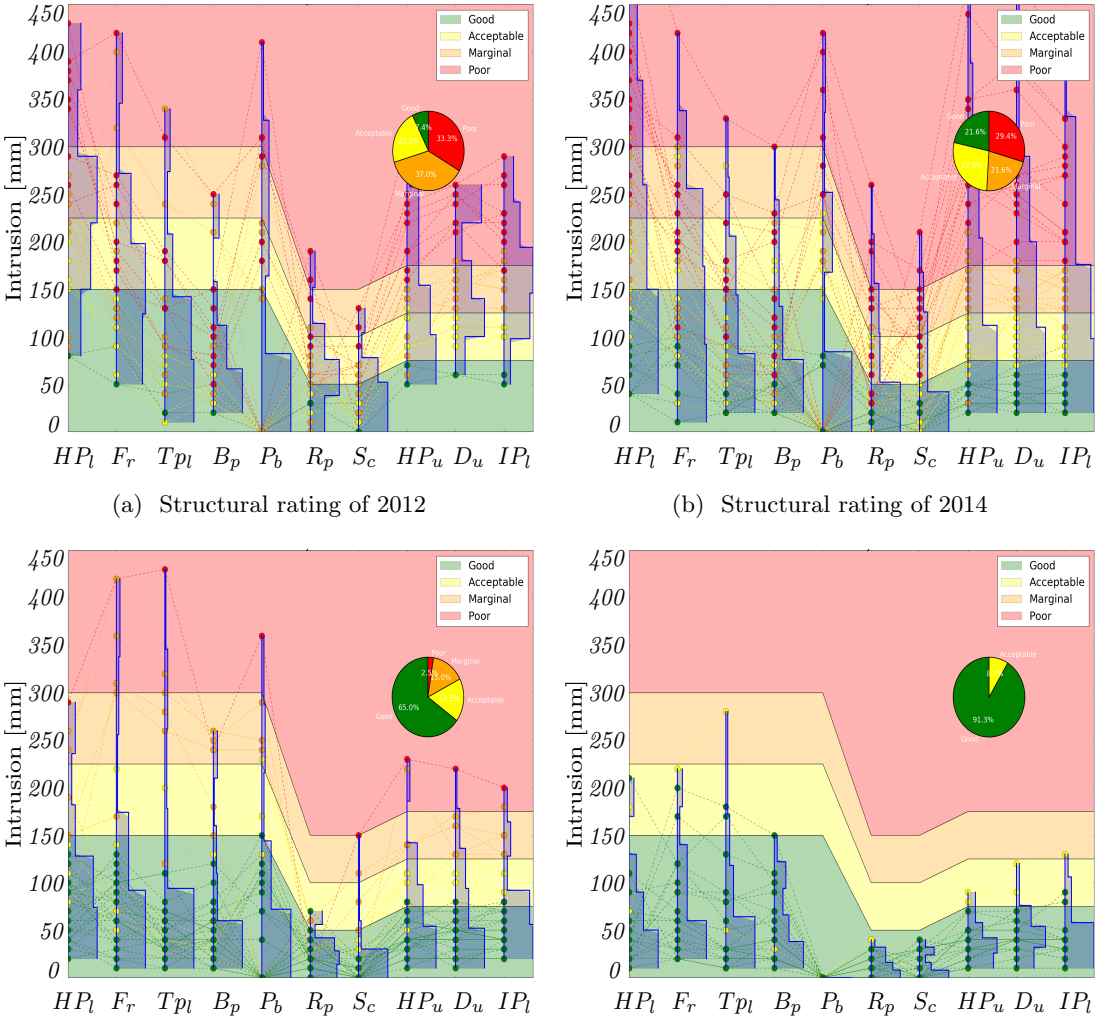

(a) Structural rating of 2012

(b) Structural rating of 2014

(c) Structural rating of 2016

(d) Structural rating of 2019

Figure 3.12 Structural rating for the years (a) 2012, (b) 2014, (c) 2016, and (d) 2019

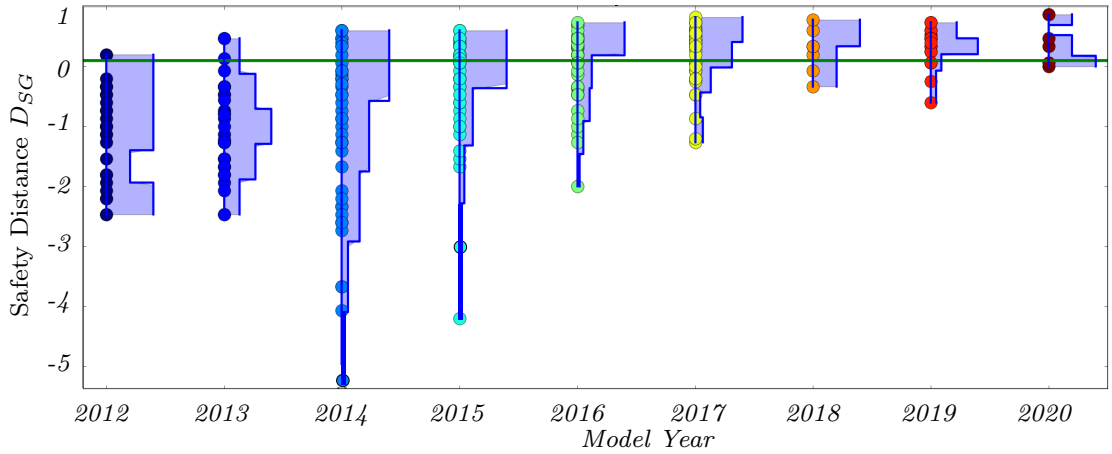

Figure 3.13 Evolution of safety distance over each year of IIHS testing. The variable *Pr* shows the fraction of vehicles tested per year out of a total population of 200 vehicles tested during the period 2012-2020. This analysis was carried out during 2020, therefore not all vehicles tested in this year are shown.

Table 3.4 Structural Rating for years 2012 to 2019 and average safety distance D_{SG}

Year	**Good**	**Acceptable**	**Marginal**	**Poor**	D_{SG} **(avg.) [%]**
2012	7.4%	22.2%	37.0%	33.3%	-110%
2013	8.3%	22.2%	36.1%	33.3%	-103%
2014	21.6%	27.5%	21.6%	29.4%	-103%
2015	50.0%	26.2%	11.9%	11.9%	-34%
2016	65.0%	17.5%	15.0%	2.5%	0%
2017	74.4%	18.6%	4.7%	2.3%	20%
2018	71.4%	28.6%	0%	0%	26%
2019	91.3%	8.7%	0%	0%	33%

3.4. Interdependencies between Vehicle Kinematics and Crashworthiness

As observed from the analyzed data, automobile manufacturers often design the vehicle structure to have a specific kinematic response when subjected to the SOF crash test. Accordingly, in the event of the crash, the structural layout can either translate the vehicle laterally to conserve a larger amount of kinetic energy (*glance-off* mode) or transform the kinetic energy into plastic deformations (*deformation* mode). The work of Cuevas-Salazar et al. (2019) shows that $GV_{P_{t_{end}}}$, previously used to differentiate the kinematic modes, describes the relative area of the vehicle that is in contact with the barrier but correlates poorly with the intrusions. Let us consider two vehicles with an equal $GV_{P_{t_{end}}} \geq 1$ but different s_L, s, $s_{\%}$. One vehicle presents lower values for s and $s_{\%}$, than the other. Thus, the first vehicle presents a larger distance from the A-Pillar to the barrier at t_{end}. This is an indication of lower intrusions since a hard contact between the Hinge Pillar and the barrier is avoided. Therefore, similar values of $GV_{P_{t_{end}}}$ lead to different intrusion values. In *glance-off* mode, a higher $s_{\%}$ percentage does not necessarily mean higher intrusions since only a small portion of the structure is actually in contact at the end of the crash. On the other hand, in the *deformation* mode, there is always a relatively larger area of the vehicle in contact with the barrier, making either s_L, s and $s_{\%}$ a better indicator of the resulting intrusions. In order to identify the appropriate set of ranges for the kinematic parameters to minimize the intrusions at the occupant compartment, a cluster and correlation analysis is performed in Section 5.2.1. The objective of this analysis is to first, identify the kinematic parameters that present a correlation with D_{SG}, and second, identify a range that corresponds to an interval of D_{SG} that offers a robust fulfillment of the structural requirements.

Chapter 4

Low-Fidelity Models for the SOF Load Case

As in any design process, the degree of flexibility available in vehicle crashworthiness systems is at its maximum in the early design phase. This flexibility comes together with an inherent lack of information regarding the system specifications, which in the case of vehicle crashworthiness, are the vehicle structural properties. However, even at this early phase, general information of the vehicle, such as the type and class, is available. This information is essential in the development of a new design and, in the case of the automotive industry, is key to the market success of the vehicle. Therefore, information concerning properties such as the overall dimensions and proportions of the vehicle is available, which triggers the first design decisions. Moreover, information regarding the regional market availability of the vehicle is known as well. This provides information on the regulatory and consumer rating context that will affect the vehicle design. With specific regard to crashworthiness design, we can already define at this stage the global targets to be achieved by the vehicle, i.e. the number of stars or the rating for a particular crash test. Consequently, structural design targets also begin to determine aspects of the vehicle structure at the early phase. As the design evolves, flexibility decreases and the cost of implementing changes increases due to tooling design cycles. For these reasons, developing a structural design strategy that takes into account the known vehicle characteristics and considers high-level structural requirements becomes a valuable tool for decision-making in the early design phase. Such a strategy is developed in this work.

The developed structural design strategy proposed in this work is based on the systems engineering approach used for crashworthiness design presented in Figure 4.1. The starting point of this workflow is the formulation of a design intent of a vehicle of a certain class. When a vehicle proposal is developed and a certain class is considered, a number of vehicle properties can already be derived. One of these properties is the vehicle mass which is partly determined by aspects other than crashworthiness, such as fuel consumption or vehicle range and driving dynamics. Other parameters derived by the vehicle class are the vehicle proportions, i.e. wheelbase, track, width, overhang,

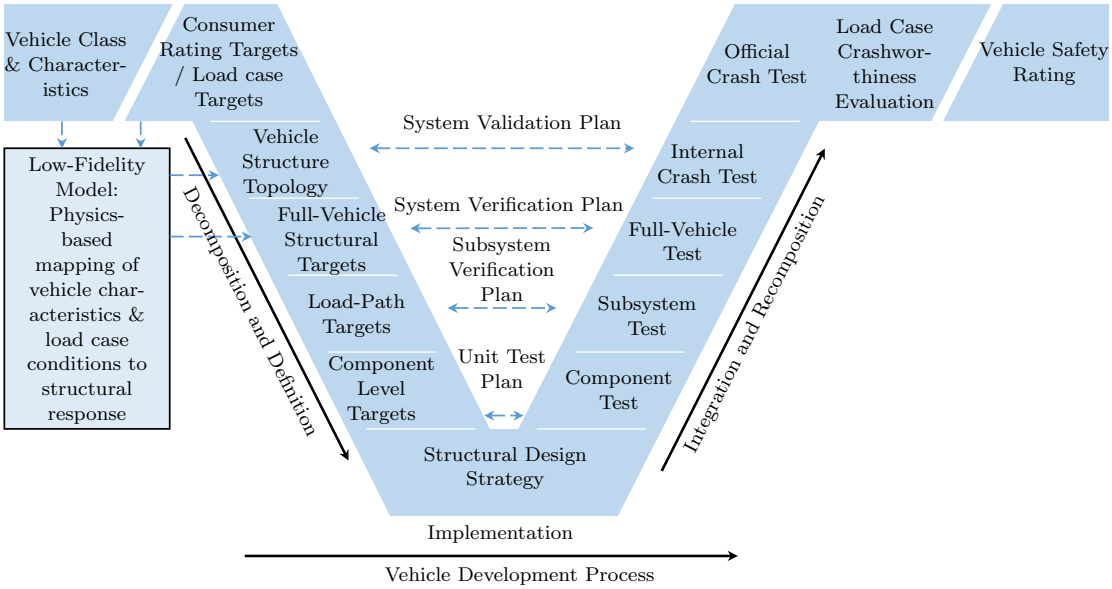

Figure 4.1 Systems engineering V-diagram for crashworthiness design and low-fidelity models for response mapping

greenhouse shape. These are determined based on the appearance of the vehicle desired by the designer. Consequently, based on this early design and other relevant factors (e.g. driving dynamics), the center of gravity as well as the rotational inertia around the principle axis can be estimated for the designed vehicle.

In addition to the car manufacturer's legal obligation to comply with homologation requirements concerning crashworthiness, vehicle performance targets in consumer tests are also defined in the early design stage. Consumer rating targets, defined for each relevant load case, represent the second item to be considered in the V-diagram in Figure 4.1. Such load-case-specific targets drive the design of the structure and restraint systems. The consequent structural targets trigger the decomposition of the entire system, into subsystems and components, and the definition of targets for all levels to collectively achieve the desired outcome. Therefore, the resulting structural topology, i.e. the way the load-paths are placed within the vehicle frame along with their connections as well as the load-carrying capacities and energy absorption properties, determine the overall crashworthiness performance of the vehicle. The exact location of structural components is usually determined at a later point, when packaging aspects and integration of other vehicle components take place. For this reason, maximizing flexibility at this design stage by abstracting the topology of the structure is key to overcoming the lack of information. When available, indications of approximate spatial locations of components as well as load-carrying capacities and energy absorption properties that fulfill the full-vehicle level targets accelerate the design process and serve as reference for the efficient and effective

use of the frontal vehicle structure.

Decomposing the targets from the full-vehicle to load-path and then to component levels, favors the design flexibility and allows for parallel and independent design loops. The load-carrying capacities and energy absorption properties for each load-path, and therefore of each component, can be designed independently from each other if their targets are defined in this way. The objective of a structural design strategy is then to define, decompose and implement such design targets at each level through a development process and verification test plan. Thus, defining the crashworthiness targets is crucial for a successful design execution and this is where the benefits of a low-fidelity physics-based crash model are most valuable. Once the targets are defined for all structural levels, the design implementation is typically done by means of FE models starting at the component level, load-path, and finally full-vehicle level. At this virtual design phase, the structure properties are measured and compared against the defined targets. It usually takes several design iterations to meet these targets. Afterwards, the integration and recomposition phase of the crashworthiness design process follows (right part of the V-diagram in Figure 4.1). During this phase, prototypes at the different structural levels are built, tested, measured, and compared against the set targets in the decomposition and definition phase (left part of the V-diagram). The cost of implementing changes at this prototypical design stage is considerably higher compared to the costs of the virtual design phase, with the cost of complete system validation through an internal full-vehicle crash test being the highest. The high cost of a full-vehicle crash test is related to the need of appropriate infrastructure and tools for carrying out the hardware test. Moreover, structural changes derived from the outcomes of such a test may result in changes in the tooling needed for the manufacturing of the vehicle. Hence, full-vehicle crash tests are usually kept to the minimum possible, making the virtual design phase crucial to the success of the vehicle design. Only when the hardware test is plausible, the series production phase of the vehicle takes place. The final stage of the crashworthiness design occurs when the vehicle is newly available in the market and a regulatory or consumer organization (e.g. IIHS) conducts its official crash test. Here, the vehicle's crashworthiness is evaluated for every load case, resulting in an official vehicle safety rating.

Following the V-diagram of crashworthiness design (Figure 4.1), this work focuses only on developing a structural design strategy for the Small-Overlap Frontal (SOF) load case. Starting with the available set of basic vehicle properties at the early design phase, a physics-based low-fidelity model can be used to estimate the vehicle kinematics. The previous section details the interdependencies between vehicle kinematics and crashworthiness for the SOF load case. Even though the kinematics of a vehicle subjected to the loads present in a crash is a complex phenomenon, basic physical principles can be applied to understand the influencing factors and their effect on the resulting trajectory of the vehicle. Therefore, the physics-based low-fidelity model can also be used to estimate the crash performance. For a successful early design, such a model should overcome the lack of detailed information and instead use it as leverage to further drive the design and thus, define the functional properties of the structure, i.e. load-carrying capacities and

energy absorption properties. The present work proposes a low-fidelity physics-based kinematic model that uses the mass and proportion characteristics of a vehicle together with the load carrying capacities and energy absorption properties of its structure to estimate the vehicle trajectory during a SOF crash which, in turn, determines the kinematic parameters and ultimately, the crash performance. This model is presented in Section 4.1.

4.1. The Kinematic Model

Ensuring safety for a vehicle from the early phase design requires designing with a model which is as simple as possible and only as complex as necessary to represent the crash event. A low-fidelity kinematic model describes and quantifies the highly nonlinear kinematic modes of the crash test by considering the kinematic relationships described in Section 3.2 and uses as input the vehicle characteristics and the functional properties of the structure. The input for the kinematic model must be available at the early design phase and consists of: mass, center of gravity, rotational inertia, vehicle width (barrier position in y), vehicle overhang and greenhouse proportions (A-pillar position in x and y and barrier position in x). The functional properties that affect the kinematic response are defined as the resistances-to-deformation of the front structure in the transversal and longitudinal directions which are represented as force-displacement curves and adopted in the model as elasto-plastic collapse elements.

A simplified predictive model allows to quickly assess structural changes and their influence on the kinematics of the vehicle. In addition, such a simplified predictive kinematic model does not require detailed information of the structure and the load paths. The starting point is the known vehicle geometry. However, obtaining early information on required force levels for structural components improves the outcome of the project in terms of cost, efficiency, and performance. Therefore, predicting such required force levels for relevant structural components to achieve a primary structural target already in the initial design phase is highly convenient and accelerates of the vehicle development process. This approach becomes even more powerful when the simplified model is combined with the concept of force-displacement solution spaces, as presented by Fender (2014) in his dissertation. If the system can be divided into several subsystems (e.g. load paths and components), a set of uncoupled force-displacement solution spaces can be generated. Then, each of these can be defined as design targets for the responsible design department. According to the principles of the V-diagram (Figure 4.1), individually designed subsystems meet the overall design goal when integrated into the crash management system. Therefore, having an upper and lower bound for the local force levels in x and y direction as a function of deformation for the force-displacement solution spaces, provides a design area in which a safe vehicle structure is guaranteed. The focus of this chapter lies on the simplified model used to predict the kinematic response of a vehicle subjected to the SOF crash test. The ansatz of the predictive kinematic model is derived from idealizing the problem as a mass-spring system, a common approach in crashworthiness applications (see Section 4.1.1). Its coupling with force-displacement so-

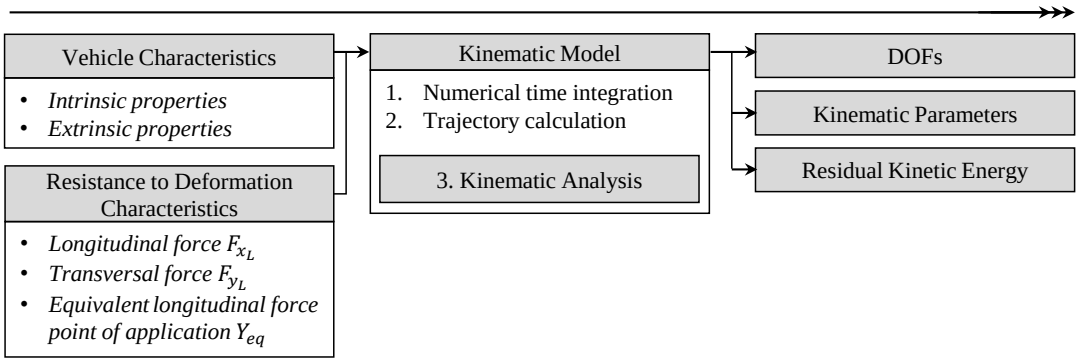

Figure 4.2 Forwards calculation of kinematic model

lution spaces and the calculation of the design area to guarantee a safe vehicle structure are addressed in the following chapter.

4.1.1. Forwards Calculation

The model described in this section is based on a prior publication of the author of this work, see (Cuevas-Salazar et al., 2017), and is here enhanced for its use in the early phase and in combination with the solutions spaces approach. The objective of the kinematic model is to link vehicle and resistance-to-deformation characteristics and vehicle kinematics. In the so-called forwards calculation presented in Figure 4.2, the resistance-to-deformation characteristics are the input and the kinematics are the output. The information available at the early phase that serves as input for the forwards calculation includes the vehicle characteristics in the form of intrinsic and extrinsic properties and the resistance-to-deformation characteristics. The input parameters used for the kinematic model are defined using the framework established in Section 3.2, maintaining the assumption of a 2-D planar motion. In this work, intrinsic properties are defined as those properties that are fixed and do not change unless the vehicle class and type change, namely, the vehicle proportions. These include the position of the A-pillar, (AP_x, AP_y), the frontal structure length or longitudinal distance from the A-pillar to the barrier, s_L, and the barrier position, B_y. The position of each load path across the structure, represented as (LP_x, LP_y), is also a relevant input parameter. Extrinsic properties, on the other hand, can change depending on the vehicle version accommodated in the platform. These include the vehicle's total mass, M_v, rotational inertia around the z axis, I_{zz}, as well as the position of the center of gravity, (CG_x, CG_y). The vehicle mass and rotational inertia are considered concentrated at the center of gravity. The extrinsic properties of a given vehicle change when a different weight distribution is used, even if the underlying structure remains the same.

The second set of input parameters represents the load-carrying capacities and energy

absorption properties of the frontal structure. These characteristics can be understood as the longitudinal and transversal forces that result from the vehicle-to-barrier contact and the corresponding structural deformation represented as F_{x_L} and F_{y_L}, respectively. In their most fundamental form, these forces provide a resistance to the deformation resulting from the crash; therefore, they are referred to as resistance-to-deformation characteristics or RDC. If the structure is analyzed at the load-path level, then longitudinal and transversal forces suffice for their structural characterization. However, at the full-vehicle level, the equivalent point of application of the total longitudinal force, Y_{eq}, is also included in the RDC since it influences the lever arm of such forces thus affecting the total moment, M_z, around z applied at the center of gravity, CG. Figure 4.3 shows the idealized lumped-mass model used in this work and displays the described input parameters.

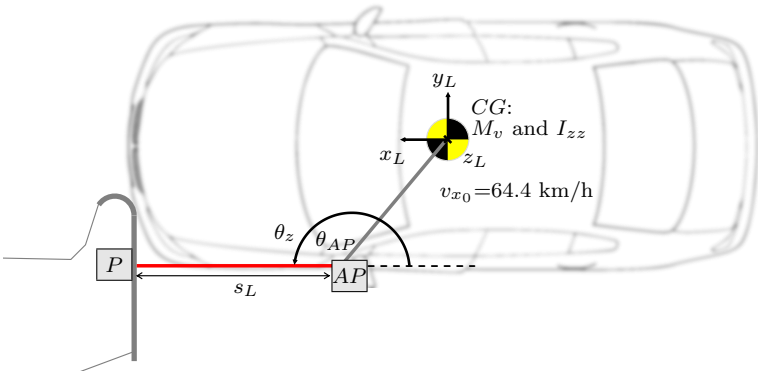

Figure 4.3 Kinematic model with input parameters

The main assumptions of the kinematic model are summarized as follows:

- Only the frontal region of the vehicle is deformable. This means that the structure located after the A-pillar along the local longitudinal axis, x_L, is assumed to be rigid.
- The longitudinal and transversal contact reaction forces of the barrier are the only forces acting on the vehicle. This implies that the vertical forces acting along the z axis as well as any other forces resulting from the interaction of the wheels and the ground are neglected.
- Only a 2-D motion is considered. Consequently, the degrees of freedom are limited to the transversal and longitudinal displacements and the rotation of the center of gravity (u_x, u_y, θ_z)
- Transversal and longitudinal resistance-to-deformation characteristics, $F_{x_L}(s)$ and $F_{y_L}(s)$, are both functions of the longitudinal deformation of the structure, s. This implies that the elasto-plastic collapse elements at either the full-vehicle or load-path level only exhibit a deformation along the local longitudinal axis and therefore, no transversal deformation is considered.
- In the case of the full-vehicle level, the equivalent point of force application, Y_{eq},

is also a function of the local longitudinal deformation. As a result, the lever arm of the transversal forces is directly considered as the local longitudinal distance between the barrier and the rigid portion of the vehicle.

Similar to the real crash, an initial velocity, v_{x_0}, of 64.4 km/h on the longitudinal x axis is imposed on the lumped mass setting the kinematic model into motion. The mass and rotational inertia are related to the CG, therefore, the offset between the application point at the barrier spring and the vehicle's CG forces the body to rotate. The planar motion of the CG, i.e. the displacements u_x and u_y, and the rotation θ_z, is modeled using a rigid body dynamics approach. As stated, the displacements u_x and u_y are functions of the vehicle mass and the longitudinal and transversal forces acting at the CG. This means that the rotational angle θ_z of the CG of the vehicle is a function of the moment caused by a resultant force, which is not applied directly at the CG, and also a function of the mass moment of inertia. This implies that not only the transversal force acting along the local axis x_L is causing the rotational moment M_z but also that the longitudinal component is contributing to it. The transversal forces originate from the geometry of the barrier, i.e. the normal forces acting at the curved section of the barrier's surface, and also from the geometry of the structural components. Thereby, defining the transversal and longitudinal forces in the local coordinate system of the vehicle, which moves and rotates along with it, is advantageous so that the forces can be related to the load-paths and to the structural components. In order to link the kinematics of the vehicle to the vehicle characteristics and RDC, a non-linear equation of motion is proposed and presented in Eq. (4.3).

$$\begin{bmatrix} M_v & 0 & 0 \\ 0 & M_v & 0 \\ 0 & 0 & I_{zz} \end{bmatrix} \begin{bmatrix} \ddot{u}_x \\ \ddot{u}_y \\ \ddot{\theta}_z \end{bmatrix} = \begin{bmatrix} F_{x_L}(s) \\ F_{y_L}(s) \\ r_y(u)F_{x_L}(s) - r_x(u)F_{y_L}(s) \end{bmatrix} \tag{4.3}$$

The vehicle properties needed to solve Eq. (4.3) are available at the early design phase. The lumped-mass matrix, **LM**, containing M_v and I_{zz} contains the mass and internal vehicle properties. While in the forwards calculation the RDC are needed as input, the backwards calculation presented in Section 5.1 enables the calculation of the RDC as a function of the desired vehicle kinematics. In this section, they are considered as a given input. Accordingly, the outputs of the non-linear equation of motion are the planar displacements and the rotation of the center of gravity, first as accelerations, ($\ddot{u}_x$, $\ddot{u}_y$, $\ddot{\theta}_z$) and then, as displacements and rotations. As observed in Eq. (4.3), the DOFs appear at both sides of the equation: on the left-hand side in their acceleration form whereas in the right-hand side as input for the calculation of the forces $F_{x_L}(s)$ and $F_{y_L}(s)$. The latter are represented as piecewise linear force-displacement curves and require an indirect calculation of the parameter s to compute the effective lever arms for the longitudinal force and transversal forces, $r_y(u)$ and $r_x(u)$, respectively. The calculation of s, as presented in Section 3.2, requires the calculation of the position vectors of the A-pillar and A-pillar projections. These position vectors are a direct result of their initial position as well as of u_x, u_y, and θ_z. Considering these geometrical and force properties as well as the

non-linearities related to the time integration, an explicit time step scheme is proposed to solve the equation of motion. The workflow of such a time integration scheme used to calculate the DOFs and generate the vehicle trajectory at the full-vehicle level is presented in Algorithm (2).

Once t_{end} is detected, the DOFs and vehicle trajectory are generated as time series. The outputs are post-processed using the kinematic analysis described in Section 3.2.2, returning the kinematic mode characterized by $GV_{P_{t_{end}}}$ and $ds_{\%}/dt_{t_{end}}$ as well as the kinematic parameters vector $\boldsymbol{\sigma}$ (i.e. total vehicle rotation, $\theta_{z_{t_{end}}}$, residual deformation length, RDL or $s_{L_{t_{end}}}$, and residual kinetic energy, RKE). These parameters are indicators of the vehicle crash kinematics and are easily comparable against different vehicle configurations. Moreover, as explained in Section 3.4, they can also predict the resulting crash performance.

4.1.2. Load Path Level

The functional properties of the frontal structure at the full-vehicle level are the total longitudinal and transversal forces, $F_{x_L}(s)$ and $F_{y_L}(s)$, and the equivalent point of force application, $Y_{eq}(s)$. This abstraction is achieved by using a single elasto-plastic collapse element represented by a force-displacement curve. Nonetheless, the proposed kinematic model is further extended to enable the calculation of the vehicle trajectory using multiple elasto-plastic collapse elements representing the different load-paths in the frontal structure. Such a decomposition of the full-vehicle properties allows for the definition of targets at the load-path level. Even if a certain degree of dependency exists with each load-path, the structural components that compose them can be designed in parallel once the target response has been defined. The active load-paths in the SOF crash test are presented in Figure 4.4 and are listed below:

1. Wheel-Firewall-Rocker
2. Shotgun
3. Subframe
4. Bumper beam-front rail

The low-fidelity kinematic model proposed in this work assumes an equally long initial deformation length, $s_{L_{j_{t_0}}}$, for each load-path j. This implies that the load-paths are distributed across the structure and located at different y coordinates, but share the same initial x coordinate on the structure and on the barrier side, which is the same x position of the A-pillar. To be consistent with the actual topology of the structure, the z position of the load-paths coincides with the location of the components in the structure and is assumed to be constant along the front of the vehicle, but does not produce any moment around the y axis, since the motion of the CG is considered to be only in the xy plane. The longitudinal and transversal forces for each load-path, $F_{x_{LP_j}}(s_j)$ and $F_{y_{LP_j}}(s_j)$, respectively, are defined in the vehicle local coordinate system and depend exclusively on the longitudinal deformation, s_j, of each elasto-plastic element.

The calculation of the kinematic model described in Algorithm (2) can be adapted to

Data: Initial position of center of gravity, CG, A-pillar, AP, and barrier B; vehicle properties M_v and I_{zz}; RDC as functions of s: $F_{x_L}(s)$, $F_{y_L}(s)$ and $Y_{eq}(s)$
Result: DOFs: u_x, u_y, θ_z; End of crash t_{end}
Define a time step Δt;
Initialize time t=0 and iteration index i=0 ;
Initialize lumped-mass matrix **LM** with M_v and I_{zz};
Initialize acceleration vector **ACC**=[$\ddot{u}_x$, $\ddot{u}_y$, $\ddot{\theta}_z$] = **0**;
Initialize velocity vector and apply initial conditions **VEL**=[v_{x_0}, 0, 0] ;
Initialize displacement vector **DIS**=[u_x, u_y, θ_z] = [v_{x_0} Δt, 0, 0] ;
Calculate initial deformation length $s_{L_{t_0}}$ as a function of CG_x, CG_y, AP_x, AP_y and B_x ;
Calculate A-Pillar projection P ;
Calculate initial lever arms $r_x(u)$ and $r_y(u)$;
while t_{end} *not detected* **do**
  Calculate current deformation length $s_L(u)$;
  Calculate deformation $s = s_{L_{t_0}}$-$s_L(u)$;
  Calculate local longitudinal forces $F_{x_L}(s)$;
  Calculate local transversal forces $F_{y_L}(s)$;
  Rotate local forces to global coordinate system: F_{x_G}, F_{y_G} Calculate equivalent point of application of longitudinal force $Y_{eq}(s)$;
  Calculate rotational moment $M_z = r_y(u)F_{x_L}(s)$ - $r_x(u)F_{y_L}(s)$;
  Update RHS: $\mathbf{F_{ext}} = [F_{x_G}, F_{y_G}, M_z]$;
  Solve for acceleration vector **ACC**= $\mathbf{LM^{-1}}$ $\mathbf{F_{ext}}$;
  Use central difference scheme to compute new **VEL** and **DIS**;
  Calculate current position vector of CG;
  Calculate current position vector of A-Pillar, AP;
  Calculate current position vector of A-Pillar projection, P;
  Calculate Glance-off Value GV_P;
  if $GV_P \geq 1$ *or* $s_i \leq s_{i-1}$ **then**
    t_{end}=t detected ;
  Update time = t+=Δt;
  Update iteration i+=1 ;
end

Algorithm 2: Kinematic model calculation work-flow

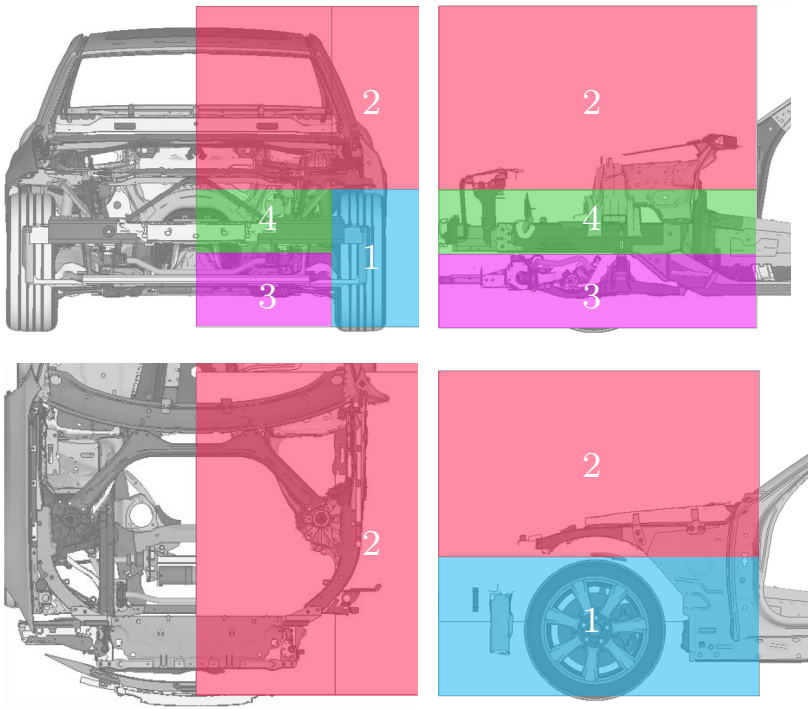

Figure 4.4 Vehicle structure load-path definition: (1) wheel-firewall-rocker, (2) shotgun, (3) subframe, (4) bumper beam-front rail

incorporate the load-path approach. To do so, the total local longitudinal force, F_{x_L}, is calculated as the sum of the force of each load-path at a certain deformation state, s_j as presented in Eqs. (4.4) and (4.5). For the calculation of the total moment, M_z, the locational vectors for each load-path, r_j, are needed as shown in Eq. (4.6). In the case of the longitudinal forces, these act along the elasto-plastic element and therefore, the transversal lever arm, Y_{LP_j}, or local transversal distance to the CG, remains constant. However, the transversal forces have a variable lever arm which is the deformation length, s_{L_j}, plus the longitudinal distance of the A-pillar to the CG, expressed in the local coordinate system. This relationship allows for a reverse calculation of Y_{eq} as expressed in Eq. (4.7). A representation of the vehicle structure and the load-path represented by elasto-plastic elements (in blue) is presented in Figure 4.5. In addition to the position vector for each load-path, a boundary box is defined and projected onto the barrier in order to identify the area belonging to each load-path. This box is useful when extracting the force time series in a FE simulation or in a hardware test. Only the force measurement devices inside the load-path box are taken into consideration when calculating the total force of each load-path.

$$F_{x_L} = \sum_{j=1}^{m} F_{x_{LP_j}}(s_j); \tag{4.4}$$

$$F_{y_L} = \sum_{j=1}^{m} F_{y_{LP_j}}(s_j); \tag{4.5}$$

$$M_z = \sum_{j=1}^{m} r_{j_y}(u) F_{x_{LP_j}}(s_j) - r_{j_x}(u) F_{y_{LP_j}}(s_j); \tag{4.6}$$

$$Y_{eq} = \sum_{j=1}^{m} (F_{x_{LP_j}} * Y_{LP_j}) / \sum_{j=1}^{m} (F_{x_{LP_j}}). \tag{4.7}$$

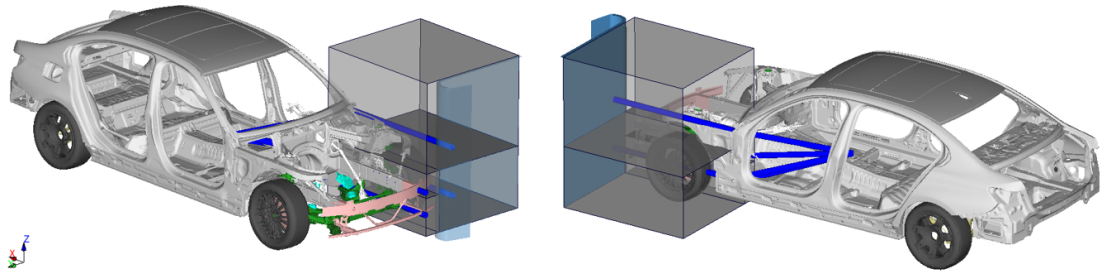

Figure 4.5 Kinematic model with multiple elasto-plastic elements

The proposed forwards calculation is efficient and suitable for the early phase design. By using a low-fidelity model that links the initial vehicle characteristics and its kinematic response, the *RDC* are characterized at the load-path and full-vehicle levels resulting in a well-defined trajectory with a predictable crash performance. However, the inverse problem statement, i.e. determining the *RDC* that produce a desired kinematic response, is of greater interest in the vehicle design. The backwards calculation of the kinematic model together with the computation of force-displacement solution spaces provide a methodology to efficiently search and find suitable *RDC* towards a robust structural target. This methodology is presented in the following chapter.

Chapter 5

Solution Spaces & Low-Fidelity Models

The core of the systems engineering approach is the design specification, from the system to component level, of the functional properties of the structure. Figure 5.1 presents a complementary step for the requirement decomposition and definition by means of the solution space approach, whose objective is to find not only one but a range of design specifications that, when implemented, the system-level response of the vehicle achieves the high-level structural requirements. In the previous chapter, the forwards calculation of the proposed kinematic model showed how a given set of resistance-to-deformation characteristics, referred as *RDC*, are used to compute the trajectory and crash performance of a vehicle subjected to a SOF load case. Nonetheless, for practical applications in the vehicle design process, the inverse problem is more relevant, specifically, which set of *RDC* produce a desired kinematic response. With such inverse or backwards approach, designing a structural load-path that follows the force-displacement curve from the *RDC* is plausible. However, defining a single curve as a target is of no practical use, since a variety of conditions and sources of uncertainty affect the response of the load-path in the crash event. For this reason, instead of using a single curve, a so-called solution space, which defines upper and lower limits for the *RDC*, is favored. As a result, a set of curves yielding a desired kinematic response, i.e. a set of feasible solutions, is obtained. The solution to this inverse problem is discussed in Section 5.1 whereas the details of the solution space calculation are presented in Section 5.1.1. Finally the definition of a desired kinematic response is addressed in Section 5.2.

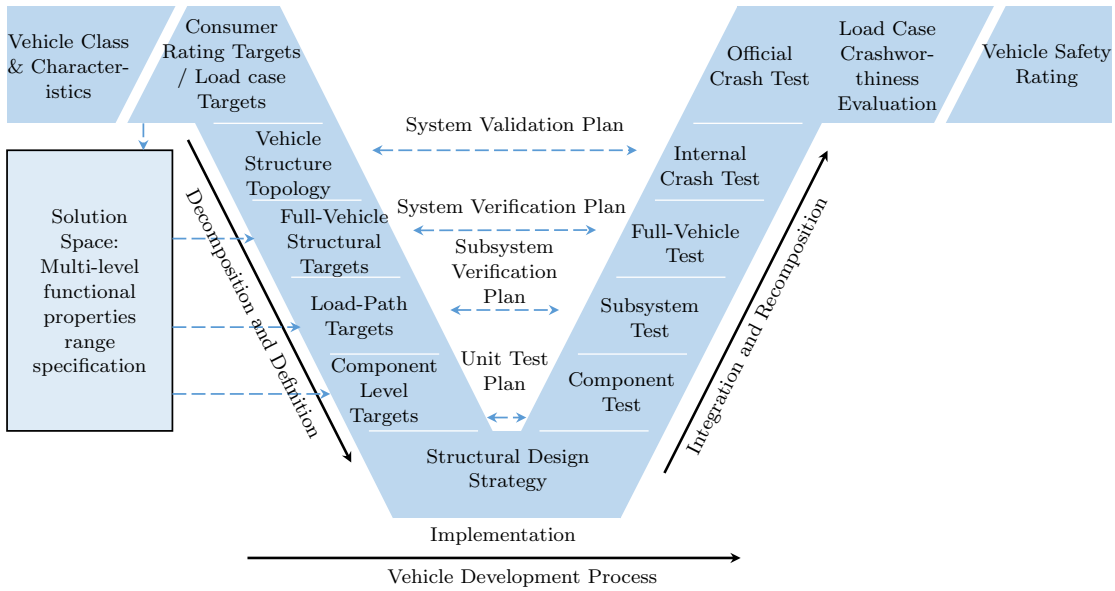

Figure 5.1 Systems engineering V-diagram for crashworthiness design and solution spaces for a multi-level functional properties range specification

5.1. Backwards Calculation

The forwards calculation presented in Section 4.1.1 couples the vehicle intrinsic and extrinsic properties and the transversal and longitudinal forces as well as the equivalent transversal force point of application with the DOFs and kinematic parameters. This coupling is performed in the kinematic model through a numerical time integration and trajectory calculation. The backwards calculation shown schematically in Figure 5.2 establishes the inverse relationship. It is observed that the input for the solution space calculator is threefold: (1) the constraints defined on the kinematic parameters at t_{end}, (2) the design bounds or design space for the resistance-to-deformation characteristics, and (3) the vehicle characteristics.

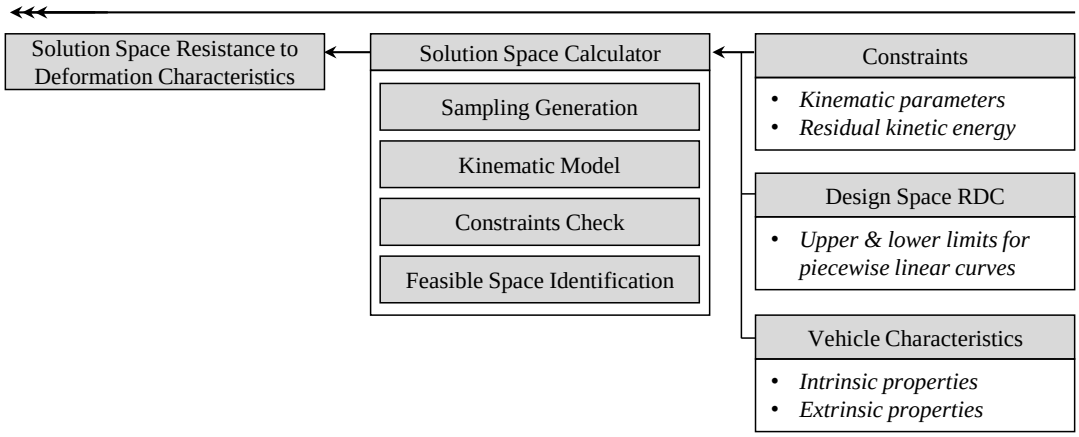

Figure 5.2 Backwards calculation

The constraints defined on the kinematic parameters at the end of the crash, t_{end}, including the residual kinetic energy, RKE, describe the desired kinematic response. Such constraints are defined as upper and lower limits for the relevant kinematic parameters. The design bounds for the RDC represent the absolute maximum and minimum force levels at each deformation level that the structure is physically capable of delivering. Starting points for the definition of such design bounds are the force-displacement characteristics of a base design or former vehicle, component tests, engineering judgment and/or experience. In the end, the defined design bounds should be achievable and realistic local transversal and longitudinal force levels. Realistic and achievable in the sense that not all force levels may be obtained at any given deformation length.

Typically, the forward parts of the frontal structure, such as the bumper and crush cans, exert a lower force level than the subsequent structures. At the initial moment of the crash, the amount of achievable stiffness and strength of components which are in first contact with the barrier is limited. The forces at the first part of the deformation are due to the deformation of the bumpers, headlamps, and radiators. These components are not able to carry high loads, hence, the upper force levels cannot be arbitrarily high. Their structural behavior can be represented by defining a lower bound for such levels of deformation. Then, as the contact with the barrier continues and after some significant amount of frontal deformation, the wheel is now in contact with the barrier. This component can withstand high force levels and, therefore, the upper design bound of the local force in x and y can be increased for the design space. The RDC design bounds are defined as piecewise linear curves where the initial discretization coincides with the features of the topology of the structure. The start and end values of deformation for each load-path are derived from the location of the represented component in the vehicle. Figure 5.3 shows a typical vehicle structure with an estimation of the correspondent design bounds or design space.

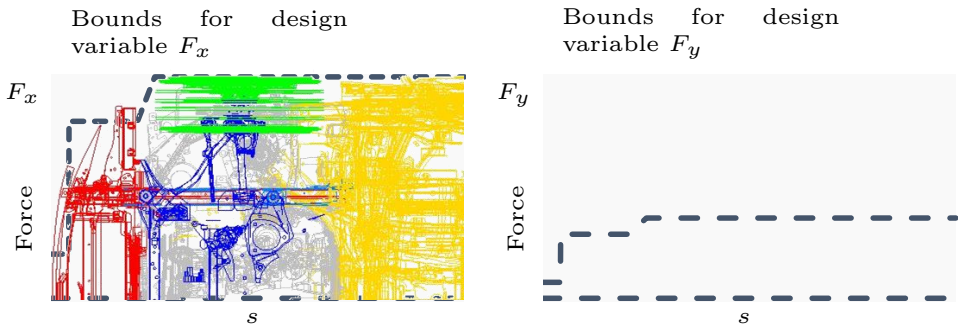

Figure 5.3 Design bounds for F_x and F_y with vehicle structure as background to represent the maximum forces available for the subsystems: bumper and front rail (red), wheel (green), suspension (blue), and occupant compartment (yellow). Note that due to the loading conditions, the upper bound of the bumper is relatively lower than the upper bound of the wheel and occupant compartment

The vehicle characteristics, i.e. its mass and rotational inertia around the z-axis as well as the positions of the center of gravity, the A-pillar, load-paths, and barrier, are considered in the forwards and backwards calculation of the kinematic model used in the solution space calculator. In the backwards calculation, only the force levels and the point of application of the transversal force are treated as design variables and not the values of the deformation length, since a given deformation space is usually already given by the overall dimensions of the vehicle. This model deformation space can be defined as the initial distance between the A-pillar point and the barrier.

The constraints, *RDC* design space and vehicle characteristics are given as input to the solution space calculator. In its most essential form, the solution space calculator generates a sample of the *RDC* that lies between the specified upper and lower bounds of the design space. This single combination of *RDC* and vehicle characteristics is used in the kinematic model to yield a vehicle trajectory, DOFs and kinematic parameters. Then, the kinematic parameters are evaluated against the defined constraints in the feasible space identification phase. If this particular design is feasible, then, it is stored as a possible solution. This process is repeated for each sampling iteration resulting in a set of feasible designs that fulfill the constraints. The objective is to calculate a convex space with only feasible solutions. It is important to notice that feasible solutions may also exist outside the solution space. However, the solution space calculator is defined in such a way that a minimum of fraction of the samples within the defined space are feasible designs and, therefore, does not take into account solutions outside it. Figure 5.4 represents this procedure in its most essential form. This serves as basis for the algorithm developed in the next section, which aims to accelerate the convergence of the solution space while maximizing its size and to efficiently map the full-vehicle properties to the load-path level.

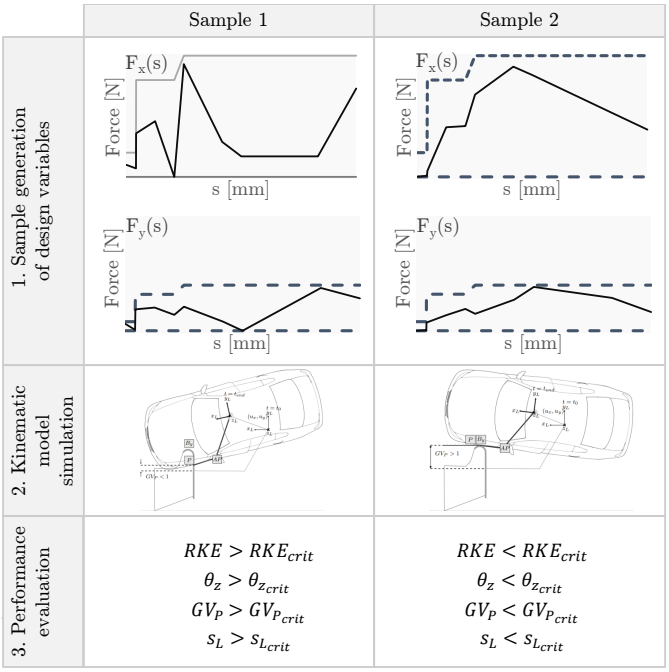

Figure 5.4 Sampling generation, kinematic model simulation and performance evaluation of the solution space calculator

5.1.1. Solution Space Algorithm for SOF-Low-Fidelity-Models

A solution space, in the context of this work, is defined as the space described by a upper and lower bounds of a set of design variables, which given a random and independent sampling within these limits returns a specific success rate, sr, defined by the fulfillment of the constraints. The set of design variables for the full-vehicle level are the piecewise-linear longitudinal and transversal forces, $F_{x_{FV}}$ and $F_{y_{FV}}$, as well as the equivalent longitudinal force point of application Y_{eq}. At the load-path level, the design variables are the longitudinal and transversal forces for each load-path j, $F_{x_{LP_j}}$ and $F_{y_{LP_j}}$, respectively.

In line with the definition of a solution space, finding only one feasible solution that fulfills the constraints implies that the upper and lower limits are identical. This solution is impractical, not only because it does not consider the range of responses inherent to a complex phenomenon such as the crash, but it also hinders the design process by reducing flexibility. Therefore, as in any engineering application, giving a range as a target facilitates the development and implementation of the solutions. In particular, for the development of a structural design, the aim is to find the largest possible solution space. The reasons for this are twofold. First, a large range is able to account for the variabilities and uncertainties associated to the crash event thus resulting in a robust design regardless of these. Second, it provides flexibility for the implementation of the structural solution by also integrating non-crashworthiness requirements and also suitable combinations of materials, cross-sections and topologies. The proposed methodology to

maximize the size of the solution space is the key aspect of this section. This methodology is used first at the full-vehicle level and then at the load-path level. The mapping between these two levels is presented in Section 5.1.2.

The solution space calculator needs to fulfill three main requirements: (1) to find feasible solutions within the design bounds, (2) to maximize the size of the solution space, and (3) to perform these tasks efficiently. To determine the best approach, it is convenient to estimate the size of the problem, i.e. the number of design variables. The size of the problem depends on the level at which the solution space is being calculated. For the full-vehicle level, the design variables consist of three curves ($F_{x_{FV}}$, $F_{y_{FV}}$, and Y_{eq}), each discretized according to the vehicle structure topology and component. Assuming a typical frontal structure length of 1.3m and a discretization of 100mm, a total of 39 values emerge. Each of these values requires its own upper and lower limit giving a total of 78 design variables (3 curves $\times$ 13 discretization points $\times$ 2 limits). For the load-path level, assuming the same length and discretization as for the full-vehicle level, and considering four load-paths and two curves each ($F_{x_{LP_j}}$ and $F_{y_{LP_j}}$), the amount of design variables rises up to 208 (2 curves $\times$ 13 discretization points $\times$ 4 load paths $\times$ 2 limits). Due to computational and time constraints in the design phase, the brute-force approach, in which the largest number of possible combinations for the design variables is evaluated, is neither efficient nor effective. To address this problem, the following steps for the solution space calculator are proposed:

1. *Exploration*: search for feasible solutions within the design bounds.
2. *Consolidation*: a solution space is found by using the curves from the exploration phase as a base, by sampling among the limits and by discarding unfeasible designs.
3. *Expansion*: once a solution space is identified, its limits are expanded while maintaining a minimum target success rate, sr_T.

Exploration. The solution space in its most essential form is a single set of values that yield feasible solutions. Following the assumption that a solution space exists within the design bounds, the first step towards building the solution space is to identify single feasible solutions. If such a solution space exists, it may contain some or all of the previously identified single feasible solutions. To identify single feasible solutions, an optimization problem is posed whose objective function is the degree of fulfillment of the n number of constraints. Since the defined constraints are related to kinematic parameters, they have different physical units and are therefore normalized. Furthermore, the restrictions are aggregated as they all have to be fulfilled at the same time for the solution to be considered feasible. The normalization and aggregation steps of the constraints are presented in Algorithm 3 in the constraint violation check section. As observed, the constraints are defined by upper and lower values, $\hat{C}_i$, $\check{C}_i$. In their normalized form, $\hat{C}_i^*$=1 and $\check{C}_i^*$=0. The value obtained directly from the model evaluation to be checked against the limits, c_i, is mapped to the normalized space as c_i^*. The mapped constraint value is zero if the constrained is fulfilled. The mapping function calculates the distance from either the upper or lower limit depending on which limit is violated, i.e. $c_i > \hat{C}_i$ or $c_i < \check{C}_i$. The total constraint violation, C_T, is the absolute sum of all the c_i^*. This value is minimized in the optimization problem. Algorithm (3) summarizes the steps of the *exploration* phase.

Once the optimization procedure converges, all curves identified as feasible are gathered and analyzed. From this set, the maximum and minimum values for each resistance-to-deformation characteristic and each deformation level are identified. They define the upper limits, $\hat{S}_0$, and lower limits, $\check{S}_0$, of the initial solution space. However, as only the feasible solutions are considered for the calculation of this solution space, non-feasible designs may also coexist in the same area. Consequently, it is necessary to compute the actual success rate of this initial solution space in order to adjust its bounds to ensure a minimum success rate; this is carried out in the *consolidation* phase.

Data: Design space vector, upper limits $\hat{L}$ and lower limits $\check{L}$; Vehicle Characteristics; Constraints vector $\hat{C}$, $\check{C}$
Result: Initial Solution Space vector, upper limits $\hat{S}_0$ and lower limits $\check{S}_0$
Design Variables: X;
Objective Function: min $F(X)$ = min C_T;
Design bounds: $\hat{L}$, $\check{L}$;
Subjected to: $\hat{C}$>c>$\check{C}$;
while *optimization convergence not achieved* **do**
  Sample, X inside design bounds, $\hat{L}$ and $\check{L}$;
  Calculate constraint values c;
  for *each constraint* i **do**
    Constraint Violation Check;
    if $c_i > \hat{C}_i$ **then**
      $c_i^* = (c_i\text{-}\check{C}_i)/(\hat{C}_i\text{-}\check{C}_i)$ -1 ;
    else if $c_i < \check{C}_i$ **then**
      $c_i^* = (c_i\text{-}\check{C}_i)/(\hat{C}_i\text{-}\check{C}_i)$;
    else
      $c_i^* = 0$;
  end
  Calculate total constraint violation C_T;
  $C_T = \sum_{i=1}^{n} \text{abs}(c_i^*)$ **if** C_T = *0* **then**
    Store feasible design variable vector X_{FS} ;
end
for *each feasible set of design variable* j **do**
  $\hat{S_{0_j}} = \max(X_{FS_j})$;
  $\check{S_{0_j}} = \min(X_{FS_j})$;
end

Algorithm 3: Solution space calculator: exploration phase

Consolidation. This phase takes as input the upper and lower limits of the initial solution space, $\hat{S}_0$, $\check{S}_0$, determined in the *exploration* phase. Algorithm (4) summarizes the steps of the *consolidation* phase. As previously stated, the objective of this phase is to find a solution space with a minimum target success rate, sr_T. In this work, a

target success rate of 95% is used so that the solution space is effectively applied for the design of the vehicle structure. The success rate, sr, is defined as the number of feasible samples, n_{FS}, with a $C_T = 0$, divided by the total number of samples, n_s, used to characterize this design space. The optimal total number of samples, n_s, is a function of the sampling efficiency, the size of the space to be characterized, and the computational cost for evaluating the model to determine C_T.

State-of-the-art sampling mechanisms such as Optimized Latin Hypercube in the case of a relatively small number of variables and Monte Carlo-schemes for high-dimensional problems, can improve the sampling efficiency, especially when the costs of optimizing the sample distribution outweigh the benefits of having maximum space coverage. The size of the solution space is highly dependent on the physical quantity in question. Specifically for force levels, a difference of less than 5kN can be considered as not significant as the changes in trajectory and the kinematic quantities it produces are relatively small. Additionally, during the *consolidation* phase, the size of the solution space is reduced in each iteration, meaning that less samples are needed to characterize the space. Therefore, the computational costs of evaluating the constraints depend directly on the implementation of the model to evaluate. At the full-vehicle level, the kinematic model is used to generate a vehicle trajectory and then, the kinematic parameters are evaluated against the pre-defined constraints. The numerical-time integration nature of the kinematic model implies a relatively high number of operations to produce a vehicle trajectory close to the real physical phenomenon. The computational power required for the overall calculation of the solution space increases significantly as the kinematic model is evaluated in each iteration.

A hierarchical optimization approach is used in this work for an efficient calculation of the solution space. At the first level of this hierarchical scheme, that of the full-vehicle, where the constraint evaluation is more complex and therefore more costly, the design variables for the solution space calculation are reduced to the three total resistance-to-deformation characteristic curves, RDC: the total transverse and longitudinal force and the force application point. This reduces the amount of evaluations needed in contrast to starting with the load-path approach directly (78 vs 208 design variables). The second hierarchical level, load-path level, requires a coupling or mapping to the full-vehicle level. For this purpose, the results from the full-vehicle level are used as constraints for the load-path level by defining simple relationships between the levels. This approach reduces the overall computational cost. Section 5.1.2 provides further details on this aspect.

Data: Initial solution space vector, upper limits $\hat{S}_0$ and lower limits $\check{S}_0$; target success rate $sr_T\%$; vehicle characteristics; constraints vector $\hat{C}$, $\check{C}$
Result: Consolidated solution space vector, upper limits $\hat{S_C}$ and lower limits $\check{S_C}$
Calculate Success Rate SR($\hat{S}_k$, $\check{S}_k$, $\hat{C}$, $\check{C}$, *Model*, n_s) **:**
  Initialize number of feasible designs, n_{FS}=0;
  for *each sample in number of samples,* n_s **do**
    Sample, X inside limits,$\hat{S}_k$ and $\check{S}_k$;
    Run *Model*;
    Calculate constraint values c;
    for *each constraint* i **do**
      Evaluate constraint $\hat{C}_i$>c_i>$\check{C}_i$;
      Map constraint value to normalized constraint space, c_i^*;
    end
    Calculate total constraint violation C_T;
    if C_T = *0* **then**
      n_{FS}+=1 ;
      Store feasible design variable vector X_{FS} ;
  end
  Calculate success rate, $sr = n_{FS}/n_s$;
  return sr, X_{FS};
Evaluate success rate, $sr_k\%$, of initial solution space $\hat{S}_0$, $\check{S}_0$;
$sr_k\%$= SR($\hat{S}_0$, $\check{S}_0$, $\hat{C}$, $\check{C}$, *Model*, n_s);
Initialize current Solution Space vector, upper and lower limits ;
$\hat{S_C}$=$\hat{S}_0$ and $\check{S_C}$=$\check{S}_0$;
while $sr_T\% > sr_k\%$ **do**
  Evaluate success rate and get feasible solutions of current solution space;
  $sr_k\%$, X_{FS_k} = SR($\hat{S_C}$, $\check{S_C}$, $\hat{C}$, $\check{C}$, *Model*, n_s);
  Re-define solution space limits ;
  for *each feasible set* j *of design variable* X_{FS_k} **do**
    $\hat{S_{C_j}} = \max(X_{FS_{k_j}})$;
    $\check{S_{C_j}} = \min(X_{FS_{k_j}})$;
  end
end

Algorithm 4: Solution space calculator: consolidation phase

After calculating the success rate of a solution space at a particular iteration k ,$sr_k\%$, the solution space limits for the next iteration, $\hat{S_C}$, $\check{S_C}$, are determined by analyzing the feasible designs X_{FS_k}. For each design variable, the minimum and maximum values in X_{FS_k} are identified. The updated solution space limits take these minimum and maximum values to calculate the success rate of the new solution space in the next iteration. In this way, this process iteratively discards regions of the design space that do not contain feasible solutions. The solution space size becomes smaller in each iteration since the upper and lower bounds of the previous solution space are discarded correspondingly. Figure 5.5 shows a graphical representation of this phase. The iterations are carried out until the success rate of the current solution space is equal or larger than the target success rate, sr_T. A noteworthy consideration is that, due to imperfections in the sampling scheme, it may be the case that regions with feasible solutions are discarded. Yet, the objective of the *consolidation* phase is to obtain a solution space with a minimum number of feasible solutions regardless of the size of the space. Nevertheless, this shortcoming is identified and addressed in the next phase of the solution space calculator, the *expansion* phase.

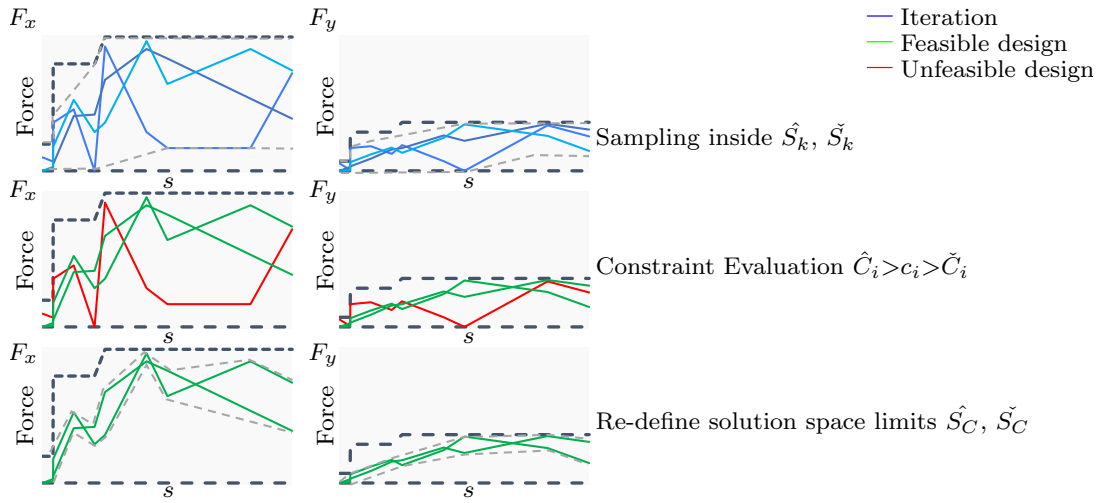

Figure 5.5 Solution space consolidation

Expansion. This phase takes as input a solution space $\hat{S_C}$, $\check{S_C}$ with a success rate larger or equal to sr_T. The size of the solution space is defined by the distances between the upper and lower limits. Even if the objective of the calculator is to maximize the size of the solution space, it is convenient to define a minimum solution space size, S_{size}, which must be satisfied. If the size of the solution space obtained in the *consolidation* phase is equal or larger than the target size S_{size_T}, then no further expansion is needed. In the opposite case, the *expansion* phase maximizes S_{size} under the constraint that the success rate of the expanded solution space, $sr_{exp}\%$, is larger or equal to the success rate of the consolidation phase $sr_{con}\%$.

Algorithm (5) shows the optimization problem statement of the *expansion* phase. The expanded limits of the design variables, $\hat{S_E}$ and $\check{S_E}$, have the original design bounds as upper bounds, $\hat{L}$ and $\check{L}$, and the consolidation limits as lower bounds $\hat{S_C}$, $\check{S_C}$. This implies that the expanded solution space exists between the consolidated space and the original design bounds. At each optimization iteration, the conditions, $sr_{exp}\% > sr_{con}\%$ and $S_{size_{exp}} > S_{size_{con}}$ are monitored, so that after convergence, the expanded solution space has a success rate larger than the consolidates success rate and at the same time, has a larger size than the consolidated space. Figure 5.6 condenses the *expansion* phase.

Data: Design space vector, upper limits $\hat{L}$ and lower limits $\check{L}$; Vehicle Characteristics; Constraints vector $\hat{C}$, $\check{C}$
Result: Expanded Solution Space vector, upper limits $\hat{S_E}$ and lower limits $\check{S_E}$
Design Variables: $\hat{S_E}$, $\check{S_E}$;
Objective Function: max $F(\ \hat{S_E}, \check{S_E}\ )$ = max S_{size};
Design bounds: $\hat{L}$, $\check{L}$ and $\hat{S_C}$, $\check{S_C}$;
Subjected to: $sr_{exp}\% \geq sr_{con}\%$;
while *optimization convergence not achieved* **do**
  Sample, $\hat{S_E}$, $\check{S_E}$ inside design bounds, $\hat{L}$, $\check{L}$ and $\hat{S_C}$, $\check{S_C}$;
  Calculate success rate of expanded solution space $sr_{exp}\%$;
  Calculate size of expanded solution space $S_{size_{exp}}$;
  if $sr_{exp}\% > sr_{con}\%$ *and* $S_{size_{exp}} > S_{size_{con}}$ **then**
    Store feasible design variable vector $\hat{S_E}$, $\check{S_E}$;
end

Algorithm 5: Solution space calculator: expansion phase

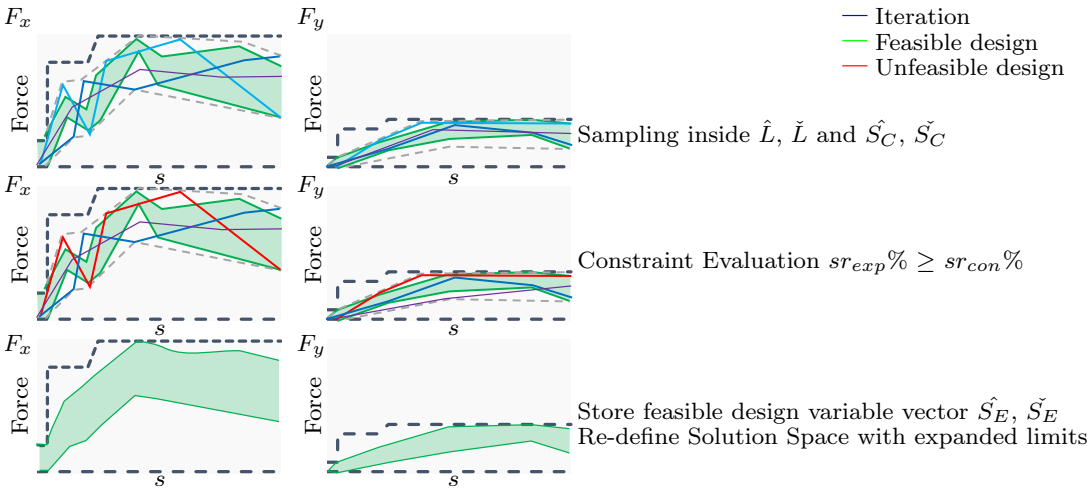

Figure 5.6 Solution space expansion

The three phases described above in general terms, *exploration*, *consolidation*, and *expansion*, provide an efficient approach to finding a solution space. The following section focuses on the implementation of the solution space calculator to find the resistance-to-deformation characteristics, RDC, as well as on the hierarchical mapping of the full-vehicle and load-path levels.

5.1.2. Full Vehicle to Load-Path Level Mapping

In Sections 4.1.1 and 4.1.2 it is stated that the kinematic model can be represented at two hierarchical levels, the top level being the full-vehicle level and the bottom level being the load-path level. The resistance-to-deformation characteristics can be expressed at both levels and an equivalence between both characteristics is constructed. While the full-vehicle level aggregates the resistance-to-deformation characteristics in two force-displacement curves and one force point of application, the load-path can be further subdivided into force-displacement curves at the convenience of the structural design strategy. The force-displacement curves at the load-path level imply an additional level of detail so that they can be used as design targets for each load-path. This level of detail means a larger number of variables to describe the resistance-to-deformation characteristics in comparison with the full-vehicle level. Therefore, a larger number of design variables is also involved in the solution space calculation. The link between the two levels is exploited so that in the first solution space calculation a solution space at the full-vehicle level is efficiently obtained using the kinematic model as the constraint evaluator. Later, the full-vehicle resistance-to-deformation characteristics in the form of a solution space are used directly as constraints for the load-path level. At the load-path level, the total sum of transversal and longitudinal forces as well as lever arm and point of application of force ratio are used as constraint evaluators. This last operation has a considerable lower computational cost in comparison to the kinematic model, since no numerical time integration scheme is needed.

The mapping of the properties and hierarchical optimization used for the solution space calculator at the full-vehicle and load-path levels are presented in Figure 5.7. At the full-vehicle level the vehicle characteristics include the vehicle mass, rotational inertia around the Z axis, the position of the center of gravity, the position of the A-Pillar as well as the barrier position. The design space contains the upper and lower bounds for the transversal and longitudinal force-displacement curves and the longitudinal force point of application-displacement curve. Finally, the constraints define the upper and lower limits of the acceptable values of selected kinematic parameters such as total vehicle rotation, θ_z, glance-off value, $GV_{P_{t_{end}}}$, rest deformation length, RDL s_L, and rest kinetic energy, RKE. The precise values of these ranges, that produce a desired kinematic response, are discussed in Section 5.2.

The solution space calculator at the full-vehicle level, takes the constraints, design space and vehicle characteristics and through the *exploration*, *consolidation*, and *expansion* phases finds a solution space for the following quantities: longitudinal, $\hat{F}_{x_{FV}}$, $\check{F}_{x_{FV}}$, and transversal forces, $\hat{F}_{y_{FV}}$, $\check{F}_{y_{FV}}$ and equivalent point of application of force, $\hat{Y}_{eq}$, $\check{Y}_{eq}$; each with their correspondent upper and lower limits. As stated before, the kinematic

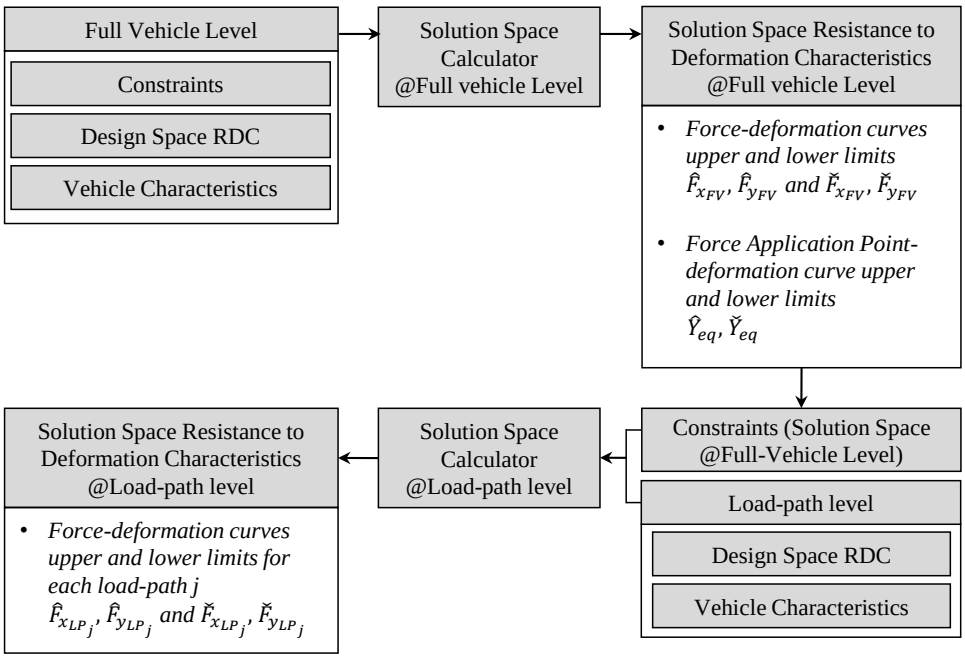

Figure 5.7 Solution space coupling: from the full-vehicle level to the load-path level

constraint evaluation is performed through the kinematic model.

At the load-path level, the design bounds are selected in the same manner as for the full-vehicle. The maximum load levels for each load-path correspond to the available topology of the vehicle structure. In contrast to the full-vehicle level, the vehicle characteristics at the load-path also define the transversal position of the load-paths across the structure. These positions, Y_{LP} are defined for each load-path j. Regarding the constraint evaluation, one alternative for the load-path level would be to use the kinematic model directly. The kinematic model admits as input force-displacement curves representing either the total forces or load-paths forces. Internally, the kinematic model sums up the forces in the load-paths in the transversal, $F_{y_{LP}}$, and longitudinal direction, $F_{x_{LP}}$, correspondingly. For the total moment around the z axis, M_z, the kinematic models considers for the transversal forces the load-path lengths as lever arms and for the longitudinal forces, the y position of the load-path as lever arm. This relationship describes the link between the point of application of force Y_{eq}, total longitudinal force $F_{x_{FV}}$ and the load-path longitudinal forces $F_{x_{LP}}$ and the load-path y positions Y_{LP}. Considering this mechanical equivalence, the solution space limits at the full-vehicle level are used as constraints at the load-path. Algorithm (6) presents this mapping procedure. It can be seen that the computational cost of the constraint mapping is relatively small compared to that for the evaluation of a kinematic model. The constraint mapping only contains sum operations for each load-path j to m and for each deformation level i to n. The *exploration*, *consolidation*, and *expansion* of the solution space calculator are

carried out at the load-path level obtaining as a result the upper and lower limits for the force levels for each load-path: $\hat{F}_{x_{LP_j}}$, $\hat{F}_{y_{LP_j}}$, $\check{F}_{x_{LP_j}}$ and $\check{F}_{y_{LP_j}}$.

This hierarchical optimization scheme defined at the full-vehicle and load-path levels used for the solution space calculation combines the benefits of coupling both levels. On one hand, the accuracy of the kinematic model is maintained at the full-vehicle level, where the number of design variables is reduced. On the other hand, the mechanical equivalence and link to the load-path level offers lower calculation cost of constraint evaluation offering the possibility to cope with the increased number of design variables and the correspondent number of iterations needed to achieve a solution space convergence. Nonetheless, the key aspect of selecting the appropriate constraints at the full-vehicle level that produce a suitable kinematic response and more importantly a desired structural rating is still open. In the following section this issue will be discussed.

Data: Solution Space @Full-vehicle level: $\hat{F}_{x_{FV}}$, $\check{F}_{x_{FV}}$, $\hat{F}_{y_{FV}}$, $\check{F}_{y_{FV}}$, $\hat{Y}_{eq}$, $\check{Y}_{eq}$
Result: Force-Displacement curves @Load-path level, $F_{x_{LP_j}}$ and $F_{y_{LP_j}}$
for *each deformation level i to n* **do**
  Longitudinal Forces:
  $\hat{F}_{x_{FV_i}} > \sum_{j=1}^{m} F_{x_{LP_{j_i}}} > \check{F}_{x_{FV_i}}$;
  Transversal Forces:
  $\hat{F}_{y_{FV_i}} > \sum_{j=1}^{m} F_{y_{LP_{j_i}}} > \check{F}_{y_{FV_i}}$;
  Equivalent point of application of longitudinal force:
  $\hat{Y}_{eq_i} > \sum_{j=1}^{m} (F_{x_{LP_{j_i}}} * Y_{LP_{j_i}}) / \sum_{j=1}^{m} (F_{x_{LP_{j_i}}}) > \check{Y_{eq_i}}$;
end

Algorithm 6: Full-vehicle to load-path level constraint mapping

5.2. Data-driven Solution Space Definition

In order to determine the functional properties of the vehicle structure, namely the resistance-to-deformation characteristics that correspond to the structural rating target, the work-flow shown Figure 5.8 is applied. As previously stated, the kinematics of the vehicle are a function of the resistance-to-deformation, and vehicle characteristics. The next step is to couple the kinematics with the structural rating. A data-driven approach is proposed, whose central objective is to characterize the vehicle kinematics of the available IIHS tests, analyze them in conjunction with its Safety Distance D_{SG}, and find regions of the previously defined kinematic parameters that increase the probability of achieving a given structural rating target.

As shown in Figure 5.8, the first step is to extract the vehicle trajectory through the video analysis of the high speed video footage as described in Section 3.2. The displacements and rotation obtained are used then in the kinematic analysis in combination with the vehicle characteristics to calculate the kinematic parameters as well as the kinematic mode. The residual kinetic energy is also calculated at t_{end} as a way to represent the amount of energy that is not absorbed by the structure by means of plastic deformations

and subsequent intrusions; but that remains in the form of translational and rotational velocity.

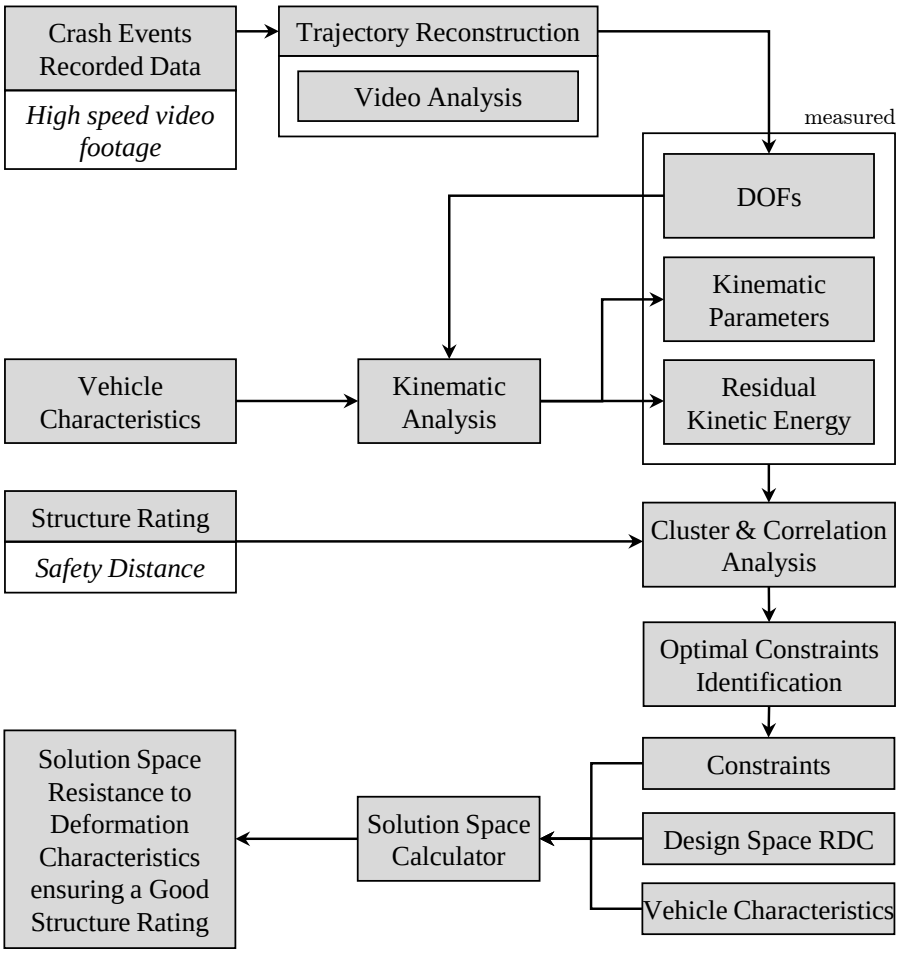

Figure 5.8 Data-driven solution space definition

The next step is to analyze the kinematic quantities and find relationships among themselves and with the D_{SG} through a cluster and correlation analysis. Afterwards the clusters of kinematic quantities or combinations of ranges that result into regions of certainty of a given D_{SG} are defined as constraints. These constraints, in the form of minimum and maximum values, in combination with the selected design bounds for the resistance-to-deformation and other vehicle characteristics are used as input for the solution space calculator. As output, the solution space for the RDC is obtained as a

function of the desired D_{SG}. In Section 5.2.1 a deeper description of the Cluster and Correlation Analysis process is presented.

5.2.1. Kinematic Behavior and Structural Performance Cluster Analysis

The rest kinetic energy integrated by the translational and rotational velocity of the vehicle at t_{end}, RKE, is expressed as a percentage of the kinetic energy at the beginning of the crash. The RKE represents the amount of energy that was not absorbed by the structure by means of plastic deformation. Ideally, if a vehicle conserved 100% of its initial kinetic energy, it would mean that there were no deformations and therefore intrusions in the occupant compartment. Since the contact between the vehicle and the rigid barrier is geometrically unavoidable and because the structure of the vehicle is not ideally rigid, some degree of deformation and consequently of energy absorption is expected. Consider two vehicles with the same mass, proportions and identically stiff occupant compartments, (same A-pillar, firewall, rocker) but different RKE and therefore different frontal structures. The vehicle with the higher RKE has absorbed less energy during the crash and consequently has less deformations, intrusions and a better rating than the other vehicle. Even if this strictly holds only for the case described before, a similar tendency can be observed in the vehicle data from the IIHS. Additionally, if a vehicle is designed to completely absorb the initial kinetic energy of the crash, it would require increased cross-sections to be able to cope with the higher amount of energy absorption demand and it would therefore mean a higher weight of the vehicle.

Figure 5.9 shows the relation between rest kinetic energy, RKE, and safety distance, D_{SG}. The vehicles analyzed show values of RKE at the low end of the spectrum from less than 10% and at the high end with more than 40%. As a $D_{SG}>0$ means a Good structural rating, it can be observed that such a D_{SG} can be achieved almost independently to the RKE. However there is a region for $RKE>30\%$ that only has $D_{SG}>0$ (see green area in Figure 5.9). The vehicles analyzed are diverse in terms of mass, proportions, type, and structure. It can be concluded that for the range of $RKE<30\%$, the D_{SG} is highly dependent on the specific layout and execution of the vehicles frontal structure and occupant compartment. But if the vehicle achieves a $RKE>30\%$ the details of the structure are of secondary importance. This data-driven approach is dependent on the current state-of-the-art materials and constructions techniques used in the automobile industry. Meaning that if different constructions and materials are available this conclusion may vary.

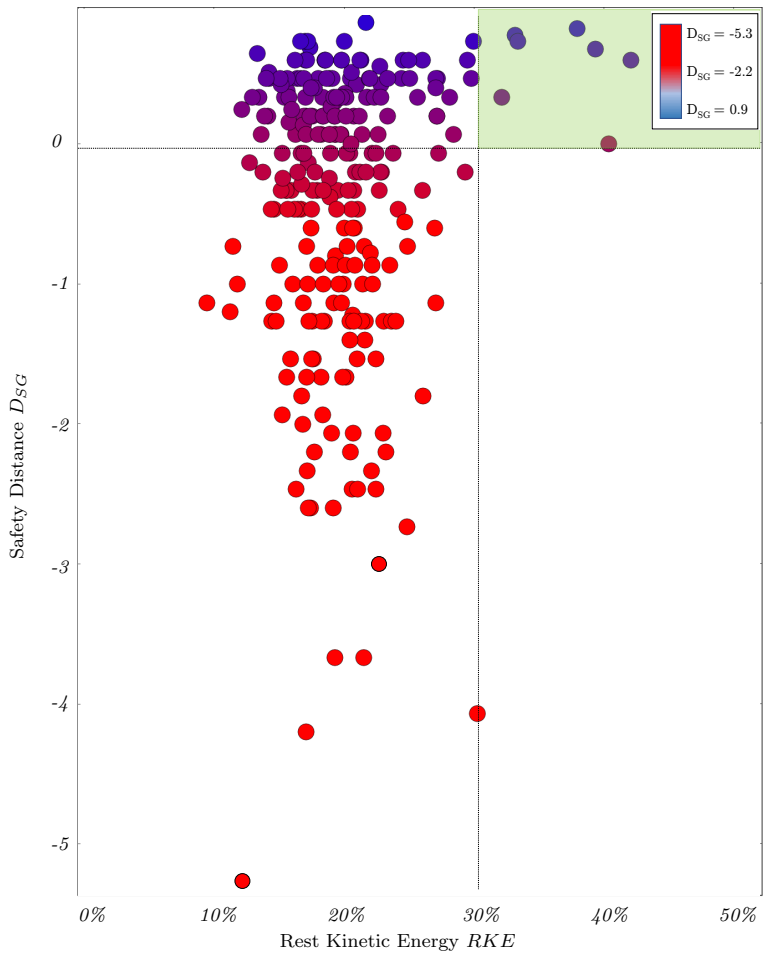

Figure 5.9 Rest kinetic energy RKE vs. safety distance D_{SG}. The green area corresponds to a region of the analyzed space where RKE>30% and D_{SG}>0

In order to confirm the location of this region with higher probability of D_{SG}>0 a hierarchical cluster analysis is performed upon RKE and is presented in Figure 5.10. Four clusters are identified and the correspondent histograms for their D_{SG} are shown. Cluster 1 has an average D_{SG}=-44%, while cluster 2 a D_{SG}=-56%, cluster 3 D_{SG}=-12% and finally cluster 4 D_{SG}=53%. The clusters are presented in occurrence order, meaning that cluster 1 contains 53% of the data, 34%, 11% and 2% correspondingly to clusters 2, 3, and 4. By inspecting their histograms and average values, it can be concluded that clusters 3 and 4 have higher probability of containing vehicles with D_{SG}>0. The correspondence between the cluster and RKE range is shown in Figure 5.11. The relevant cluster 3 and 4 have a RKE range of [25%,35%] and [35%,43%] correspondingly. Within cluster 3, all of the vehicles with values of RKE>30% observe a D_{SG}=0%. Therefore RKE>30% is taken as the main constraint derived from the kinematic quantities that maximize the probability of obtaining a good structural rating.

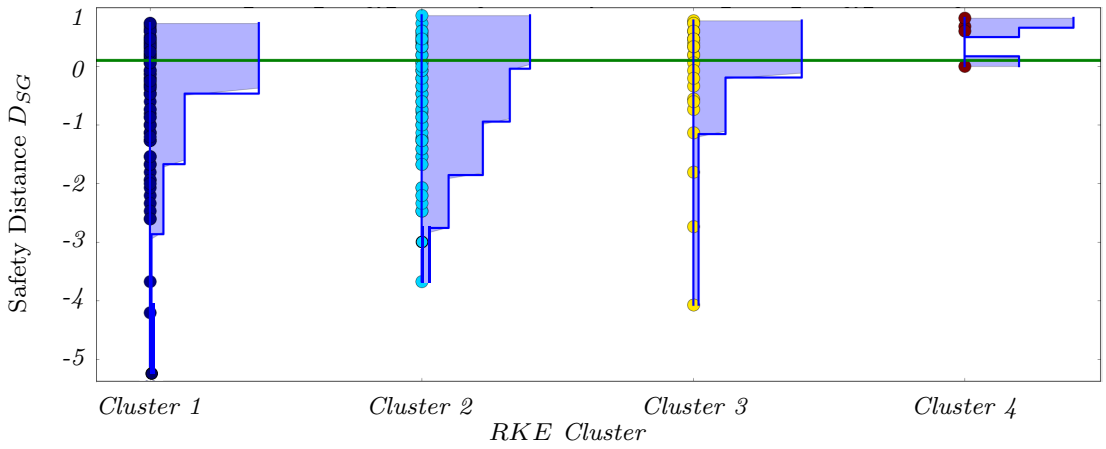

Figure 5.10 Rest kinetic energy RKE cluster vs. safety distance D_{SG}

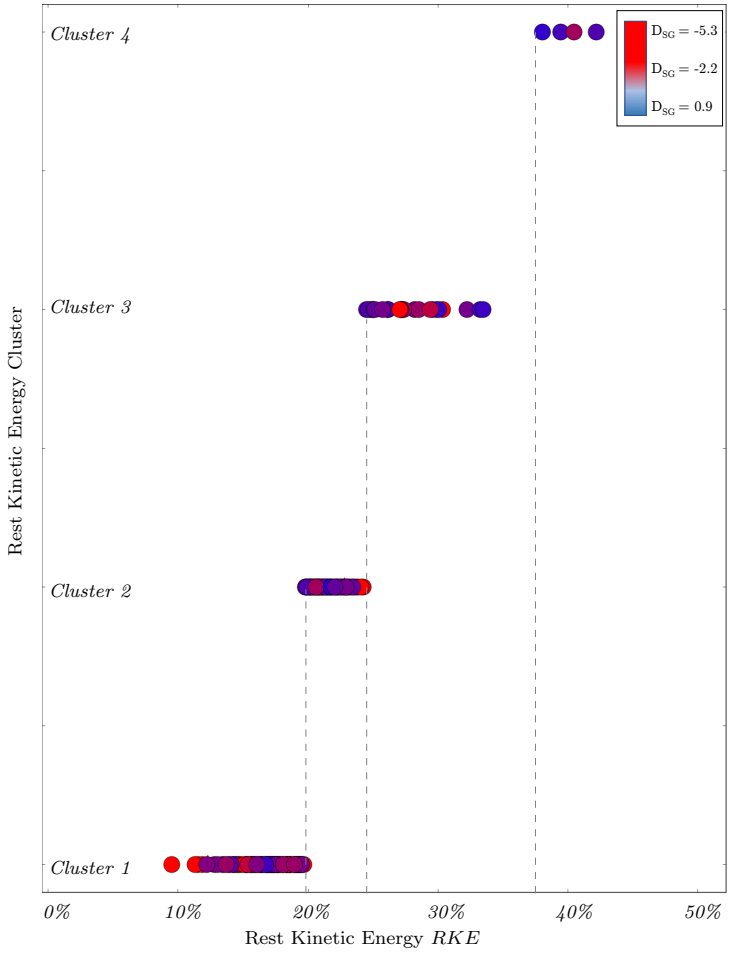

Figure 5.11 Rest kinetic energy RKE cluster vs. rest kinetic energy RKE

Other relevant kinematic parameters and their relation to D_{SG} and RKE are shown in Figures 5.12, 5.13, and 5.14, where the following conclusions are derived. First, the Figure 5.12(a) shows a weak correlation between the total vehicle rotation around z, θ_z, and D_{SG}. Generally, for higher rotation values θ_z>10° lower D_{SG} values are observed, and for lower rotations θ_z<0° the probability of D_{SG}>0 increases. However, the relation of θ_z with RKE is stronger than with D_{SG}. In order to achieve values of RKE>30% only negative rotations are present.

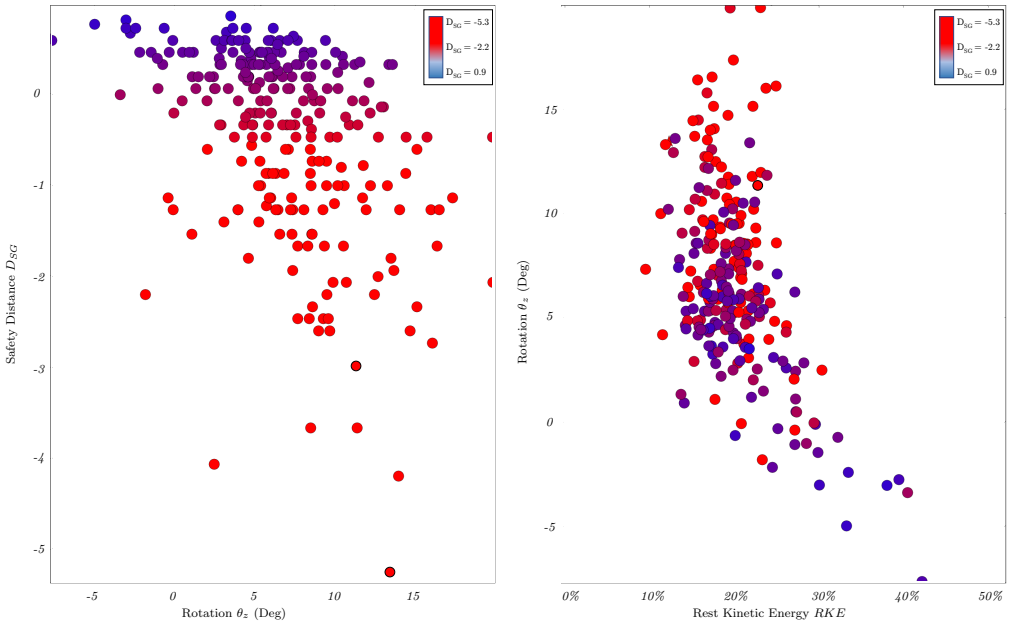

(a) Total vehicle rotation in z vs. safety distance D_{SG}

(b) Total vehicle rotation in z vs. rest kinetic energy RKE

Figure 5.12 Total vehicle rotation in z vs. safety distance (a) and rest kinetic energy (b)

Second, for the glance-off value relation with D_{SG}, the range of D_{SG} is completely independent. Glance-off values <1 and >1 observe similar probability of D_{SG}>0. Nonetheless, Figure 5.13(b) shows that values of RKE>30% coincide only with Glance-off values > 1. Finally, for the rest deformation length, RDL s_L, the plots are shown in Figure 5.14. Although higher values of s_L coincide with higher values of D_{SG} that does not hold for the relation with RKE, where no clear correlation is observed. For these reasons, even if the other quantities do not show a strong correlation with D_{SG}, secondary quantities such as θ_z and glance-off value can be identified that produce higher probability of RKE>30% and consequently D_{SG}>0.

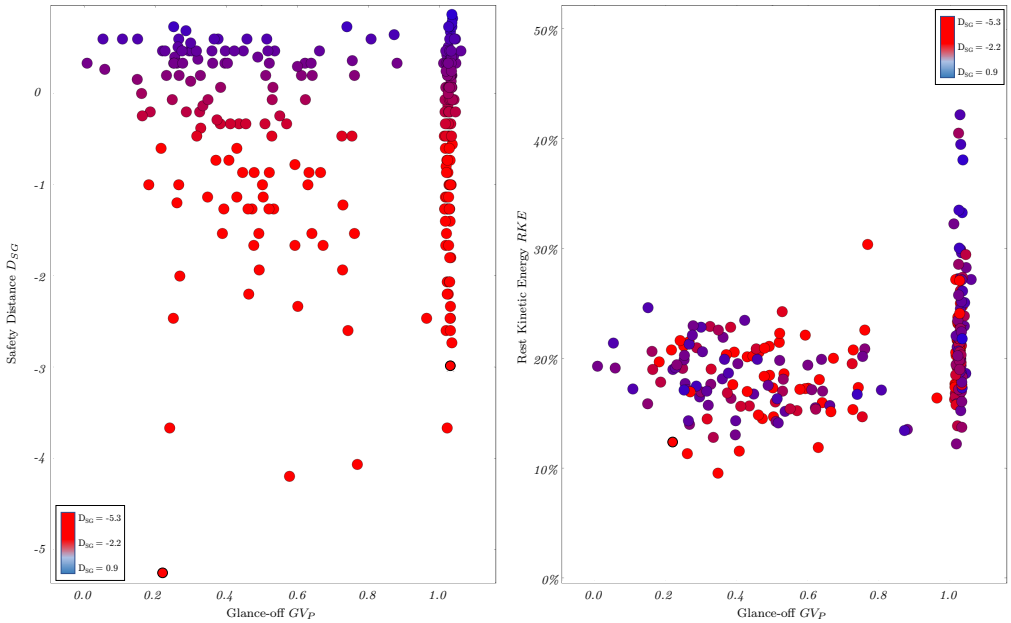

(a) Glance-off value vs. safety distance D_{SG} (b) Glance-off value vs. rest kinetic energy RKE

Figure 5.13 Glance-off value vs. safety distance (a) and rest kinetic energy (b)

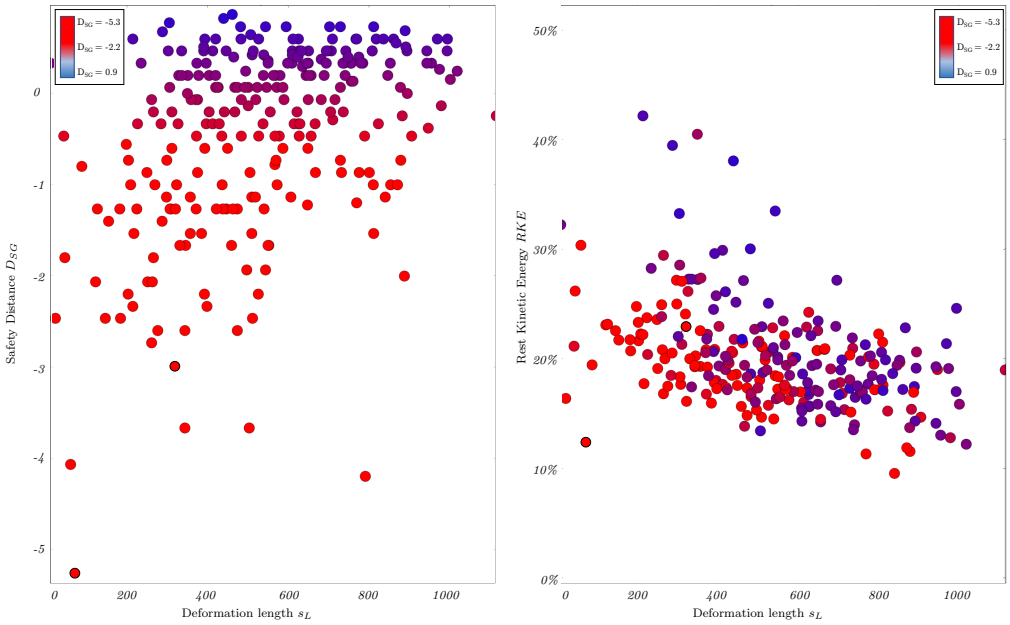

(a) Rest deformation length, RDL s_L vs. safety distance D_{SG}

(b) Rest deformation length, RDL s_L vs. rest kinetic energy RKE

Figure 5.14 Rest deformation length, RDL s_L vs. safety distance (a) and rest kinetic energy (b)

5.2.2. Optimal Constraints Identification

A set of constraints identified from the analysis presented in the previous section together with the resistance-to-deformation design bounds as well as the vehicle characteristics are given as an input to the solution space calculator. The outcome is a set of force-displacement curves and force application point-displacement curve at the total vehicle level and force-displacement curves at the load-path level, which in essence result in vehicles with a Good structural rating. The link between the rating and resistance-to-deformation characteristics are the vehicle kinematics and consequently the constraints given upon them. Table 5.1 summarizes the selected constraints. The RKE constraint is dominant and has a direct relation with the deformations occurring during the crash as well as the structural rating. The θ_z and GV_P are given as a mean to achieve the requested RKE with a kinematic behavior that is possible to achieve considering the state-of-the-art materials and construction techniques. Even if achieving a RKE>30% is physically possible with a different combination of θ_z and GV_P it would deviate from the current industry capabilities. Lastly, the rest deformation length constraints ensures that the glance-off and therefore t_{end} comes before a hard contact between the A-Pillar and the barrier takes places. Where the RKE constraint can be understood as a measure of efficiency, the s_L constraint represents a certain degree of safety.

Table 5.1 Constraints defined upon relevant kinematic parameters that maximizes the probability of D_{SG}>0

Kinematic quantity	**Constraint**
Rest Kinetic Energy	$RKE > 30\%$
Total Vehicle Rotation	$\theta_z < 0°$
Glance-off	$GV_P \geq 1$
Rest Deformation Length	$s_L > 10mm$

Chapter 6

Solution Space-based Iterative Simulation Scheme

The virtual design and verification of the functional properties of the structure is represented at the right side of the V-Model in Figure 6.1. As stated previously, the system must be able to provide the appropriate response even under a varying test environment. As costly as the virtual design phase can be, the advantage of using simulation tools, particularly FE models, for the vehicle development is certain. However, the effective use of these simulation tools to drive the structural design is not trivial. The broad spectrum of possible and the subset of feasible and optimum solutions often elude the design engineer. In consequence, it does not suffice to define and derive the global and local requirements but to use them as objective functions in the iterative simulation-based design. This work recognizes this issue and proposes a solution space-based iterative simulation scheme or SSBISS. The SSBISS takes the requirements defined in the early phase for each subsystem, namely resistance-to-deformation characteristics for each load-path, as objective function and determines the level of violation of the solution space for each design proposal while explicitly considering the relevant sources of uncertainty and the variation they produce in the output variables.

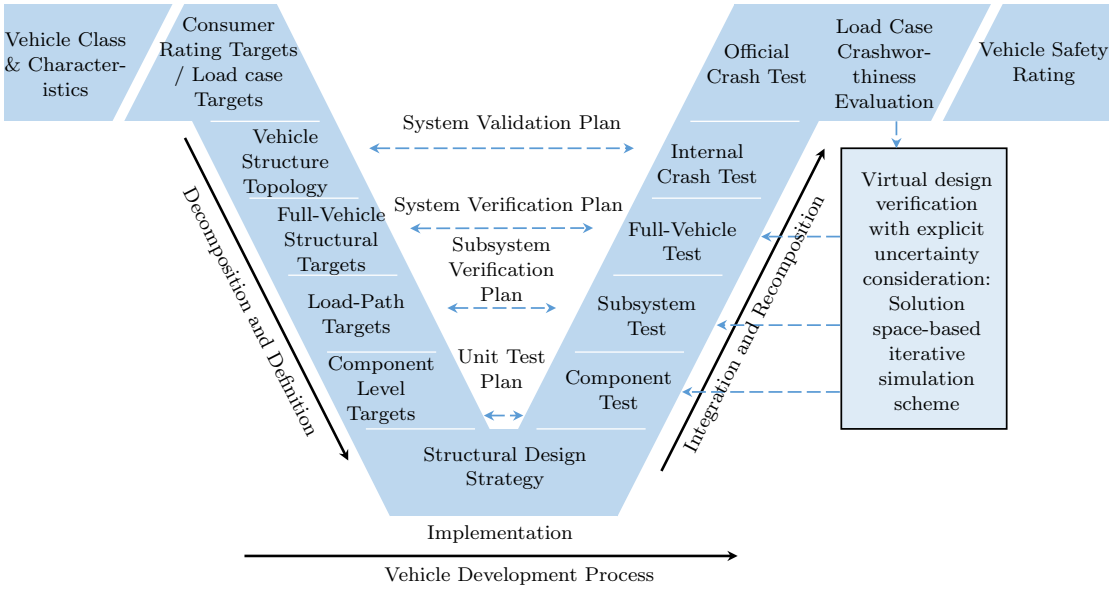

Figure 6.1 Systems engineering V-diagram for crashworthiness design and virtual design verification with explicit uncertainty consideration: solution space-based iterative simulation scheme

The general work-flow of the SSBISS is presented in Figure 6.2. The starting point of the scheme is a FE model where an initial structural topology and the correspondent component geometry and properties are represented. Not only a single simulation is carried out but a set of simulations containing variations of the relevant input parameters. The relevant input parameters and their correspondent uncertainties are characterized and samples are generated to represent such variations. This first set of simulation results is preprocessed to obtain the relevant outputs including the nodal displacements and the forces time series of the Small Overlap rigid barrier. From the nodal displacements of the vehicle, the kinematic DOFs (u_x, u_y, θ_z) are calculated. These DOFs together with the force signals and the vehicle characteristics are post-processed in the kinematic analysis. As a result of this analysis, the kinematic parameters, residual kinetic energy RKE, and resistance-to-deformation characteristics are obtained.

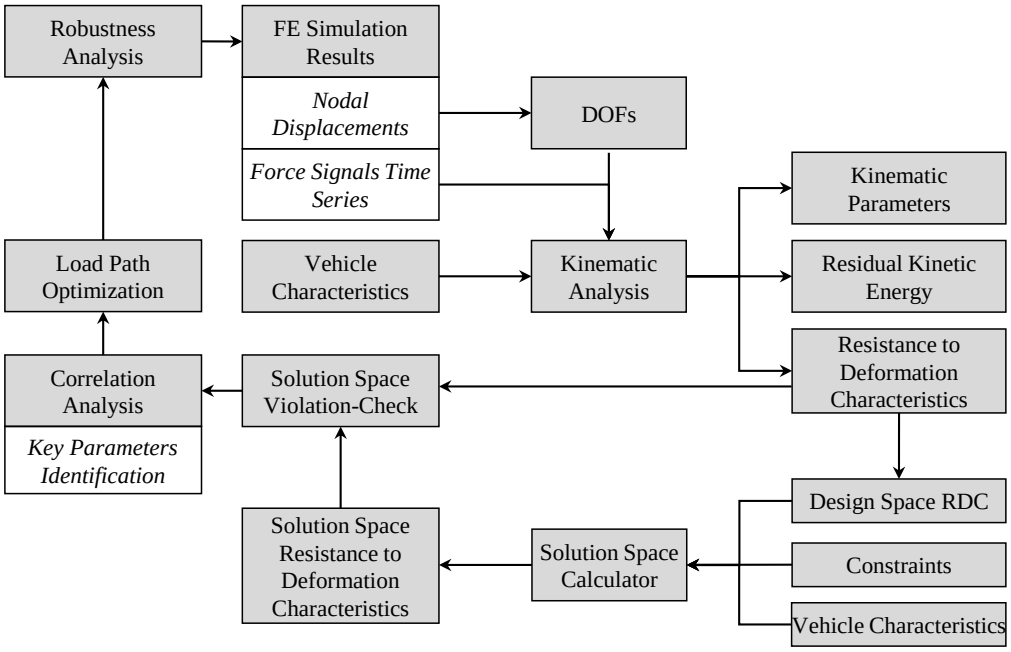

Figure 6.2 Solution Space-based Iterative Simulation Scheme

The first iteration is used as a base to define the design bounds for the resistance-to-deformation characteristics. These force-displacement curves are taken as estimators from the performance of the load-paths. The characteristics of the curves, start, end, and local minimum and maximum are a representation of the topology of the structure and by scaling them a design space can be defined as stated in Section 5.1.1. This design space together with the constraints defined upon the kinematic parameters and the vehicle characteristics are given as an input to the solution space calculator, where the solution space of the RDC is obtained in the form of piecewise linear force-displacement curves and additionally for the total vehicle level a point-of-application-of-force-displacement curve.

For subsequent iterations, the RDC obtained from the simulation are compared against the solution space through a violation-check procedure. A scalar value indicating to what degree is the curve of the simulation inside of the solution space is reported and correlated with key parameters in order to identify the sensitivities and guide the design to a complete fulfillment of the solution space requirements. By comparing the current RDC to the solution space, regions in the load-path that need an increase or decrease of the force levels are identified and optimized. The final step is a robustness analysis that evaluates the degree of solution space fulfillment in context of the uncertainty of the relevant parameters. A so-called robustness index is reported. Then, the FE model

including the new set of optimized geometries and topologies obtained from this analysis is once again, together with the set of samples characterizing the uncertainties, simulated and evaluated until a complete and robust fulfillment of the solution space is achieved. Most of the sub-steps of the SSBISS were defined in the previous sections. However, for the newly introduced procedures of solution space violation-check and robustness analysis this work dedicates the following sections.

6.1. Solution Space Violation-Check

The solution space violation-check is the way to quantify the degree of fulfillment of the *RDC* requirements. This degree of fulfillment drives the development of the design. Each design iteration has the goal to increase it. Once the degree of fulfillment is 100% and the robustness evaluation has been carried out, the probability of achieving the structural rating target in the subsequent hardware test is maximized. The previously calculated solution space for the resistance-to-deformation characteristics at the load-path level in its piecewise linear form, namely the upper and lower limits, $\hat{F}x_{LP_j}$, $\hat{F}y_{LP_j}$, $\check{F}x_{LP_j}$ and $\check{F}y_{LP_j}$, is compared against the force-displacement curves obtained in the simulation, $FSIMx_{LP_j}$ and $FSIMy_{LP_j}$. Algorithm (7) summarizes the necessary calculations defined in this solution space violation-check procedure.

The violation check is carried out for both directions x and y for each load path. Since it could be the case that the solution space limits and the obtained force signals from the simulation are defined with a different discretization level, the first step is to map both items using the same discretization delta in mm, here called *dc*. The active period of the force signals may vary among the load-paths; therefore, the identification of the end of each force-displacement curve is carried out. This active period is determined by either the point when the load-path has no longer a geometrical projection onto the barrier and consequently the force-signal reaches zero or when the load-path reaches a rebound state and the displacement starts to decrease. For the first case, a local glance-off value is used to determine the end point. For the second case, the rebound of a load-path will coincide with the global rebound identified in the kinematic analysis. In both cases, the solution space degree of fulfillment (SSDOF) vectors either at the load-path level, $F_{x_{FF_j}}$ and $F_{y_{FF_j}}$; or total level, $F_{x_{FF}}$ and $F_{y_{FF}}$ are only calculated for the active period of the force-signal. For each deformation level using the *dc* discretization, the SSDOF is calculated as: (a) the positive difference between the simulation force-signal, $FSIMa_{LP_{j_i}}$, and the lower limit of the solution space $\check{F}a_{LP_j}$ when the force signal is smaller than the lower limit or (b) the negative difference between the force-signal, $FSIMa_{LP_{j_i}}$, and the upper limit, $\hat{F}a_{LP_j}$, when the force signal is larger than the lower limit. Otherwise it is zero. This implies that the level of fulfillment is directly expressed as the force difference. This differences are stored in the $F_{a_{FF_j}}$ for each load-path j until the force-signal ends or the solution space definition is no longer active, meaning that both upper and lower limits are equal to zero as defined by the design bounds. Afterwards, the SSDOF at load-path level is the absolute sum $F_{a_{FF_j}}$ for each deformation level. Finally the total SSDOF for each direction x and y is the sum of the SSDOF of each load-path.

Due to the fact that the SSDOF at the load-path level, $F_{a_{FF_j}}$ is also expressed in the same spatial discretization as the deformation vector, the regions where changes in the force levels are needed can be directly mapped to regions of the vehicle structure. If for a particular deformation level $F_{a_{FF_{j_i}}}>0$, then the force in the load-path needs to be decreased, since the upper limit of the solution space is violated. On the contrary, if $F_{a_{FF_{j_i}}}<0$, meaning that the lower limit is violated, the force level needs to be increased. If at total level, the SSDOF value is relatively high, it means that there are considerable deviations from the solution space. Therefore, the objective is to minimize its value so that it is closer to zero.

Data: Force-Displacement Curve @Load-path (j) level, $FSIMy_{LP_j}$ and $FSIMx_{LP_j}$; Solution Space Resistance-to-Deformation Characteristics upper and lower limits $\hat{F}x_{LP_j}$, $\hat{F}y_{LP_j}$, $\check{F}x_{LP_j}$, $\check{F}y_{LP_j}$; Curve Discretization in mm dc
Result: Solution Space degree of fulfillment @Load-path level, $F_{x_{FF_j}}$ and $F_{y_{FF_j}}$; and total, $F_{x_{FF}}$ and $F_{y_{FF}}$

```
for F_a in F_x and F_y do
    for each load-path j to m do
        Map solution space curves F̂a_LPj, F̌a_LPj to dc;
        Map simulation curves FSIMa_LPj to dc;
        Initialize Solution Space degree of fulfillment vectors F_aFFji;
        for each deformation level i to n do
            if F̌a_LPj>0 and F̂a_LPj>0 then
                if FSIMa_LPj<F̌a_LPj then
                    F_aFFji = F̌a_LPj - FSIMa_LPji ;
                else if FSIMa_LPj>F̂a_LPj then
                    F_aFFji = F̂a_LPj - FSIMa_LPji ;
        end
        SSDOF @Load-path level: F_aFFj = Σ_{i=1}^{n} abs(F_aFFji);
    end
    Total SSDOF: F_aFF = Σ_{j=1}^{m} abs(F_aFFj);
end
```

Algorithm 7: Solution space violation-check

The solution space violation-check is carried out for each of the simulations corresponding to the sample set defined in the robustness analysis. Each of the force-displacement characteristics obtained from this simulation set includes the variation of the relevant parameters producing the scattered response. Considering this group of simulations, the goal is to minimize the larger SSDOF in the set, meaning that the larger deviation from the solution space is as small as possible. These iterations are carried out until the SSDOF is minimized and consequently all of the load-paths lie inside the solution space

while also considering the scatter of the response. In the following section, the details on how to generate the samples set, characterize the sources of uncertainty and evaluate the robustness of the design are discussed.

6.2. Robustness Analysis

For a design to be considered robust, it must achieve the predefined targets under nominal conditions as well as considering the variation in the input parameters inherent to a physical phenomenon such as a crash test. The proposed methodology to ensure that the performance of the structure fulfills the requirements is presented in Figure 6.3. As first step, the sources of uncertainty that produce variation in the result are identified and classified as relevant parameters. Then, the correspondent set of samples that efficiently represent the scatter of the input parameters are generated. Afterwards, a set of FE models are simulated using the input variables samples defined earlier and the correspondent output variables are generated through a post-processing routine. Finally, the robustness of the relevant output parameters is evaluated by means of the calculation of a so-called robustness index. In the following sections, the relevant parameter identification, sample generation and robustness index calculation procedures are described.

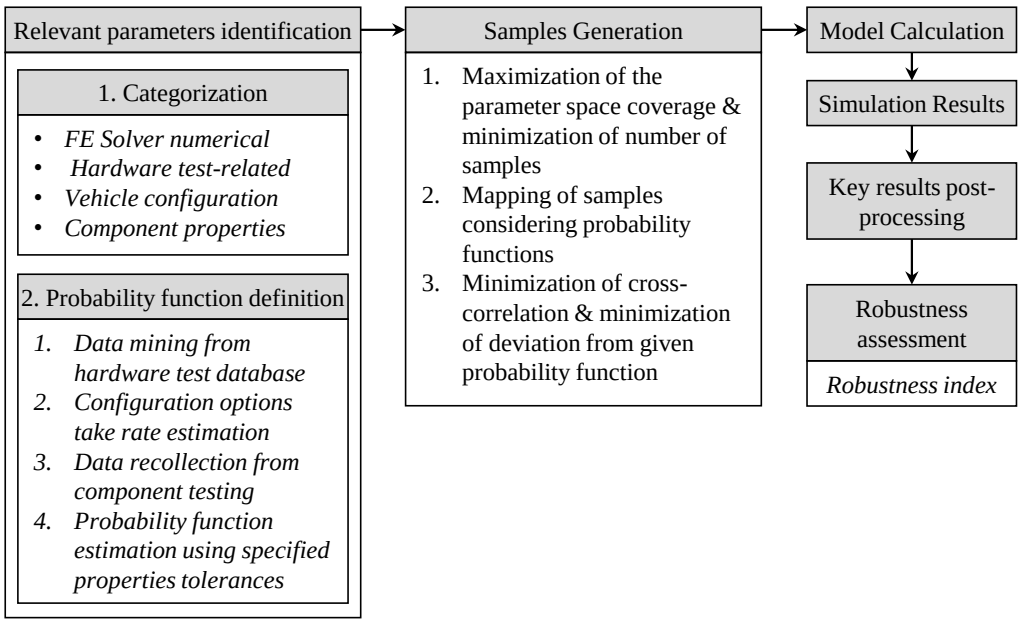

Figure 6.3 Robustness analysis framework

6.2.1. Identification of Sources of Uncertainty

Any crash test is a controlled experiment to a certain degree. However, several parameters that affect its outcome may be uncertain due to lack of information at an early stage of the design, variations in the hardware use to conduct the test, variations of the conditions of the test and variation in the tolerances and properties of the components. Additionally, during the virtual phase of the development and in context of the computer aided engineering and explicit finite element models, variations in the simulation may also occur due to numerical issues of the solver used even if the model is identically defined. Different strategies can be developed to tackle each of these sources of uncertainty. In some cases it may be possible to eliminate the source of uncertainty if sufficient information is gathered and used in the corresponding design phase. For a large majority, it would be unpractical to actually measure the exact values that each of the relevant parameters would take prior to the experiment. Therefore, having a methodology to include these uncertainties during the design phase is advantageous in order to produce a robust design. To best understand and generate the appropriate strategies, it is beneficial to categorize the sources of uncertainty into FE solver numerics, hardware test conditions, vehicle configuration, and component properties related.

The uncertainties related to the FE solver numerics have mainly to do with two factors, one is the domain decomposition of the FE model and the second is the time-step of the solver. In modern FE solvers, the domain decomposition is done automatically and depends on the number of processors used to perform the calculations. Increasing the amount of parallel processors used for the simulation decreases the calculation time to a certain degree until the communication among them becomes dominant and produces a bottleneck that prevents a linear scaling of the number of processor and decrease of calculation time. Present-day high performance computer clusters can handle a considerable amount of simultaneous FE simulations and their correspondent parallel processors. However, in order to speed up the total time needed from the model generation to the post-processing of the results, a possible range of the parallel processors to be used can be specified. This speeds up the queuing time in the HPC-Clusters, since as long as any number of processors specified in the range is available, the solver calculations can start. Hence, using always the same number of processors is possible although it is not convenient for day-to-day applications.

The second factor mentioned, namely the time-step is also particularly critical for explicit calculations. The critical time-step is available to the user at each point during the calculation. In modern FE solvers, a minimum time-step can be specified to avoid increasing the calculation time specially during phases of the simulation where elements with smaller size may become dominant and require smaller time-steps. If these dynamic critical time-steps reach the user-specified value a mass-scaling procedure will take place to take this time-step back to the defined range. These two factors of numerical variation are also a convenient way to identify unstable structural configurations. A practical way to study the numerical stability at the early stages of the virtual design is to maintain constant the amount of processors and parametrize this minimal time-step in the model and use it as a relevant input parameter. In this problem statement, a variation of

maximum of 0.0001% delta was used among 10 different simulations. The numerical stability provides a baseline to compare the real effect of the other parameters. If the variation of a certain parameter is smaller than the variation in the output introduced by the numerical variation, the effectiveness of this parameter is questionable and a better design may be introduced.

The hardware test equipment and facilities are subjected to high standards and are well-maintained and calibrated. During the physical prototype test, the cost of conducting a crash test is overshadowed by the cost of the prototype itself. It is convenient for the test facilities and design teams to ensure a high degree of repeatability so that the information gathered can be efficiently used to validate the vehicle's structural design. In the Small Overlap crash test, three main factors can be identified that are directly related to the test conditions themselves, namely the mass of the vehicle, the velocity at impact and the initial overlap of the barrier and the vehicle. For these three factors, ranges are stipulated in the test protocol and can be then associated with the vehicle preparation procedure and the acceleration of the vehicle towards the barrier. During the preparation procedure, the measurement equipment is setup and attached to the vehicle. This equipment may include, on-board cameras, crash test dummies, and acceleration and rotational velocity sensors, and their correspondent electronic equipment that gathers and retrieves the data. The exact position in the vehicle and type of this auxiliary measurement equipment is not known prior to the test and may vary depending on availability and resources of the test facility. However, a target weight and distribution is specified in order to maintain consistency during the design process and the official test by the IIHS. Complementary to this target weight, an acceptable range or tolerance is given. Even if the exact vehicle weight is not known prior to the vehicle setup, the range in which it will lie is known. The second factor, the velocity at impact, is determined by the acceleration device used to tow and accelerate the vehicle until it achieves its target velocity and contacts the rigid barrier. This initial velocity determines the kinetic energy of the vehicle and therefore the deformation that will take place during the crash as well as the maximum energy that may be absorbed by the structure. As mentioned before, these acceleration devices are often calibrated but a variation is always expected. The third factor, the initial overlap, is the result of the relative position of the vehicle and the barrier. Despite the fact, that this relative distance can be precisely measured before accelerating the vehicle, the alignment of the towing rails and the distance between the vehicle in free fly and the barrier have an influence on the initial overlap.

The amount of optional equipment and versions of a certain vehicle model must also be considered when designing a robust structure. In certain ways, different equipment and version combinations do not affect the stiffness or energy absorption capabilities of the vehicle's structure. However, factors such as the power-train, adaptive suspension, brake calipers size and wheel size, material and styling may affect the outcome of the crash. Different power-train options such as all-wheel drive, AWD, or rear-wheel drive, RWD, may affect the stiffness of the sub-frame as a result of the additional components needed to support it. In a similar way, the adaptive suspensions may affect the stiffness of the suspension strut and shock absorber changing the wheel kinematics. The brake caliper

size affects the mass and overall size of the remaining block consistent of the knuckle, disc brakes and caliper. Lastly, the wheel size affects the free space for the wheel motion and the styling and material affect the ultimate load and therefore the total force in the wheel load-path. A so-called take-rate is calculated to estimate the most probable combination to be tested also based on the sales volume of the vehicle. Even so, an accurate prognosis cannot be achieved regarding the exact combination of power-train, wheel and other options that the vehicle in the official test will contain.

One of the main differentiators of the Small-Overlap load case is the fact that the suspension and wheel components take a central role in the crash since they represent the main load-path. A certain degree of variability in the metal and other material components will exist. However, the wheel itself is a moving part of the vehicle and therefore its trajectory, brake loads, and impacting location are difficult to predict. The trajectory is mainly controlled by the suspension links, control arms, and attachment points properties. Even if crashworthiness is a central part of vehicle design, the main function of the suspension is not the energy absorption, stiffness or trajectory control of the wheel during the crash. For this reason the properties of the links, control arms and attachment points are mainly driven by the driving dynamics requirements. If a certain wheel kinematic is particularly beneficial to the structural rating, an additional separation force or stiffness requirement may be introduced. The advantage is that even if these suspension requirements are not driven by crashworthiness, the properties of the components and tolerances are known and usually controlled in component tests. Be that as it may, there are variations in properties such as the tire-floor contact and tire-wheel interaction that will also affect the wheel kinematics and the attempt to measure and collect the actual data is impractical. For this last set of uncertainties only an estimation of the variation can be derived and considered in the design process.

6.2.2. Uncertainty Quantification

The relevant parameters' identification conducted in the section above provides the possibility to develop the strategy to characterize each source of uncertainty in the best possible and practical manner. Perhaps the easiest of these strategies is the one concerning the variables related to the hardware test equipment and procedure. State-of-the-art crash test facilities offer the possibility to retrieve and collect the relevant data for each test. As stated before, the relevant variables for this subject are: the difference between the target mass and actual mass of the vehicle tested, the impact velocity, and the initial overlap between vehicle and barrier.

Here, the data on the difference of the target weight and the measured weight at the time of the crash test was collected for more than 200 test vehicles of 3 different test facilities. Even if the data collected is specific to these test facilities, the fact that the industry standards are followed indicates that this variation can be arguably representative for the whole industry. Figure 6.4 shows the reconstructed probability density function, *pdf*. This *pdf* is symmetric and with its mode on 0kg, with a minimum and maximum of ±26kg. The absolute delta value is independent of the specific vehicle weight and dependent as stated before on the availability of the measurement devices. However,

considering a 2 ton. vehicle, this represents a delta of ±1.35% in mass and subsequently also in the initial kinetic energy. The fact that the probability of the weight delta being in the range of ±5kg is >65% reflects the accuracy of the preparation procedures.

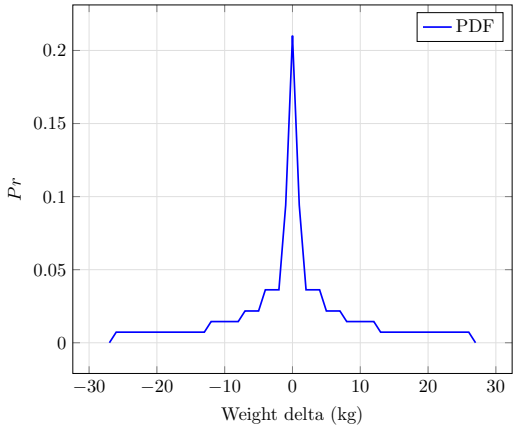

Figure 6.4 Reconstructed PDF vehicle mass delta

The IIHS provides for each of its internally conducted tests the actual impact velocity. This data is presented in Figure 6.5(a). Compared to the vehicle mass delta *pdf*, it can be observed that the impact velocity delta is not symmetric. The protocol allows for a deviation of ±1km/h in the Small-Overlap test. The impact velocity delta has a range of [-0.496 0.224]km/h and due to the unsymmetrical nature of its probability distribution, 70% of the time a slower impact velocity than the targeted can be expected. Starting from a delta of 0km/h in order to contain 60% of the data, a range of [-0.1 0.08]km/h is needed. This range corresponds for a 2 ton. vehicle to a delta of initial kinetic energy of [-0.31 0.25]%, considerably less than the delta of ±3.1% allowed by the protocol considering ±1km/h. A higher velocity means an increase on kinetic energy and therefore higher deformations. From the shape of the impact velocity *pdf* it can be concluded that the acceleration devices used in the test facility are calibrated more towards not exceeding the target velocity rather than being close to it.

Similarly to the mass delta, the barrier position delta from which the initial overlap can be calculated exhibits a symmetrical behavior as shown in Figure 6.5(b). The IIHS protocol states that a deviation of 1% of the vehicle width is allowed. Considering a vehicle of 1860mm in width, a deviation of 1% overlap produces a delta of 18.6mm. The absolute maximum deviation observed from the data collected is ±20mm. According to the barrier y position delta *pdf*, 65% of the data finds itself within ±5mm of the target position. Structural designs with specific topologies that take advantage of the geometry of the Small-Overlap barrier, namely its radius, are particularly sensible to the barrier position delta and therefore its sensitivity should be taken into account in the design.

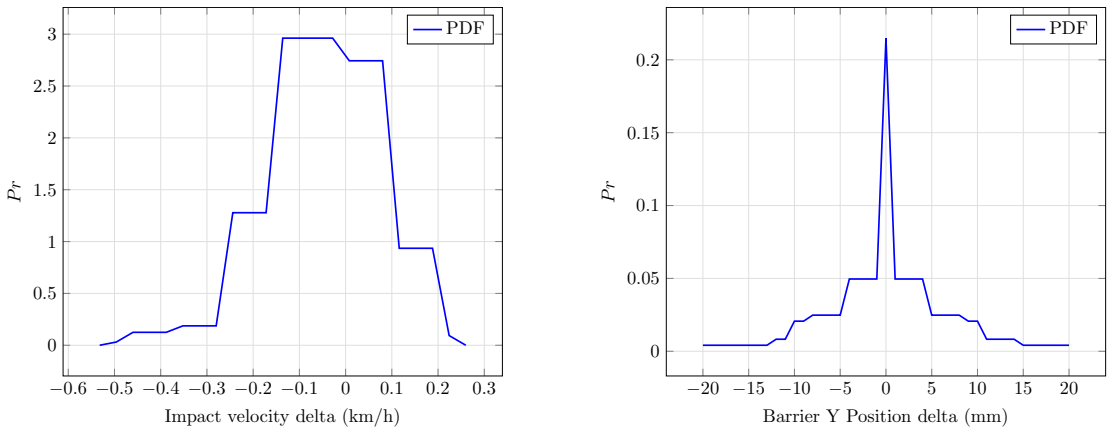

(a) Reconstructed PDF impact velocity delta

(b) Reconstructed PDF barrier y-position delta

Figure 6.5 Hardware test related variation PDF for impact velocity (a) and barrier y position (b)

The next type of uncertainties is related to the vehicle version and options or configuration. The take-rate for each combination can be estimated a priori giving a vague idea of the most probable combination of options that the vehicle chosen to be tested will have. It is often impractical, even in the simulation, to consider all of the probable combinations that a vehicle could have. The approach taken in this work is to limit the relevant factors to the power-train, brake and wheel size, and styling to determine the critical combinations. The AWD configurations include additional components that stiffen the sub-frame also increasing the resistance-to-deformation characteristics of the load-path and in general decreasing the deformations. Therefore, the FWD is considered critical. The brake size has to be considered in combination with the wheel size. Larger brake calipers generally represent larger remaining blocks and intrusions if the wheel remains totally or partially attached during the crash. The wheel size influences the amount of space available to move and rotate. Large wheels are generally more consistent with regards to the rupture mechanism and failure forces. The styling of the wheel also influences the failure forces. The combination of wheel orientation and styling affect the failure loads, therefore it is convenient to include the extreme configurations regarding wheel size and failure forces. Once these critical combinations are determined, it is sufficient to define the estimated take-rates and use them directly to characterize their probability of occurrence by the official test.

The properties of the relevant components that are designed to achieve a certain target such as minimum force before detachment can be characterized by truncated Gaussian distributions for parameters with a symmetrical deviation behavior or skewed distributions for non-symmetrical. The target values are complemented by a minimum and maximum to describe a range in which the property is considered to fulfill the requirement.

This range is used to define the truncation point of the distribution. If these components are subjected to tests for quality control, then the reconstruction of the probability function is trivial. Constant probability functions are reserved for parameters where only the minimum and maximum values are known but no additional information regarding the type of distribution can be obtained. These parameters represent variables for which targets are set upon but which only variate randomly inside a given interval. Examples of these variables that are directly related to the wheel load-path are the tire and rim-bed properties.

These strategies are implemented to characterize the uncertainties. The next step is to develop and implement an efficient sampling mechanism that ensures that three key conditions are fulfilled. One, that the complete range described by the relevant parameter *pdf* is covered. Second, that the interaction between the parameters is also considered together with the combined probabilities. And third, that while maximizing the coverage the sampling mechanism is efficient so that the number of samples to characterize the uncertainty space is minimized. The following section will address these matters of efficient and effective sampling.

6.2.3. Efficient Sampling

The maximization of the parameter range coverage, the minimization of the number of samples to achieve such coverage and the representation of the interaction of the parameters considering their probability functions are the key requirements of the sampling mechanism. There are well-established sampling mechanism such as Optimized Latin Hypercube, OLHC, that offer a certain degree of efficiency. This method is used as a base and is expanded in order to fulfill the additional requirements stated above. Algorithm (8) summarizes the necessary calculations defined in this OLHC expanded sampling scheme. The relevant parameters, RP, and their correspondent *pdf* are read. The first step is to calculate the cumulative density function, *cdf*, for each RP. Then, a normalized set of samples is generated using the OLHC algorithm and an initial random seed. The application of the probability of the RP is done by mapping the normalized space to the real parameter space via its *cdf*. Figure 6.6 shows this mapping operation for two variables v_1 and v_2 with a Gaussian *pdf* with 59 as a mean. The condition that the relevant parameters are independent from each other needs to hold to properly characterize the joint probability of the variables. Once all of the RP have been mapped, the output *cdf* is reconstructed from the samples and compared against the input *cdf*. The deviation from input and output *cdf* is characterized by the Kolmogorov-Distance and the maximum value for all the relevant parameters is named *cdfdev*. Then, a Spearman correlation matrix is calculated to identify any artificial linear and non-linear dependencies among the relevant parameters. Its maximum value is named *corr*. Target values are defined for both error quantification values, *cdfdev* and *corr*, $cdfdev_{allowed}$ and $corr_{allowed}$, correspondingly. The normalized samples set creation, probability mapping, and sampling error quantification are done iteratively until the targets for the error values are achieved, or the maximum number of iterations is reached. In the latter case, the mapped samples set, $samples_{mapped_{best}}$ is reported.

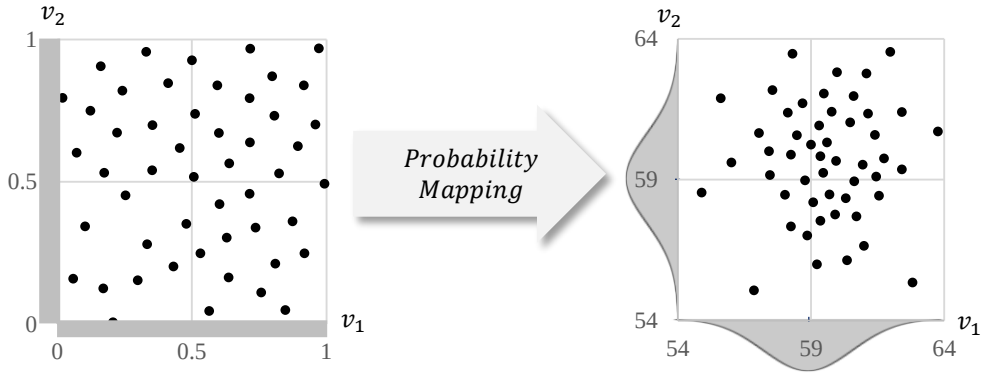

Figure 6.6 Normalized sampling space and mapping of probability of two variables v_1 and v_2

Data: Relevant parameters *RP pdf*, number of samples, Max. number of iterations $iteration_{max}$, Max. *cdf* deviation allowed $cdfdev_{allowed}$, Max. correlation allowed $corr_{allowed}$
Result: Relevant parameter samples
for *each RP* **do**
| Calculate *cdf*
end
for *i in* $iterations_{max}$ **do**
| Generate normalized samples using OLHC and random seed;
| **for** *each RP* **do**
| | Map probability using input *cdf* and normalized samples as input;
| | Set $samples_{mapped_i}$;
| | Reconstruct output *cdf* from samples;
| | Characterize max. deviation $cdfdev_i$ between input and output *cdf* with Kolmogorov-Distance;
| **end**
| Calculate correlation matrix of mapped samples;
| Identify max. correlation $corr_i$;
| **if** $cdfdev_i < cdfdev_{allowed}$ *and* $corr_i < corr_{allowed}$ **then**
| | Return $samples_{mapped_i}$;
| **else if** $cdfdev_i < cdfdev_{best}$ *and* $corr_i < corr_{best}$ **then**
| | Update $cdfdev_{best} = cdfdev_i$;
| | Update $corr_{best} = corr_i$;
| | Save $samples_{mapped_{best}} = samples_{mapped_i}$;
| **else if** $i = iterations_{max}$ **then**
| | Return $samples_{mapped_{best}}$;
end

Algorithm 8: OLHC Sampling mechanism with probability mapping and sampling error minimization

The amount of samples should be minimized in order to accelerate the analysis since the simulation of a full vehicle FE model can be costly. Therefore, an optimum number of samples, meaning the minimum number of samples that fulfill the sampling error requirements, is beneficial to estimate. The optimum number of samples depends on two factors: (i) the amount of relevant parameters to sample and (ii) the complexity of the input pdf. The amount of RP increases the needed samples as well as the increased complexity of the pdf. In this problem statement a pre-study is conducted to empirically find this optimum.

6.2.4. Robustness Quantification

In Section 2.6.3, several methods for robustness quantification were introduced. Each of these definitions may be more appropriate for certain applications. The first aspect considered to derive the characterization of robustness or robustness index, RB_I, is its capability of application for the type of quantities relevant to this problem statement. In this work, two types of quantities need to be analyzed. The first relates to scalar values such as degrees of freedom of displacements or velocities, forces, energy and abstract quantities such as the glance-off value. These scalar values are snapshots of the vehicle state at a relevant time point. The second type of quantities are curves describing the scalar values mentioned before. Characterizing the robustness at several time points gives an indication if a bifurcation occurs and when in time such event happens. The following robustness index definition offers the advantage of being able to characterize the robustness at a certain point in time as well as throughout the complete crash duration.

The second aspect considered to derive the robustness index is its flexibility to be defined as a means to compare the obtained distribution quantities to a target distribution. Different amount of variability is expected from the relevant quantities. Therefore, it is advantageous to include this variability in the robustness index target definition. Additionally through a more strict definition, an implicit prioritization can be imposed in the quantities to study. Namely if a quantity is of critical importance, its variability should be smaller compared to the others and consequently an acceptable robustness index should be more difficult to achieve.

The third aspect considers the fact that in praxis, the amount of data that can be generated to evaluate its robustness is costly and tends to be relatively scarce. For this reason an approximation of the probability distribution based on the available data is generated assuming a given distribution type and then this approximation is compared against the target distribution. This approximation efficiently recreates the expected distribution of the relevant quantities with a relatively reduced amount of data giving the possibility to characterize the robustness of a certain quantity without performing a costly amount of experiments. The following subsections will provide more details on the derivation of the robustness index.

6.2.5. Robustness Index

One of the key factors of the proposed robustness index is that it is based on a comparison to a target distribution. Meaning that the robustness index is the Kolmogorov distance between the approximation of the probability density function of the quantity to study and the target distribution. This offers the advantage to represent the robustness index as a scalar quantity from -1 to 1. The first possibility is a negative robustness index indicating that the approximation of the *pdf* of the samples is more spread out than the target distribution, meaning that the required robustness was not achieved. The second possibility is a robustness index with a value of zero, that indicates that the approximation *pdf* of the samples and the target distribution are exactly as spread out, meaning that the robustness target was precisely achieved. The third possibility is to have a robustness index larger than zero. This means that the robustness target was achieved and that the approximated *pdf* of the samples has less variability than the target distribution. The larger-than-zero case and smaller-than-zero case are presented in Figures 6.7 and 6.8 for the toepan and steering column intrusion points respectively.

To calculate the robustness index of a given set of samples contained in a vector $Y_{current}$, the first step is to determine the target distribution. Considering the risk-management-nature of the problem stated, a minimum number of experiments or acceptable percentage of target achievers, $TA_{acc_{\%}}$, that fulfill the requirements is specified. Additionally, a virtual requirement can be considered as the fulfillment of the condition that the value must lie inside a given range defined by a lower value, lim_{l_t}, and an upper limit, lim_{u_t}. It is convenient to define such range as a function of a deviation from a reference value, ref. Therefore, the target distribution is here the distribution that contains a certain percentage of target achievers inside a given range $[lim_{l_t}, lim_{u_t}]$. After the assumption of *pdf* for the output quantities to be analyzed, the standard deviation can be calculated. Assuming for example a normal distribution with a *cdf* with probability $Pr(x)$ of

$$Pr(x) = \frac{1}{2}\left(1 + \text{erf}\left(\frac{x-\mu}{\sigma/\sqrt{2}}\right)\right), \tag{6.8}$$

and by replacing the mean μ by ref, the x by lim_{l_t} and the probability Pr by $(1 - TA_{acc_{\%}})/2$ (taking advantage of the symmetry of the distribution) an expression is obtained to describe the standard deviation of the target distribution σ_t as a function of $TA_{acc_{\%}}$, ref and the range $[lim_{l_t}, lim_{u_t}]$.

$$\sigma_t = \frac{lim_{l_t} - ref}{\sqrt{2}\,\text{erfinv}(-TA_{acc_{\%}})}, \tag{6.9}$$

The standard deviation σ_t defined in Eq. (6.9) is then used to reconstruct the *cdf* of the target distribution, cdf_t. The next step is to define the *pdf* approximation of the available data contained in $Y_{current}$ assuming the same type of probability function as the target distribution. The base for this calculation is $TA_{acc_{\%}}$. The absolute distances of all of the samples contained in $Y_{current}$ to ref are calculated. The distances are sorted starting with the smallest one. One by one the distances are collected until $TA_{acc_{\%}}$ percentage of

the total amount of samples of $Y_{current}$ are aggregated. The sample value corresponding to this last distance is then taken as the upper and lower limits $[lim_{l_s}, lim_{u_s}]$ assuming a symmetrical range with ref exactly in the middle. Then, in the same manner as with the target distribution, the standard deviation of this distribution approximation, σ_s, is calculated assuming the same distribution type and considering $TA_{acc_{\%}}$. Subsequently, the *cdf* of the approximated sample distribution, cdf_s, is reconstructed and the Kolmogorov distance between it and the target distribution is calculated and represented by RB_I. Algorithm (9) summarizes the steps to calculate the robustness index.

As stated in the Algorithm (9), the input quantities to calculate the RB_I of a given set of values are the reference value, ref, and the target distribution characteristics $TA_{acc_{\%}}$, $[lim_{l_t}, lim_{u_t}]$. The strategy to define the target distribution characteristics was stated at the beginning of this section. However, the ref can be defined according to the type of data set and the analysis to conduct. On the one hand, for quantities that are relevant to the problem statement such as total moments in the vehicle structure, velocities or t_{end} that do have an effect on the total outcome but are not critical for the fulfillment of the requirements defined at any level, it is convenient to define a ref that allows us to monitor them but at the same time is flexible and automatically available for each simulation set. The mean of the parameter set $Y_{current}$ fulfills such conditions. On the other hand, for quantities that are critical to the outcome and that can be related to a specific target; i.e. θ_z, GV_P, s_L or RKE; the ref value can be defined also as a target around which the data set can oscillate within certain limits defined complementary by $TA_{acc_{\%}}$. The key factors to determine which approach to take are first to define if the variable has to reach a given target or if it is considered a monitoring variable. And second, if the objective of the assessment is to evaluate the robustness of the models or to evaluate the robustness of the models and target fulfillment.

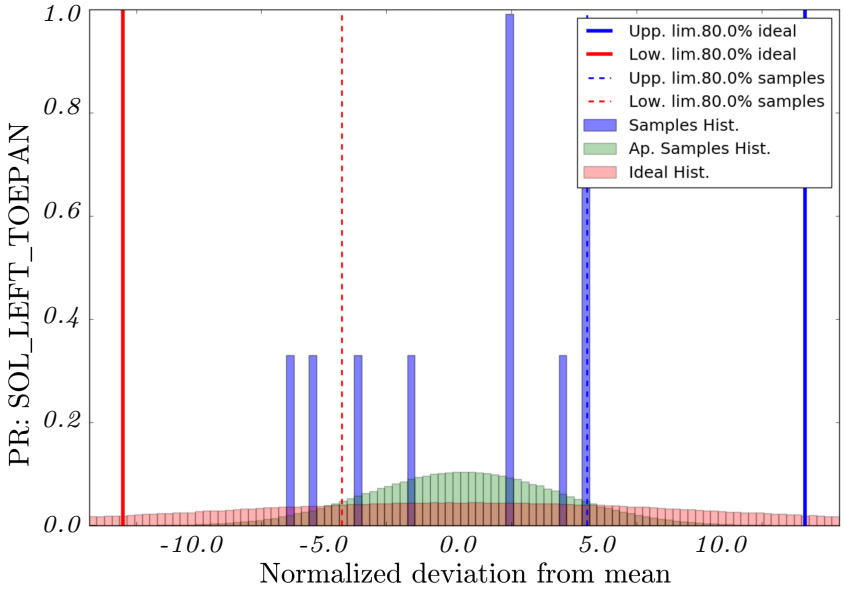

(a) Samples histogram, approximated samples PDF, ideal PDF and 80% ideal and samples limits

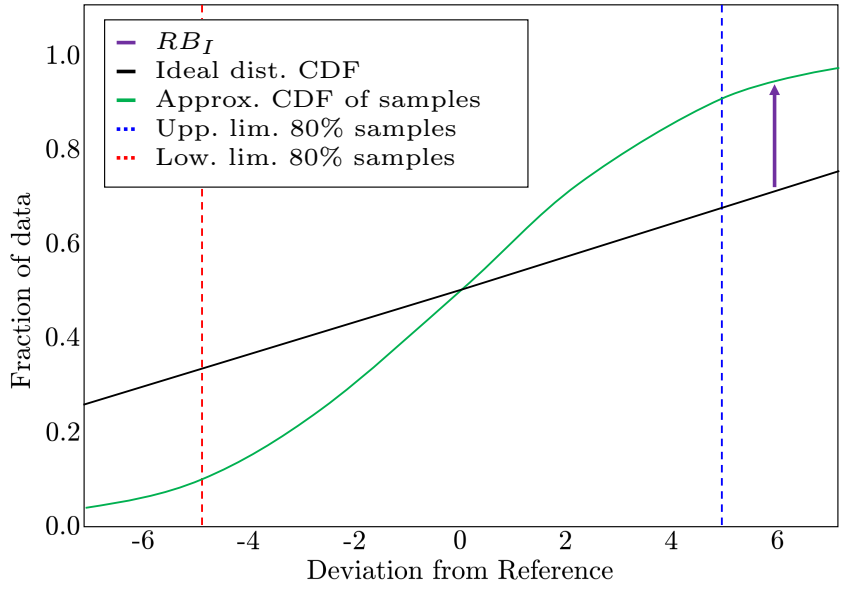

(b) Samples CDF, approximated samples CDF, ideal CDF; 80% ideal and samples limits, and Kolmogorov distance between approximated samples CDF and ideal CDF

Figure 6.7 Probability density function (a) and cumulative density function (b) are depicted to show the Kolmogorov distance for the intrusion point left toepan presenting a $RB_I = 0.456 > 0$)

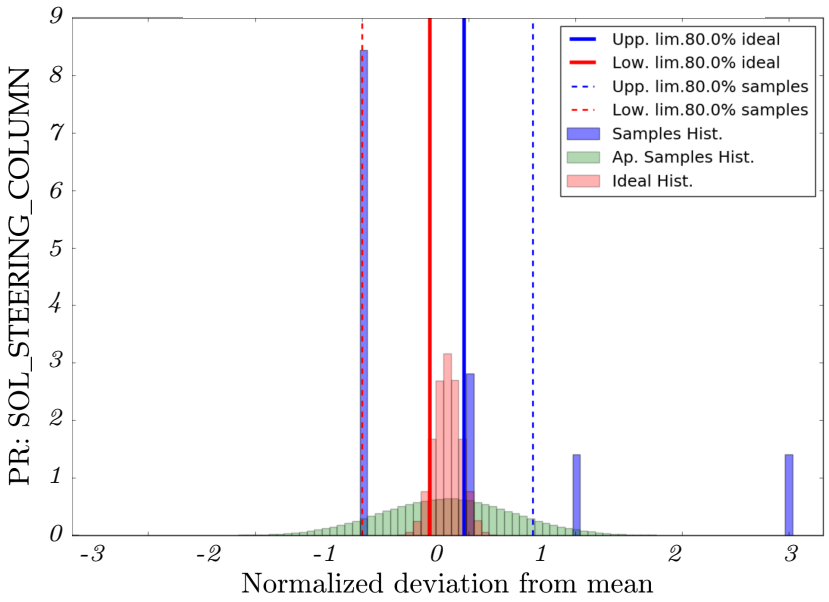

(a) Samples histogram, approximated samples PDF, ideal PDF and 80% ideal and samples limits

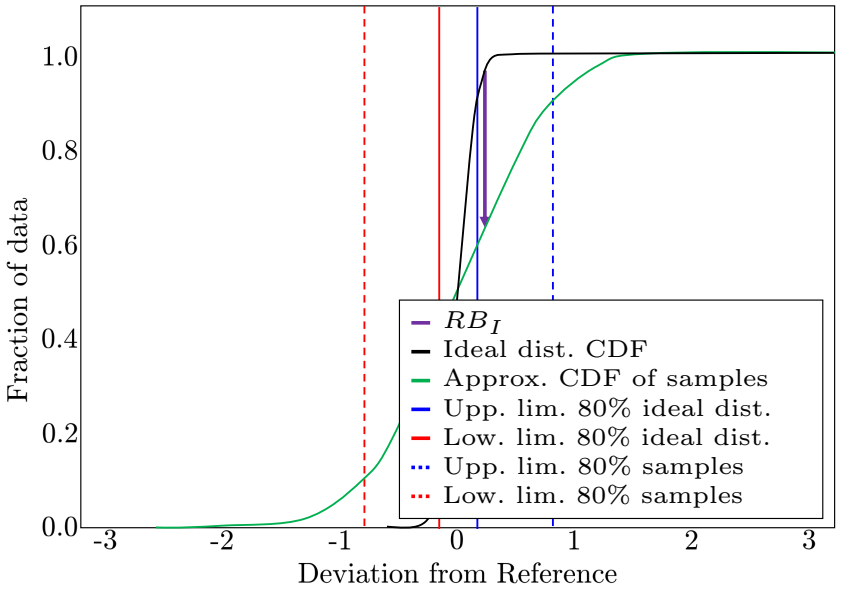

(b) Samples CDF, approximated samples CDF, ideal CDF; 80% ideal and samples limits, and Kolmogorov distance between approximated samples CDF and ideal CDF

Figure 6.8 Probability density function (a) and cumulative density function (b) are depicted to show the Kolmogorov distance for the intrusion point steering column presenting a $RB_I = -0.647 < 0$

The definition of a ref becomes of particular interest when analyzing a complete time series of a given quantity. Figure 6.9(a) shows the example of the time series of total moment, M_z, in the vehicle structure for a set of 10 simulations where a variation of the time-step was performed in order to investigate the numerical stability of the finite element model. For this case, a deviation of 20% from the reference to calculate [lim_{l_t}, lim_{u_t}], a $TA_{acc_{\%}} = 80\%$, and a ref defined as the mean of the maximum values for each of the 10 simulations are selected to generate a global target distribution cdf_t. For each point in time, the cdf_s is approximated and compared against the global cdf_t using the Algorithm (9) to calculate the RB_I. As seen in Figure 6.9(a), the [lim_{l_t}, lim_{u_t}] are constant. One alternative to this approach would have been to have at each point of the time series a local cdf_t. However, this would mean that small variations among the 10 samples specially at the beginning and at the end of the time series (regions with less relevance) would have dominated the RB_I calculation. This can be done if it is of particular interest to analyze the small variations of the time series specially at the beginning. Nonetheless, the current problem statement requires the characterization of the global behavior observed in the time series. With this approach in mind, it can be observed in Figure 6.9(b) that the RB_I time series is closer to the value of 1, indicating a robust behavior at the beginning of the time series. This instinctively coincides with the fact that at the beginning of the crash, the small changes brought by the variation of the time-step have not produced a large enough impact on this quantity. Approximately at 60ms the RB_I reaches its lowest value coming closer to 0. This indicates that at this point in time the small numerical variations have produced a large enough impact to be detected by the RB_I analysis. In the last part of the time series, the RB_I retakes its tendency towards 1, due to the fact that the quantity in the simulations moves towards zero.

For quantities that are the result of a cumulative operation, i.e. a time integration, the RB_I may only decay. An example of this behavior is shown in Figure 6.10. For this case, the robustness index at the end of the time series takes the most relevance. However, for this problem statement, and for the relevant kinematic parameters, the robustness index is calculated either considering the maximum values in the time series or the value at the t_{end}.

Input: reference value: ref & target distribution characteristics: $TA_{acc_{\%}}$, $[lim_{l_t}, lim_{u_t}]$
Output: Robustness index: RB_I, standard deviation of target and approximated distributions σ_t,σ_s and limits for approx. distribution $[lim_{l_s}, lim_{u_s}]$
Data: samples: $Y_{current}$
SD Target Distribution SDTD($TA_{acc_{\%}}$, $[lim_{l_t}, lim_{u_t}]$):
  $\sigma_t = (lim_{l_t}\text{-}ref)/(\sqrt{2}\text{erfinv}(-TA_{acc_{\%}}))$
  return σ_t

SD Approximated Distribution SDAD($Y_{current}$, $TA_{acc_{\%}}$):
  Calculate distance of samples to reference
  for *each* $Y_{current}$ **do**
    distances(i)=abs($Y_{current}$(i)-ref)
  end
  Sort distances
  $distances_{sorted}$ = sort(distances)
  Identify lim_{u_s}
  $current_{\%} = 0\%$
  i = 0
  while $current_{\%} < TA_{acc_{\%}}$ **do**
    $lim_{u_s} = ref + distances_{sorted}(i)$
    $current_{\%}$ = i/length($distances_{sorted}$) i+=1
  end
  $lim_{l_s} = ref\text{-}(lim_{u_s}\text{-}ref)$
  $\sigma_s = (lim_{l_s}\text{-}ref)/(\sqrt{2}\text{erfinv}(-TA_{acc_{\%}}))$
  return σ_s

Robustness Index RB_I(σ_s, σ_t):
  SDTD($TA_{acc_{\%}}$, $[lim_{l_t}, lim_{u_t}]$)
  SDAD($Y_{current}$, $TA_{acc_{\%}}$)
  cdf_t: Reconstruct target distribution cdf using σ_t
  cdf_s: Reconstruct approximation distribution cdf using σ_s
  RB_I = Kolmogorov-Distance(cdf_t,cdf_s)
  return RB_I
return

Algorithm 9: Calculation of robustness index

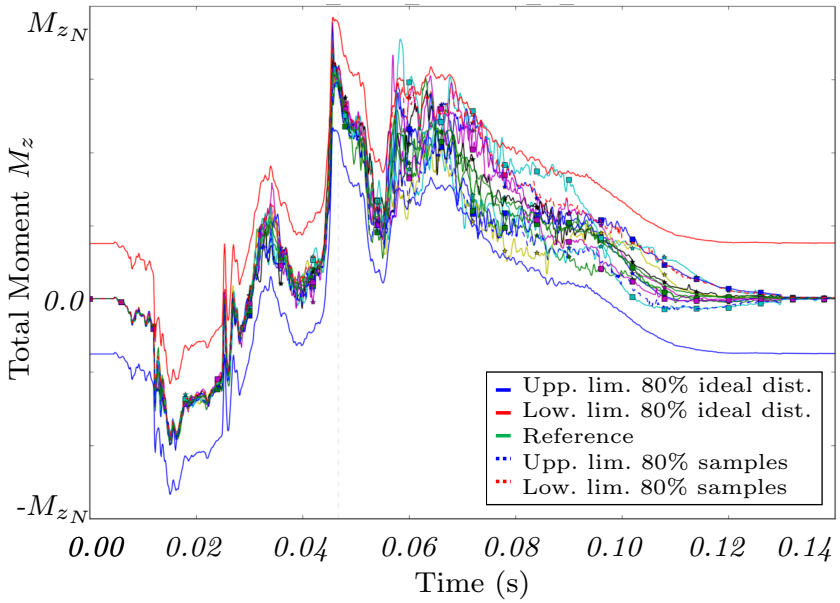

(a) Total M_z time series of 10 simulations taken from the numerical uncertainty analysis (not included in the legend), upper and lower limits for the approximated samples distribution as well as the ideal distribution, and reference curve calculated as the average of the 10 simulations

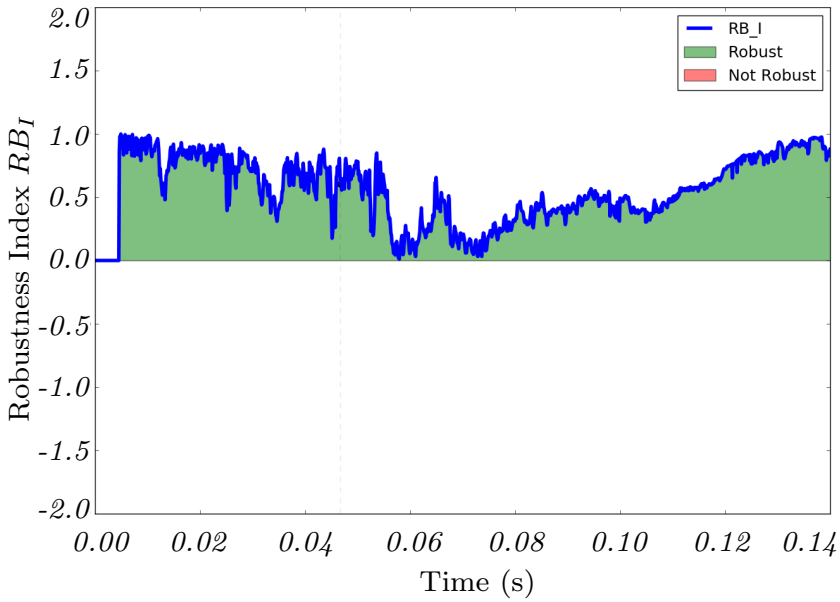

(b) RB_I of total M_z time series

Figure 6.9 Time series of the total moment M_z (normalized by M_{z_N}) for a set of 10 simulations (a) including its resulting RB_I time series (b)

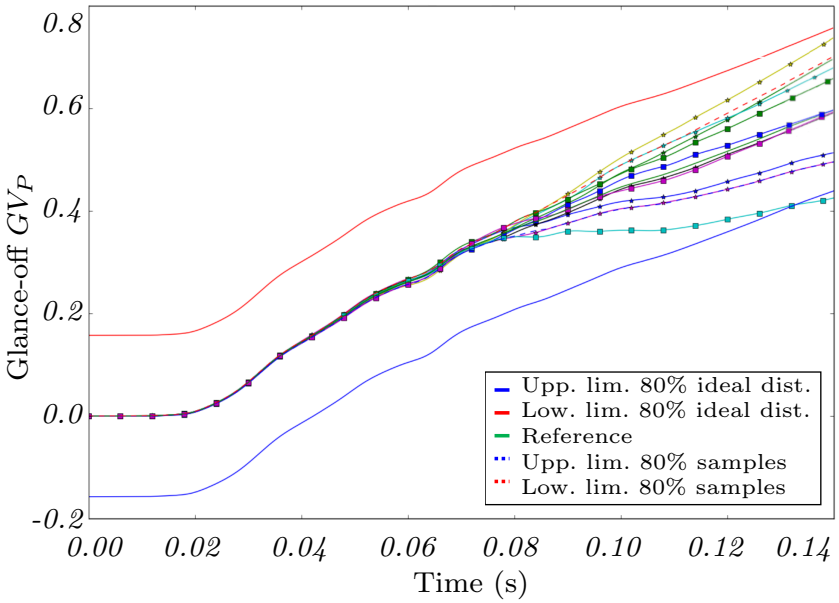

(a) Total glance-off value time series of 10 simulations taken from the numerical uncertainty analysis (not included in the legend), upper and lower limits for the approximated samples distribution as well as the ideal distribution, and reference curve calculated as the average of the 10 simulations

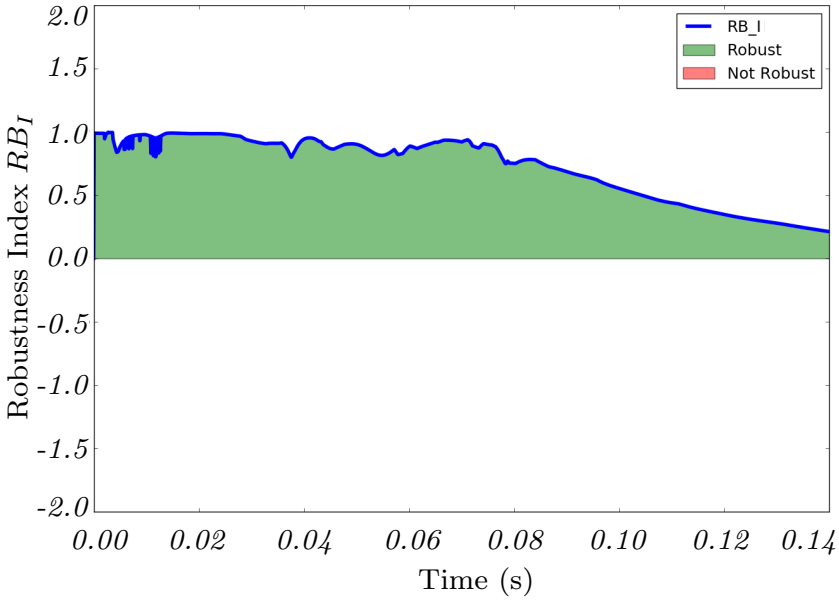

(b) RB_I of glance-off value time series

Figure 6.10 Time series of the glance-off value for a set of 10 simulations (a) including its resulting RB_I time series (b)

6.2.6. Re-visiting the Solution Space

As stated previously, the robust fulfillment of the requirements in the virtual design phase, maximizes the chances of obtaining a successful result in any of the subsequent hardware tests. Both aspects, the fulfillment and the robustness are the drivers of the iterative simulation scheme. On one hand, the fulfillment of the solution space is measured by the SSDOF according to the agreement of the force-displacement curves and their corresponding upper and lower limits. On the other hand, the robustness index characterizes the variability of the outcome including the sources of uncertainty in the simulation set. The two aspects can be understood as a way to characterize if a given signal exists inside a range either defined by the backwards calculation in the force-displacement space or by the target distribution for any other output signal. The use of this simulation scheme until convergence and therefore robust fulfillment of the requirements makes the virtual design phase more effective and efficient.

Chapter 7

Validation of Kinematic Model and Solution Space

The essence of the methodology presented in this work lies in the low-fidelity kinematic model and its use in the calculation of solution spaces of the resistance-to-deformation characteristics at the full-vehicle and load-path levels. In this section, both approaches are validated by comparing the results using real crash data. First, the vehicle trajectory and kinematic parameters of a Small Overlap crash are compared with the vehicle trajectory and kinematic parameters of the reconstruction of the same crash using the low-fidelity kinematic model. The trajectory is calculated using the resistance-to-deformation characteristics, RDC, directly extracted from the analyzed crash event. The validation of the kinematic model approach is presented in Section 7.1. Second, the solution space methodology is validated by comparing the RDC that are produced by the solution space calculation with a set of constraints defined upon the kinematic parameters that result in the same vehicle trajectory as the crash event used as reference. The solution space calculation is carried out at the full-vehicle and load-path level and presented in Section 7.2.

The Figure 7.1 presents the validation scheme of both methodologies. The starting point of the validation of the kinematic model is the analysis of the crash event recorded data in the form of acceleration and rotational velocity time series of the vehicle's body in white, BIW, and the force signals time series obtained from the force measurement barrier. The acceleration and rotational velocity signals are post-processed in the trajectory reconstruction procedure. The acceleration signals originally collected in the sensor and therefore vehicle local coordinate system are rotated according to the rotational velocity signals and initial position of the sensor in order to produce an acceleration signal in the global coordinate system. This global acceleration signal is numerically integrated with respect to time to first obtain the velocities and then the displacement of the center of gravity CG, where the sensor is located in the vehicle. Similarly, the rotational velocity signal is also transformed into the global coordinate system and used to represent a complete 3-D rigid body motion of the vehicle. The result of the trajectory reconstruction

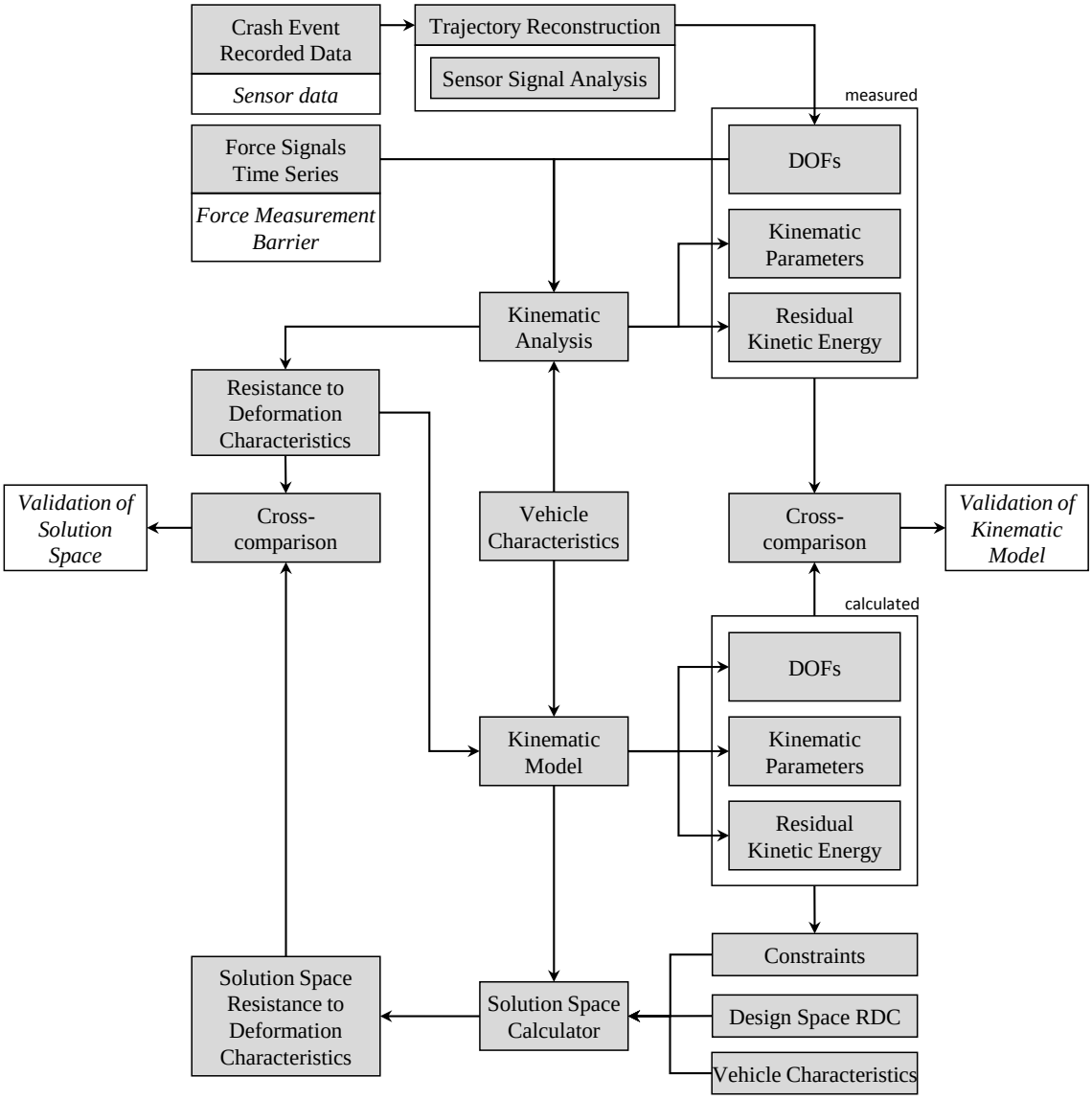

Figure 7.1 Validation framework

procedure, together with the force signal is used as an input for the kinematic analysis which produces as output the relevant DOFs, i.e. 2-D displacements and rotation of the CG: u_x, u_y and θ_z. Additionally, the kinematic analysis uses the DOFs to calculate the kinematic parameters $\boldsymbol{\sigma}$, i.e. glance-off value GV_P, total vehicle rotation, $\theta_{z_{t_{end}}}$, residual deformation length, RDL or $s_{L_{t_{end}}}$ and residual kinetic energy, RKE. The last output of the kinematic analysis are the RDC at the full-vehicle: longitudinal F_{x_L} and transversal F_{y_L} forces and the equivalent point of application of the total longitudinal force, Y_{eq}; and at the load-path level: longitudinal, $F_{x_{LP_j}}$, and transversal, $F_{y_{LP_j}}$, forces. The second phase of the validation of the kinematic model consists of using the RDC extracted from the previous step and together with the vehicle intrinsic and extrinsic characteristics defined in Section 4.1.1 performing the $Forwards - Calculation$ to obtain the correspondent vehicle kinematic response. Finally, the two sets of DOFs and kinematic parameters coming from the crash event analysis and from the kinematic model $Forwards - Calculation$ are compared and the error is quantified, which confirms the capability of the low-fidelity kinematic model of condensing the mechanical phenomenon of the crash to its essence and reproduce, to a certain degree and with reduced calculation costs, the vehicle trajectory as in the real crash event.

The validation of the solution space calculation uses as input constraints that describe the same kinematic behavior as the analyzed crash test, i.e. $\theta_{z_{t_{end}}}$, RDL, RKE and GV_P, as well as the vehicle characteristics of the test and a design space for the RDC. As presented in Section 5.1 a set of upper and lower limits of the RDC is the outcome of the solution space calculator. The comparison is carried out at both, full-vehicle and load-path level. At the full-vehicle level, the RDC extracted from the crash, F_{x_L}, F_{y_L}, Y_{eq} are compared against the upper and lower limits that describe the solution space, $\hat{F}_{x_{FV}}$, $\check{F}_{x_{FV}}$, $\hat{F}_{y_{FV}}$, $\check{F}_{y_{FV}}$, $\hat{Y}_{eq}$, $\check{Y}_{eq}$. At the load-path level, the longitudinal and transversal forces for each load-path j (F_{x_L} and F_{y_L}), are compared against the solution space $\hat{F}x_{LP_j}$, $\hat{F}y_{LP_j}$, $\check{F}x_{LP_j}$, $\check{F}y_{LP_j}$. The fact that the RDC from the crash lie inside the solution space establishes the capacity of the solution space calculator to find RDCs that correspond to a given kinematic behavior at both levels.

The validation procedures were conducted using data from an internal BMW Small Overlap test following the IIHS protocol. The vehicle tested is a sedan with the characteristics described in Table 7.1. The intrinsic characteristics: A-Pillar position, AP_x, AP_y, the frontal structure length or longitudinal distance from the A-Pillar to the barrier, s_L, and the barrier position B_y as well as the load-path positions LP_x, LP_y, are expressed using a standard global coordinate system where the front wheel axis is located at x=0. The extrinsic vehicle characteristic, total mass M_v was measured directly from the vehicle. The center of gravity position, CG_x, was derived from the weight distribution of the front and rear axles, while CG_y is assumed to be exactly at the middle of the vehicle, implying CG_y=0. Finally the rotational inertia around the z axis I_{zz} was estimated using a FE model. The force levels are presented in a normalized format, taking as reference the maximum total force in the F_x time series and represented by F_N.

Table 7.1 Vehicle characteristics

Characteristic	**Variable**	**Value**
Intrinsic		
A-Pillar position	AP_x, AP_y	*567, -774 mm*
Barrier position	B_x, B_y	*-792, -457 mm*
Distance A-P to the barrier	s_L	*1360 mm*
LP position Wheel-Firewall-Rocker	LP_{x_1}, LP_{y_1}	*567, -774 mm*
LP position Shotgun	LP_{x_2}, LP_{y_2}	*567, -758 mm*
LP position Bumper beam-front rail	LP_{x_3}, LP_{y_3}	*567, -421 mm*
LP position Sub-frame	LP_{x_4}, LP_{y_4}	*567, -422 mm*
Extrinsic		
Vehicle Total Mass	M_v	*1800 kg*
Rotational Inertia around z axis	I_{zz}	*3340740 kg mm^2*
Center of Gravity position	CG_x, CG_y	*1415.24, 0.0 mm*

7.1. Kinematic Model

The validation of the low-fidelity kinematic model starts with the extraction of the functional properties or *RDC* in the form of force-displacement curves and the reconstruction of the vehicle trajectory and kinematic DOFs (u_x, u_y, θ_z). These signals are further used to calculate the kinematic parameters that are then compared against the results from the kinematic model.

7.1.1. Trajectory Reconstruction

The trajectory reconstruction uses the information produced by two sensors located at the vehicle's *CG*: the accelerations and rotational velocities. The normalized raw data is shown in Figure 7.2(a,b). As presented in Section 3.1.1, the transformation of the signals from local-sensor coordinate system to the global coordinate system is carried out by using the simultaneous orthogonal rotations theorem. At each time point available, the coordinate system of the sensor is rotated by integrating in time the local rotational velocity vector $\dot{\theta}_L = [\dot{\theta}_{x_L}, \dot{\theta}_{y_L}, \dot{\theta}_{z_L}]$. Likewise, the acceleration vector is rotated using the same rotational matrix used for the rotational velocity, $\ddot{u}_L = [\ddot{u}_{x_L}, \ddot{u}_{y_L}, \ddot{u}a_{z_L}]$. The global signals are presented in Figure 7.2(c,d), which show the dominance of the $\ddot{u}_{x_L}$ and $\ddot{u}_{y_L}$ accelerations and $\dot{\theta}_{z_L}$ rotational velocity, justifying the 2-D planar motion simplification used in the analysis.

After obtaining their global representation, the signals are integrated to obtain the correspondent velocities and displacements. The DOFs: u_x, u_y and θ_z obtained by the trajectory reconstruction are presented in Figure 7.12. These displacements and rotation of the *CG* are used afterwards as described in Sections 3.1 and 4.1.2 to obtain the resistance-to-deformation characteristics, represented at the full-vehicle level by $F_{x_L}(s)$,

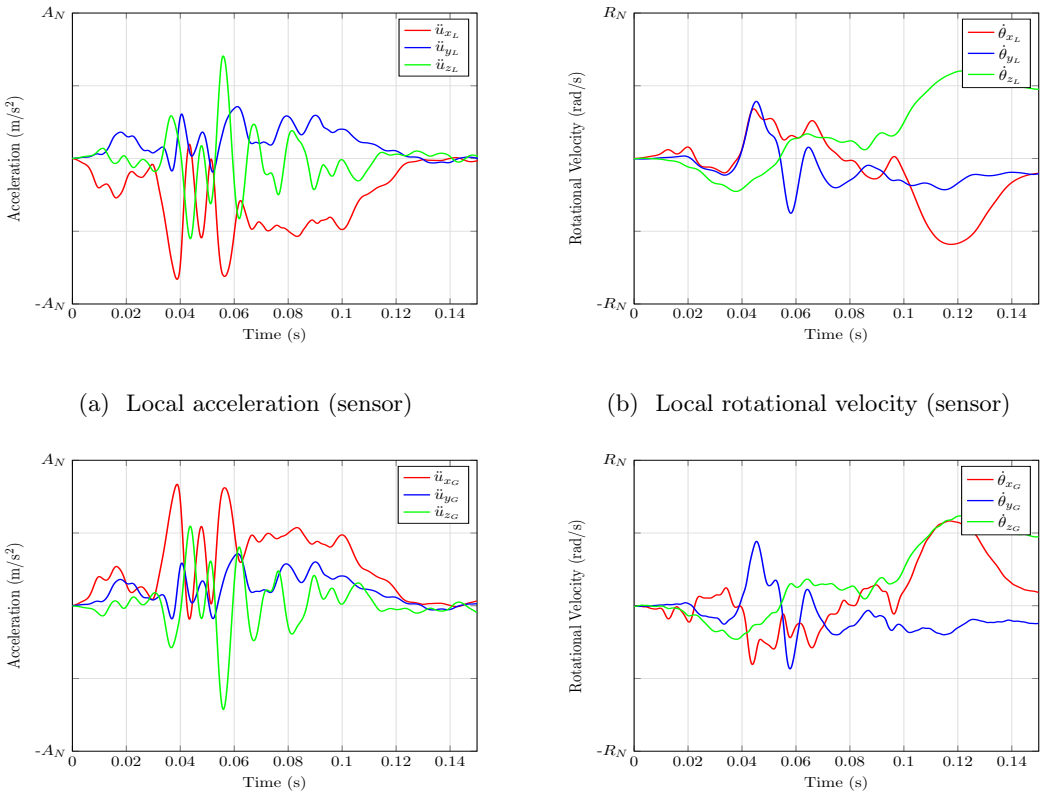

(a) Local acceleration (sensor)

(b) Local rotational velocity (sensor)

(c) Global acceleration

(d) Global rotational velocity

Figure 7.2 Time series of the sensor acceleration, normalized by A_N, (a) and sensor rotational Velocity, normalized by R_N, (b) and global acceleration (c) and global rotational velocity signals (d)

$F_{y_L}(s)$, and $Y_{eq}(s)$ and at the load-path level by $F_{x_{LP_j}}(s_j)$ and $F_{y_{LP_j}}(s_j)$, which are used in a subsequent step as input for the low-fidelity kinematic model. Additionally, the u_x, u_y and θ_z extracted from the test are used as reference to calculate the error with the DOFs obtained from the kinematic model.

7.1.2. Force Time Series Analysis

A state-of-the-art force-measuring barrier was used in this hardware test. The force-measuring barrier has 60 cells, 12 along the vertical direction and 5 along the horizontal direction which are capable of measuring normal and transversal forces. In a later step using the positions of the load-paths in the vehicle structure it is determined which group of cells contributes to the total force of each load-path. The time series of the sum of the force along the longitudinal, F_{x_G}, and transversal, F_{y_G}, global axis are presented in Figure 7.4. It can be observed that the dominant component is the force acting along

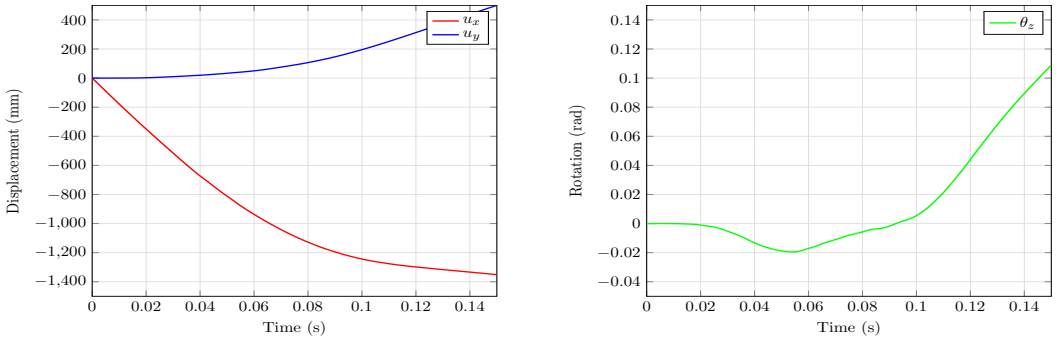

(a) Global longitudinal and transversal displacements

(b) Global rotation

Figure 7.3 Time series of the global longitudinal, u_x and transversal u_y displacements (a) and rotation around z axis, θ_z (b)

the longitudinal axis, F_{x_G}, which coincides also with the observations made regarding the acceleration measurements presented previously. For the first 20 ms, F_{x_G} and F_{y_G} increase in a similar manner. On one side, after reaching a local maximum, F_{y_G} starts to decrease until 85 ms when the second local maximum is reached. On the other side, F_{x_G} continues to increase until 30ms where a significant drop in the force level is observed. Afterwards, the F_{x_G} increases reaching a maximum at 55ms and observing a relatively constant force level until 80 ms when the signal decays. The curve characteristics observed in the time series are directly related to the topology of the structure and load-paths, i.e. position of components and orientation. The transformation from the time to space representation provides more insight on this spatial-force-level correlation. In the next section, these force-time series in combination with the previously obtained displacements and rotations are used to recreate the RDC, i.e. force-displacement and force-application-point-displacement curves.

7.1.3. Kinematic Analysis

The objective of the kinematic analysis is to use the reconstructed trajectory in the form of the DOFs u_x, u_y, and θ_z to calculate the kinematic parameters: rest kinetic energy, RKE, glance-off value, GV_P, rest deformation length, s_L. To achieve this, the correspondent position vectors, displacements and rotations are calculated according to the methodology presented in Section 3.2. The values of the kinematic parameters obtained at the end of crash, t_{end}, are presented in Table 7.2, while the time series representation is presented in Figure 7.12. The crash is classified as a deformation mode since a minimum deformation length of $s_{L_{t_{end}}}$ or rest deformation length of, RDL, 160mm is reached before the vehicle has reached a GV_P=1 as observed in Figure 7.12(b,c). The vehicle reaches its RDL at 112ms and from then on starts the rebound phase, which also

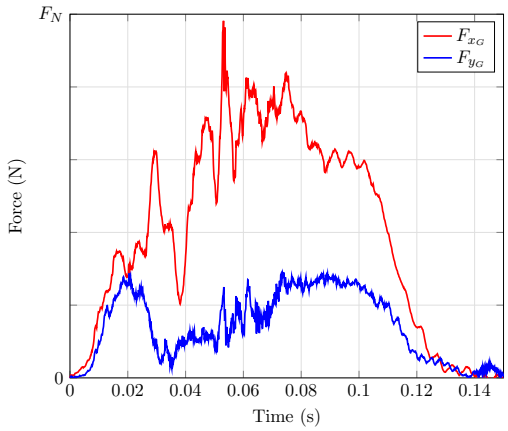

Figure 7.4 Time series of the global longitudinal F_{x_G} and transversal F_{y_G} forces

can be understood as the deformation velocity $ds_{\%}/dt$ reaching zero. The kinetic energy at the end of the crash, RKE, reaches a value of 13%. This value, in context of the data analysis performed using the available IIHS tests presented in Figure 5.11, finds itself at the lower end of RKE values. The structural rating Good and a safety distance of D_{SG}=31% of this crash test positions this vehicle in the industry standard range. The relatively high energy absorption indicates the need of structural components capable of delivering such performance which in many cases translates into additional mass in the structure, opening the possibility for further optimization. In the next sections, the position vectors describing the trajectory of the load-paths are used to calculate the local deformation lengths and the projection regions onto the barrier. The deformation lengths are used in the next section to characterize the resistance-to-deformation characteristics at the full-vehicle and load level.

Table 7.2 Kinematic parameters

Kinematic quantity	**Value**
Crash End	*112ms*
Rest Kinetic Energy	*13 %*
Total Vehicle Rotation	*2.6°*
Glance-off	*0.65*
Rest Deformation Length	*160mm*

7.1.4. Extraction of Resistance-to-Deformation Characteristics

Using the force-time series presented in Figure 7.4 and calculating the shortening of the deformation length, s, at the full-vehicle level, the force signal is mapped to the

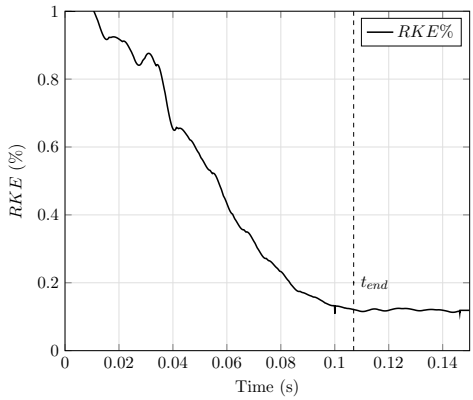

(a) Rest kinetic energy percentage

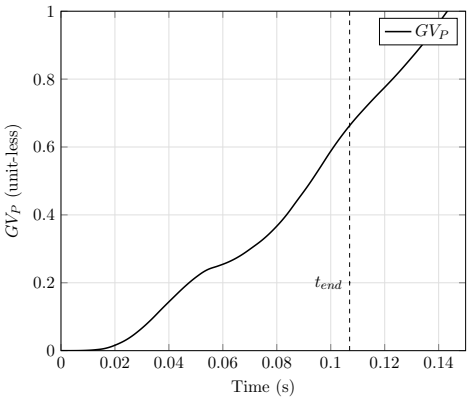

(b) Glance-off value

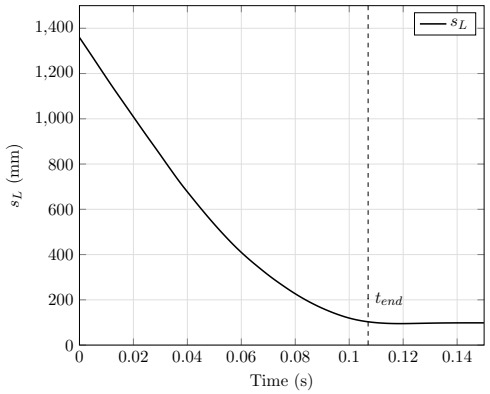

(c) Rest deformation length

Figure 7.5 Kinematic parameters: rest kinetic energy, RKE (a), glance-off value, GV_P (b), rest deformation length, s_L (c)

displacement space. The result of the mapping for the transversal and longitudinal forces is shown in Figure 7.6(a). As stated before, the mapping allows for the interpretation of the force levels with the components in the structure that produce them. Figure 7.6(b) shows a side view of the vehicle structure to scale. The characteristic of the force curve observed previously is also present in its displacement-space representation. The initial increase of the force levels until 400mm is related to the deformation of the components positioned in front of the wheel, e.g. bumper and support-frame. From 400mm to 600mm the barrier contacts the wheel and pushes it towards the rocker and firewall structures. From 600mm onwards the force levels are dominated by the interaction of the barrier, wheel and rocker-firewall structures. The maximum force level observed in F_{x_L} can be explained by the rupture load of the wheel.

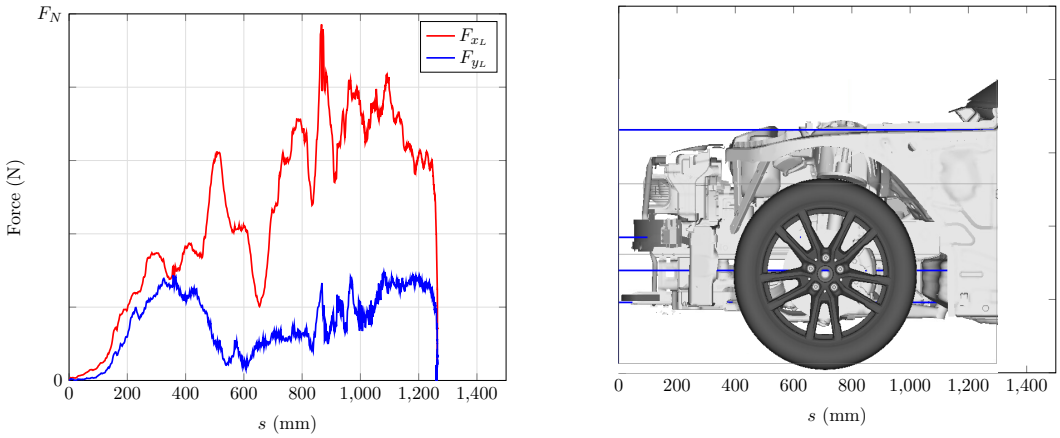

(a) Longitudinal and transversal forces at full-vehicle level vs. deformation space (s)

(b) Undeformed vehicle structure side view vs. deformation space (s)

Figure 7.6 Full-vehicle longitudinal and transversal forces: F_{x_L}, F_{y_L} (a) and undeformed vehicle structure side view (b)

At the full-vehicle level a key simplification is the consideration of an equivalent point of application of longitudinal force, Y_{eq}, which is also a function of the local longitudinal deformation. This implies that the different components across the structure and along the transversal axis produce different load-levels and combined with different positions along the y axis, produce a variable lever arm for the longitudinal forces. As stated previously, the lever arm of the transversal forces is considered directly as the local longitudinal distance between the barrier and the rigid portion of the vehicle. Figure 7.7(a) shows the normalized Y_{eq} extracted by the test using the 60 cells available in the barrier and relative positions to the vehicle. A Y_{eq}=1 implies that the point of application of the transversal force occurs at the most inwards possible location, i.e. 25% of the vehicle with relation to the vehicle centerline, which also corresponds to By at the barrier's side at the beginning of the crash. In contrast, Y_{eq}=0 means that the longitudinal force is applied at the most outwards possible location in the structure having contact with the barrier. The Y_{eq} is expressed in the local coordinate system of the vehicle. Comparing the curve characteristic with the structure shown in Figure 7.7(b), it can be observed that at the beginning of the crash and due to the topology of the structure Y_{eq} is approximately 0.8. The contour and styling of the front of the vehicle dictates where space is available for structural components. For the first 400mm the application of the force is dominated by the bumper, sub-frame and support-frame. When the deformation reaches the wheel area at around 500mm, Y_{eq} moves outwards reaching a value of ca. 0.3. In the last phase of the crash at around s=1200mm, the application of the force moves to the most outwards point of the structure, coinciding with the location of the A-Pillar and Rocker, where the force level produced by such components becomes dominant.

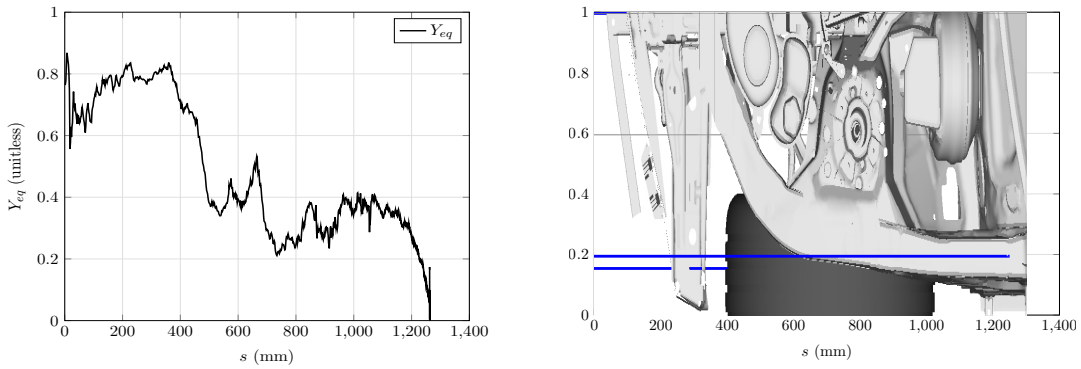

(a) Equivalent point of application of longitudinal force vs. deformation space (s)

(b) Undeformed vehicle structure top view vs. deformation space (s)

Figure 7.7 Full-vehicle normalized equivalent point of application of longitudinal force: Y_{eq} (a) and vehicle structure top view (b)

The forces and equivalent point of application can be further decomposed in their load-path representation. Similarly to the full-vehicle representation, Figure 7.8 shows the longitudinal and transversal forces mapped to the displacement space for each load-path. The conclusions of the analysis of the component location load-level done at the full-vehicle level hold also for the load-path *RDC*. The decomposition makes clear that the Wheel-Firewall-Rocker load-path is dominant, indicating force-levels double as high in both directions $F_{x_{LP_1}}$ and $F_{y_{LP_1}}$ in any of the other load-paths. Two distinct phases are observable, the first one from 0-650mm and the second one from 650mm onwards. The first phase is not active until 400mm and then corresponds to the bending of the contact of the support-frame, its contact with the wheel and the displacement of the wheel towards the BIW. This first phase only presents significant force levels in the longitudinal direction since the point of contact with the barrier corresponds to the flat surface of the barrier. The second phase corresponds to the wheel compression and eventual rupture due to the contact of the barrier and the rocker and firewall. Due to the kinematic of the wheel, the second phase is where a significant force-level can be observed in the transversal direction, which implies that the wheel moves inwards and rotates so that it has the possibility to contact the barrier at its curved surface.

The first increase of the force levels of the second load-path, coincide with the geometrical location of the shotgun. In a second increase, the wheel arches region is active. This load-path is dominated by its longitudinal forces. The outwards position of the components of the load-path limits the interaction with the curves surface of the barrier, producing mostly $F_{x_{LP_2}}$ force-levels.

The third load-path, i.e. bumper beam-front rail dominates the total longitudinal and transversal forces for the first 500mm of deformation. The fact that both $F_{x_{LP_3}}$ and $F_{y_{LP_2}}$ have similar force levels along the deformation length implies that the point of

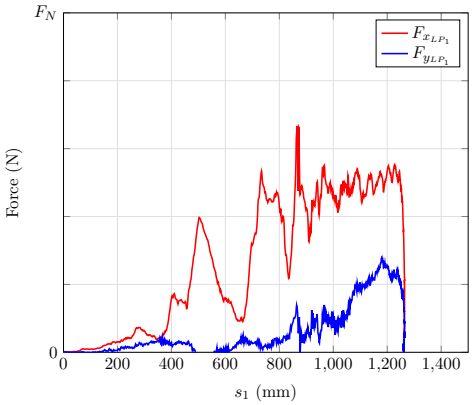

(a) Load-path 1: wheel-firewall-rocker longitudinal and transversal forces vs. deformation space (s_1)

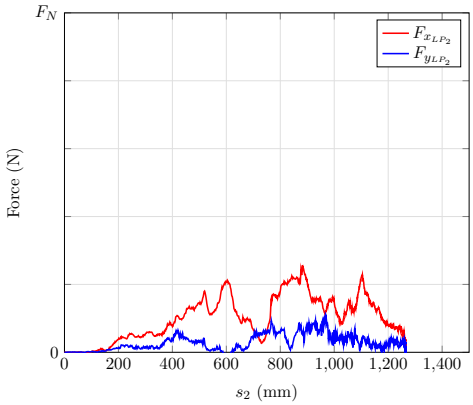

(b) Load-path 2: shotgun longitudinal and transversal forces vs. deformation space (s_2)

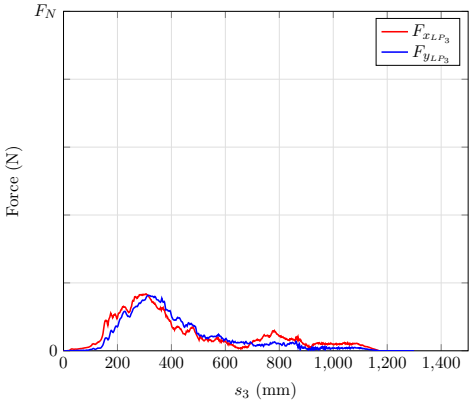

(c) Load-path 3: bumper beam-front rail longitudinal and transversal forces vs. deformation space (s_3)

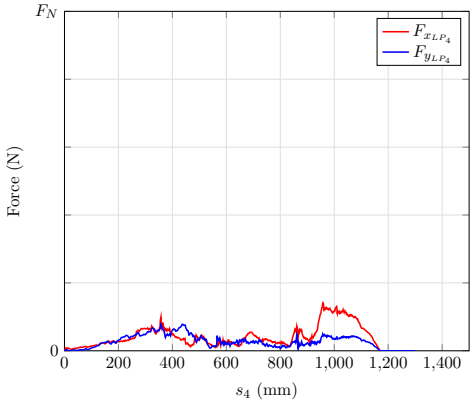

(d) Load-path 4: sub-frame longitudinal and transversal forces vs. deformation space (s_4)

Figure 7.8 Load-path longitudinal and transversal forces: wheel-firewall-rocker(a), shotgun(b), bumper beam-front rail (c), sub-frame(d)

contact with the barrier is first in the curved surface of the barrier and second close to the 45° location where the normal of the barrier surface produces equally larger forces for both directions. The maximum force reached by the load-path represents ca. one third of the force-levels reached by the wheel-firewall-rocker load path. The significance of a front-loaded load-path becomes evident when the objective is to maximize the negative moments M_z that rotate the vehicle away from the barrier to produce a glance-off mode. The most forward location of the load-path is where the lever arm for the transversal forces is at its maximum, therefore maximizing the mentioned M_z. However, there is

typically not enough construction space available at the frontal part of this load-path since its y position is dictated by the position of the front-rail. Locating the front-rail more outwards would increase the overlap with the barrier at its curved surface and consequently also increase the transversal forces, but imply an additional set of challenges for other requirements of the vehicle and the packaging and interference of the wheel space needed for steering and for providing an acceptable turning circle.

The load-path composed by the sub-frame structures is for this vehicle test and topology the one reaching the lowest force-levels. A first increase occurs in the first 400mm, analogously to the third load-path, $F_{x_{LP_4}}$ and $F_{y_{LP_4}}$ provide similar levels of force. Afterwards, the load-path becomes inactive only to observe an increase towards the end of the crash due to the compression of the remaining suspension and sub-frame components by the barrier and BIW. In a development exercise this load-path has the most potential to increase its load-levels and improve the vehicle kinematics reaching also a more efficient structural design.

After extracting the resistance-to-deformation characteristics and by using the vehicle characteristics presented in Table 7.1, the complete set of input parameters is ready to recreate the vehicle's behavior by means of the low-fidelity kinematic model.

7.1.5. Forwards Calculation

The objective of the low-fidelity kinematic model is to produce as output a vehicle trajectory defined by the DOFs u_x, u_y, θ_z representing the displacements and rotation of the CG of the vehicle. This objective is achieved through the use of the vehicle characteristics and a set of resistance-to-deformation characteristics, either at the full-vehicle or load-path-level, as input and the solution of the non-linear equation of motion presented in Eq. (4.3). The DOFs are used in a post-processing step to calculate the kinematic parameters. In this section, both outputs, the DOFs and the kinematic parameters from the reference crash test are compared to the output of the low-fidelity kinematic model to quantify its error and sensitivity to the parameters used for the simplification of the phenomenon.

As presented in Algorithm (2), for the solution of the kinematic model, the lumped mass matrix **LM** is constructed using the information from Table 7.1. The RHS of the equation is set up accordingly to the initial position of CG and load-paths defined in the vehicle characteristics. The force-displacement and point of application of force-displacement curves extracted from the test, are defined as piecewise-linear interpolators so that for each deformation length a force-level is available. In the next sections, the low-fidelity model is used to calculate the vehicle trajectory using the full-vehicle and load-path level RDC and the outcome is compared with the reference test. The kinematic model is calculated to a maximum of 150ms using a constant time step, dt. Additionally, aspects are considered such as, the effect of the time step size on the accuracy and computational cost, which will become relevant in the use of the solution space calculator. The sensitivity to variations of the RDC as well as the smoothness of the curves are also analyzed.

7.1.6. Kinematic Model at the Full-Vehicle Level

At the full-vehicle level, the *RDC* are represented by the longitudinal force, $F_{x_L}(s)$, transversal force, $F_{y_L}(s)$, and equivalent point of application of longitudinal force $Y_{eq}(s)$. The LHS expresses the inertial effects of the masses and inertias and the accelerations, which are directly the time derivatives of the displacements and rotations of the *CG*. The three *RDC* are expressed as functions of the deformation, s, of a single load-path, which is in turn dependent on the displacements and rotations of the *CG*. The solution of the non-linear equation of motion requires a numerical integration scheme. An explicit central difference scheme is selected, which is sensitive to the time step size, dt. The first quantities to compare are the DOFs and Figure 7.12 presents the displacements, $u_{x_{km}}$ and $u_{y_{km}}$, and rotation $\theta_{z_{km}}$ obtained from using a $dt = 1e^{-4}$. A visual inspection of the curves makes clear that the characteristics of the reference curves, $u_{x_{ref}}$, $u_{y_{ref}}$ and $\theta_{z_{ref}}$ are captured from the results achieved from the kinematic model. On one side, the displacement curves $u_{x_{km}}$ and $u_{y_{km}}$ show a relatively low deviation w.r.t. the references at ca. 80ms. On the other side, the curve characteristic of the rotation shows an initial negative rotation reaching a minimum at ca. 50ms and then increases until reaching a maximum positive value at 150ms of ca. 6°. The larger deviation of the rotation produced by the kinematic model, $\theta_{z_{km}}$, is present in the form of a larger rotational velocity than seen in the reference from 60ms to 100ms. Considering the relative magnitudes involved in the crash test, the deviations with respect to the reference curve are acceptable.

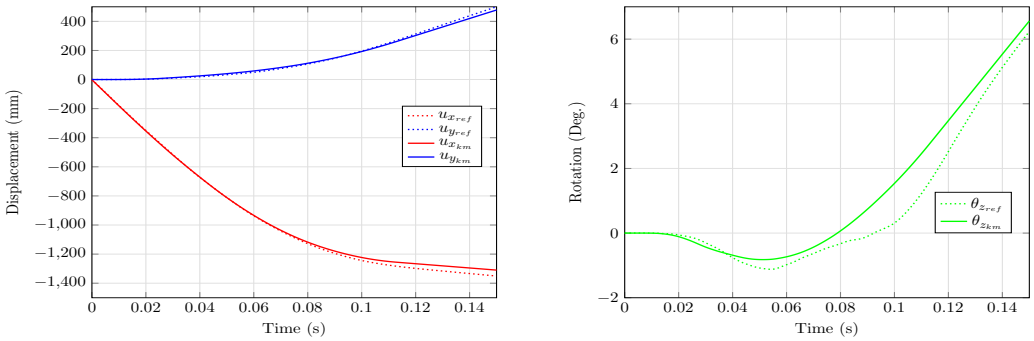

(a) Global longitudinal displacements of reference test and kinematic model

(b) Global rotation of reference test and kinematic model

Figure 7.9 Reference test (ref) and kinematic model (km) time series of the global longitudinal, u_x and transversal u_y displacements (a) and rotation around z axis, θ_z (b)

The two key factors to determine the optimum dt are the sensitivity of the output and the computational cost. To carry out this analysis, the first aspect to be compared to the reference are the kinematic parameters including the end time of the crash. A total of 4 time step sizes of $[1e^{-3}, 1e^{-4}, 1e^{-5}, 1e^{-6}]$s is considered. The decrease in time step size implies a linear increase of the iterations needed to reach the given simulation time

of 150ms. The results reported in Table 7.3 aid in the selection of a time step size whose further decrease does not produce a significant change in the outcome of the kinematic model. This table enables an analysis of the convergence of the results w.r.t. time step size. In order to prevent unnecessary computational costs, selecting a smaller time step size beyond the point of convergence is avoided.

Table 7.3 Kinematic Parameters Comparison: Reference Crash Test v. Kinematic Model

Kinematic Parameter	**Reference**	**KM:** $dt = 1e^{-3}s$	**KM:** $dt = 1e^{-4}s$	**KM:** $dt = 1e^{-5}s$	**KM:** $dt = 1e^{-6}s$
t_{end} **(ms)**	*112*	*114*	*113*	*113*	*113*
θ_z **(Deg.)**	*2.6*	*2.92*	*2.78*	*2.76*	*2.75*
s_L **(mm)**	*160*	*142*	*141*	*141*	*141*
GV_P	*0.65*	*0.69*	*0.67*	*0.67*	*0.67*
RKE **(%)**	*13*	*13.3*	*13.2*	*13.2*	*13.2*

Independent from the time step, all results produced by the kinematic model present the same kinematic mode as the reference test. The results obtained for the end time of the crash, t_{end}, observe a maximum deviation of 2ms, which is in the context of the crash event an acceptable outcome. The other kinematic parameters presented in Table 7.3 are taken for t_{end}. Considering the conclusions drawn from the inspection of Figure 7.12(b), the maximum deviation of the total rotation, θ_z, is less than 1 degree. Meanwhile, the larger deviations are observed in the rest deformation length, s_L, with a maximum of 19mm. The IIHS rating defines the limit of 150mm for the lower hinge pillar intrusion to achieve a Good structural rating. Which means that the deviation of s_L represents only 13% of this quantity defining the structural rating. The next kinematic parameter reported is the glance-off value, GV_P. This parameter has a maximum deviation of 0.04 with respect to the reference test. Finally, the rest kinetic energy RKE, which is in itself a quantity dependent on rotational and translational velocities, presents a deviation of max. 3%. Additionally to the results summarized in Table 7.3, Figure 7.10 provides a graphical representation of the kinematic parameters in its time series form. The curve characteristics of RKE_{km}, $GV_{P_{km}}$ and $s_{L_{km}}$ coincide with the reference curves. The relative absence of oscillations of the curves, specially for the RKE_{km}, $GV_{P_{km}}$ provides an insight into the filtering properties of the kinematic model in contrast to the oscillatory nature of the signals obtained from the sensor tests.

In order to conclude with the selection of the optimal time step, the relative error of the kinematic parameters with respect to the number of iterations that this time step implies is depicted in Figure 7.11. Even if from the absolute values presented in Table 7.3, it was concluded that the low-fidelity kinematic model produced acceptable results, an inspection of the relative errors assists in the selection of an optimum time step. For a time step $dt \geq 1e^{-4}s$ which corresponds to 1500 iterations, the resultant kinematic parameters do not change more than 2% with respect to the values obtained from using the smallest time step of $1e^{-6}s$. For this reason $dt = 1e^{-4}s$ is selected as time step for

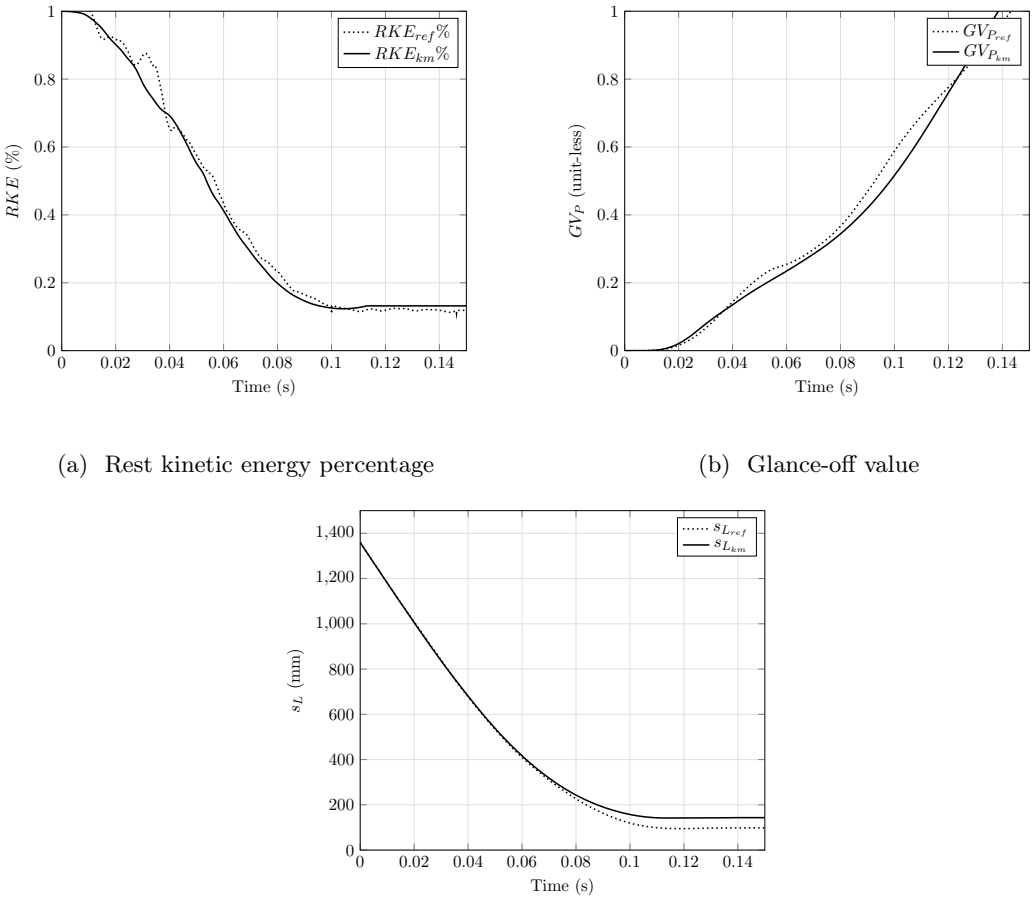

(a) Rest kinetic energy percentage

(b) Glance-off value

(c) Rest deformation length

Figure 7.10 Reference test (ref) and kinematic model (km) kinematic parameters: rest kinetic energy, RKE (a), glance-off value, GV_P (b), rest deformation length, s_L (c)

all further applications of the kinematic model.

The quantity with the largest relative error is s_L with almost 12%. In contrast to the other kinematic parameters, this quantity does not decrease with a reduced time step. The relative error of RKE, GV_P, s_L and θ_z decreases when the time step is also decreased. Even though the absolute errors produced by the kinematic model are acceptable, the fact that the relative errors decrease but do not converge towards zero confirms the fact that the assumptions of the low-fidelity model defined in Section 4.1.1 are enough to produce meaningful results but in essence define a slightly different problem than the real crash phenomenon.

The quantities extracted from the reference test offer the possibility to compare the results with the kinematic model. However the signals obtained from the measuring

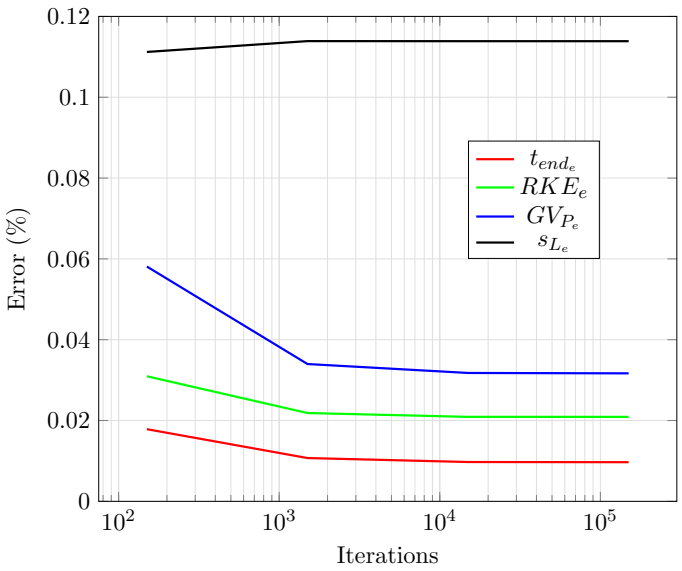

Figure 7.11 Relative error of kinematic parameters vs. iterations at kinematic model at the full-vehicle level

devices, e.g. sensors and force cells from the barrier, as in any other measurement can be affected by measurement errors and deficiencies in the calibrations and general wear of the sensors. These defective inputs can also result into deficiencies in the results produced by the kinematic model. In order to study the sensitivity of the kinematic parameters to changes in the input *RDC* the following study is conducted. The original *RDC*, i.e. $F_{x_L}(s)$, $F_{y_L}(s)$ and $Y_{eq}(s)$ are scaled by $\pm$ 5%, which is more than the error expected from state-of-the-art devices, i.e. $\pm$ 2%. The space between the minimum and maximum of the three *RDC* curves is sampled independently and using a uniform *pdf* with a total of 500 sets of curves. The histograms of the obtained kinematic parameters are shown in Figure 7.12.

The variation of $\pm$ 5% introduced in the *RDC* provides a symmetrical deviation from the original results for $RKE_{km_{org}}$, $GV_{P_{km_{org}}}$, $s_{L_{km_{org}}}$, $\theta_{z_{km_{org}}}$. The variation of *RKE* is $\pm$ 0.1%, while for s_L is $\pm$ 10mm. The rotation changes by $\pm$ 0.7°. Lastly, the GV_P has a variation of $\pm$ 0.02 with respect to the original kinematic model calculation. The size of these variations becomes relevant when defining the set of constraints for the solution space calculation. Constraints with a resolution smaller than the one introduced by the $\pm$ 5% in the *RDC* cannot be considered insignificant since they lie inside the scatter produced by the possible measurement error of the input parameters.

The previously introduced filtering nature of the kinematic model can be explained by the fact that the DOFs are the outcome of a numerical time integration. This implies that slightly different acceleration signals can produce similar outcomes at the DOFs level,

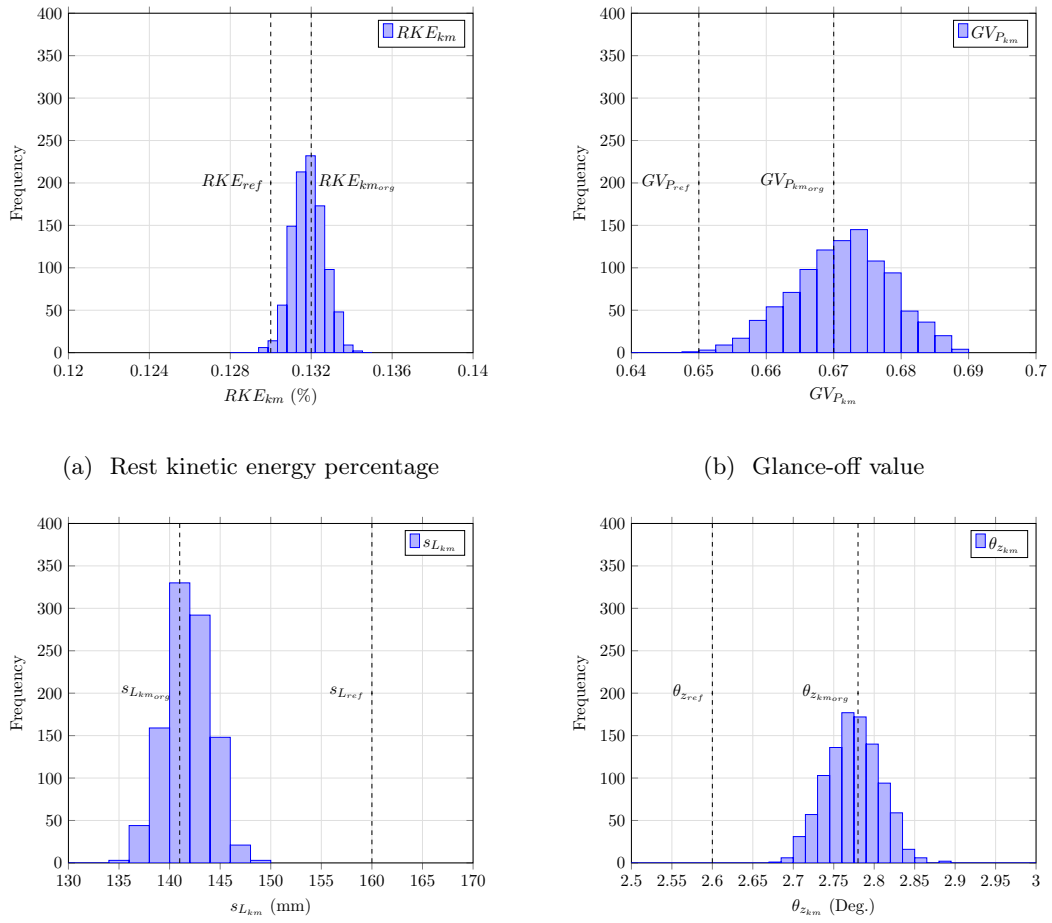

(a) Rest kinetic energy percentage

(b) Glance-off value

(c) Rest deformation length

(d) Total rotation

Figure 7.12 Kinematic parameter sensitivity to input: rest kinetic energy, RKE (a), glance-off value, GV_P (b), rest deformation length, s_L (c), total rotation, θ_z (d)

meaning that RDC with high frequency oscillations and their correspondent smoothed representations can produce kinematic parameters with relatively small deviations. The motivation behind the smoothing of the RDC lies in the fact that a curve with high frequency oscillations requires a larger amount of points to be described. A smoother signal can be represented by less points in a piecewise-linear form. The benefits of this information efficiency become clear in the steps required for the solution space calculation. A larger number of points to describe the curve also implies a larger amount of sample points to characterize the space and therefore greater computational costs. Considering this, to quantify the effect of smoothing the curves of the RDC a set of filters is applied and the effect on the kinematic response is analyzed. The filtering of the curves is defined in the deformation spaces and a moving average to a given window size specified

in millimeters is applied. The window sizes analyzed are 5, 10, 20, 30, 40, and 50mm. These filters are applied to the original *RDC* curves and filtered curves are shown in Figure 7.13.

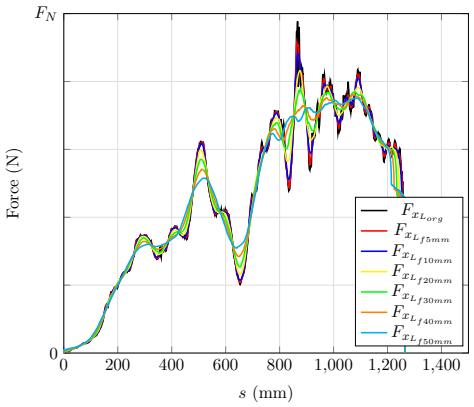

(a) Longitudinal forces vs. deformation space (s)

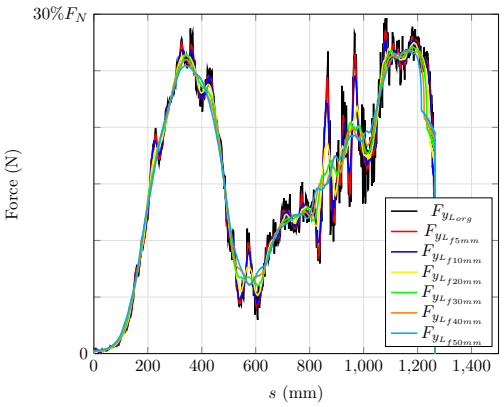

(b) Transversal forces vs. deformation space (s)

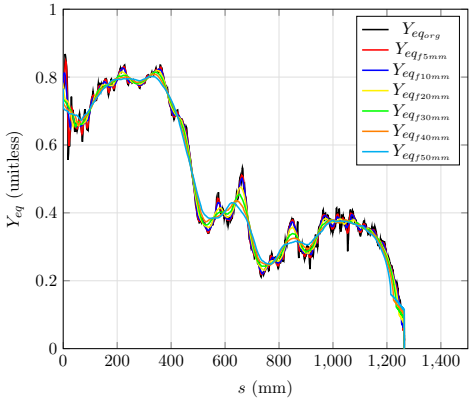

(c) Equivalent point of application of longitudinal force vs. deformation space (s)

Figure 7.13 Full-vehicle longitudinal F_{x_L} (a), transversal forces F_{y_L} (b) and normalized equivalent point of application of longitudinal force, Y_{eq} (c) for filters: 0mm, 5mm, 10mm, 20mm, 30mm, 40mm and 50mm

The effect of the filtering of the longitudinal force, F_{x_L} is particularly evident between 800mm and 1200mm. The dominant load-path at this deformation level is the wheel-firewall-rocker. The complex mechanics of the barrier, wheel, and BIW contact and rupture of the wheel can also be represented as observed in Figure 7.13(a) by a monotonically increasing force signal. Similarly, the effects of the filter are evident in the F_{y_L} curve from 600mm to 1200mm. Regarding the equivalent point of application

of longitudinal force, Y_{eq}, the signal filtering at the early phase of the curve, i.e. from 0 to 200mm, assists with the simplification of the highly oscillating signal produced by the relatively low forces and changing lever arm taking place at the most frontal part of the structure.

Similarly to the selection of the optimal time step, the selection of the window size for the filter considers two aspects. On one side, the larger the window size the less amount of points are needed for the calculation of the solution space. Moreover, the filter size should be large enough to filter the high frequency oscillation in the curve. On the other side, the results obtained from the use of filtered RDC should not present a significant deviation from the original results. Considering these aspects, only the filters with window size f$\geq$40mm eliminate the effects of the oscillations. To consider the second aspect, the DOFs and kinematic parameters obtained from the different filters are presented in Figure 7.14.

As expected from the smoothing nature of the low-fidelity kinematic model, no observable difference is present in either the DOFs, u_x, u_y and θ_z, nor in the kinematic parameters, RKE, GV_P and s_L. The next step in selecting the window's size is to quantify the relative error introduced to the kinematic parameters at t_{end} by the application of the filter. Figure 7.15 presents the relative error as a function of the window size of the filter. RKE observes a stable 2% error independent of the window size. However for GV_P, s_L and θ_z, the relative error remains flat until a window size of 50mm is reached. The highest increase comes from GV_P where the relative error jumps from less than 4% for a window size of 40mm to an error larger than 6% using a filter of 50mm.

Taking into account the smoothing effect in the input curves as well as the relative error in the kinematic parameters for each one of the filter sizes, a 40mm window size is selected. This window size offers the largest possible decrease of points needed to characterize the curve, acceptable smoothing effects and no significant deviations in the output of the kinematic model. The 40mm window size is also enough to represent specially the components in the structure and their correspondent force-levels. The use of a larger window size would not only decrease the accuracy of the kinematic model but also hinder the capability of mapping the force-level to specific components. A similar study at the load-path level is also conducted to study the effect of the filtering, where it is confirmed that the features and characteristics of the load-path's force-displacement curves are still present after applying the filter.

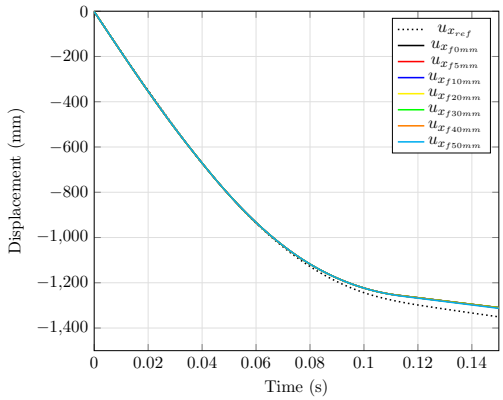

(a) Longitudinal displacements

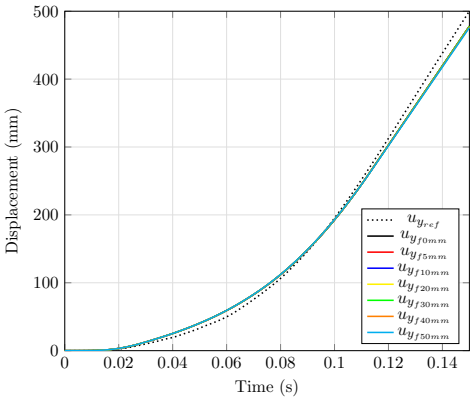

(b) Transversal displacements

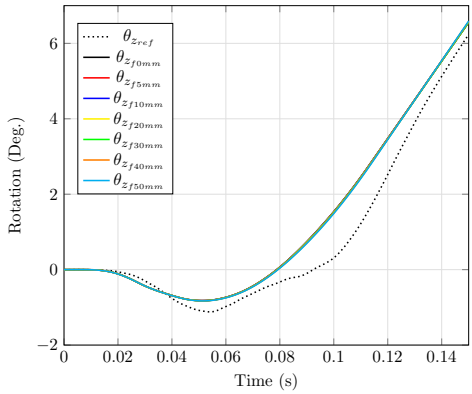

(c) Total rotation

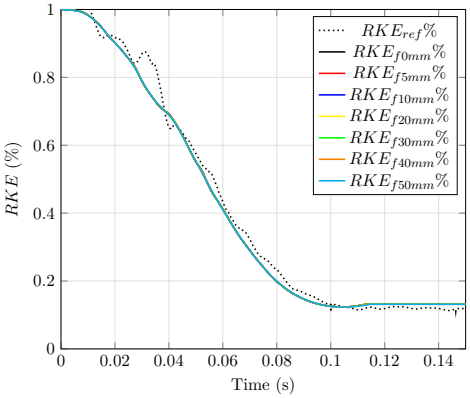

(d) Rest kinetic energy

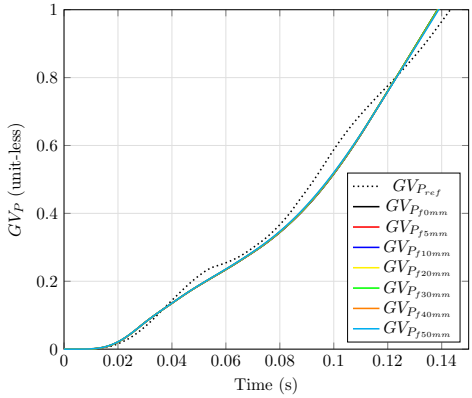

(e) Glance-off value

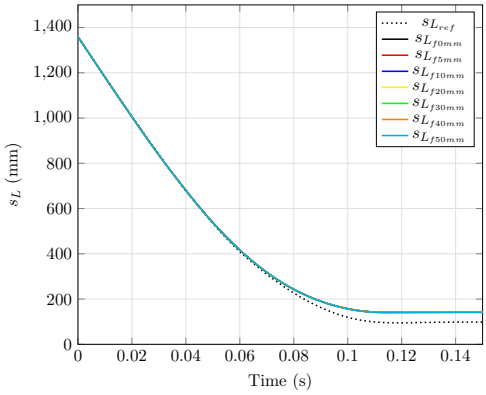

(f) Rest deformation length

Figure 7.14 Kinematic model and reference longitudinal, u_x (a), and transversal displacements, u_y (b), rotation, θ_z (c), rest kinetic energy, RKE (d), glance-off value GV_P (e), rest deformation length s_L (f) for filters: 0, 5, 10, 20, 30, 40, and 50mm

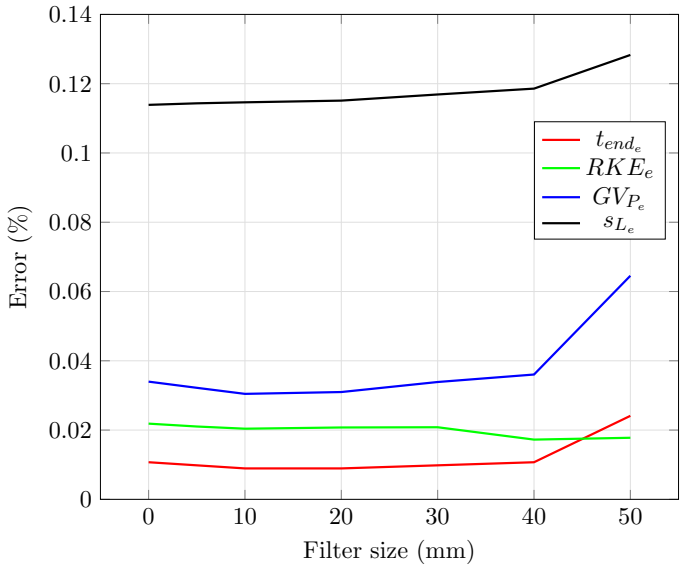

Figure 7.15 Relative error of kinematic parameters vs. filter size in mm at kinematic model at the full-vehicle level

7.1.7. Kinematic Model at the Load-path Level

In the previous section, the low-fidelity kinematic model results where compared to those of a reference crash test. The *RDC* were defined at the full-vehicle level with one longitudinal, F_x, and one transversal, F_y, force as well as curve for the equivalent point of application of longitudinal force, Y_{eq}. The main differences at the load-level with respect to the load-path level is the decomposition of the total forces into load-paths and the lack of a Y_{eq}. This means that the total longitudinal and transversal forces are simply the sum over all the load-paths while the moment is calculated using the lever arm as a function of the position of the load-path along the y instead of using an equivalent point of application for the total longitudinal force. Therefore, a different rotational response relatively to the full-vehicle approach is expected.

Similarly to the comparison made at the full-vehicle level, the kinematic model at the load-path level is calculated using the original longitudinal, $F_{x_{LP_j}}(s_j)$, and transversal, $F_{y_{LP_j}}(s_j)$ curves and also the filtered curves using the selected 40mm window size. The original curves and their filtered representation are shown in Figure 7.16. The effect of the decomposition and filtering of the force-displacement curves is most evident in the wheel load-path. As observed in the full-vehicle presentation the 40mm window size minimizes the high frequency oscillations. The wheel load-path characteristic is reduced to first a relatively high force-level increase from 600mm to 700mm explained by the response before rupture from the compression of the wheel. The second phase contains

a relatively lower force-level increase from 700mm until 1200mm which is related to the pressuring of the remaining block, i.e. knuckle and wheel remains, towards the rocker and firewall. The rest of this load-path characteristic as well as the other load-paths remain relatively unaffected by the filter.

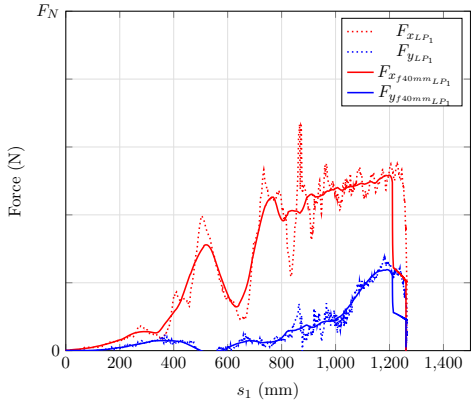

(a) Load-path 1: wheel-firewall-rocker longitudinal and transversal forces vs. deformation space (s_1)

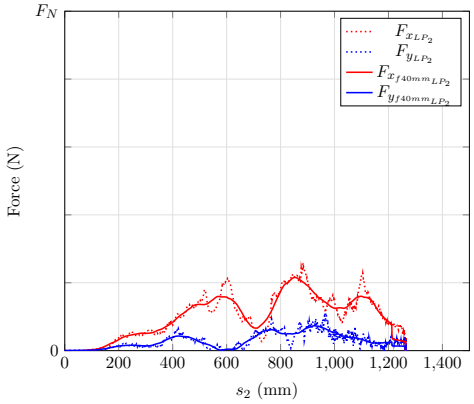

(b) Load-path 2: shotgun longitudinal and transversal forces vs. deformation space (s_2)

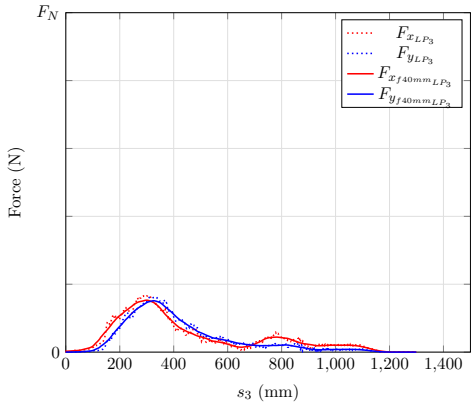

(c) Load-path 3: bumper beam-front rail longitudinal and transversal forces vs. deformation space (s_3)

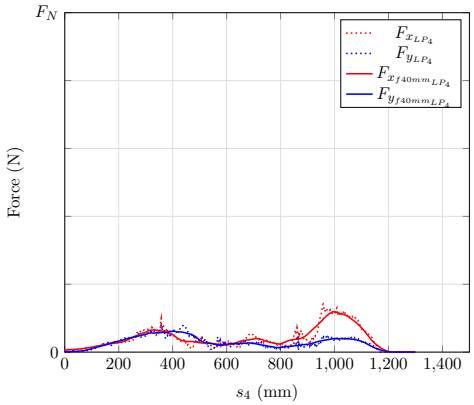

(d) Load-path 4: sub-frame longitudinal and transversal forces vs. deformation space (s_4)

Figure 7.16 Load-path longitudinal and transversal forces: wheel-firewall-rocker(a), shotgun(b), bumper beam-front rail (c), sub-frame(d) with filter size 40mm

The results of the kinematic model at the full-vehicle, FV, and load-path level LP with and without the 40mm filter as well as the reference test are shown in Figure 7.17. A slight offset in the response of the displacement u_x, the rotation, θ_z and the rest deformation length s_L is observed between the FV and LP approaches. The deviation becomes

observable in θ_z at ca. 40ms, while the different response for u_x and s_L becomes apparent after 90ms. The $\theta_{z_{LP}}$ with and without filter presents a larger negative rotation from 40ms to 80ms than the $\theta_{z_{FV}}$ which takes it closer to the reference $\theta_{z_{ref}}$. No significant deviation between FV and LP is observed for u_y, RKE and GV_P. Furthermore, in all of the DOFs and kinematic parameters no observable difference is present between the response from the filtered and original RDC, confirming the convenience of selecting 40mm as a window size.

An objective quantification of the deviation of the kinematic parameters and the effect of the filter at the LP level is presented in Table 7.4. The relative errors (R.E.) with respect to the reference are not significantly different for both the kinematic model using the filtered and original RDC. The deviations between the LP and FV are larger than the ones produced by the use of the filter. The load-path level approach produces relatively lower errors for s_L, GV_P, RKE and t_{end} than the full-vehicle level. The highest gain is present in s_L, where the FV approach produced a relative error of almost 12%, meanwhile the LP approach produced an error of only 4%. However, an increase in the relative error of θ_z is present at the LP level. Nonetheless, this relatively higher error still remains a difference of less than 1 degree in absolute terms.

Table 7.4 Kinematic Parameters @ Load-path level and relative errors using a filter size of 0mm and 40mm

K. Parameter	**KM:LP** $nofilter$	**KM:LP** $40mm$	**R.E. KM:LP** $nofilter$	**R.E. KM:LP** $40mm$
t_{end}	*112ms*	*112ms*	*0%*	*0%*
RKE	*12.8%*	*12.7%*	*1%*	*2%*
θ_z	*2.2°*	*2.2°*	*15%*	*14%*
GV_P	*0.66*	*0.67*	*2%*	*2%*
s_L	*155mm*	*154mm*	*3%*	*4%*

After this comparison, the effectiveness of the low-fidelity kinematic model is confirmed. The error introduced by the simplification of the model is characterized and the sensitivity to the input is analyzed for both the full-vehicle and load-path levels. This validation procedure of the kinematic model serves as corner stone for the second validation phase where the kinematic model is used to find the necessary RDC to achieve the same kinematic as the one observed in the test.

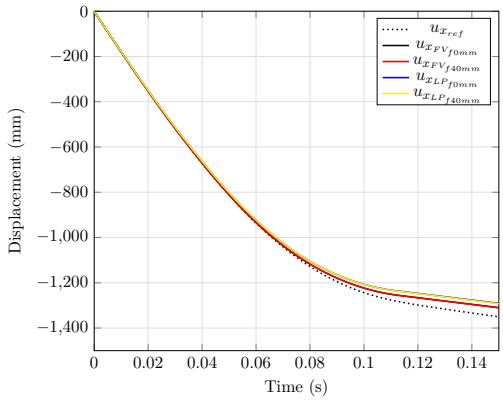

(a) Longitudinal displacements

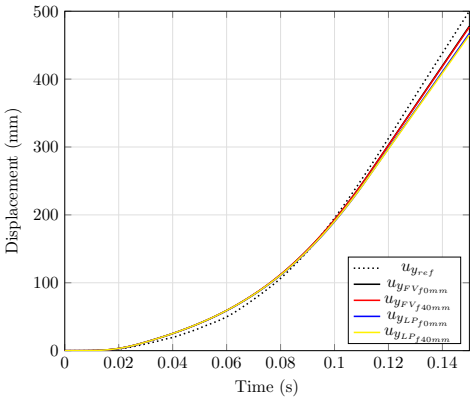

(b) Transversal displacements

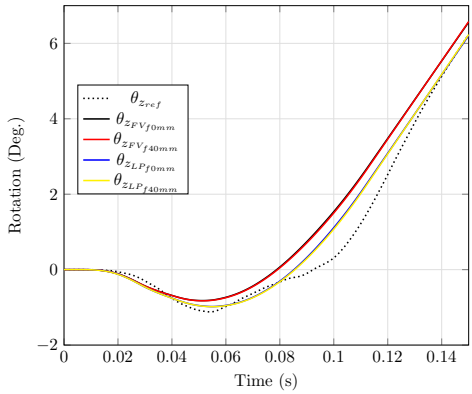

(c) Total rotation

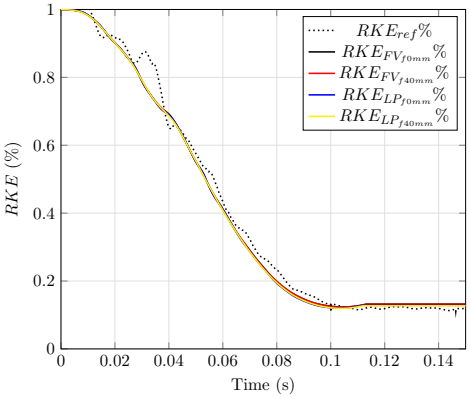

(d) Rest kinetic energy

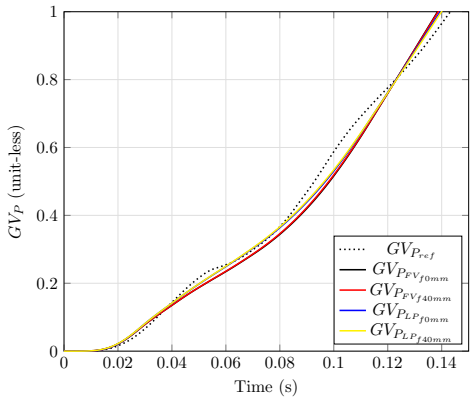

(e) Glance-off value

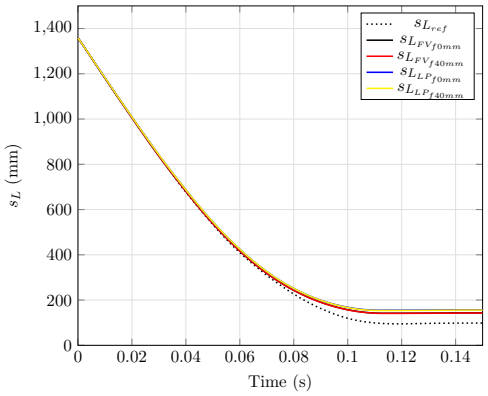

(f) Rest deformation length

Figure 7.17 Kinematic model and reference longitudinal, u_x (a), and transversal displacements, u_y (b), rotation, θ_z (c), rest kinetic energy, RKE (d), glance-off value GV_P (e), rest deformation length s_L (f) for filters: 0, 5, 10, 20, 30, 40, and 50mm; at full-vehicle (FV) and load-path (LP) levels

7.2. Backwards calculation & Solution Space

In the previous section it is established that within an acceptable range of error, the low-fidelity kinematic model is capable of reproducing the kinematic behavior of a crash test given a set of vehicle characteristics such as total mass, rotational inertia, position of CG, load-path location and relative position of the barrier as well as a set of RDC at the full-vehicle and load-path levels. The kinematic parameters of the $forwards\ calculation$ were compared to the values from the reference test. Nonetheless, the identification of functional properties such as the RDC so that a given kinematic response is achieved is a more relevant task in the crashworthiness design than reproducing the result of an already existing vehicle. The methodology describing the *backwards calculation* for the solution space is introduced and validated in this section. In the case of an existing crash, both the kinematics and RDC of the vehicle are known. Therefore, the problem statement for the validation of the solution space calculation is defined as the search for the solution space that contains the RDC measured in the test and whose kinematic response matches to the one observed in the test. A set of constraints upon RKE, θ_z, GV_P, s_L, and t_{end} are defined so that the values from the test exist inside the upper and lower limits of the constraints. As defined in Section 5.1 the solution space calculation is first carried out at the full-vehicle level and in a second step at the load-path level. The success of the validation procedure is measured by comparing the solution space for RDC to the measured characteristics from the test.

7.2.1. Full-Vehicle Level

At the full vehicle level, the reference kinematics are characterized by the set of constraints presented in Table 7.5. An upper and lower limit based on the reference values observed in the test and a symmetrical offset around it are defined for t_{end} and the kinematic parameters, RKE, θ_z, GV_P, s_L. These constraints only represent the values of the kinematic parameters at t_{end}, but as it will be observed in this section, this is enough to have a comparable characteristic of the time series. For this reason no explicit criterion along the duration of the crash but only the value at t_{end} is defined as constraint. The reference values are considered as the values obtained from the kinematic model at the full-vehicle level using a $dt = 1e^{-4}s$ and a filter size of 40mm, (Table 7.3) and a $\pm$ 10% symmetrical offset. By using the results of the kinematic model as reference, the error introduced by the solution space calculator is analyzed independently from the error introduced from using the low-fidelity model itself.

As previously stated, the use of filtered RDC allows for the reduction of the number of points needed to represent the curve characteristics. Consequently, a discretization of s=[0, 100, 300, 400, 500, 600, 650, 700, 750, 1100, 1250, 1400, 1600]mm was selected in order to minimize the number of variables involved in the solution space calculation and at the same time to be able to represent the curve characteristics. This discretization is used to define the design bounds of F_{x_L}, F_{y_L}, and Y_{eq}.

The design bounds of the full-vehicle longitudinal and transversal forces, $\hat{F}_{x_{FV_L}}$, $\check{F}_{x_{FV_L}}$ and $\hat{F}_{y_{FV_L}}$, $\check{F}_{y_{FV_L}}$, as well as $\hat{Y}_{eq_{FV_L}}$, $\check{Y}_{eq_{FV_L}}$ are defined by considering the structural

Table 7.5 Constraints defined upon relevant kinematic quantities that represent the kinematics of the reference test

Kinematic quantity	**Constraint**
Rest Kinetic Energy	$11.8\% \leq RKE \leq 14.5\%$
Total Vehicle Rotation	$2.5° \leq \theta_z \leq 3.05°$
Glance-off	$0.60 \leq GV_P \leq 0.74$
Rest Deformation Length	$127mm \leq s_L \leq 156mm$
End of Crash	$101ms \leq t_{end} \leq 124ms$

topology and the curve characteristics described in Section 7.1.4. The Figure 7.18(a) shows that the lower limits of the design bounds of the longitudinal force, $\check{F}_{x_{FV_L}}$ are divided into 3 phases. The first phase, an ascending slope from 0 to 300mm represents the minimum force levels expected from the contact of the most forward structures. The next phase, from 300mm to 700mm, is represented by a plateau describing the minimum force expected from the deformation of the bumper, sub-frame, support-frame and first section of the shotgun. For the third phase, from 700mm onwards, a minimum force for the wheel-structure interaction is defined. On a similar fashion, the upper limits of the design bounds for $\hat{F}_{x_{FV_L}}$ are selected also adding an additional force-level plateau between 500mm and 600mm. The force level in this region are mainly defined by the interaction of the barrier, supporting-frame, and wheel. A drop in the force levels due to the translation of the wheel towards the structure is also explicitly defined in $\hat{F}_{x_{FV_L}}$ at 650mm. The design bounds of the transversal force, $\hat{F}_{y_{FV_L}}$ and $\check{F}_{y_{FV_L}}$, have a similar characteristic as the longitudinal counterpart with the exception that the upper and lower bounds of the first and last phases are defined as constant. The design bounds of equivalent point of application of the longitudinal force, $\hat{Y}_{eq_{FV_L}}$, $\check{Y}_{eq_{FV_L}}$, also present two distinct phases, namely before and after the wheel area with a transition at 650mm.

Once the constraints and design bounds are defined, the solution space calculation is started. The three phases, exploration, consolidation, and expansion are conducted. The Figure 7.18 presents the results of the exploration phase. This phase identifies curve sets that exist within the design bounds that fulfill the constraints set upon the kinematic parameters regardless of the dependency of the variables or the success rate of the subspace itself. In other terms, the regions outside the exploration-phase solution space do not contain curves that satisfy the constraints. The upper and lower limits of the exploration phase are designated as $\hat{F}_{x_{FV_{S0}}}$ and $\check{F}_{x_{FV_{S0}}}$ for the longitudinal forces, $\hat{F}_{y_{FV_{S0}}}$ and $\check{F}_{y_{FV_{S0}}}$ for the transversal, and $\hat{Y}_{eq_{FV_{S0}}}$ and $\check{Y}_{eq_{FV_{S0}}}$ for the equivalent point of application of force. The inspection of Figure 7.18(a) results in the identification of several regions without any feasible designs for the longitudinal force. At the first phase, a minimum value for $\check{F}_{x_{FV_{S0}}}$ at 500mm becomes evident. Additionally, the minimum force-level is increased relative to the lower design bound for the wheel region from 750mm onwards. From the perspective of the upper limit of the exploration solution space, the first phase follows closely the upper limit design bound. However, at the

wheel region a clear maximum force-level, which is lower than the upper design bound in this section, emerges. To recapitulate, the exploration phase indicates that a minimum force level is needed at the support-frame and wheel regions, and at the same time a maximum force-level at the wheel region must be achieved in order to be able to fulfill the constraints. Considering the transversal forces, the upper limit of the exploration solution space, $\hat{F}_{y_{FV_{S0}}}$, shows a decreased force-level with respect to the design bound. The lower limit $\check{F}_{y_{FV_{S0}}}$ follows closely the design bound in the first phase but produces an increased minimum for the wheel-region. Lastly, only the lower limit of $\check{Y}_{eq_{FV_{S0}}}$ presents a significant deviation from the design bounds. Once again, at the wheel region, an equivalent point of application of force larger than the design bound is required to fulfill the constraints.

The exploration-phase solution space shows the necessary minimum and maximum values required to define a space with a success rate, $SR>0$. As a matter of fact, the success rate of the exploration solution space shown in the Figure 7.18 reaches 6%. With these initial conditions, the consolidation phase begins. For each consolidation iteration 20,000 samples are evaluated. The explicit objective of this phase is to find a solution space with a minimum of success rate of 95%. Therefore, after the sampling of the active space in each iteration, the regions without feasible designs are discarded. Figure 7.18 also shows the solution space at iteration 5, 500, and 1500. It can be observed from $\hat{F}_{x_{FV_{C_5}}}$, $\check{F}_{x_{FV_{C_5}}}$, $\hat{F}_{y_{FV_{C_5}}}$, $\check{F}_{y_{FV_{C_5}}}$, $\hat{Y}_{eq_{FV_{C_5}}}$, and $\check{Y}_{eq_{FV_{C_5}}}$ that already in an early stage of a consolidation process, regions of significant size are discarded. The effect of the rapid consolidation and the reduction of the solution space size is shown in Figure 7.19(a) and (b) respectively. A total of 2631 iterations are required to achieve the targeted total success rate SR_{Total}.

The iterations shown in Figure 7.18(a) concerning the consolidation of the longitudinal force solution space show a considerable increase relative to the exploration phase limits in the force-levels of the lower limits of $\check{F}_{x_{FV_C}}$ from 300mm to 700mm. In contrast, the upper limit for this same region $\hat{F}_{x_{FV_C}}$ decays relatively less in the first iterations. On the wheel region, both upper and lower limits depart from the values obtained in the exploration phase. With regard to the transversal forces, a similar effect is present in Figure 7.18(b), where a significant increase of the lower limit takes place at the early phase of deformation. As with the longitudinal force, both upper and lower limits of $\hat{F}_{y_{FV_C}}$ and $\check{F}_{y_{FV_C}}$ deviate from the exploration phase limits. However, the reduction of the upper limit specially at 750mm is considerably larger than the increase that the lower limits exhibits. For $\hat{Y}_{eq_{FV_C}}$ and $\check{Y}_{eq_{FV_C}}$ the first iterations do not show a considerable effect in the deformation region from 0mm to 300mm. Nonetheless, $\hat{Y}_{eq_{FV_C}}$ shows a substantial decrease from 400mm to 600mm indicating that an equivalent point of application of force which exists more inwards in the structure, specially in the early deformation stages would produce a different kinematic than the reference. Furthermore, at the wheel region, the lower limit, $\check{Y}_{eq_{FV_C}}$, must be increased, i.e. application point moved inwards, to increase the SR.

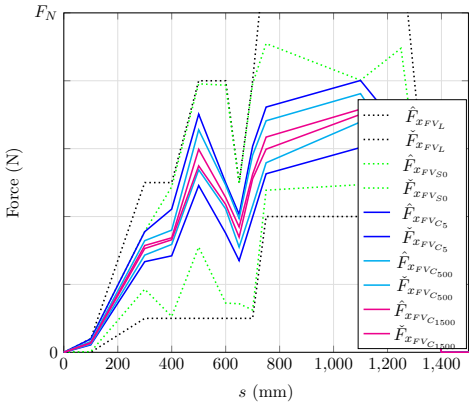

(a) Longitudinal forces vs. deformation space (s)

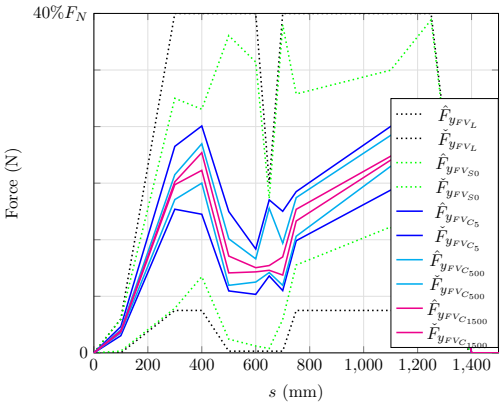

(b) Transversal forces vs. deformation space (s)

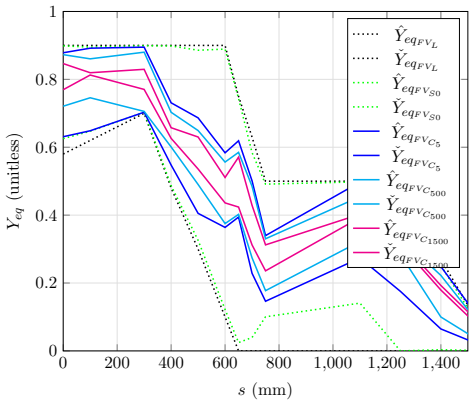

(c) Equivalent point of application of longitudinal force vs. deformation space (s)

Figure 7.18 Design space limits L, exploration solution space at full-vehicle level for: $\hat{F}_{x_{FV_{S0}}}$ and $\check{F}_{x_{FV_{S0}}}$ longitudinal forces, $\hat{F}_{y_{FV_{S0}}}$ and $\check{F}_{y_{FV_{S0}}}$ transversal and $\hat{Y}_{eq_{FV_{S0}}}$ and $\check{Y}_{eq_{FV_{S0}}}$; and iteration 5 (C_5), 500 (C_{500}), and 1500 (C_{1500}) of the consolidation solution space

The total success rate SR_{Total} and its decomposition into each constraint as a function of the number of iterations are depicted in Figure 7.19(a). The consolidation and evolution of SR_{Total} can be understood as two periods with different consolidation velocities. The first period from 0 to 1500 iterations present an average consolidation velocity of 0.43% each 10 iterations. While the second phase from 1500 to 2631 has an average consolidation velocity of 0.22%, half as fast as the first phase. Being SR_{Total} the result of the evaluation of the different constraints, it is also relevant to analyze their individual effects. The constraint that reaches a stable behavior the fastest is the RKE. At iteration 1000 it has already a RKE_{SR}>95%. Since the kinetic energy is a combination of

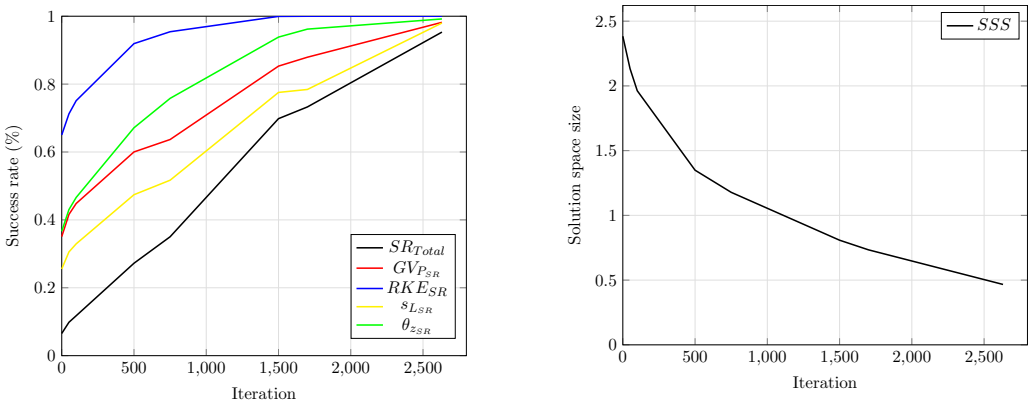

(a) Success rate

(b) Solution space size

Figure 7.19 Total and constraint success rate (a) and solution space size (b) vs. solution space consolidation iteration

several translational and rotational quantities, also several combinations exist to reach a desired range. This constraint is followed by θ_z, which reaches $\theta_{z_{SR}}$>95% 500 iterations later. The s_L and GV_P constraints present a similar consolidation speed, being the deformation length constraint the slowest in reaching $s_{L_{SR}}$>95%. On the other side, the solution space size also presents two phases with different reduction velocities. In the first 1000 iterations the solution space shrinks to less than half the original size, while it takes the rest 1631 iterations to again be reduced to half of the size. This effect coincides with the observations from Figure 7.18 where the difference between the first iterations are more noticeable than the difference between the last ones.

After reaching the target success rate, the consolidated solution space is taken as start point for the expansion phase. Figure 7.20 shows the reference F_{x_L}, F_{y_L} and Y_{eq} as well as the consolidated solution space limits, $\hat{F}_{x_{FV_C}}$, $\check{F}_{x_{FV_C}}$, $\hat{F}_{y_{FV_C}}$, $\check{F}_{y_{FV_C}}$ and $\hat{Y}_{eq_{FV_C}}$, $\check{Y}_{eq_{FV_C}}$ and the final expanded limits, $\hat{F}_{x_{FV_E}}$, $\check{F}_{x_{FV_E}}$, $\hat{F}_{y_{FV_E}}$, $\check{F}_{y_{FV_E}}$ and $\hat{Y}_{eq_{FV_E}}$, $\check{Y}_{eq_{FV_E}}$. Figure 7.20(c) makes evident that the expanded version of the solution space is considerably larger than the consolidated version for $\hat{Y}_{eq_{FV_E}}$ and $\check{Y}_{eq_{FV_E}}$. In this case, the additional computational cost of conducting an expansion phase shows its benefits. Figure 7.18(c) already indicated the possibility of finding feasible designs at the deformation region above 1200mm with a $\check{Y}_{eq_{FV_E}}$ closer to 0. During the consolidation iterations this region was discarded but then recuperated in the expansion phase. Apart from this, only marginal gains are made for the expanded versions of the longitudinal and transversal forces.

In this application and to evaluate the efficacy of the method, the solution space should yield to *RDC* that coincide with the reference curves. An inspection of Figure 7.20 points to the conclusion that even if the reference curves are not completely enclosed by the

expanded solution space along the complete deformation space, the curve characteristics obtained from the solution space capture well the characteristics of the reference curves. The longitudinal forces solution spaces capture well the local minimum present at 650mm as well as the local maximum at 500mm. The largest deviations are present in the wheel region, where even though the increasing nature of the force levels is present in the solution space, the maximum forces do not fully coincide. Eventually, a reference curve with a filter with a larger window size could take out the oscillations that generate the difference to the solution space. However, as seen previously, the filtering of the *RDC* has also its limits when maintaining the accuracy of the output of the low-fidelity kinematic model. Concerning the transversal forces, the effect of the selected discretization of the deformation space also becomes evident. The maximum value of the first phase of F_{y_L} is achieved when s is ca. 350mm. Yet, the two nearest points in the s vector are 50mm apart. Therefore, this local maximum cannot be captured entirely. At the wheel region, the oscillations issue seen in the longitudinal forces is also present. This time, the solution space overestimates the forces needed in this region while at the same time capturing the increasing nature of the reference curve. The largest deviation takes place in the early section of $\check{Y}_{eq_{FV_E}}$. A local minimum at ca. s=75mm is not captured by the solution space. A possible solution for such issues is to increase the number of samples used in each consolidation iteration to increase the probability of also detecting such feasible designs.

Even though the constraint fulfillment guarantees that the kinematic parameters should lie within a certain range, it is also important to confirm that the curve characteristics of the kinematics produced by *RDC* within the design space also coincide with the references. Figure 7.21 shows the complete set of reference kinematic outputs including the DOFs and kinematic parameters as well as the kinematic response obtained from sampling the expanded solution space. The comparison is done explicitly from the results of the kinematic model and not to the reference hardware test to isolate the error produced by the solution space calculation from the error introduced by the kinematic model itself. For every curve, the differences are not significant and the curve characteristic in the reference kinematic model is also present in the samples from the expanded solution space. Only for GV_P and θ_z an observable difference exist for the time range from 30ms to 80ms. Both kinematic parameters are functions of the moment applied at the CG. The deviations observed in the early deformation stages for Y_{eq} affect the moment calculation directly and are therefore a possible cause for the difference in the time series.

As final check of the quality of the solution space calculation, the space within the upper and lower limits is sampled and the distribution of the scatter of the kinematic parameters at t_{end} is presented in Figure 7.22. The distributions show that as expected that at least 95% of the data is contained in the range defined by the constraint for each kinematic parameter. Nonetheless, in cases such as s_L an observable portion of the distribution exists outside the constraint range, specially towards the lower limit of the constraint. Signifying that a portion of the samples inside the solution space would still yield unfeasible solutions. However, by means of the introduced solution space methodology, this portion of unfeasible designs can be quantified and reduced. In this

section, the solution space calculation was validated at the full-vehicle level, in the next section the validation at the load-path level is carried out.

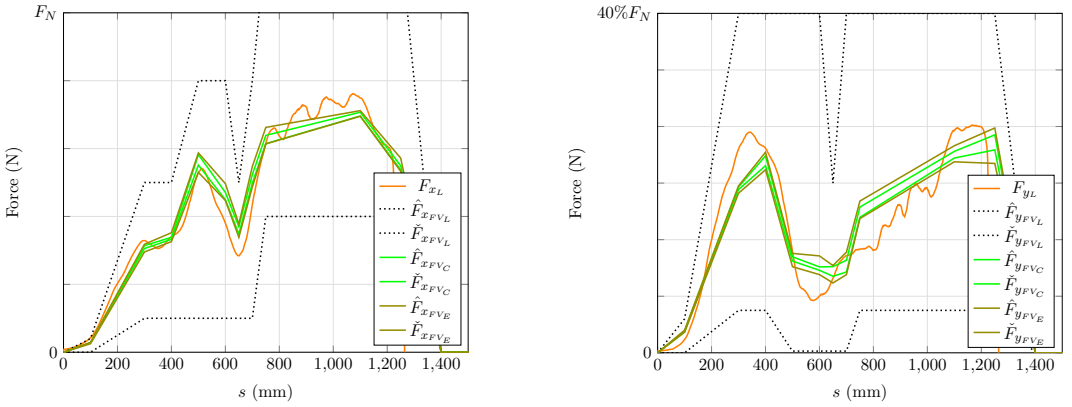

(a) Longitudinal forces vs. deformation space (s)

(b) Transversal forces vs. deformation space (s)

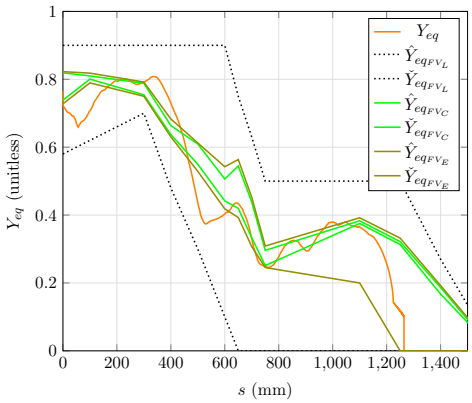

(c) Equivalent point of application of longitudinal force vs. deformation space (s)

Figure 7.20 *RDC* Consolidated and expanded solution space and reference: reference F_{x_L}, F_{y_L} and Y_{eq} as well as the consolidated solution space limits, $\hat{F}_{x_{FV_C}}$, $\check{F}_{x_{FV_C}}$, $\hat{F}_{y_{FV_C}}$, $\check{F}_{y_{FV_C}}$ and $\hat{Y}_{eq_{FV_C}}$, $\check{Y}_{eq_{FV_C}}$ and the final expanded limits, $\hat{F}_{x_{FV_E}}$, $\check{F}_{x_{FV_E}}$, $\hat{F}_{y_{FV_E}}$, $\check{F}_{y_{FV_E}}$ and $\hat{Y}_{eq_{FV_E}}$, $\check{Y}_{eq_{FV_E}}$.

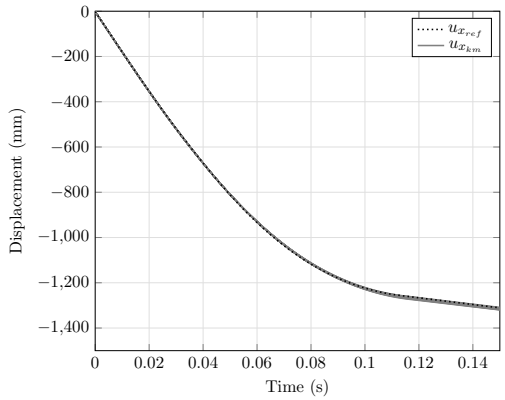

(a) Longitudinal displacements

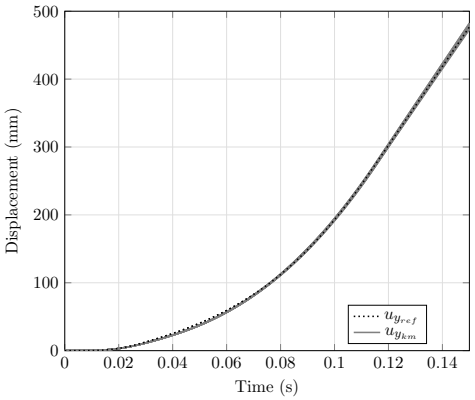

(b) Transversal displacements

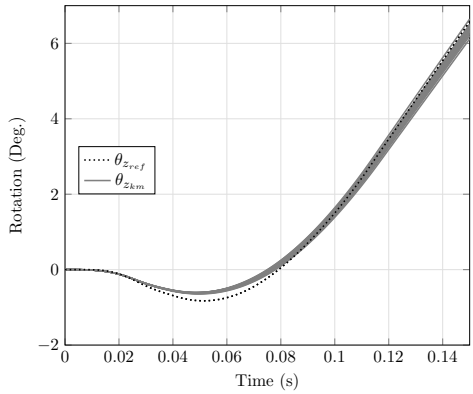

(c) Total rotation

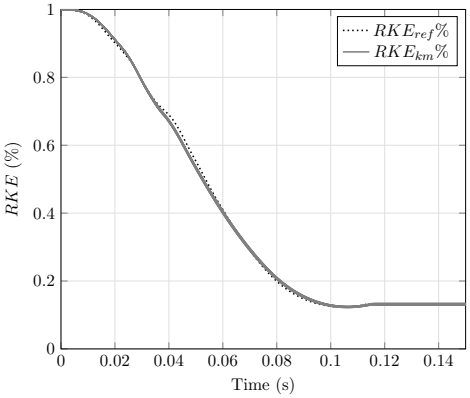

(d) Rest kinetic energy

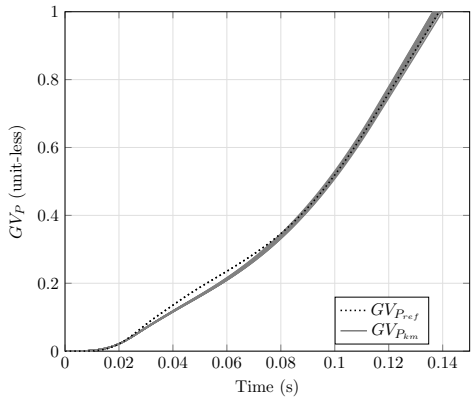

(e) Glance-off value

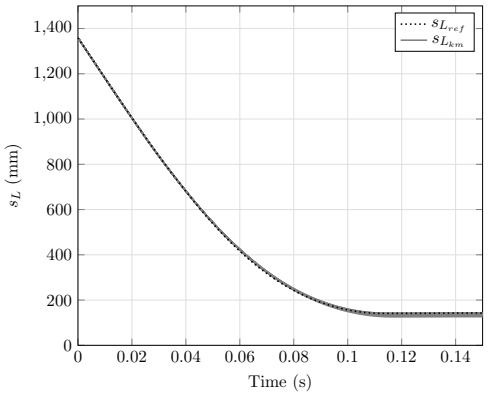

(f) Rest deformation length

Figure 7.21 Kinematic model (km) and reference (ref) sampled solution space longitudinal, u_x (a), transversal displacements, u_y (b), total rotation, θ_z (c), rest kinetic energy, RKE (d), glance-off value GV_P (e), rest deformation length s_L (f)

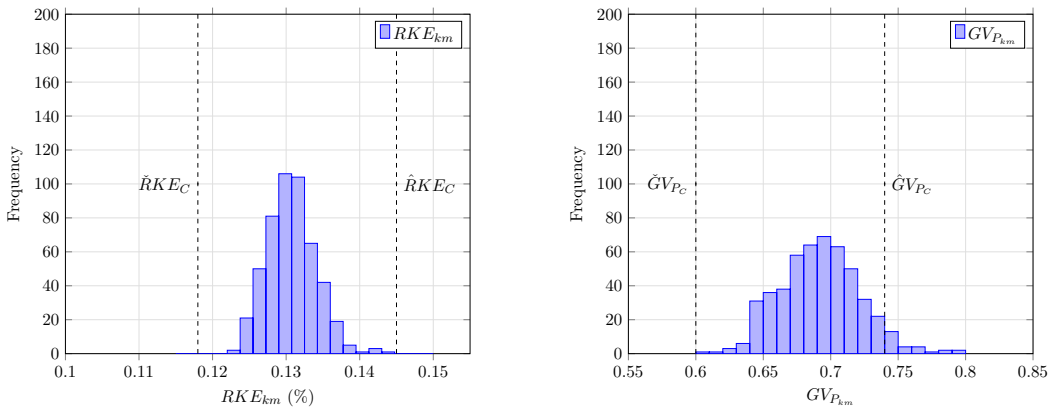

(a) Rest kinetic energy percentage

(b) Glance-off value

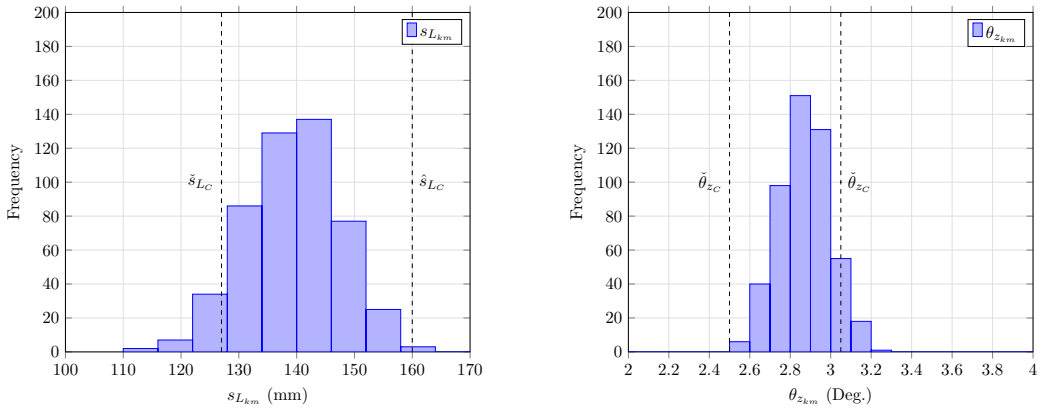

(c) Rest deformation length

(d) Total rotation

Figure 7.22 Kinematic parameter constraint check: rest kinetic energy, RKE (a), glance-off value, GV_P (b), rest deformation length, s_L (c), total rotation, θ_z (d)

7.2.2. Load-path Level

The solution space obtained from the calculation at the full-vehicle level, i.e. $\hat{F}_{x_{FV}}$, $\check{F}_{x_{FV}}$, $\hat{F}_{y_{FV}}$, $\check{F}_{y_{FV}}$, $\hat{Y}_{eq}$ and $\check{Y}_{eq}$, is used as constraints for the solution space calculation at the load-path level. As stated in Section 5.1.2, the methodology takes advantage of the possibility of property matching among the levels. The sum of the transversal and longitudinal forces of the j load-paths, $F_{x_{LP_j}}$, $F_{y_{LP_j}}$, must be equal to the total force at the full-vehicle level. At the same time, the position of the load-level together with its position across the structure must yield to the equivalent point of application of the longitudinal force. By evaluating these three constraints for each deformation level in the RDC, the exploration, consolidation, and expansion phases are carried out using the same vehicle characteristics as for the reference case. The same discretization of the deformation vector s as the one in the full-vehicle calculation is used at the load-path level. To evaluate the quality of the solution space, the transversal and longitudinal forces for each load-path used in Section 7.1.7 to validate the kinematic model, are compared against the obtained upper and lower limits.

The results obtained by the solution space calculation are shown in Figures 7.23 and 7.24 for the longitudinal and transversal forces correspondingly. As in the full-vehicle level, the design bounds, $\hat{F}_{x_{LP_{j_L}}}$ and $\check{F}_{x_{LP_{j_L}}}$ are selected for each load-path. As before the wheel-firewall-rocker load-path is dominant. This is also reflected in the selection of the upper and lower design bounds selected for this load-path. Considering the longitudinal force and at the first and second deformation phases, a relatively high and constant load-level is selected as upper design bound. Nonetheless, the expected drop in the force-levels at 650mm caused by the topology of the structure and suspension of the vehicle is also characterized. The deformation phase related to the wheel area includes the definition of a lower bound whose role is to assure that a minimum force level is considered from the wheel-structure interaction. The transversal upper and lower design bounds of the wheel load-path also follow a similar logic with the exception that only the wheel-region has a significant upper bound while the first deformation stages are only characterized by a relatively low upper bound.

The rest of the load-paths has a lower design bound defined as zero for the entirety of the deformation space. The upper bound is the one that follows, to a certain extent the characteristics of the reference curve. The shotgun and sub-frame load-paths present an initial increase in the force levels and for the rest of the deformation space, they have a constant upper bound until the load-path is no longer considered active. The bumper-beam load-path however, has for both the longitudinal and transversal forces a maximum value for the upper bound at 300mm. Before and after reaching this peak a linear increase and decrease is implemented to define the load-levels of the rest of the deformation space.

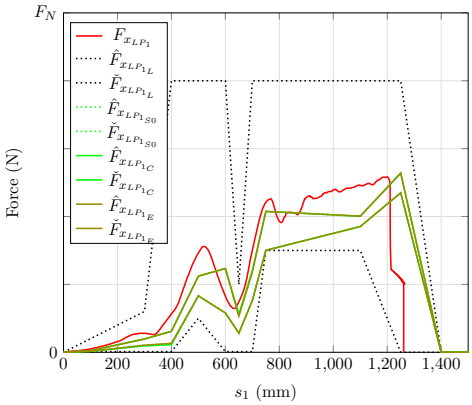

(a) Load-path 1: wheel-firewall-rocker longitudinal forces vs. deformation space (s_1)

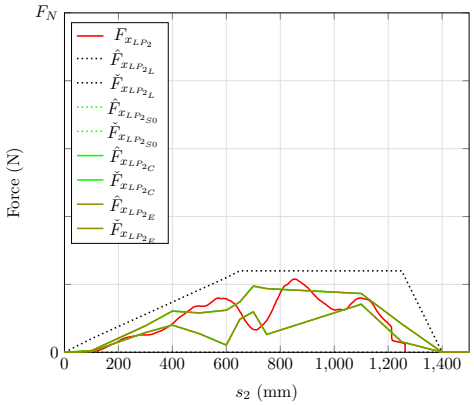

(b) Load-path 2: shotgun longitudinal forces vs. deformation space (s_2)

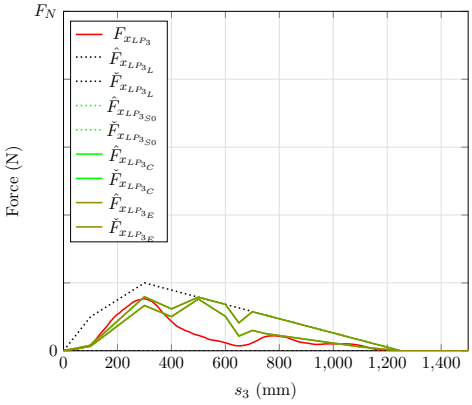

(c) Load-path 3: bumper beam-front rail longitudinal forces vs. deformation space (s_3)

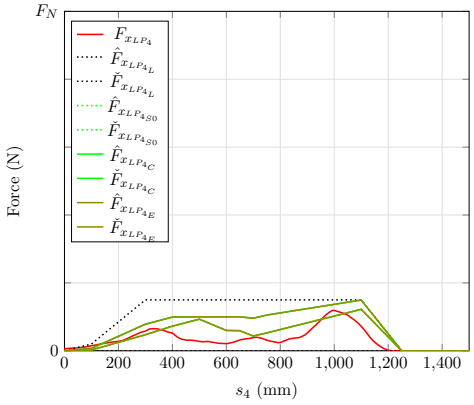

(d) Load-path 4: sub-frame longitudinal forces vs. deformation space (s_4)

Figure 7.23 Design space limits (L), exploration ($S0$), consolidation (C), and expansion (E) phases of solution space as well as reference curves for the longitudinal $\hat{F}_{x_{LP}}$, $\check{F}_{x_{LP}}$ forces of the load-paths wheel-firewall-rocker(a), shotgun(b), bumper beam-front rail (c), sub-frame(d)

The results from exploration phase $\hat{F}_{x_{LP_{jS0}}}$, $\check{F}_{x_{LP_{jS0}}}$, $\hat{F}_{y_{LP_{jS0}}}$ and $\check{F}_{y_{LP_{jS0}}}$ provide the first indications of the location of the feasible regions. Starting with the wheel load-path, the regions with higher force levels which are closer to the upper design bound are discarded moving the exploration solution space towards the lower bounds. That is the case for both longitudinal and transversal forces. In contrast, for the other load-paths in the longitudinal forces, the solution space tends to move towards the upper design bounds. This phenomenon is most evident for the bumper beam-front rail. The exploration solution space is in some regions of the deformation space even above the reference

curves. These regions, where $\check{F}_{x_{LP_{3_{S0}}}}$ overestimates the reference force-levels, coincide with a slight underestimation of the longitudinal forces at the wheel load-path. The shotgun and sub-frame load-paths yield solution space towards the upper bounds. On the other side the upper and lower limits of the exploration solution space for the transversal forces show a relatively good agreement with the reference curves. The maximum force of the bumper load-path is particularly well characterized by $\check{F}_{y_{LP_{3_{S0}}}}$ and $\hat{F}_{y_{LP_{3_{S0}}}}$.

The consolidated solution space $\hat{F}_{x_{LP_{j_C}}}$, $\check{F}_{x_{LP_{j_C}}}$, $\hat{F}_{y_{LP_{j_C}}}$ and $\check{F}_{y_{LP_{j_C}}}$ does not deviate significantly from the exploration phase results. Only a symmetrical reduction of the size of the solution space is observable while the curve characteristics remain unchanged. The expanded version $\hat{F}_{x_{LP_{j_E}}}$, $\check{F}_{x_{LP_{j_E}}}$, $\hat{F}_{y_{LP_{j_E}}}$ and $\check{F}_{y_{LP_{j_E}}}$ only offer marginal gains along the deformation space. In contrast to the full-vehicle stage, the load-path solution space calculation is governed by the result obtained from the exploration phase. This effect can be explained by several factors. On one side, the number of variables to describe the *RDC* at the load-path level increases from 78 at the full-vehicle level to 104. On the other side, and due to the decomposition of the forces into load-paths the individual solution space sizes decreases. And at the same time the number of constraints increases from 10 at the full-vehicle level considering lower and upper limit of the kinematic parameters range to 84 at the load-path level. Despite of these factors, the final solution space obtained yields the selected target for the success rate and captures well the characteristics of the force-level in the load-paths and provides an efficient method to map the full-vehicle *RDC* into subsystems and components.

As a final check the expanded solution space is sampled at the load-path level and the total sum of forces and calculation of the equivalent force application point is carried out. Figure 7.25(a) shows that the sum of the forces matches to the full vehicle *RDC* design space, $\hat{F}_{x_{FV_E}}$, $\check{F}_{x_{FV_E}}$, $\hat{F}_{y_{FV_E}}$ and $\check{F}_{y_{FV_E}}$. While Figure 7.25(b) shows that the reconstructed equivalent application point exists between $\hat{Y}_{eq_{FV_E}}$ and $\check{Y}_{eq_{FV_E}}$. With this, the validation of the solution space calculation is concluded. In the next section, this validated methodology integrated into the complete Solution Space-based Iterative Simulation Scheme is applied for the development of a vehicle structure with the target of achieving a robust fulfillment of the structural rating targets.

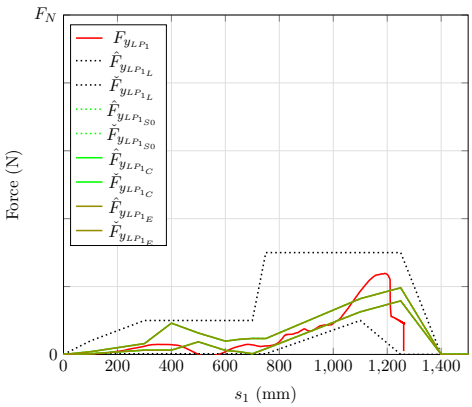

(a) Load-path 1: wheel-firewall-rocker transversal forces vs. deformation space (s_1)

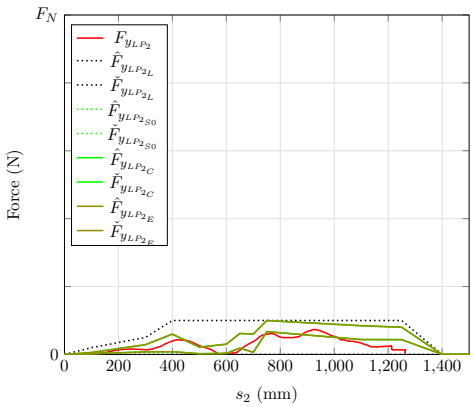

(b) Load-path 2: shotgun transversal forces vs. deformation space (s_2)

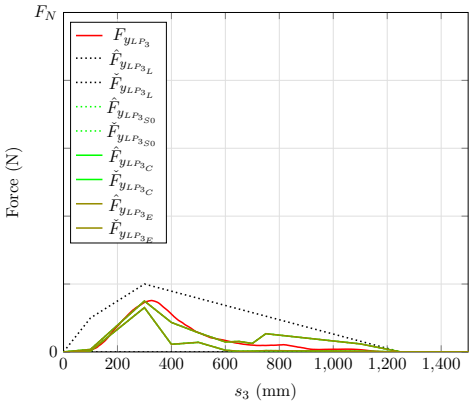

(c) Load-path 3: bumper beam-front rail transversal forces vs. deformation space (s_3)

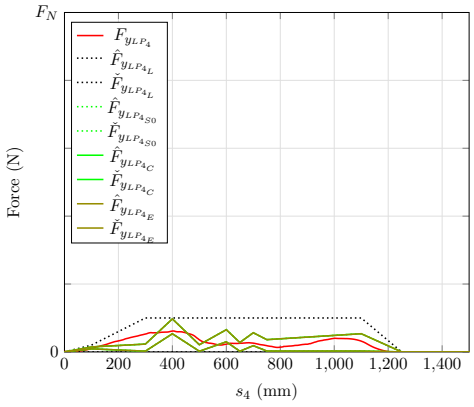

(d) Load-path 4: sub-frame transversal forces vs. deformation space (s_4)

Figure 7.24 Design space limits (L), exploration ($S0$), consolidation (C), and expansion (E) phases of solution space as well as reference curves for the transversal $\hat{F}_{y_{LP}}$, $\check{F}_{y_{LP}}$ forces of the load-paths wheel-firewall-rocker(a), shotgun(b), bumper beam-front rail (c), sub-frame(d)

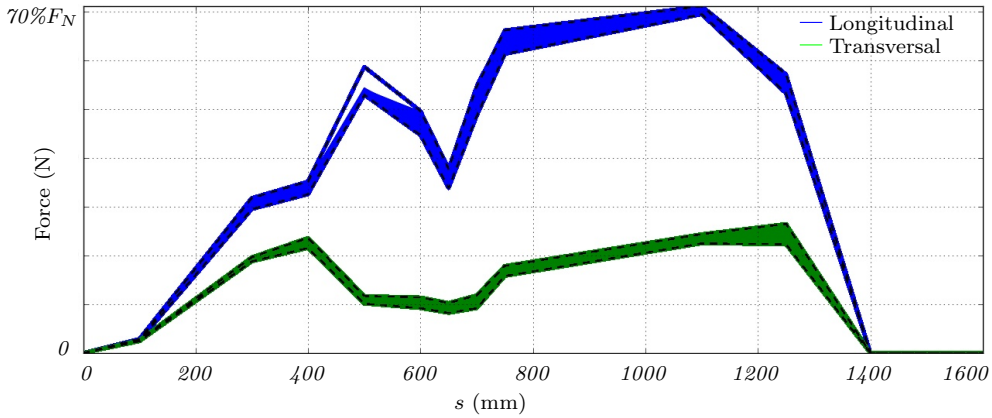

(a) Reconstructed longitudinal and transversal full-vehicle forces

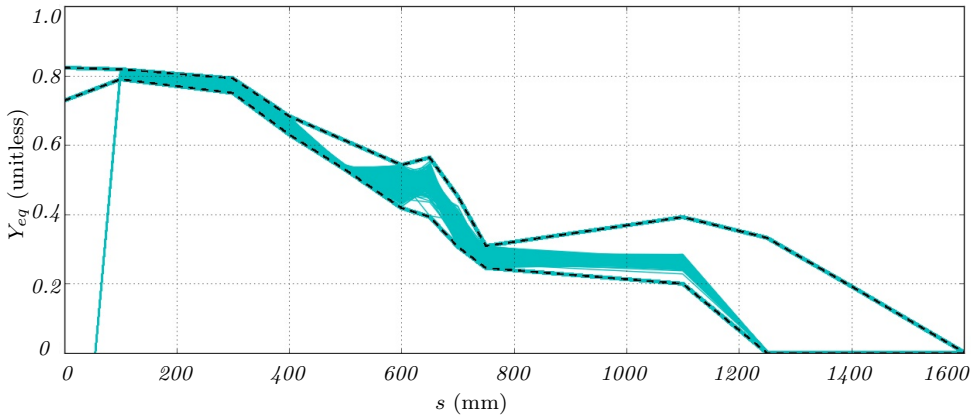

(b) Reconstructed equivalent point of application of longitudinal force

Figure 7.25 Comparison of sum of load-path and full-vehicle longitudinal and transversal forces (a) and equivalent point of application of longitudinal force (b)

Chapter 8

Results

After the validation of the low-fidelity kinematic model and the solution space methodology in the previous section, in this section the probabilities of a robust target achievement of a vehicle are increased through the redesign of its structure by applying the solution space-based iterative simulation scheme. The SSBISS is applied to a mature structural design where robustness deficiencies were identified. First, the load case targets for the structural redesign are defined. Then, the performance of the base structure is analyzed and quantified through the use of an Abaqus Explicit FEM. The kinematic response as well as the structural rating with its correspondent D_{SG} are reported and quantified. Next, the robustness of the performance of the vehicle is analyzed by following the methodology described in Section 6.2. The resistance-to-deformation characteristics are extracted at the full-vehicle and load-path level. Additionally, the relevant sources of uncertainty are identified and characterized and the robustness index is calculated for the relevant outputs. Once the base performance of the vehicle is completely characterized, areas that allow topology and RDC changes needed for the fulfillment of the new targets are identified. Later, the RDC solution space that ensures the fulfillment of the structural and kinematic requirements is calculated. Then, the structural changes that lead to the fulfillment of the solution space are implemented in the FE model. Finally, the robustness of the structural changes are characterized and studied.

8.1. Requirement Definition

The relationship between the kinematics of the vehicle during the crash, represented by the kinematic parameters, and its structural performance expressed as the safety distance to a Good structural rating, D_{SG}, in the Small Overlap load case is identified and presented in Section 5.2.1. This relationship allows for the use of the solution space methodology to find the set of RDC that produces a certain kinematic response that lies inside regions in the kinematic parameters space that maximize the probabilities of

obtaining a certain D_{SG}. The cluster analysis indicates that vehicles having relatively high kinetic energy values at the end of the crash, i.e. RKE>30%, minimize the probabilities of obtaining a structural rating different than Good. It is also established that the statistics of the vehicles analyzed showed that a relatively high value of RKE is possible only through certain combination of vehicle rotation, θ_z and Glance-off value, GV_P.

The primary load case target is to achieve a Good structural rating. Meaning that the full vehicle structural target is to obtain a D_{SG}>30% so that the performance of the vehicle matches the industry standard. This primary target must be achieved with the explicit consideration of the uncertainty parameters that affect the performance in the Small Overlap load case, leading to a robust design. This primary target is mapped to the kinematic performance, consequently defining a secondary target of achieving a RKE>30%. This secondary target is decomposed into requirements for the load-levels in each load-path by the calculation of a solution space for the RDC. In the next section the base performance of the vehicle is analyzed with their correspondent possible strategies to accommodate the necessary structural changes that lead to the ultimate goal of achieving the primary load case target.

8.2. Base Design

The starting point for the SSBISS is in this application example a full-vehicle FE model defined in Abaqus Explicit. The characteristics of the model are in line with the characteristics of the vehicle presented in Table 7.1 used in the validation procedures. The FE model contains the subsystems relevant for this load case. In order to generate a baseline for the vehicle performance and to follow the principles defined in the SSBISS a set of 10 simulations is generated with different time steps. A variation of ± 0.0001% from the original time step is introduced to consider the numerical effects of the use of the explicit FE model from the beginning. These numerical effects are defined in Section 6.2.1 as one of the sources of uncertainty that affect the response of the vehicle and that are relevant in the virtual design process. Even if different FE solvers and modeling techniques may yield different sensitivities to the outcome, this approach allows for a more meaningful comparison of the effects of the other sources of uncertainty to the effects of pure numerical variations.

8.2.1. Vehicle Kinematics

The kinematic analysis is performed for the set of 10 simulations where the numerical uncertainty, num, is characterized. In each case a GV_P<1, and therefore a deformation kinematic mode is present. The variation of the time series of the kinematic parameters can be observed in Figure 8.1. From 0 to 80ms the values of θ_z, RKE, GV_P, and s_L for the simulations lie relatively close to each other. After 80ms, the total rotation, glance-off value, and rest deformation length present an observable deviation. The kinetic energy time series shows the least amount of variation relative to the other kinematic parameters. Despite of these variations, the curve characteristic is conserved in every case. This subjective appreciation of the variation in the outcome of the numerical

uncertainty phase are later quantified by means of the robustness index at the curve and scalar level in Section 8.2.4.

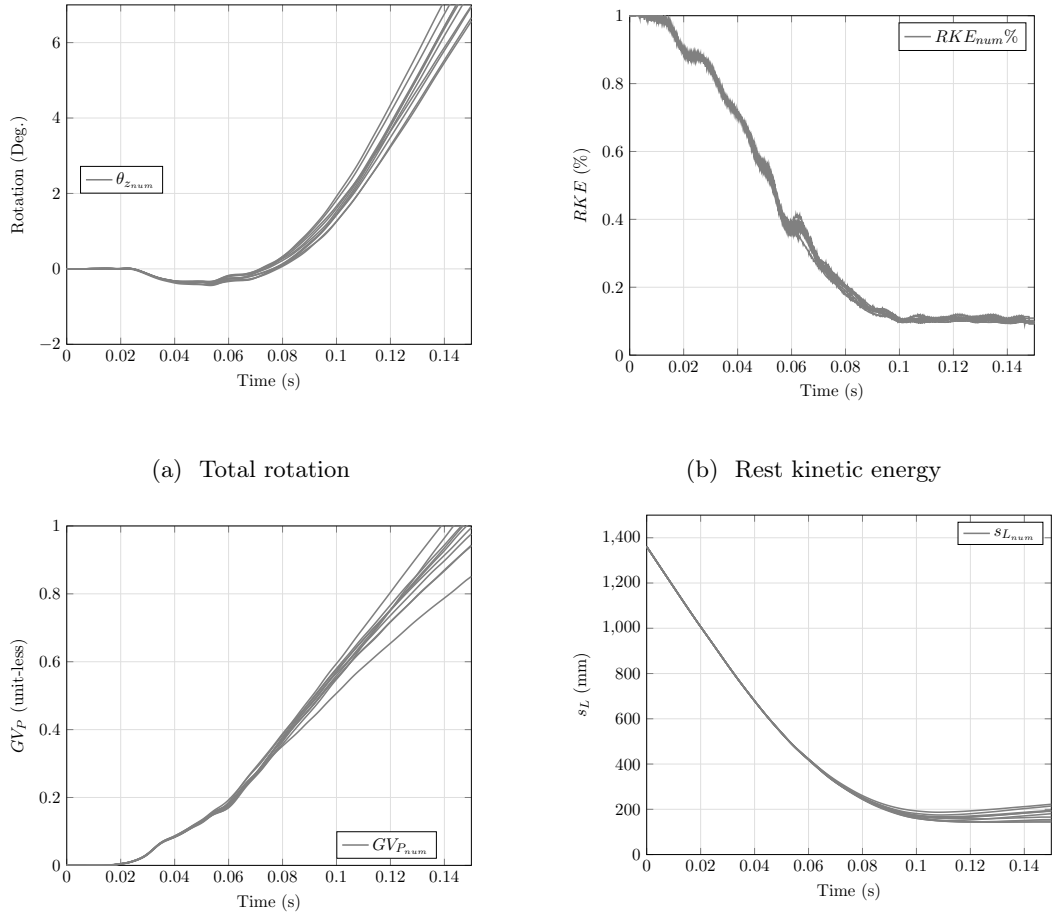

(a) Total rotation

(b) Rest kinetic energy

(c) Glance-off value

(d) Rest deformation length

Figure 8.1 Kinematic parameters extracted from base simulation after applying a time step variation (num), total rotation, θ_z (a), rest kinetic energy, RKE (b), glance-off value GV_P (c), rest deformation length s_L (d)

The values measured at t_{end} are presented in Figure 8.2. The RKE values as observed in their curve representation lie close to each other and have an average of 11%, relatively far apart from the target of 30%. The GV_P shows a range from 0.6 to 0.9, which indicates that even if the base design is far from a glance-off behavior, if the right combination of wheel kinematics and rupture takes place, the behavior can be close to the glance-off. The total rotation θ_z shows that even if there are glance-off values that are close to 0, a positive rotation indicates that the total longitudinal and transversal forces and their correspondent moment are not enough to produce a negative rotation that moves the

vehicle away from the barrier. The s_L>0 values indicate that there is no hard contact present between the A-Pillar and the barrier, which is also confirmed by the results obtained from calculating the structural rating and D_{SG}.

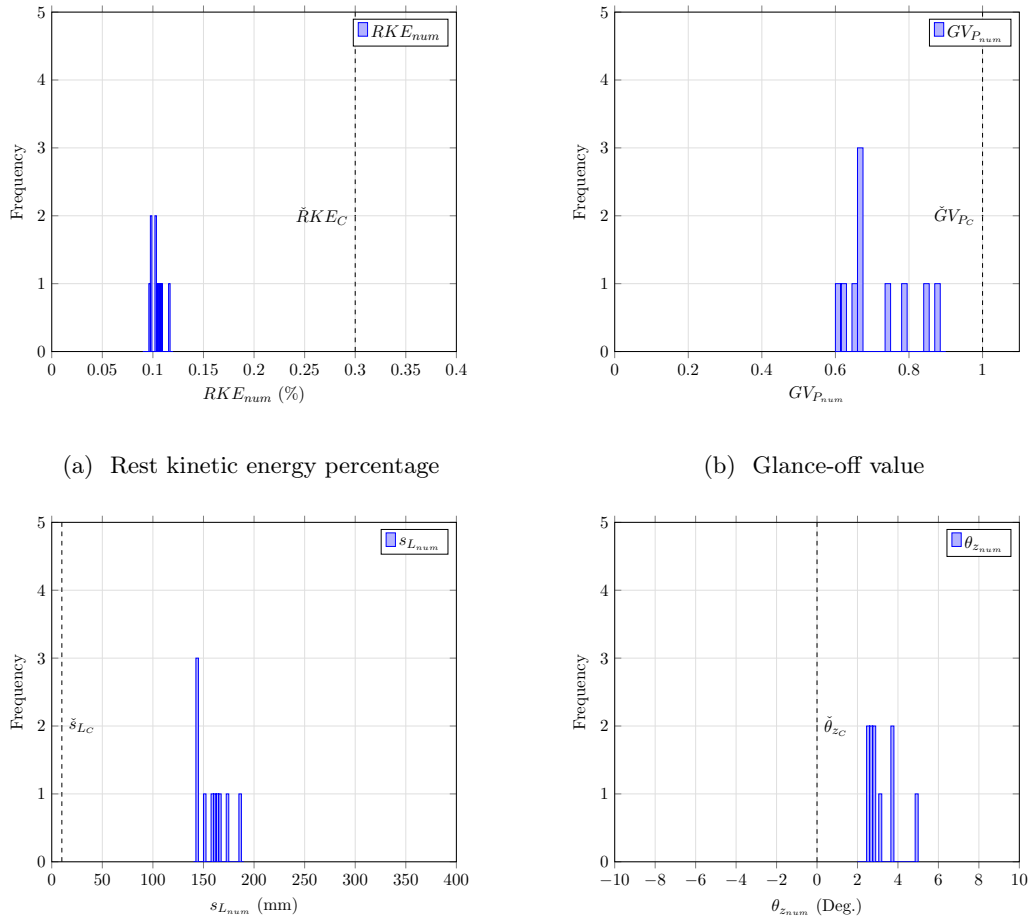

(a) Rest kinetic energy percentage

(b) Glance-off value

(c) Rest deformation length

(d) Total rotation

Figure 8.2 Kinematic parameters extracted from base simulation: rest kinetic energy, RKE_{num} (a), glance-off value, $GV_{P_{num}}$ (b), rest deformation length, $s_{L_{num}}$ (c), total rotation, $\theta_{z_{num}}$ (d)

8.2.2. Structure Topology & Resistance-to-deformation Characteristics

To make the implementation of the structural changes possible, the first step is to extract the longitudinal and transversal forces as a function of the deformation of the structure at the full-vehicle and load-path levels. In the same manner as in the previous chapter, the force levels are presented in a normalized format, taking as reference the maximum total force in the F_x time series and represented by F_N. In the case of the full-vehicle

level the equivalent point of application of longitudinal force is also extracted. As stated previously, the location of the components as well as the load carrying capacities result in the different force-levels across the structure. At the full-vehicle level, Figure 8.3(a) depicts the total longitudinal force along the structure. The minimum and maximum values are plotted in the force-displacement diagram to represent the variation from the simulation set. These longitudinal force signal begins with a significant load level at 200mm and continues with a steady increase until 500mm where a drop is present. Afterwards, the maximum force-levels in the curve are reached at ca. 850mm. A slight decay from the maximum levels leads the way to a plateau until 1100mm where a drop to zero in the forces indicates that the vehicle has started its global rebound phase.

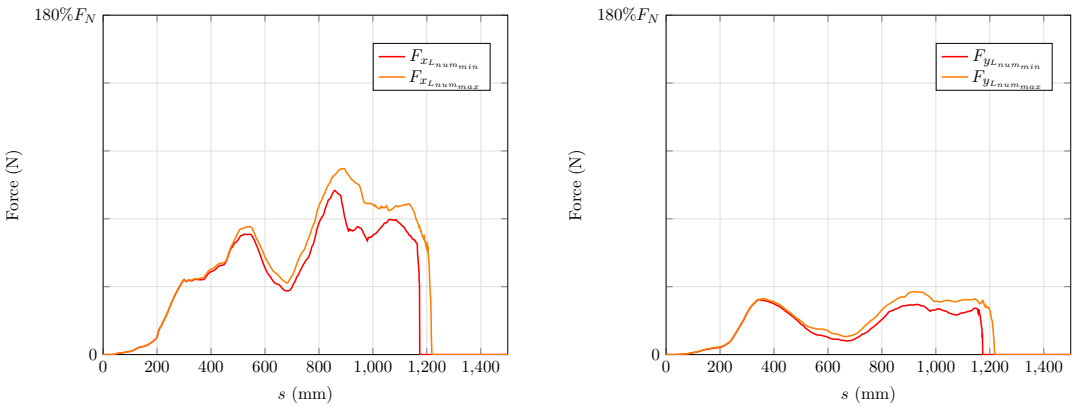

(a) Longitudinal forces vs. deformation space (s)

(b) Transversal forces vs. deformation space (s)

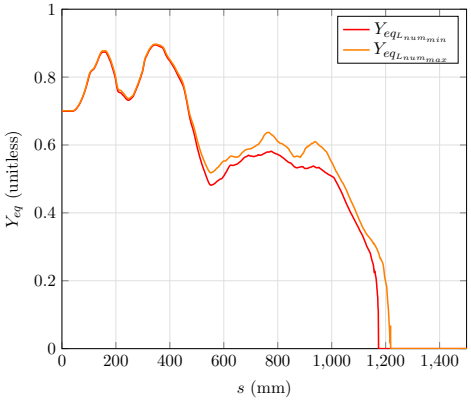

(c) Equivalent point of application of longitudinal force vs. deformation space (s)

Figure 8.3 *RDC* at full-vehicle level extracted from base simulation: longitudinal (a), transversal (b) forces and Y_{eq}(c)

The longitudinal forces, similarly to their longitudinal counterparts present an increase starting at 200mm but ending at 300mm. A minor decay is present in the force signal until 500mm, where similarly to F_{x_L} the last increase takes place. The transversal forces are maintained until the rebound phase begins. Regarding Y_{eq}, it can be observed in Figure 8.3(c) that two clear phases characterize the equivalent point of application of force. The first one from 0 to 400mm has an oscillating nature with an average Y_{eq}=0.75, which indicates an inwards application of the force. From 600mm until the rebound phase, Y_{eq} drops to ca. 0.55, indicating the presence of a inwards rotating wheel, which as it will be observed in the next subsection can cause an increased intrusion in the lower occupant compartment.

The load-path level analysis yields as in the hardware test analysis that the wheel-firewall-rocker is the dominant load-path. The longitudinal force of this load-path presented in Figure 8.4(a) indicates that two main components influence the characteristic of the force-displacement curve. The first one is the supporting-frame attached sideways to the front rail and sub-frame. The increase in force starting at 400mm and culminating with the local maximum present at 500mm is a consequence of the contact of the barrier and the supporting-frame, its bending, contact with the tire and displacement of the wheel backwards towards the firewall. The second one is clearly the wheel itself and its interaction with the BIW. The difference between the maximum and minimum forces extracted from the simulation set is larger from 800mm until the end of the crash, which is the wheel-dominated region. These deviations are considerably larger than the deviations observed in any other load-path. The slightly different trajectories of the wheel introduced by the numerical variations result in different contact points with the structure as well as different loading angles triggering different failure modes of the wheel.

The second set of significant contributors of longitudinal force are the bumper beam-front rail and sub-frame load-paths. The bumper load-path is specially relevant in the first deformation phase from 200mm to 600mm. After the bumper is bent and the front structure continues to slide, the force-levels of this load-path drop. The sub-frame contribution to the longitudinal forces is twofold. The first contribution occurs from 200mm to 600mm where the sub-frame itself and suspension rods contact the barrier. Later at 800mm the rest block formed by the partially detached suspension rods are compressed against the BIW. At this stage the scattered behavior introduced by the wheel load-path is also reflected. The shotgun load-path contributes relatively less to the longitudinal and also to the transversal forces.

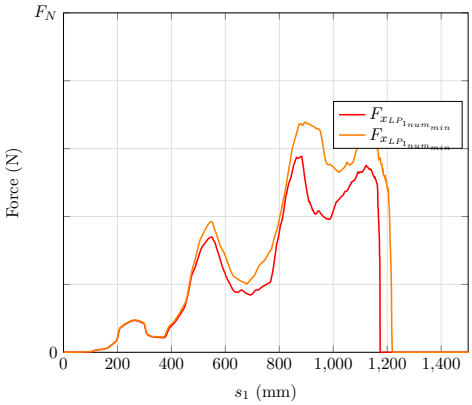

(a) Load-path 1: wheel-firewall-rocker longitudinal forces vs. deformation space (s_1)

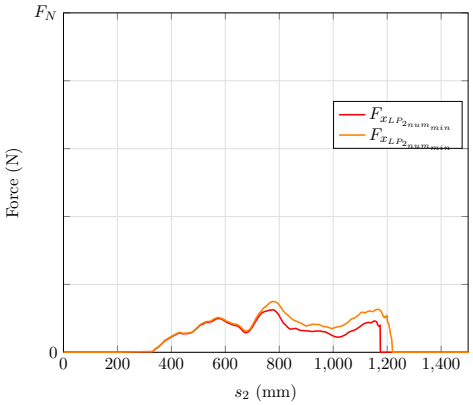

(b) Load-path 2: shotgun longitudinal forces vs. deformation space (s_2)

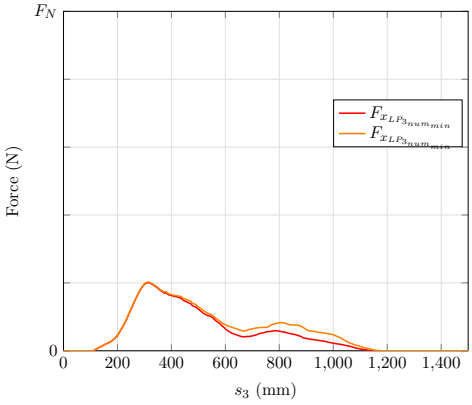

(c) Load-path 3: bumper beam-front rail longitudinal forces vs. deformation space (s_3)

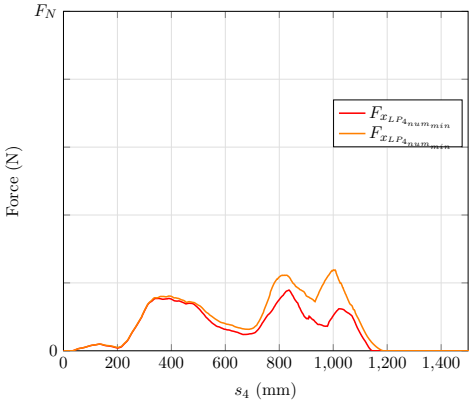

(d) Load-path 4: sub-frame longitudinal forces vs. deformation space (s_4)

Figure 8.4 *RDC* extracted from base simulation: longitudinal forces for load-paths wheel-firewall-rocker(a), shotgun(b), bumper beam-front rail (c), sub-frame(d)

The load-path transversal forces shown in Figure 8.5 indicate that the wheel-load-path only makes significant contributions at its later stage. This means that the supporting-frame is only contacting the flat surface of the barrier. It can also be seen that only the wheel rotation and over-all displacement of the vehicle allow this load-path to generate transversal forces. The bumper load-path on the other side is a reflection of its behavior in the longitudinal direction, with a relevance limited to the first 600mm. Similarly, the sub-frame load-path follows the characteristic of F_{x_L} and contributes to the transversal force at early and later stages of deformation.

In most cases, the cost of introducing changes to the BIW are relatively higher due

to the manufacturing constraints than introducing changes to other subsystems of the vehicle that are assembled separately at a later stage. This indicates that changes to the bumper and sub-frame load-paths are easier to implement and industrialize. That makes both load-paths the focus of this structural design exercise.

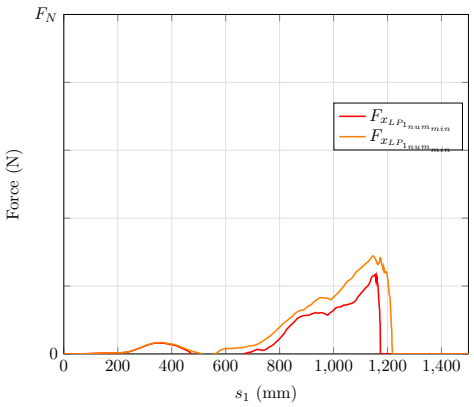

(a) Load-path 1: wheel-firewall-rocker transversal forces vs. deformation space (s_1)

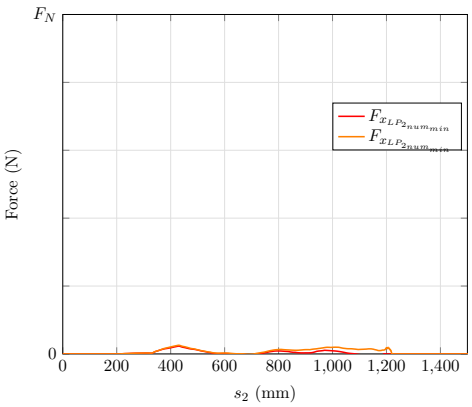

(b) Load-path 2: shotgun transversal forces vs. deformation space (s_2)

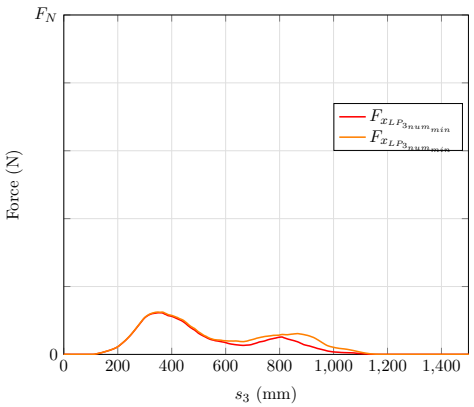

(c) Load-path 3: bumper beam-front rail transversal forces vs. deformation space (s_3)

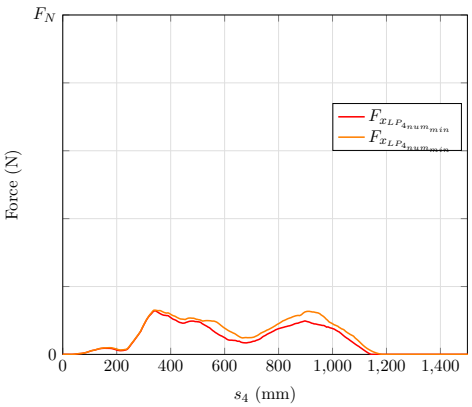

(d) Load-path 4: sub-frame transversal forces vs. deformation space (s_4)

Figure 8.5 *RDC* extracted from base simulation: transversal forces for load-paths wheel-firewall-rocker(a), shotgun(b), bumper beam-front rail (c), sub-frame(d)

8.2.3. Structural Rating and Safety Distance

The values reported for s_L in the previous section are an indication of the absence of a hard contact between the occupant compartment and the rigid barrier. Figure 8.6 shows

the structural rating of the simulation set. A structural rating Good is always achieved. The intrusions are relatively higher at the lower occupant compartment indicating the possibility of an inwards-rotating wheel kinematic. The safety distance $D_{SG_{num}}$ shows a range from 20% to 45%. Although, these results may not appear enough to justify any changes in the structure, the explicit consideration of the other uncertainty sources will make clear that even if in nominal conditions the primary target is achieved, different combinations of parameters may yield to results that miss the target.

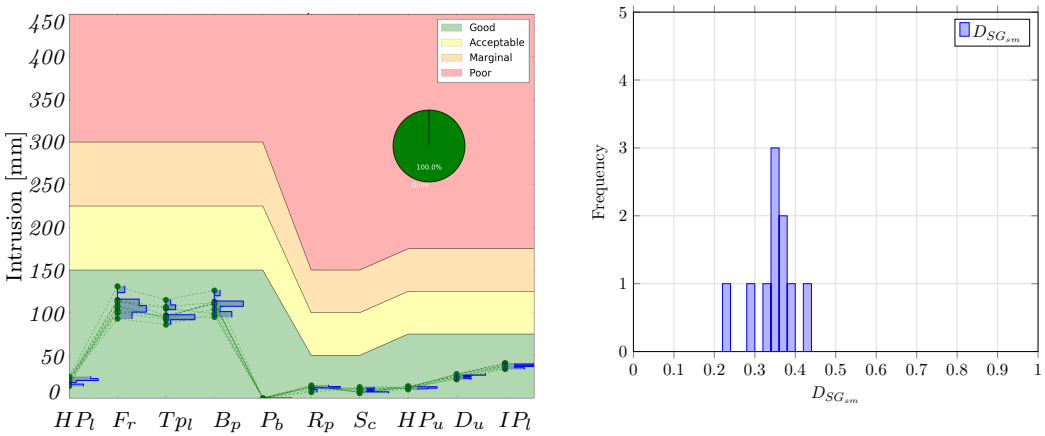

(a) Structure rating (b) Safety distance

Figure 8.6 Structure rating (a) and safety distance,$D_{SG_{num}}$,(b) from base simulation

8.2.4. Robustness Evaluation

The different time-steps used in the simulation set introduce a slight numerical variation in the FE solver that is reflected in the scatter of the kinematic parameters, *RDC* and intrusions. In order to characterize and quantify this variation so that the influence of the relevant sources of uncertainty introduced in Section 6.2.1 can be effectively and efficiently compared, the robustness index defined in Section 6.2.5 is calculated for the kinematic parameters and a selection of variables such as velocities, forces, and intrusions.

The set of 10 curves corresponding to the rest kinetic energy, glance-off value, rest deformation length, and total rotation extracted from the simulation shown in Figure 8.1 are analyzed and the robustness index RB_I is calculated at each time point using the following settings. The reference value from which the deviation from each simulation is calculated is defined as the mean of the complete set. Considering this base, a deviation of $\pm$ 20% with respect to the absolute maximum in the curve is defined as allowable range, i.e. $[lim_{l_t}, lim_{u_t}]$. While the percentage of target achievers is $TA_{acc_{\%}}$=80%. Lastly, a Gaussian distribution is selected to characterize the target distribution.

Figure 8.30(a) shows that the rest kinetic energy percentage for the entirety of its time series has a RB_I closer to 1. This confirms the observations made from Figure 8.30(b).

The glance-off value shows also a RB_I closer to 1 that tends to decay after 112ms. The rest deformation length is also consistently reaching a value of 1 with a slight decay starting at 100ms. The kinematic parameter with the most significant decay in its RB_I is the total rotation. As it is expected, in the early stages of the crash, where the numerical effects have not gained significance and caused any bifurcation points in the behavior, RB_I is close to 1. The decay for this kinematic parameter starts at ca. 50ms and by the end of the simulation at 114ms we have a RB_I of ca. 0.49. Meaning that, as in the case of the other kinematic parameters, the samples distribution is always more compact than the target, i.e. the signal is considered robust. However, the rotation at the end of the simulation reached half the robustness levels observed at the beginning of the simulation. Because the rotations are the result of the total moment applied to the structure, differences in the transversal and longitudinal forces as well as the different lever arms caused by differences in the wheel kinematics, the behavior of this kinematic parameter is understandable.

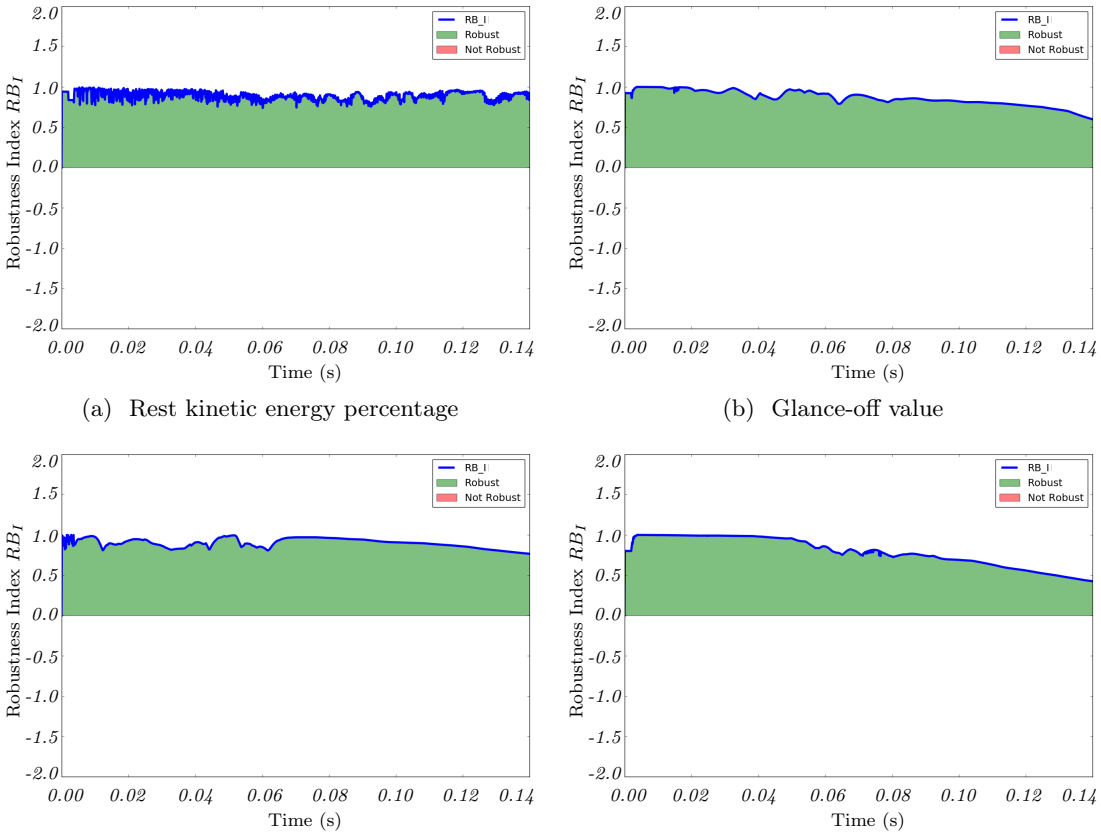

(a) Rest kinetic energy percentage

(b) Glance-off value

(c) Rest deformation length

(d) Total rotation

Figure 8.7 Kinematic parameters robustness index extracted from base simulation: rest kinetic energy, RKE (a), glance-off value, GV_P (b), rest deformation length, s_L (c), total rotation, θ_z (d)

Additionally to the time series representation of RB_I, a scalar representation of the robustness of a selection of relevant variables is presented in Figure 8.8. For the calculation of the robustness index of the intrusion values, t_{end}, local x and y velocities, total moment M_z, global and load-path forces and kinematic parameters the base setting defined to calculate the RB_I for quantities without specific targets is applied. For the kinematic parameters, t_{end} and velocities, the values are taken at the end of crash. For the forces and moments, the values at the maximum deviation points are used. The scalar intrusions are taken directly to calculate their robustness indexes.

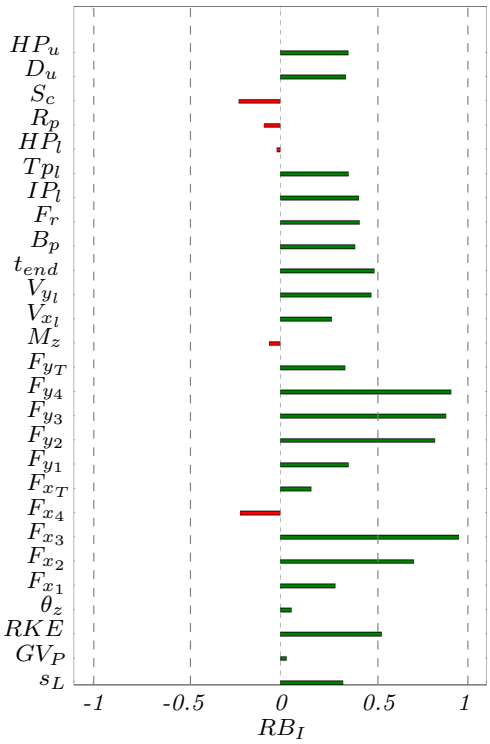

Figure 8.8 Robustness Index for the numerical robustness analysis of the base simulation

The effect of the numerical variations of the FE solver that are present in the output are expected to be negligible, since they are always present in the simulation iterations and are in most cases unavoidable. Considering this, Figure 8.8 only shows 5 quantities with RB_I<0. The intrusion points, steering column, rocker panel, and lower hinge pillar have RB_I values of -0.22, -0.087 and -0.018 respectively. The steering column being the intrusion point with the lowest robustness indicates that the modeling of this particular subsystem is sensitive to small numerical variations introduced by the different time steps and should be improved to increase the robustness of the results. The other two robustness indexes are close enough to zero but also are affected by local deformation at the area of the measurement.

The next quantity to present a negative RB_I is the total moment with a value of

-0.059. The reasons for this behavior mentioned earlier are also backed by the fact that the fifth quantity observing a non-robust behavior is the transversal force of the sub-frame load-path. Even if the deviations of the wheel load-path are also noticeable, the relatively lower force-levels and their deviation in the sub-frame load-path yield a worse RB_I.

With this assessment, the response and robustness of the base model are quantified. In the next subsections, the influence of the other sources of uncertainty is reported and compared against this baseline.

8.2.5. Vehicle Configuration Uncertainty

The exact configuration of the vehicles acquired by the IIHS to conduct the crash tests is not known *a priori*. In many cases, the optional equipment available for a certain vehicle is irrelevant for the crash performance. However, considering the nature of the Small Overlap test, where the initial contact with the barrier only accounts for 25% of the vehicle's width, the suspension components and specially the wheel and brake size become relevant. The influence of different wheel sizes stated in Section 6.2.1 is considered explicitly in this phase of the robustness analysis. The base model included a wheel size of 18 inches, which is the base wheel for this vehicle. Nonetheless, an optional 17 inches wheel is also available for this model. As a consequence, a set of 10 additional simulations, with the same time-step variation as before, is conducted with the smaller wheel size. The robustness index of the kinematic parameters for the configuration uncertainty phase, *con*, is presented in Figure 8.9.

The RB_I time series of the glance-off value and total rotation for the numerical uncertainty analysis present a clear tendency to decay towards the end of the simulation. This effect is maximized at the configuration phase. Both parameters present RB_I values closer to 1 until ca. 60ms. At this point in time, a decay starts and stabilizes until ca. 100ms when the RB_I of both parameters reach a value of 0.25. This value indicates that the samples distribution still meets the prescribed $TA_{acc_{\%}}$ within the acceptable range, but shows clearly that once the wheel-structure interaction becomes dominant, the rotation and glance-off are affected. On the other side, the kinetic energy and deformation length robustness indexes remain similar to the previous phase and for the complete duration of the simulation reaching values closer to 1. A comparison between the absolute values of the parameters is carried out in Section 8.2.8.

The calculation of the RB_I of the selected quantities for this phase is shown in Figure 8.10. The quantities with negative robustness indexes identified in the previous phase are also present in the configuration uncertainty analysis. Two new intrusion points, namely the hinge pillar and upper dash, with negative RB_I join the three intrusion points from the numerical phase. The steering column decreased its RB_I from -0.22 to -0.63, which confirms the need for a more stable modeling.

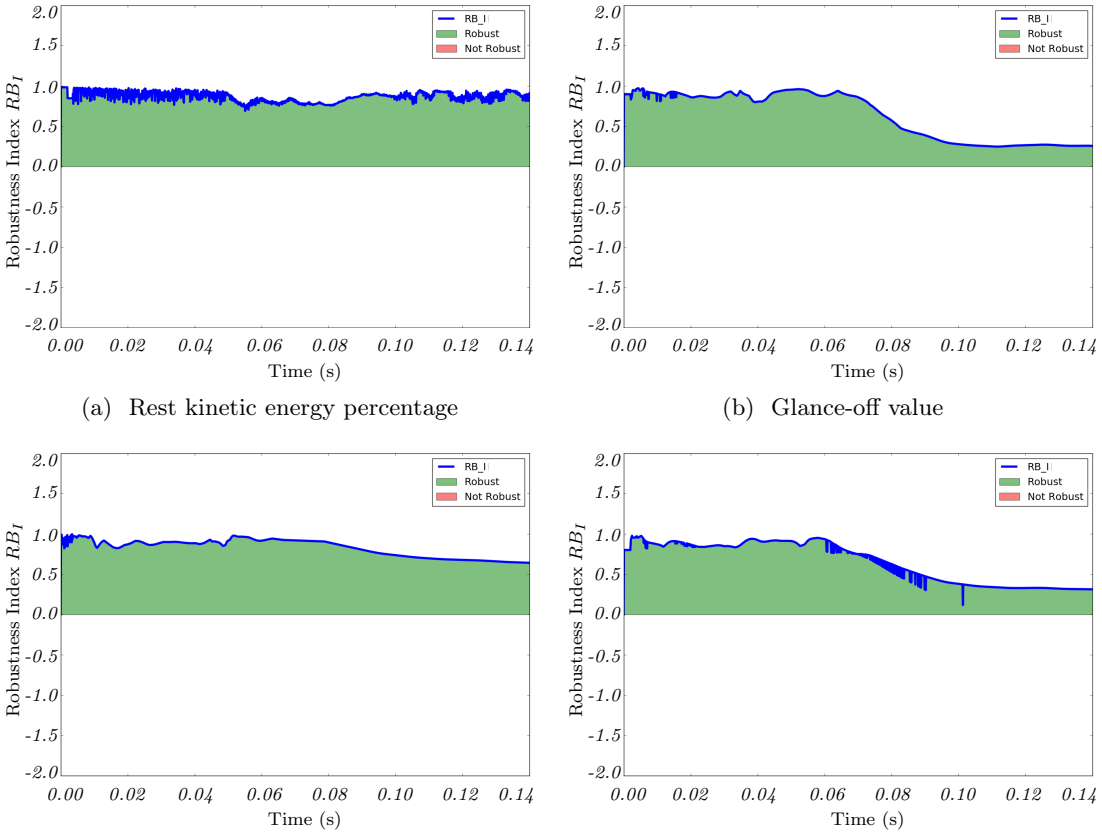

(a) Rest kinetic energy percentage

(b) Glance-off value

(c) Rest deformation length

(d) Total rotation

Figure 8.9 Kinematic parameters robustness index for configuration uncertainty analysis extracted from base simulation: rest kinetic energy, RKE (a), glance-off value, GV_P (b), rest deformation length, s_L (c), total rotation, θ_z (d)

The total moment, M_z also worsened its robustness index. The effect of the small wheel size is to produce variations in the wheel trajectory and the contact point with the structure due to the fact that it has more space to rotate and has larger displacements. This effect is detected with the worsening of the RB_I of the total moment. Additionally, the wheel load-path and its transversal force exhibit a RB_I=-0.82, establishing the decrease of the robustness of the model by the inclusion of the small wheel. The only kinematic parameter presenting a negative RB_I for the values taken at t_{end} is the glance-off value. In contrast to the time series analysis where all of the values are collected at the same time point, the $RB_{I_{GV_P}}$=-0.18.

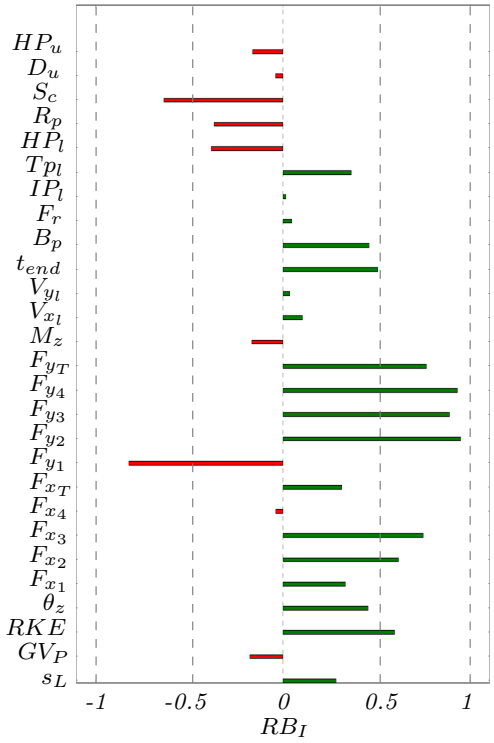

Figure 8.10 Robustness Index for the configuration uncertainty analysis of the base simulation

8.2.6. Test Conditions Uncertainty

The uncertainty assessment of the test conditions includes the three relevant parameters identified in Section 6.2.2, namely the deviations from the nominal velocity, weight, and initial relative position of the barrier. To determine the optimum number of samples and the quality of the probability mapping, two aspects are considered. First, the maximum deviation from the input *pdf* with respect to the samples-reconstructed *pdf* for each parameter. Second, the maximum cross-correlation among the samples. Both metrics are evaluated for different sample sizes from 10 to 50. While the first parameter makes sure that the output distribution resembles the input, the second one minimizes the dependency of the variables.

The overall maximum deviation from input distribution, considering the three parameters as shown in Figure 8.11(a), makes evident that increasing the sample size, the minimum, average and maximum deviations decrease. The largest improvement is made from a sample size increase from 10 to 30. Afterwards, the reduction in the error is relatively less. Figure 8.11(b) shows the maximum Spearman correlation coefficient present among the samples. From 20 to 50 samples the max. coefficient is in average 0.05, meaning that the selected OLHC sampling scheme is effective in producing a samples set without auto-correlation.

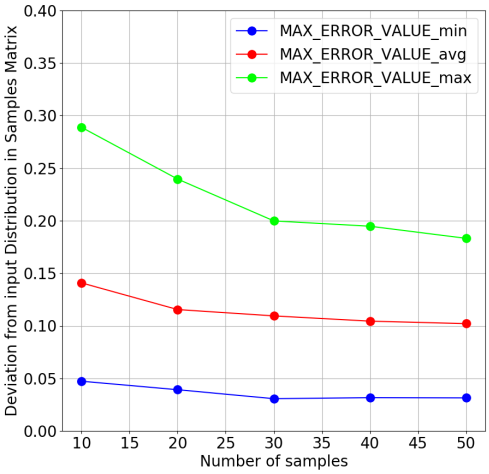

(a) Max. deviation from input distribution

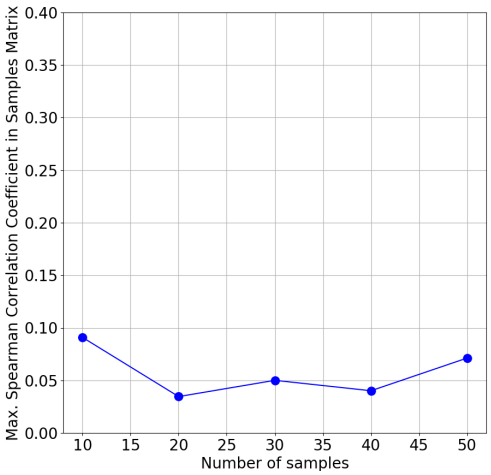

(b) Maximum cross-correlation coefficient

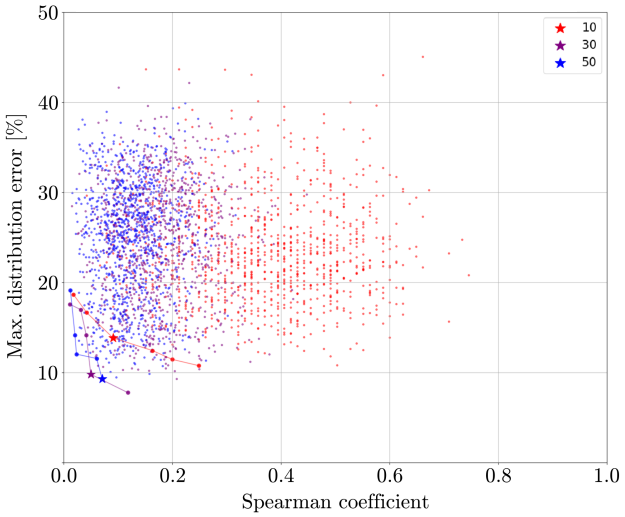

(c) Pareto front cross-correlation vs. max. deviation from input distribution for samples size 10, 30 and 50

Figure 8.11 Samples quality evaluation: max. deviation from input distribution (a), maximum cross-correlation coefficient (b) vs. number of samples, pareto front cross-correlation vs. max. deviation from input distribution (c)

The Pareto front presented in Figure 8.11(c) shows the combination of both metrics. It is observed that neither a low maximum error nor a low correlation coefficient guarantees that the other metric is also low. Therefore, the Pareto front identification, and from there the minimum resultant error, i.e. the Euclidean distance considering both metrics, is selected for a given number of samples. Being the samples size of 50 the one offering the lowest deviation from input distribution and lowest combined error, it is selected for

this phase sampling.

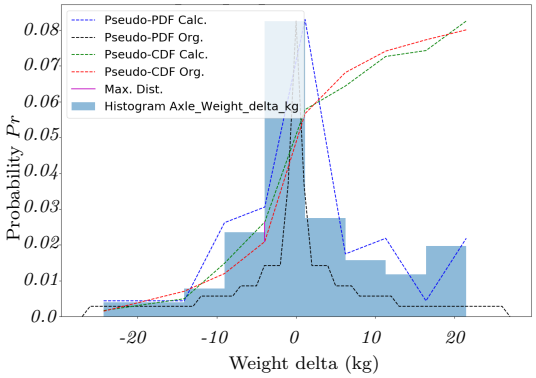

(a) Input-output distribution: mass deviation from nominal

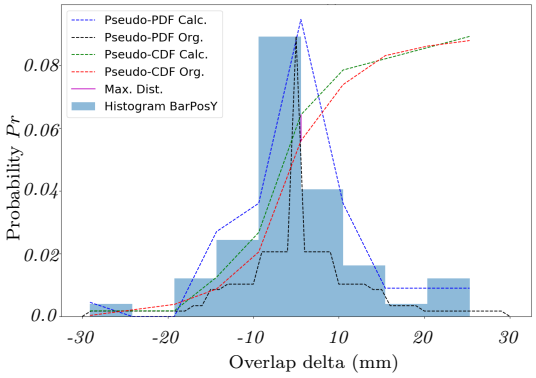

(b) Input-output distribution: velocity deviation from nominal

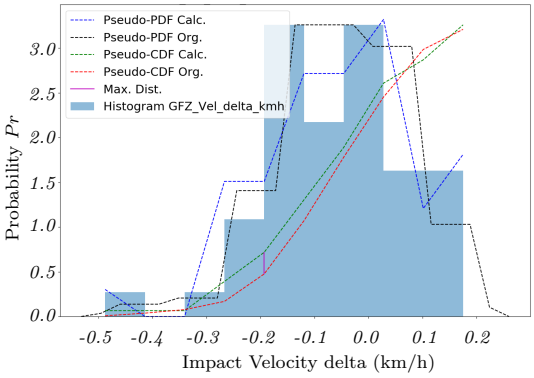

(c) Input-output distribution: barrier position deviation from nominal

Figure 8.12 Samples quality evaluation: input-output distribution: mass deviation (a), velocity deviation (b), barrier position deviation (c) from nominal values

A set of 50 samples for the three parameters is created using the correspondent *pdf* of each parameter. The *pdf* reconstructed from the samples as well as their correspondent input distributions are shown in Figures 8.12. The reconstructed mass deviation *pdf* slightly overestimates the probability of having a delta larger than 15kg. Meanwhile, the deviation in the barrier position offers a good coverage of the extreme behaviors. Lastly, the unsymmetrical input *pdf* of the velocity deviation is well characterized by the samples. With this selection of sample size and having analyzed the characterization of the input *pdf*s, the robustness of the results produced by this set of 50 simulations considering the test conditions uncertainty, tes, is analyzed.

The combination of different, barrier positions, masses and velocities produce a scatter in the kinematic parameters. This scatter is observable in the form of the decay of the RB_I for the time series of the glance-off value and rotation presented in Figures 8.13(b,d).

In contrast to the configuration phase where the RB_I had an accelerated decay and later stabilizes, for both kinematic parameters the decay starts at ca. 40ms, before the wheel is active, and continues steadily until the end of the simulation. The minimum value reached for both values is RB_I<0.2. While a decay in the RB_I is also observable in the rest deformation length, this decay is considerably lower than the one observed in the other two parameters. The rest kinetic energy is stable with values closer to 1 along the time series as in the other two previous phases. The analysis of the RB_I of the scalar values shown in Figure 8.14 indicates that the number of variables with negative robustness indexes has increased with respect to the other two uncertainty analysis phases. As before, the intrusion points, upper hinge pillar, upper dash, steering column, rocker panel, and lower hinge pillar present a non-acceptable robustness value.

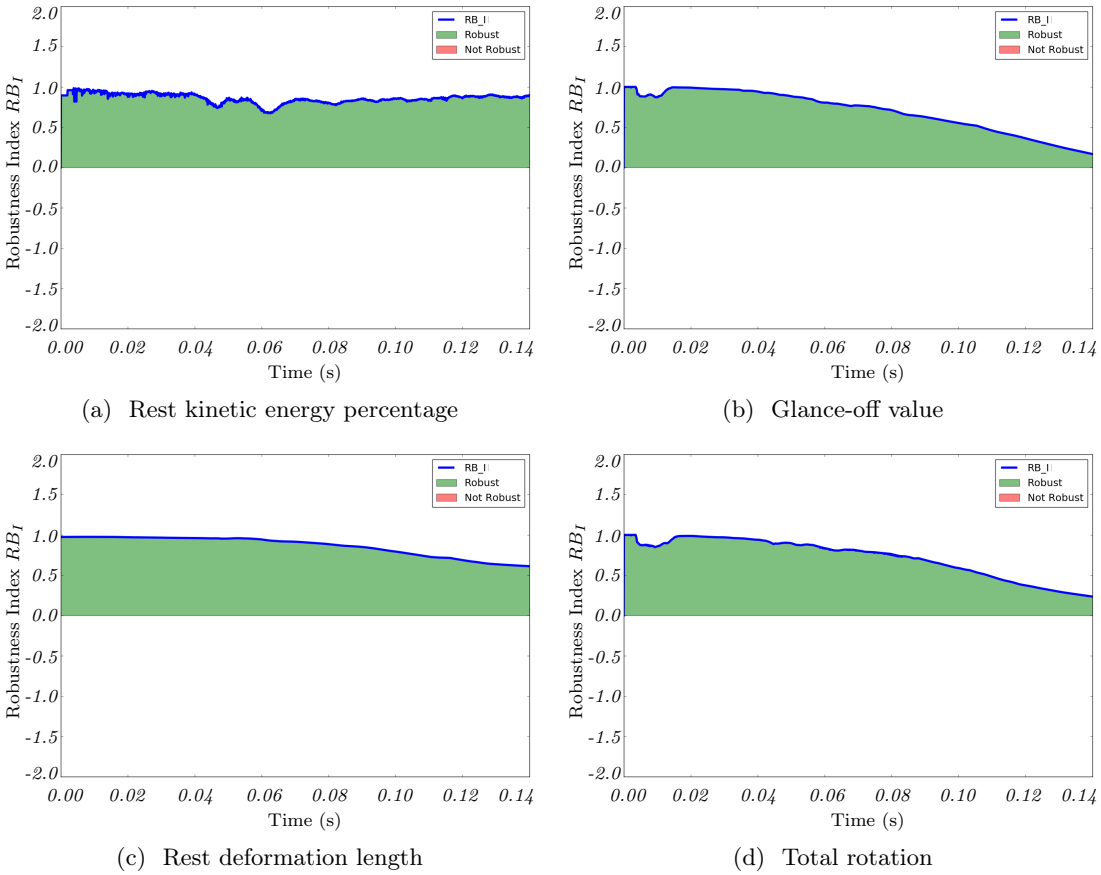

(a) Rest kinetic energy percentage

(b) Glance-off value

(c) Rest deformation length

(d) Total rotation

Figure 8.13 Kinematic parameters robustness index for test uncertainty analysis extracted from base simulation: rest kinetic energy, RKE (a), glance-off value, GV_P (b), rest deformation length, s_L (c), total rotation, θ_z (d)

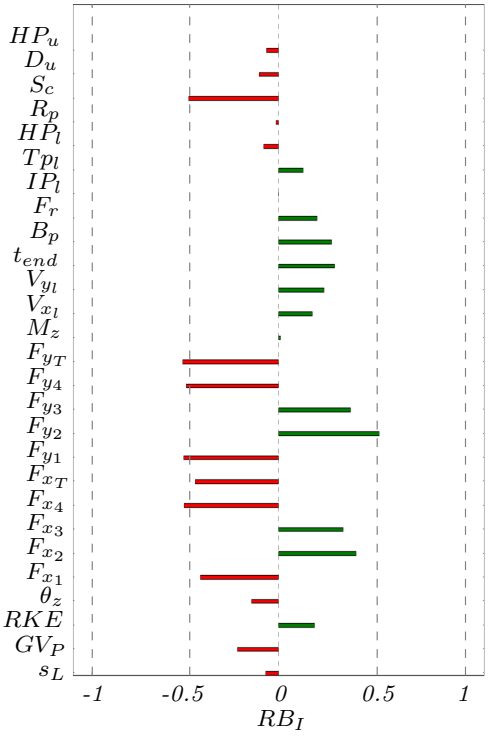

Figure 8.14 Robustness Index for the test uncertainty analysis of the base simulation

The effects of the different barrier positions, masses and velocities that affect the deformation modes and load-levels of the components in the structure become evident when analyzing the RB_I of the load-path forces. The total transversal force as well as the sub-frame and wheel load paths present RB_I of -0.5. The longitudinal force levels are affected in a similar way, i.e. the total force and the sub-frame and wheel load-paths. The different test conditions influence mainly how the suspension and wheel react. This effect is also noticeable in the RB_I of the rotation, glance-off and deformation length at t_{end}, with values of -0.14, -0.22 and -0.07, respectively. This means that the effect of the test conditions uncertainty is higher than that of the other two cases.

8.2.7. Component Properties Uncertainty

The variability in the component properties is characterized in this section by a total of 7 variables. The fact that the suspension components are directly involved in the Small Overlap crash test makes this load-case distinct to the rest of the frontal load-cases. Therefore, these 7 variables describe parameters directly related to the wheel, suspension, and components that influence the wheel kinematics. Two of them describe the aleatory variability of the properties of the wheel and tire assembly. One variable affects directly the properties of the tire by varying its wall thickness. The second variable

affects the rupture of the wheel itself by varying the thickness of the rim bed. A uniform distribution within a range of ± 10% from the nominal value is used to characterize these parameters. Next, 4 parameters are used to describe the failure forces of the joints of the push-rod, lower control arm, and tie-rod. The failure forces are defined at the sub-frame side for the three joints and the tie-rod. The failure of the tie-rod at the steering gear side is also defined. The last variable defines the wall-thickness of the seam weld of the support-frame. Even if the support-frame is not explicitly a part of the suspension, it influences the wheel kinematics when it contacts the barrier, bends and pushes the wheel backwards towards the BIW. The variation of the last 5 parameters was characterized by a truncated Gaussian distribution with limits at ± 10% of the nominal properties. After defining the component properties uncertainty and following the same methodology as in the previous sections, a sample size of 100 is selected to produce the next simulation set.

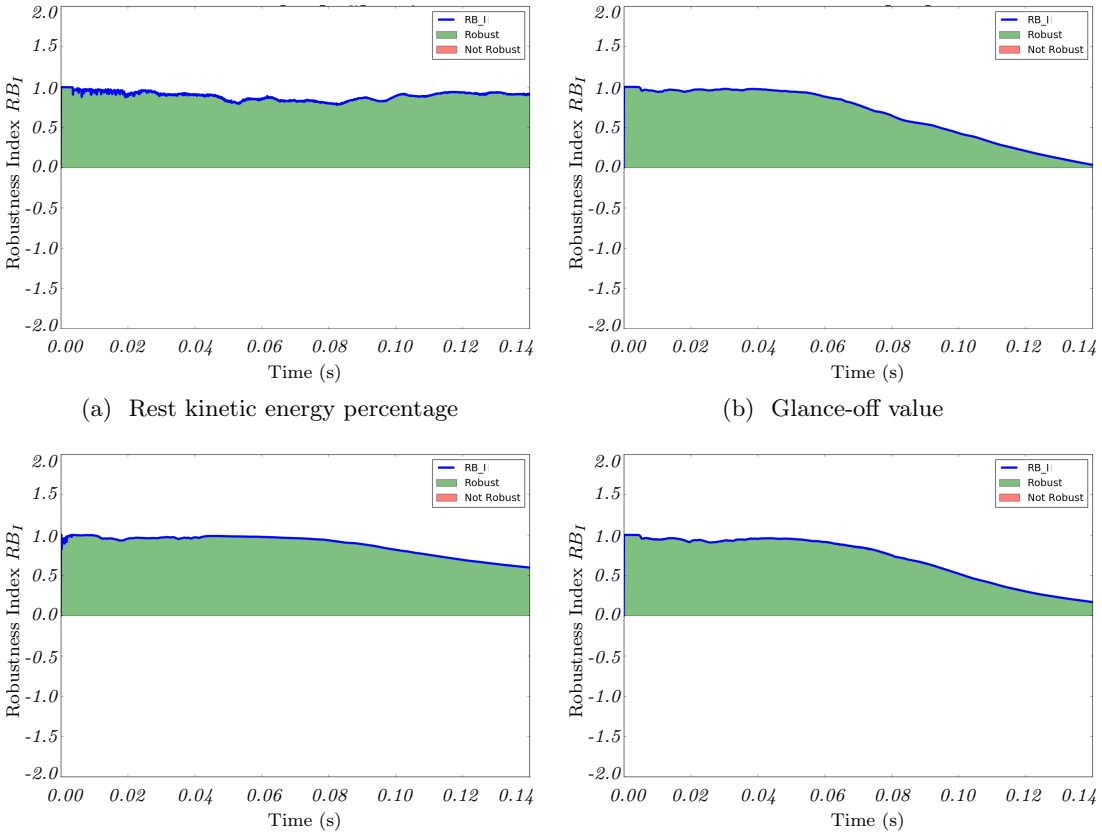

(a) Rest kinetic energy percentage

(b) Glance-off value

(c) Rest deformation length

(d) Total rotation

Figure 8.15 Kinematic parameters robustness index for component uncertainty analysis extracted from base simulation: rest kinetic energy, RKE (a), glance-off value, GV_P (b), rest deformation length, s_L (c), total rotation, θ_z (d)

The robustness analysis of the time series of the kinematic parameters contributes to the confirmation of the trend identified in the other studies. Figure 8.15 shows that the kinetic energy is stable with $RB_I \approx 1$ and the rest deformation length presents a slight decay towards the end of the simulation. In this phase however, the glance-off value almost reaches a $RB_I = 0$ at the end of the simulation, while the total rotation is $RB_I \approx 0.1$. As expected, the decay in RB_I starts at ca. 60ms when the wheel kinematics relevance begins.

With respect to the RB_I of the rest of the scalar values, the first 5 intrusion points present a negative robustness index. Additionally, the left instrument panel also presents a marginally unacceptable RB_I=-0.033. In contrast to the test sources of uncertainty, the component phase produces a negative RB_I only for the transversal force of the wheel load-path, longitudinal force of the sub-frame and marginally also for the total longitudinal force. For the scalar representation of the kinematic parameters only the glance-off has an unacceptable RB_I=-0.21. Although the over-all robustness of the model considering the uncertainty from the suspension components properties can be considered higher than the robustness considering the test conditions; the relevant kinematic parameters are still negatively affected.

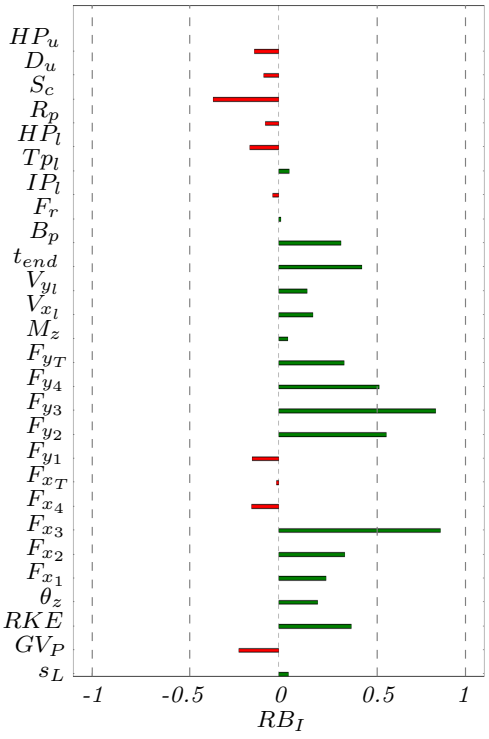

Figure 8.16 Robustness Index for the component uncertainty analysis of the base simulation

8.2.8. Aggregated Uncertainty

In this last uncertainty and robustness analysis, the parameters from the numerical, configuration, test conditions, and component properties phases are combined in order to evaluate the robustness of the vehicle with respect to a so-called aggregated uncertainty. In real life the different uncertainty sources act in the crash event at the same time. With this uncertainty aggregation, the combined effects of all of the parameters can also be analyzed and quantified. The total amount of variables considered rises to 12. In order to properly characterize and minimize the auto-correlation and deviation from the input distributions a sample size of 200 simulations is used.

The RB_I time series shown in Figure 8.17(b) shows that the robustness index of the glance-off value reaches the negative region at the end of the simulation. This trend identified from the previous phases consummates into an unacceptable robustness for GV_P at the end of the simulation. The decay in the robustness of the total rotation is slightly worsened by the aggregation of the sources of uncertainty but the robustness value is still in the positive region. The rest kinetic energy and rest deformation length show no changes from the previous phase.

The results of the robustness analysis of the selected scalar parameters considering the aggregated uncertainty are presented in Figure 8.18. All of the intrusion points but the footrest and brake pedal present a negative RB_I in the aggregated uncertainty phase. However, both of them present values closer to zero. Moreover, the total moment, total transversal and longitudinal forces as well as the wheel-firewall-rocker load-path also exhibit $RB_I<0$. From the perspective of the kinematic parameters at t_{end}, both the glance-off value and rotation present unacceptable RB_Is.

Figure 8.30 presents in a boxplot representation the variability of the output parameters. This enables the comparison of the effect that each source of uncertainty has on the kinematic parameters and safety rating. As it was observed from the calculation of the robustness indexes for each uncertainty phase, rest kinetic energy remains relatively unchanged. The configuration uncertainty slightly shifts the box plot to smaller values with respect to the numeric phase, being then $RKE_{con}<10\%$. The test, component and aggregated uncertainties only differ by the size of the range, but the average value remains unchanged relative to the numeric phase, i.e. 10%. This indicates that even if the different sources of variation affect the response of the vehicle, they are not enough to significantly change the kinetic energy at the end of the crash.

The variation of the rest deformation length shown in Figure 8.30(c) demonstrates that the smaller wheel size generates the larger shift in the response. The average RDL of the other phases is ca. 175mm while the smaller wheel size increases it to 300mm. Meanwhile, the aggregated uncertainty presents the larger range with minimum and maximum of 120mm to 260mm. The total rotation of the vehicle was the kinematic parameter with the second worst RB_I, after the glance-off values. However, considering the absolute values of the rotation, they all lie within a range of 2 to 5 degrees. Note that the configuration uncertainties are causing the least variation.

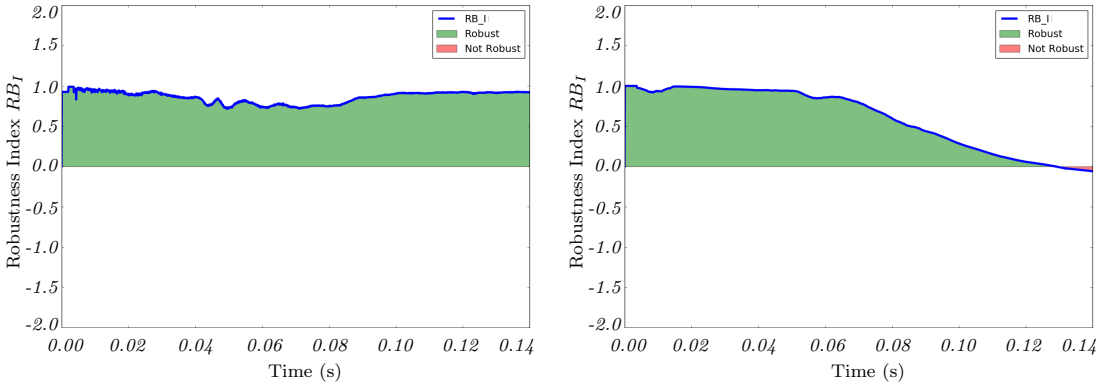

(a) Rest kinetic energy percentage

(b) Glance-off value

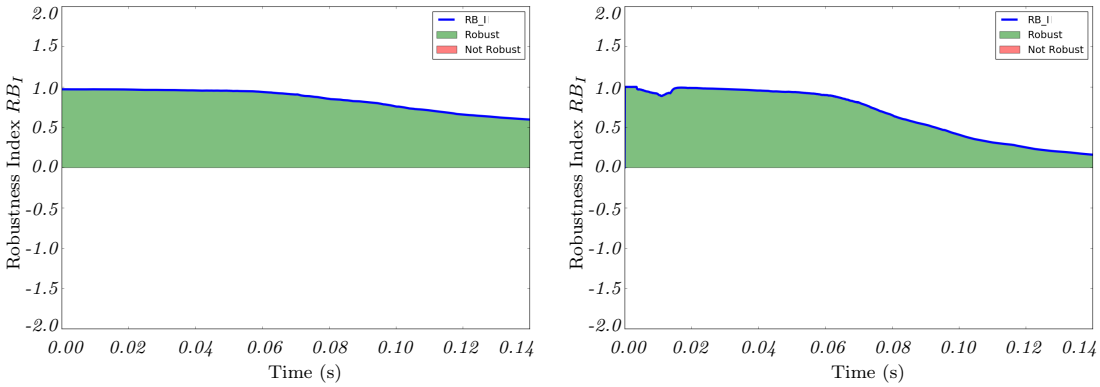

(c) Rest deformation length

(d) Total rotation

Figure 8.17 Kinematic parameters robustness index for aggregated uncertainty analysis extracted from base simulation: rest kinetic energy, RKE (a), glance-off value, GV_P (b), rest deformation length, s_L (c), total rotation, θ_z (d)

The glance-off value is the kinematic parameter that is affected the most from the uncertainty sources. The numeric uncertainty phase produced an average value of GV_P of 0.65. The integration of the small wheel in the model reduced the range to an average of 0.3, taking the vehicle further away from achieving a complete glance-off. Nonetheless, the variability introduced in the test phase was enough to produce minimum values of ca. 0.4 while at the same time achieving in the extreme cases a GV_P=1. The change in the test conditions and the use of the base 18 inches wheel could lead with a certain combination of parameters to a glance-off behavior. The component and aggregated uncertainty sources pushed GV_P towards the deformation mode, producing average values of 0.5 and 0.4, respectively.

The effect of the wheel size and the varying test conditions on the kinematic parameters justifies the improvement of the robustness of the structural design for this particular vehicle. Being the kinematic parameters, in particular the RKE secondary targets, it

is also important to analyze the effect the different sources of uncertainty have on the structural rating and Safety Distance, D_{SG}. The average D_{SG}=30% of the numeric phase considered as baseline was not enough to support the need for further improvement. Nevertheless, all but the configuration uncertainty decreases the minimum D_{SG} observed in each simulation set. The aggregated sources of uncertainty even produce in an extreme case a combination of parameters that yield a structural rating with a D_{SG}≈0. Due to the fact that in reality this combined uncertainties are present and that the combination of parameters are produced following the realistic ranges and probability of variation, a design that under certain conditions does not fulfill the primary target is not acceptable. For this reason and following the solution-space-based iterative simulation scheme the correspondent design improvements will be implemented virtually. The solution space approach combined with the robustness assessment are used to produce a structural design capable of achieving the primary and secondary targets even in the explicit consideration of the sources of uncertainty present in the load-case.

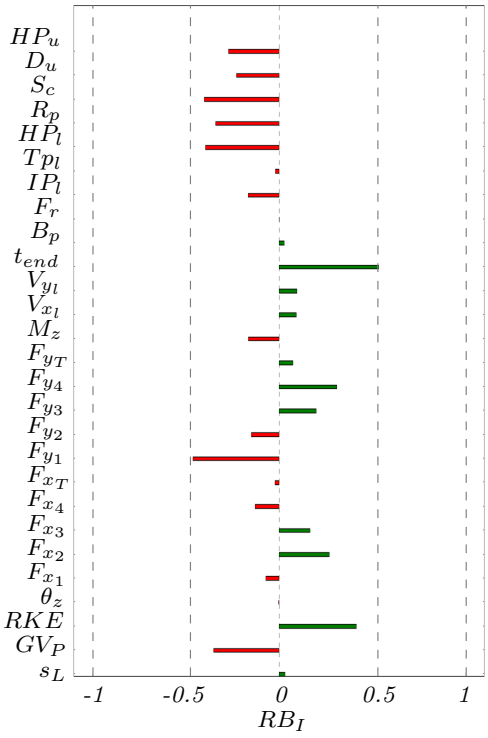

Figure 8.18 Robustness Index for the aggregated uncertainty analysis of the base simulation

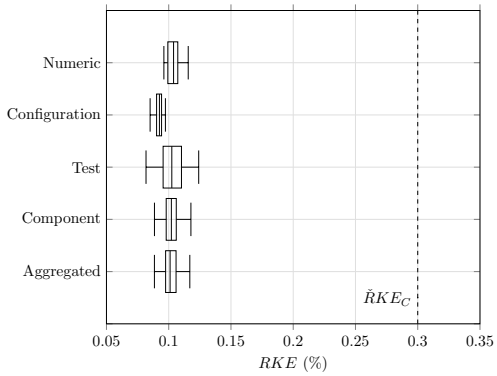

(a) Rest kinetic energy percentage

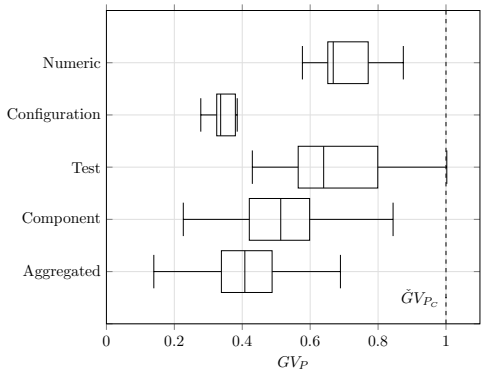

(b) Glance-off value

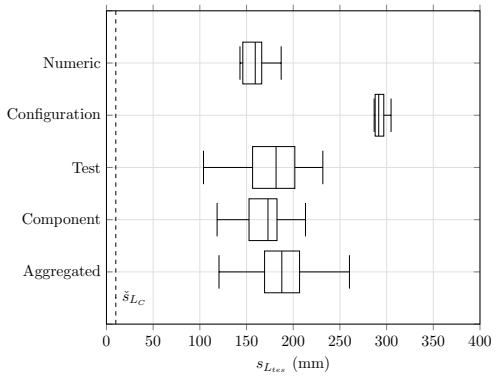

(c) Rest deformation length

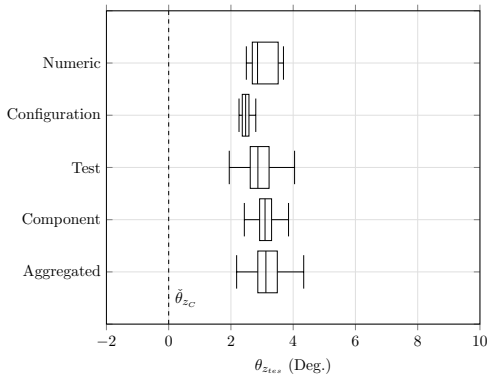

(d) Total rotation

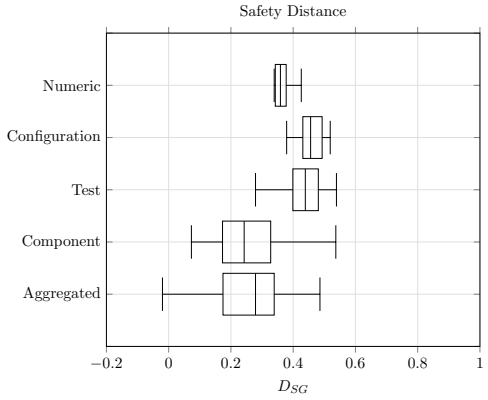

(e) Safety Distance, D_{SG}

Figure 8.19 Kinematic parameters boxplot for numerical, component, test and aggregated robustness analysis: rest kinetic energy, RKE (a), glance-off value, GV_P (b), rest deformation length, s_L (c), total rotation, θ_z (d), and safety distance, D_{SG}(e)

8.3. Solution Space Calculation

During the robustness analysis of the base model it was established that the primary goal of achieving a D_{SG} of at least 30% is not achieved under the full set of uncertainty sources. In order to increase the robustness of the model and achieve the structural target under the explicit consideration of all of the uncertainties, a secondary target regarding the vehicle kinematics was defined. By performing a cluster and correlation analysis of the vehicle kinematic response and the structural rating of the vehicles presented in the IIHS database, it was determined that to minimize the possibility of achieving anything but a Good structural rating a RKE of at least 30% must be achieved. In essence to achieve the primary structural target, a secondary target upon the rest kinetic energy is defined.

As stated in Section 5.2.2, there are different combinations of translational and rotational behaviors that yield a kinetic energy above 30%. However, the kinematic analysis of the data set indicated that statistically such a high value of RKE is achievable with a combination of negative total rotation angles and a glance-off of 1. Additionally, a constraint set upon the rest deformation length so that it has a minimum of 10mm at t_{end} ensures that the glance-off is achieved before the occupant compartment has a hard contact with the rigid barrier. This set of constraints defined upon the kinematic parameters as well as the vehicle characteristics are given as an input to the solution space calculator to define a set of upper and lower limits for the force-displacement curves describing the RDC at the load-path level. The fulfillment of this solution space is used as an objective function to drive the structural design changes in the load-paths. In a final step, a robustness analysis considering all of the sources of uncertainty is conducted to ensure that the structural changes lead to a robust fulfillment of the primary target.

Additionally to the constraint set and vehicle characteristics, the solution space calculation requires the definition of design bounds for the RDC. These design bounds determine the search space for solutions that fulfill the constraints. Hence, a good initial estimation of the feasible regions accelerate the calculation. To achieve this, a basic understanding of the effects the forces in the structure have on the vehicle kinematic is essential. The current RDC of the base model are dominated by the longitudinal forces of the wheel-firewall-rocker load-path. Furthermore, the robustness analysis showed that the wheel behavior played a key role in the scatter of total rotation and glance-off values. Therefore, the structural design changes should include countermeasures that at the same time regulate the forces in the load-path so that the desired kinematic is achieved; at the same time the relevance of the wheel behavior itself should be reduced. The first part of this task is then to determine the changes in the force-level that lead to the desired kinematic.

The Eq. (4.3) representing the non-linear equation of motion describing the essence of the Small Overlap load case provides the first indications on how to determine a set of RDC that produce higher RKE values, negative rotations and a glance-off value of 1. First, the initial kinetic energy comes from the initial velocity in the x direction. That implies that in order to conserve as much as possible from the initial kinetic energy

the deceleration along the x axis has to be kept to a minimum. In other words, the transversal force in the structure has to be minimized. Second, a glance-off of 1 can be reached by a certain combination of transversal displacement and negative rotation. The transversal displacement is achieved by maximizing the transversal forces in the structure. Third, the negative total rotations are the product of negative moments. This negative moments are reached by maximizing the moment produced by the transversal force and its correspondent longitudinal lever arm. At the same time, the positive moments caused by the longitudinal forces and their transversal moments should be minimized.

These changes of the forces at the full-vehicle level have to be decomposed into the load-paths and later be materialized into changes in the component of the structure. However, certain design limitations also exist in the implementation of the structural changes. As it is usual in a later design stage, some of the structure characteristics are fixed. For this design exercise, no changes are allowed in the BIW. Changes in the bumper system only allow for modifications in the wall-thickness of the components. And, the topology of the structure can only be influenced by the integration of additional components that fit into the existing packaging constraints.

Taking this into account, to translate the necessary changes in the force levels, the following three strategies are proposed. First, the minimization of the longitudinal forces of the wheel-firewall-rocker load-path. Second, the maximization of transversal forces from the sub-frame load-path. Third, the increase in transversal forces of the sub-frame load-path should take place at the most frontal position of the load-path maximizing the longitudinal lever arm and consequently maximizing the negative moments needed to fulfill the rotation and glance-off constraints.

In that respect, the design bounds of the full-vehicle and load-path level RDC are selected. Next, the solution spaces at both levels are calculated and the RDC of the current model are compared. This comparison determines at which deformation level to increase or decrease the transversal or longitudinal forces. Then, these changes are mapped to the current structure so that later, the adjustment in the force levels translate into increase or decrease of wall-thickness or integration of additional components at the selected positions and load-paths.

8.3.1. Full Vehicle Solution Space

The exploration, consolidation, and expansion phases defined in Section 5.1.1 were carried out in combination with the vehicle characteristics of the base model and the same discretization of the deformation spaced used in the validation procedure. The considerations defined in the previous section regarding the design bounds are also implemented obtaining the solution spaces for the longitudinal, transversal and Y_{eq} at the full vehicle level shown in Figure 8.20 as a result.

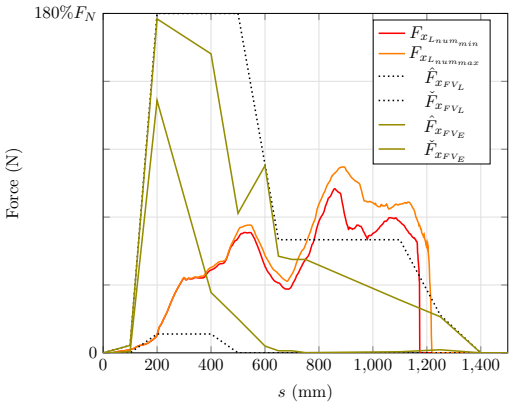

(a) Longitudinal forces vs. deformation space (s)

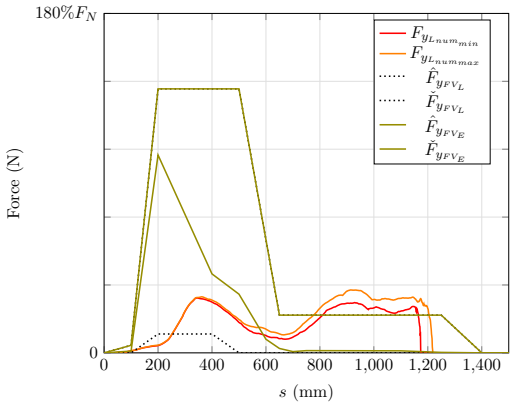

(b) Transversal forces vs. deformation space (s)

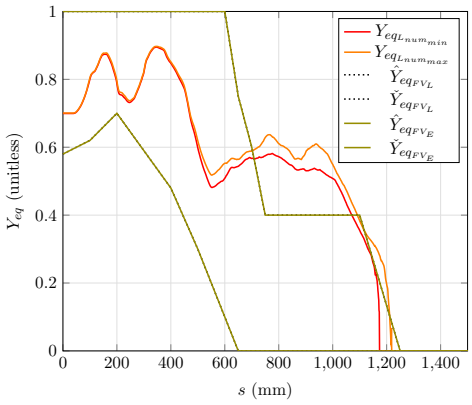

(c) Equivalent point of application of longitudinal force vs. deformation space (s)

Figure 8.20 Maximum and minimum *RDC* at full-vehicle level extracted from numerical uncertainty analysis of base simulation and solution space for $D_{SG} \geq 30\%$: longitudinal (a), transversal (b) forces, and Y_{eq}(c)

The maximization of the lever arm for the transversal forces leads to a much more front-loaded distribution of the force levels. For both the longitudinal and transversal forces, the maximum values limited by the design bounds and obtained from the solution space, are located in the first deformation phase until 600mm. Even if the objective is only to increase the transversal forces, the longitudinal component cannot be decoupled. The transversal forces are the result of the interaction of the structure with the curved surface of the barrier. At this position and dependent on the contact angle, the normal of the surface of the barrier is capable of producing transversal as well as longitudinal forces. At a 45° angle, the normal of the surface will maximize both components of the

force. For this reason, both the transversal and longitudinal components are allowed to present relatively high force-levels.

Figure 8.20(a) also shows that the maximum force obtained at the wheel region, is decreased from the base model. This goes in line with the strategy to take relevance out of the wheel load-path and at the same time decrease the longitudinal deceleration. It can be argued that the higher longitudinal forces in the early deformation phases act against this principle. However, as stated before, the transversal forces cannot be decoupled from the longitudinal. Moreover, an early deceleration decreases the kinetic energy at a phase where there is still a relatively high amount, per definition, of energy available. Therefore, even if the loss is considerable it is subtracted from the initial kinetic energy yielding still an acceptable rest kinetic energy at the end of the crash. Considering this, the upper limit of the solution space for the longitudinal force in the early stages is of most relevance. In contrast, the lower limit of the transversal force will dictate the minimum force-level that is capable of producing a kinematic that fulfills the constraints. It is noticeable that the upper limit and upper design bound coincide. Meaning that the solution space calculator takes as much transversal force as possible given the design limits.

The equivalent point of application of longitudinal forces solution space and design bounds coincide for the entirety of the deformation levels. This indicates that the fulfillment of the constraints is dominated by the forces and not Y_{eq}. This also aligns to the strategy of producing a design that is independent of the wheel kinematic. However, the avoidance of an inwards rotating wheel is implicitly enforced by moving the upper limit of Y_{eq} at the wheel region towards the rocker.

8.3.2. Load Paths Solution Space

The full-vehicle level solution spaces obtained in the previous section are taken as input for the load-path level calculation. The total force levels and Y_{eq} are decomposed into load-path forces yielding the results presented in Figures 8.21 and 8.22 for the longitudinal and translational forces accordingly.

The upper design bounds of the wheel-firewall-rocker load-path are defined as constant with the maximum force-level of the base model as reference. The solution space for this load-path results into force levels of roughly the same magnitude as the average of the base model for the first 600mm and a decay for the rest of the deformation space. Due to the fact that modifications to the BIW are not considered, the solution space of the shotgun load-path presents an average load level as the one observed in the base model along the deformation space.

The significant changes in the load-levels take place at the bumper and specially at the sub-frame load-paths. The longitudinal forces of the bumper system remain relatively unchanged. However, the transversal component requires a lower limit that is higher than the load levels of the current base model. This follows the need to increase the transversal forces at the earliest deformation level as possible.

Being the sub-frame a subsystem that allows for the integration of additional components, the most significant adjustments to the force levels are reserved for this load-path.

As in the full-vehicle level a relatively high upper design bound is defined. Similarly also to the full-vehicle level the relevant limits are the upper one for the longitudinal component and the lower one for the transversal. Considering the selected discretization of the deformation space, the maximum values should be reached at 200mm. In the next section, these adjustments to the forces in the load-paths are materialized into changes in the frontal structure of the vehicle.

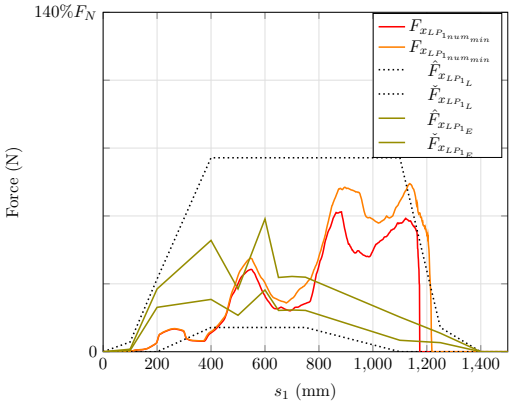

(a) Load-path 1: wheel-firewall-rocker longitudinal forces vs. deformation space (s_1)

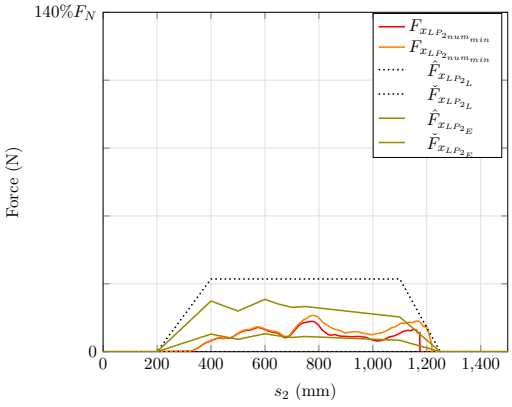

(b) Load-path 2: shotgun longitudinal forces vs. deformation space (s_2)

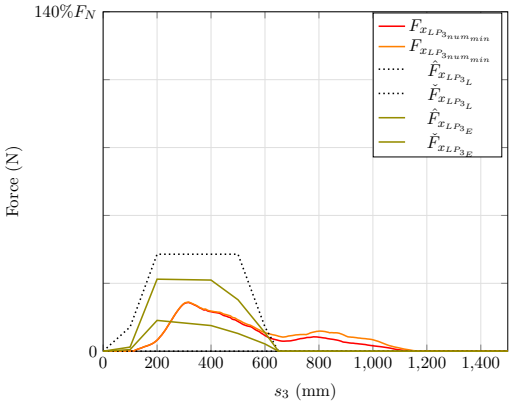

(c) Load-path 3: bumper beam-front rail longitudinal forces vs. deformation space (s_3)

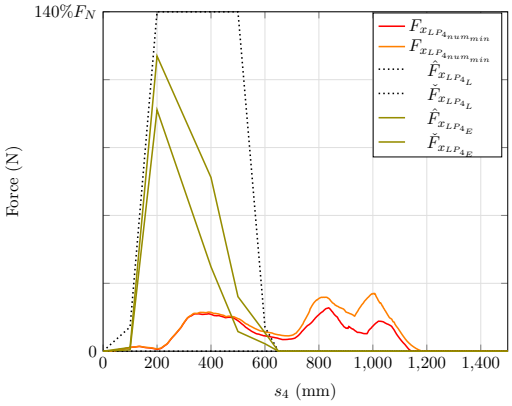

(d) Load-path 4: sub-frame longitudinal forces vs. deformation space (s_4)

Figure 8.21 Maximum and minimum longitudinal forces at load-path level extracted from numerical uncertainty analysis of base simulation and solution space for $D_{SG} \geq 30\%$: wheel-firewall-rocker(a), shotgun(b), bumper beam-front rail (c), sub-frame(d)

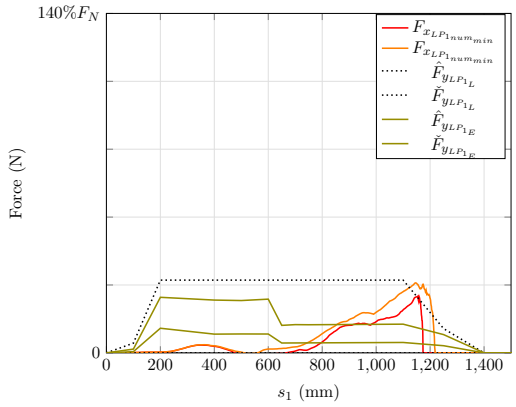

(a) Load-path 1: wheel-firewall-rocker transversal forces vs. deformation space (s_1)

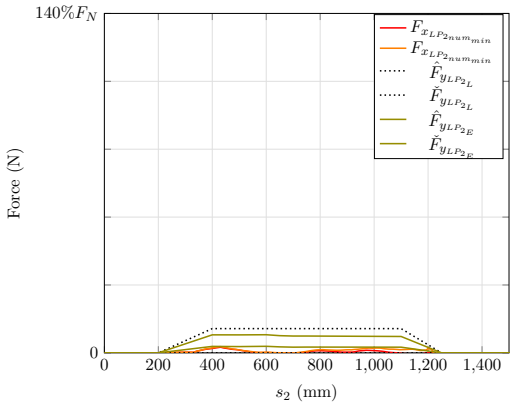

(b) Load-path 2: shotgun transversal forces vs. deformation space (s_2)

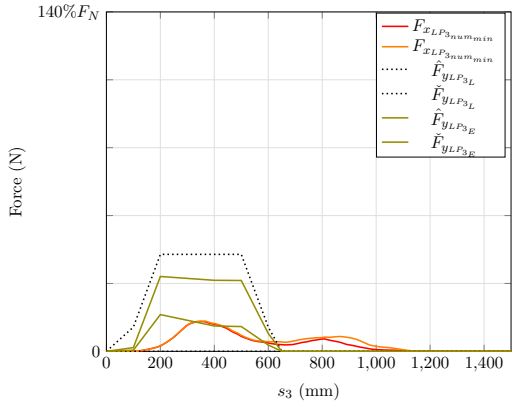

(c) Load-path 3: bumper beam-front rail transversal forces vs. deformation space (s_3)

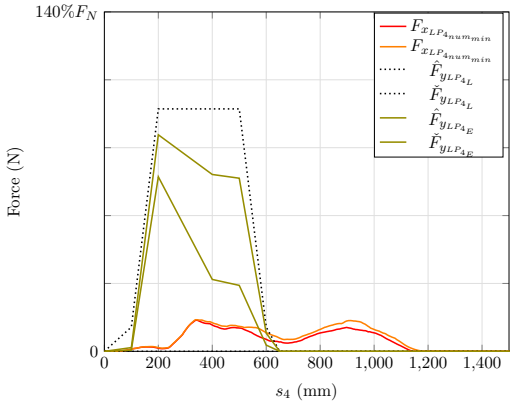

(d) Load-path 4: sub-frame transversal forces vs. deformation space (s_4)

Figure 8.22 Maximum and minimum transversal forces at load-path level extracted from numerical uncertainty analysis of base simulation and solution space for $D_{SG} \geq 30\%$: wheel-firewall-rocker(a), shotgun(b), bumper beam-front rail (c), sub-frame(d)

8.4. Simulation-based Design

The solution space methodology produces a set of minimum and maximum force levels in the different load-paths of the structure; it also enables a degree of flexibility and at the same time clear direction in the design that would not be possible otherwise. The solution spaces indicate at which deformation levels should the force level be adjusted. The deformation space is mapped directly to the structure topology making clear where and how to modify the structural components. A set of countermeasures are defined and

implemented in order to fulfill the solution space for the *RDC* of the structure.

8.4.1. Development of Countermeasures

The strategies defined previously to fulfill the solution spaces and achieve the secondary and primary target are in this section translated into concrete countermeasures to change the load-carrying capacities of the selected load-paths and sub-systems. The Figure 8.23 is used as reference to map the deformation space to the structure of the vehicle. The changes dictated by the solution space have the first 600mm in focus. Meaning that the components located in this region are candidates for the implementation of countermeasures. Additionally in the case of the sub-frame load-path, a maximum force level should be reached before 200mm. Consequently, the following structural design changes are proposed.

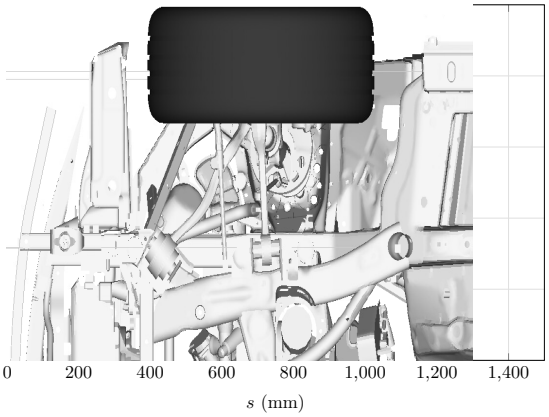

Figure 8.23 Undeformed vehicle structure bottom view vs. deformation space (s)

The main adjustment concerns the sub-frame and its transversal forces. The maximization of transversal forces from the sub-frame load-path is achieved through the integration of an additional component attached to the frontal portion of the sub-frame. This sub-frame extension is positioned in the y axis such that for the expected variation of the barrier position, it contacts the curved surface maximizing the transversal forces. The elongation of the sub-frame and the contact with the curved surface of the barrier does not only increase the transversal forces but also maximizes the longitudinal lever arm needed to increase the negative moments to achieve the rotation and glance-off requirements. This elongation begins at ca. 200mm and is connected to the rest of the sub-frame at 400mm to match the peak forces indicated by the solution space. The longitudinal and transverse rigidity of the sub-frame is also increased in order to be able to cope with the expected force increase due to the elongation. To contribute to the increment of transversal forces, the wall-thicknesses of the bumper beam and the support-frame are increased by 20% to improve the load carrying capacity of the components.

On the other side, the minimization of the longitudinal forces of the wheel-firewall-

rocker load-path is achieved through the integration of a predetermined breaking point in the rim. This notch is a stress concentrator that decreases the breaking load of the wheel. Additionally, this predetermined breaking point also allows for a more consistent failure of the wheel increasing the robustness of the kinematic response. With these modifications, the FE model is again simulated and the *RDC* are extracted. The *RDC* of the new model, here named as RKE_{30} are compared to the solution spaces and in a later stage the uncertainty analysis is carried out to confirm the robustness of the new design.

8.4.2. Solution Space Violation Check

The model with the integrated countermeasures described previously is simulated using a variation of the time-step analogously to the procedure for the base model. The analysis of the set of 10 simulations allows for the characterization of the sensitivity of the model to the numeric uncertainties of the FE solver.

The kinematic analysis is carried out and the *RDC* are extracted. Figure 8.24 presents the *RDC* of the RKE_{30} model in context of the solution space calculated fulfilling the secondary kinematic targets. For both, the transversal and longitudinal forces, the maximum force levels are within the upper and lower limits of the solution space. The longitudinal force from the RKE_{30} model lies completely inside the corridor except for the initial increase at 100mm. Considering the selected discretization of the deformation space, a slight shift of 50mm exists in the position of the peak forces. The maximum forces for both components take place at ca. 250mm. The largest deviation from the corridor occurs in the transversal forces in the region from 400mm to 600mm. A more pronounced drop in the extracted *RDC* contrasts with the lower limit of the solution space. However, the effect on the fulfillment of the constraints is minor and is analyzed in the next section. The Y_{eq} lies completely inside the corridor and indicates no inwards rotating wheel since the point of application of force is located outwards at the wheel region. As a whole, the *RDC* at the full-vehicle level RKE_{30} model are dominated by the front-loaded transversal and longitudinal forces.

The decomposition of the force levels into load-paths makes evident that the new dominant load-path is the sub-frame. This statement applies to the longitudinal as much as to the transversal forces. Figure 8.25(d) and Figure 8.26(d) show that the maximum force values reach the lower limit and are close if not slightly exceeding the upper limit of the load-path solution space. As in the full-vehicle level, the discretization of the solution space influences the fulfillment during the first increase. Moreover, a steeper than expected change from the force specially in the longitudinal region is also observable. Despite of these discrepancies, the role of the sub-frame extension is evident.

One of the other design changes relates to the increase of the wall-thickness of the bumper, which leads to a higher bending stiffness of the subsystem. The effect of this countermeasure is observable in Figures 8.25(c) and 8.26(c). In both cases the maximum forces of the RKE_{30} model are in agreement with the solution space and present an increase with respect to the base model. However, both the transversal and longitudinal components present a more pronounced drop in the force levels than the solution space

prescribes.

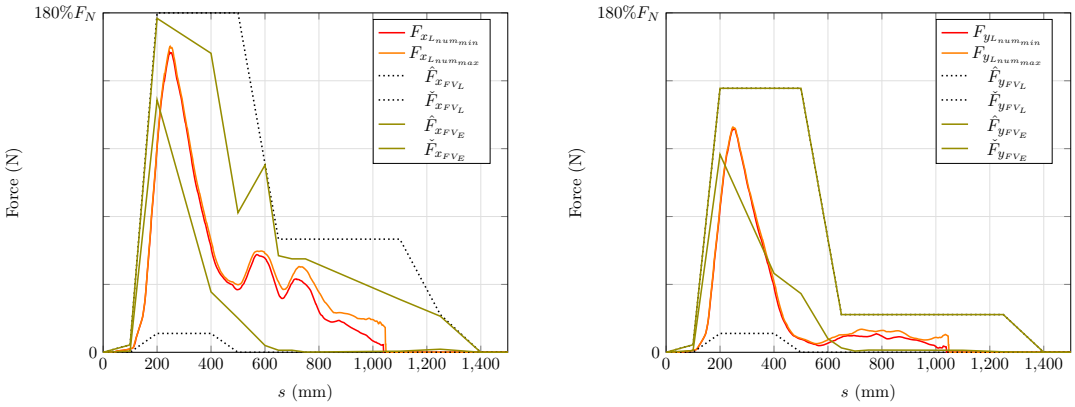

(a) Longitudinal forces vs. deformation space (s)

(b) Transversal forces vs. deformation space (s)

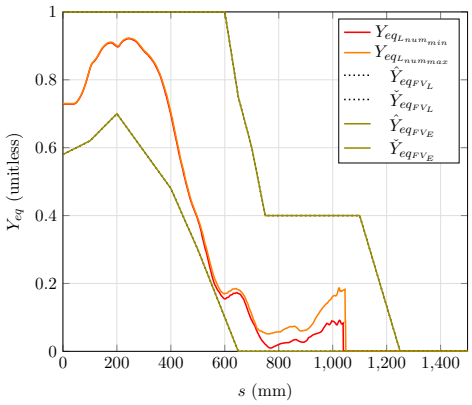

(c) Equivalent point of application of longitudinal force vs. deformation space (s)

Figure 8.24 Maximum and minimum RDC at full-vehicle level extracted from numerical uncertainty analysis of RKE_{30} simulation and solution space for $D_{SG} \geq 30\%$: longitudinal (a), transversal (b) forces, and Y_{eq}(c)

The diminished role of the shotgun load-path becomes evident when observing the force levels in Figures 8.25(b) and 8.26(b). In contrast, the adjustments caused by the changes in the support-frame and wheel are noticeable in Figures 8.25(a) and 8.26(a). The original characteristics of these curves presented the highest force levels towards the end of the deformation space. In the RKE_{30} model from 200mm to 400mm, and due to the increase in the load-carrying capacity of the support-frame, an increase is observed in both force components. Nevertheless, the most significant change exists in the wheel region. The maximum forces are reduced by 50% with respect to the base model. This

indicates that the wheel assembly as a whole transmits less force to the firewall and rocker structures.

In essence, the RKE_{30} model with its set of countermeasures produces a set of RDC with good agreement with the calculated solution space. The kinematic analysis of the new model together with the robustness evaluation is presented in the next sections to ensure that the primary and secondary targets are achieved with the explicit consideration of the uncertainties.

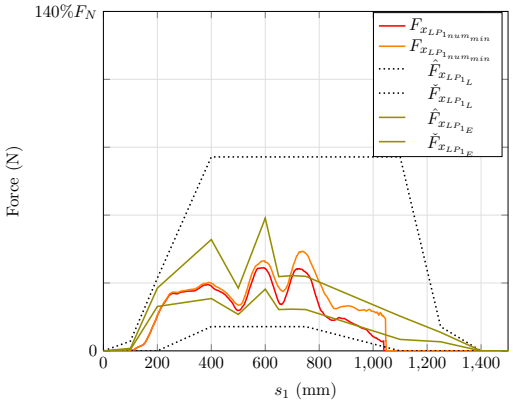

(a) Load-path 1: wheel-firewall-rocker longitudinal forces vs. deformation space (s_1)

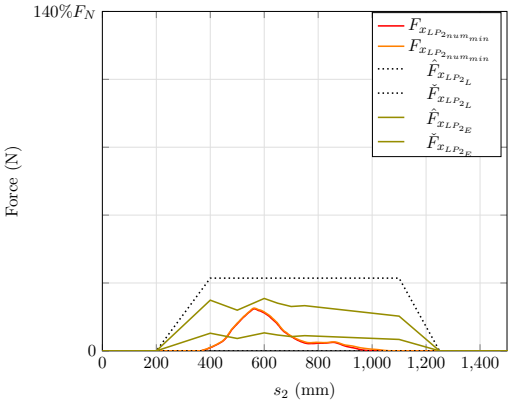

(b) Load-path 2: shotgun longitudinal forces vs. deformation space (s_2)

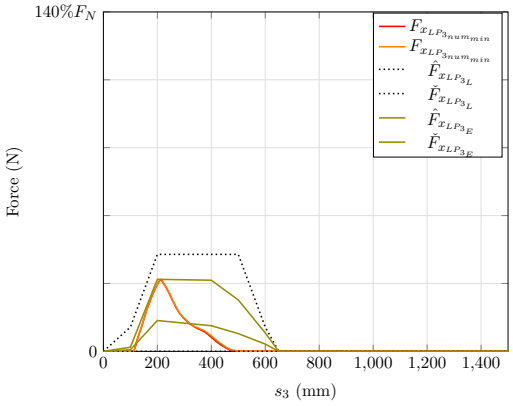

(c) Load-path 3: bumper beam-front rail longitudinal forces vs. deformation space (s_3)

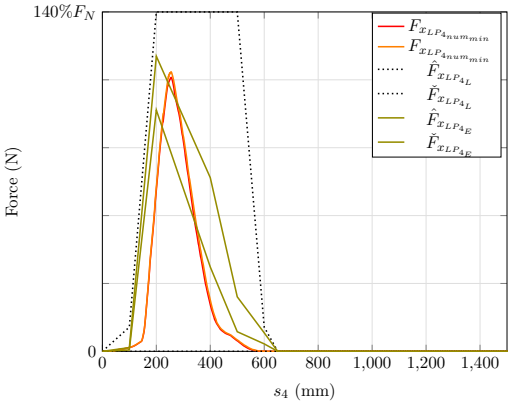

(d) Load-path 4: sub-frame longitudinal forces vs. deformation space (s_4)

Figure 8.25 Maximum and minimum longitudinal forces at load-path level extracted from numerical uncertainty analysis of RKE_{30} simulation and solution space for $D_{SG} \geq 30\%$: wheel-firewall-rocker(a), shotgun(b), bumper beam-front rail (c), sub-frame(d)

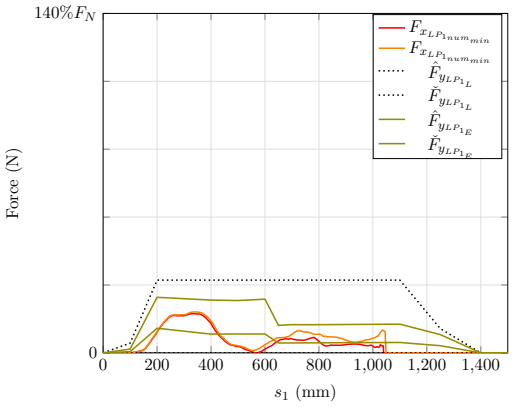

(a) Load-path 1: wheel-firewall-rocker transversal forces vs. deformation space (s_1)

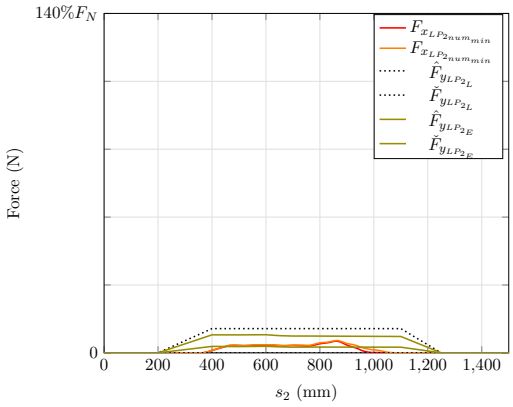

(b) Load-path 2: shotgun transversal forces vs. deformation space (s_2)

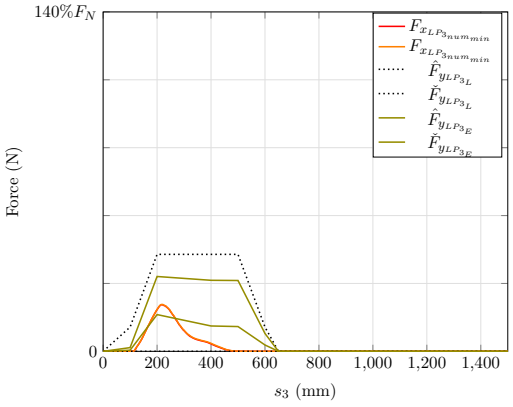

(c) Load-path 3: bumper beam-front rail transversal forces vs. deformation space (s_3)

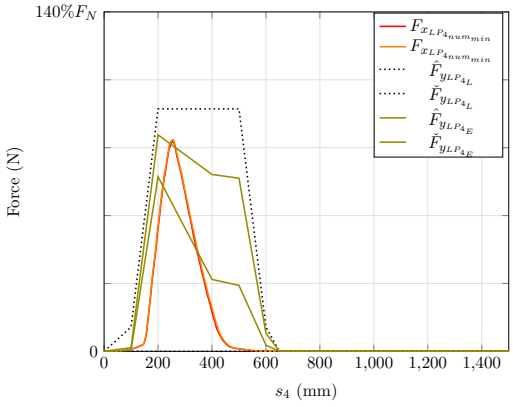

(d) Load-path 4: sub-frame transversal forces vs. deformation space (s_4)

Figure 8.26 Maximum and minimum transversal forces at load-path level extracted from numerical uncertainty analysis of RKE_{30} simulation and solution space for $D_{SG} \geq 30\%$: wheel-firewall-rocker(a), shotgun(b), bumper beam-front rail (c), sub-frame(d)

8.4.3. Robustness Check

The same sampling scheme as well as variable selection and uncertainty characterization used to evaluate the robustness of the base model is now used to analyze the performance of the RKE_{30} model. As first control, the average force levels of the load-paths for each uncertainty phase are compared to each other and against the solution space. The load-path force levels are presented in Figures 8.27 and 8.28 for the longitudinal and transversal components, respectively. The different sources of uncertainty affect the response of the components in different manners. A different barrier position implies that the extension

of the sub-frame may make contact at a different angle causing variations in the force components. On the other side, the variation of the failure forces of the suspension components affect the detachment times of the wheel assembly causing variations in its trajectory and in consequence in the force levels produced.

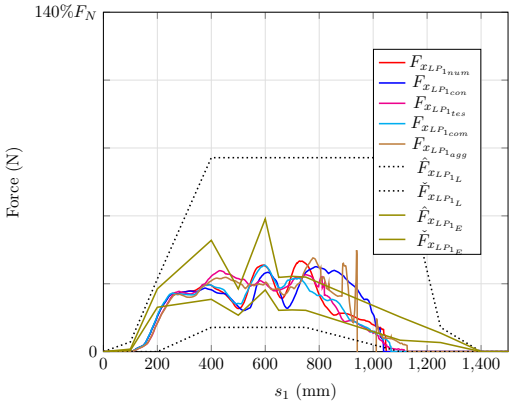

(a) Load-path 1: wheel-firewall-rocker longitudinal forces vs. deformation space (s_1)

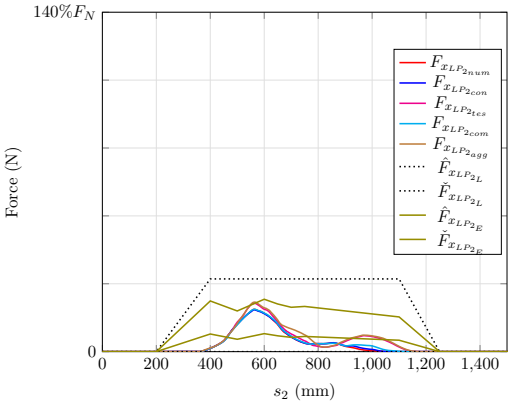

(b) Load-path 2: shotgun longitudinal forces vs. deformation space (s_2)

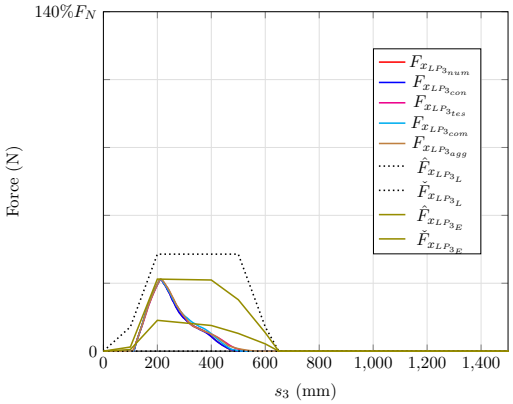

(c) Load-path 3: bumper beam-front rail longitudinal forces vs. deformation space (s_3)

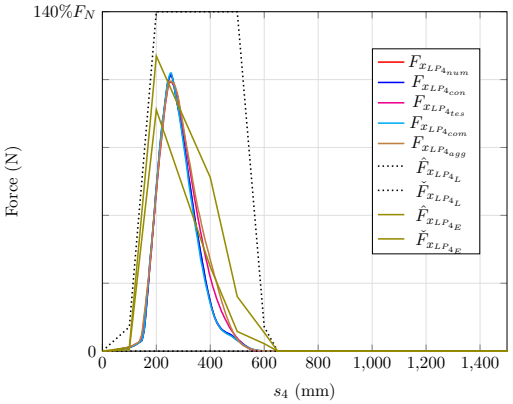

(d) Load-path 4: sub-frame longitudinal forces vs. deformation space (s_4)

Figure 8.27 Maximum and minimum longitudinal forces at load-path level extracted from numeric (*num*), configuration (*con*), test (*tes*), component (*com*), and aggregated (*agg*) uncertainty analysis of RKE_{30} simulation and solution space for $D_{SG} \geq 30\%$: wheel-firewall-rocker(a), shotgun(b), bumper beam-front rail (c), sub-frame(d)

The scatter introduced by the uncertainties is mainly present in the wheel-firewall-rocker and sub-frame load-paths, as expected. The variations in the load-levels for the shotgun and bumper load-paths are negligible. The maximum longitudinal forces of

the sub-frame lie within a compact range, independent of the uncertainty phase. However, two clear clusters appear when considering the maximum transversal force of this load-path. The load levels corresponding to the numeric, configuration, and component phases are closely packed together, while the curves belonging to the test and aggregated uncertainties lie slightly lower in comparison. As stated previously, mainly the variation in barrier position affects the maximum force created by the interaction of the curved surface of the barrier and the sub-frame extension.

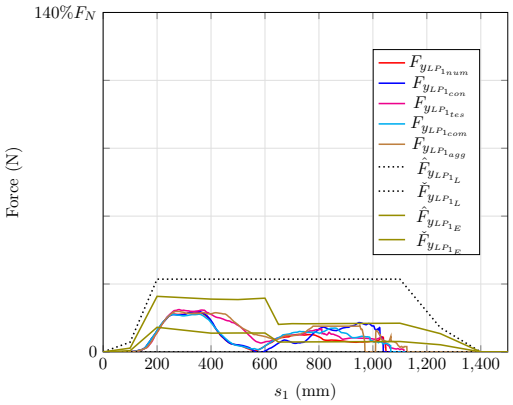

(a) Load-path 1: wheel-firewall-rocker transversal forces vs. deformation space (s_1)

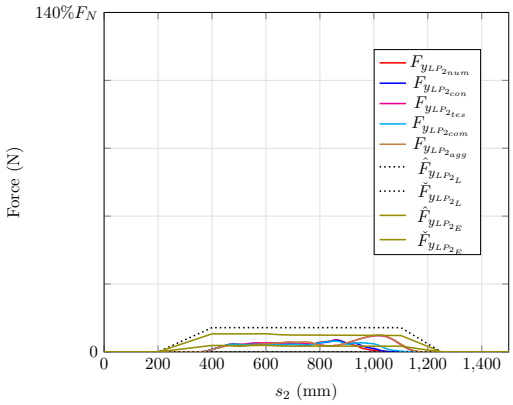

(b) Load-path 2: shotgun transversal forces vs. deformation space (s_2)

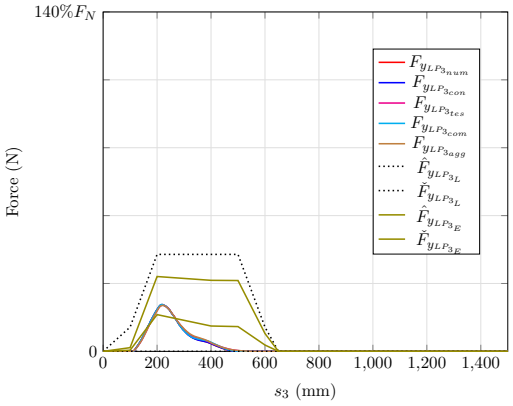

(c) Load-path 3: bumper beam-front rail transversal forces vs. deformation space (s_3)

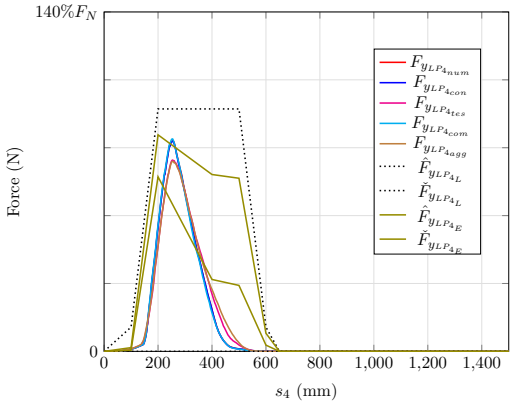

(d) Load-path 4: sub-frame transversal forces vs. deformation space (s_4)

Figure 8.28 Maximum and minimum transversal forces at load-path level extracted from numeric (*num*), configuration (*con*), test (*tes*), component (*com*), and aggregated (*agg*) uncertainty analysis of RKE_{30} simulation and solution space for $D_{SG} \geq 30\%$: wheel-firewall-rocker(a), shotgun(b), bumper beam-front rail (c), sub-frame(d)

The most noticeable deviations from the curves corresponding to the numerical uncertainty analysis are present in the wheel load-path starting at 400mm. Before this deformation state, only the supporting-frame is active and the countermeasures integrated in the RKE_{30} model result in a stable curve characteristic. After 400mm, the test and aggregated responses maintain a higher load level in contrast to the sharper drop presented for the other sources of uncertainties. The average response for these two phases can be explained by the introduction of the different wheel size. A smaller wheel implies that the bending of the support-frame is dominant for a larger portion of the deformation spaces until it reaches the wheel and displaces it backwards causing the drop in the force levels. The effect these discrepancies to the solution space have in the kinematics are now quantified.

Ultimately, the deviations observed in the RDC at the load-path level are explained by the different effects introduced by the variations brought by the uncertainties and even if the corridor is not completely fulfilled along the entirety of the deformation space, the effect on the fulfillment of the kinematic constraints is acceptable. The time series of the total rotation, θ_z, rest kinetic energy, RKE, glance-off value GV_P, rest deformation length s_L for the RKE_{30} model considering the numerical uncertainties are shown in Figure 8.29.

The total rotation of the vehicle has changed its characteristic completely from the base model. The set of design changes produces a negative rotation for the entirety of the simulation time that starts at ca. 20ms. A scatter of the curves is observable towards 100ms, however the complete simulation set presents the same curve characteristic. The GV_P now presents an accelerated increase towards 1. The 10 simulations reach the glance-off mode before 80ms and the scatter is less than the one observed in the rotation. The rest deformation length fulfills the s_L>10mm constraints with enough space by reaching a minimum average value of 310mm.

It was stated that the statistically secure way to achieve a RKE>30% is for the vehicle to have a combination of negative rotations with a glance-off behavior. These two constraints are fulfilled and consequently the secondary target of achieving at least 30% rest kinetic energy is also achieved. Figure 8.29(b) shows that the kinetic energy decays relatively faster in the first 20ms and then presents a slower decrease until 80ms where an average of 31% is reached. This coincides with the point where all of the 10 simulations have reached the glance-off state and it is therefore considered as the t_{end} of the crash. It can be concluded that at least considering the numerical uncertainties involved in the FE solver, the countermeasures integrated in the structure lead to the achievement of the secondary targets.

Considering that the aggregated uncertainties caused the most significant worsening and decay of RB_I, and therefore the largest variation in the kinematic parameters, the time series of the robustness indexes of the kinematic parameters are presented in Figure 8.30. The two most affected quantities were the glance-off value and the total rotation. The kinematic analysis conducted in the simulation set of the aggregated uncertainty study results into a decaying RB_I starting at 20ms for both kinematic parameters. In the case of GV_P the RB_I at the end of the simulation reaches 0.6 and for the total ro-

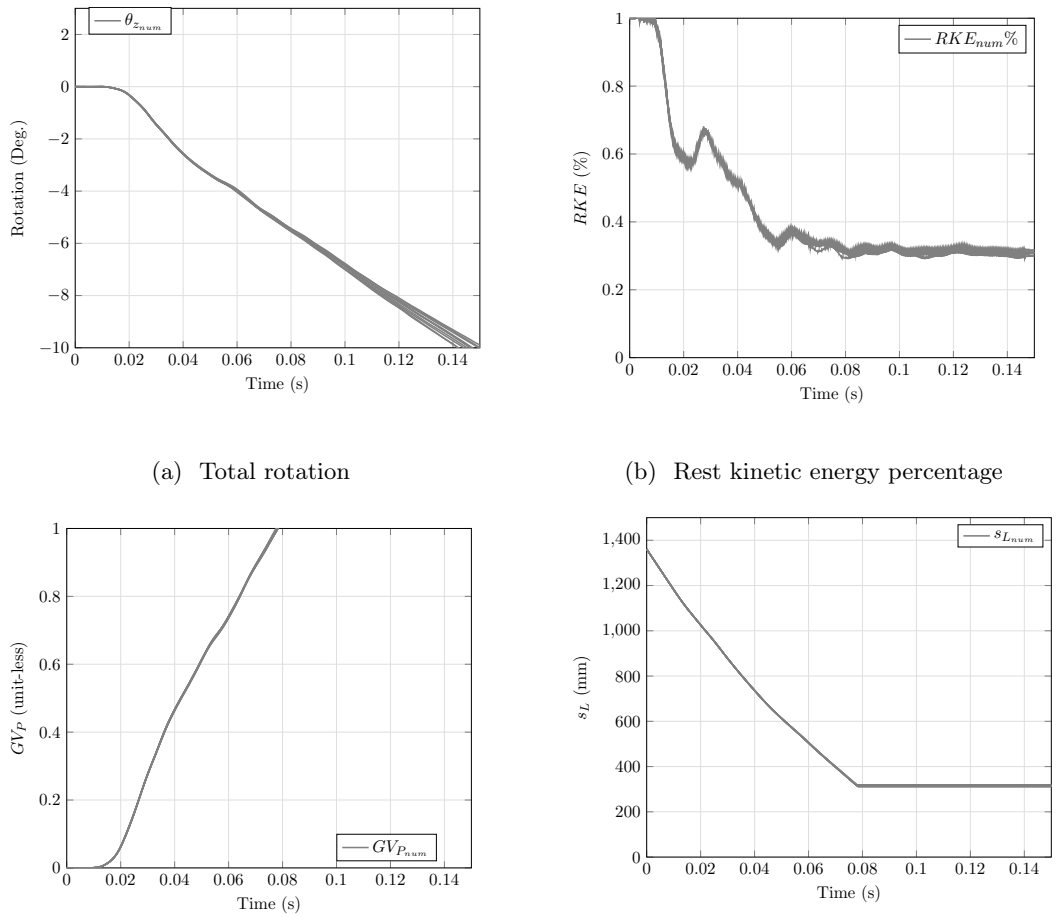

(a) Total rotation

(b) Rest kinetic energy percentage

(c) Glance-off value

(d) Rest deformation length

Figure 8.29 Kinematic parameters extracted from RKE_{30} simulation from numeric uncertainty analysis, total rotation, θ_z (a), rest kinetic energy, RKE (b), glance-off value GV_P (c), rest deformation length s_L (d)

tation 0.4. Both values imply an acceptable robust behavior and an improvement with respect to the same phase of the base model.

It is also noticeable in Figure 8.30(c) that even if the absolute values are considered stable, a decay at 80ms is present in the RB_I time series of s_L. As mentioned before around this time point, the vehicles start to reach a GV_P=1, which means that the s_L is fixed to the value reached at the point of glance-off. Therefore a slight delay or speedup of the glance-off affects the RB_I of s_L. At the end of the simulation the RB_I of the rest deformation length reaches a value of 0.6, which is comparable to the values achieved from the base model. Ultimately, the RB_I of RKE fulfills the robustness requirements for the entirety of the simulation time. To sum up, the robustness indexes of the kinematic

parameters in their time series representation result in a robust behavior and present an improvement with respect to the base model. The next step is to revisit the robustness assessment of the scalar values.

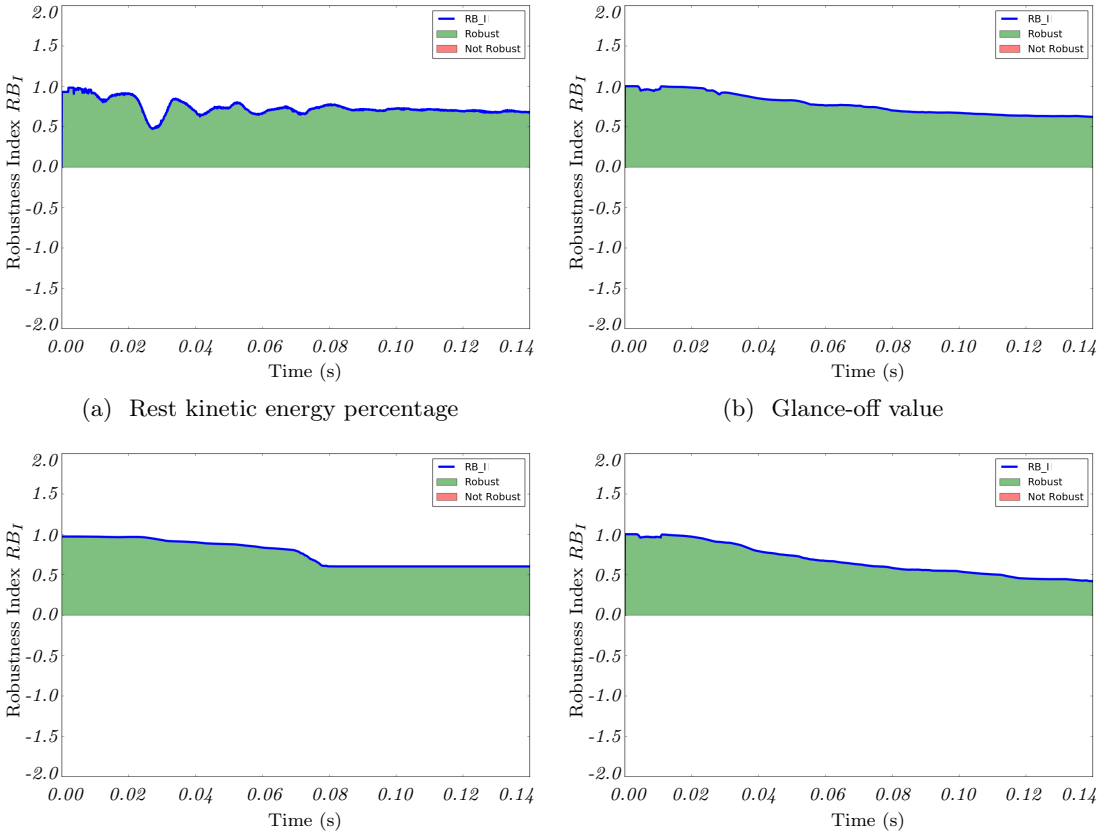

(a) Rest kinetic energy percentage

(b) Glance-off value

(c) Rest deformation length

(d) Total rotation

Figure 8.30 Kinematic parameters robustness index for aggregated uncertainty analysis extracted from RKE_{30} simulation: rest kinetic energy, RKE (a), glance-off value, GV_P (b), rest deformation length, s_L (c), total rotation, θ_z (d)

In the base model, a total of 14 quantities presented a RB_I<0 at the aggregated uncertainty phase. In the RKE_{30} model this amount is reduced to 6. The steering column and left toepan intrusion points still present deficiencies with respect to the robustness and as before the revision of the modeling of the steering column subsystem is advisable. The brake pedal has also marginally reached a RB_I<0. From the perspective of the forces and moments in the structure, only the total moment and transversal forces of the wheel and shotgun load-path present a non-robust behavior. Taking that into consideration, the revision of the modeling of the rim, specially the characterization of the material failure is advisable. From the stand point of the kinematic parameters all of them present acceptable values of RB_I>0. The kinematic parameter with the smallest

RB_I is the s_L with 0.05, followed by the RKE with 32%. The total rotation and glance-off value have RB_Is of 0.6 and 0.99, respectively. This assessment also confirms that not only the countermeasures lead to a design that achieves the secondary targets but also that they do so while increasing the robustness with respect to the base design.

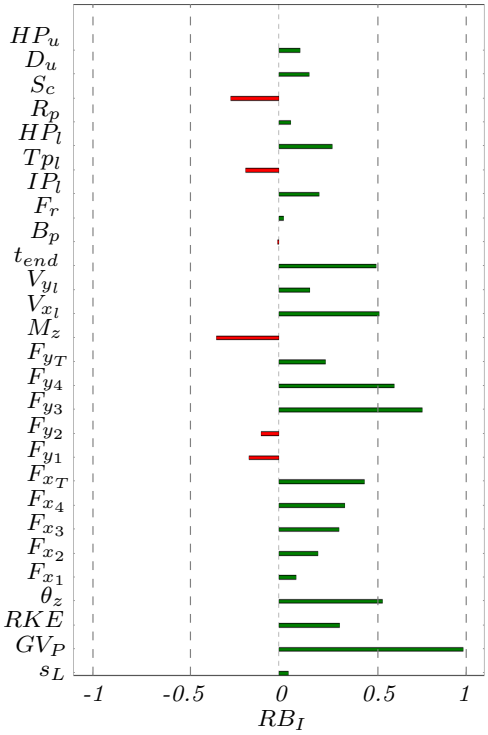

Figure 8.31 Robustness Index for the aggregated uncertainty analysis of the RKE_{30} simulation

As a final assessment of the sensitivity of the RKE_{30} model, its primary target achievement and its robustness, the box plots of the relevant kinematic parameters and safety distance are presented in Figure 8.32. The effect of the countermeasures is evident in the scatter or lack thereof in the glance-off value. For the 5 uncertainty assessments, all of the 370 simulations present a glance-off mode. This glance-off effect is achieved by means of a negative rotation. The range of rotation at t_{end} for all of the simulations is -6° at the lower end and -5° at the higher end. The largest variability is the result of the aggregated uncertainties but still only represents a delta of 1° in absolute values. The rest deformation length shows in absolute values the largest variability. However, in each of the 5 uncertainty assessments the constraint of reaching a minimum of 10mm is comfortably reached. Once again the aggregated phase is responsible of introducing the largest range of variation. The minimum s_L reaches values slightly smaller than 250mm, while the maximum values reach more than 450mm.

That being the case, the secondary target of RKE>30% is reached in the majority of the simulations. The numeric and configuration phases show almost a 100% target

achievement. Meanwhile the test and component phases present a target achievement of ca. 75% each. The minimum values for both phases reach RKE=27%. The largest variability of the RKE is introduced by the aggregated sources of uncertainty. The minimum values reach in this phase 25% and at the same time 75% of the results have a RKE>30%. Even if this is a clear improvement from the base model, the small but yet present deviations of the RDC with respect to the solution space explain this miss in the achievement of the secondary targets. A total fulfillment of the solution space implies a 95% fulfillment of the constraints. Therefore, in order to increase the success rate, adjustments have to be made in the force-levels, specially in the transversal forces of the sub-frame load-path that present an earlier than expected drop.

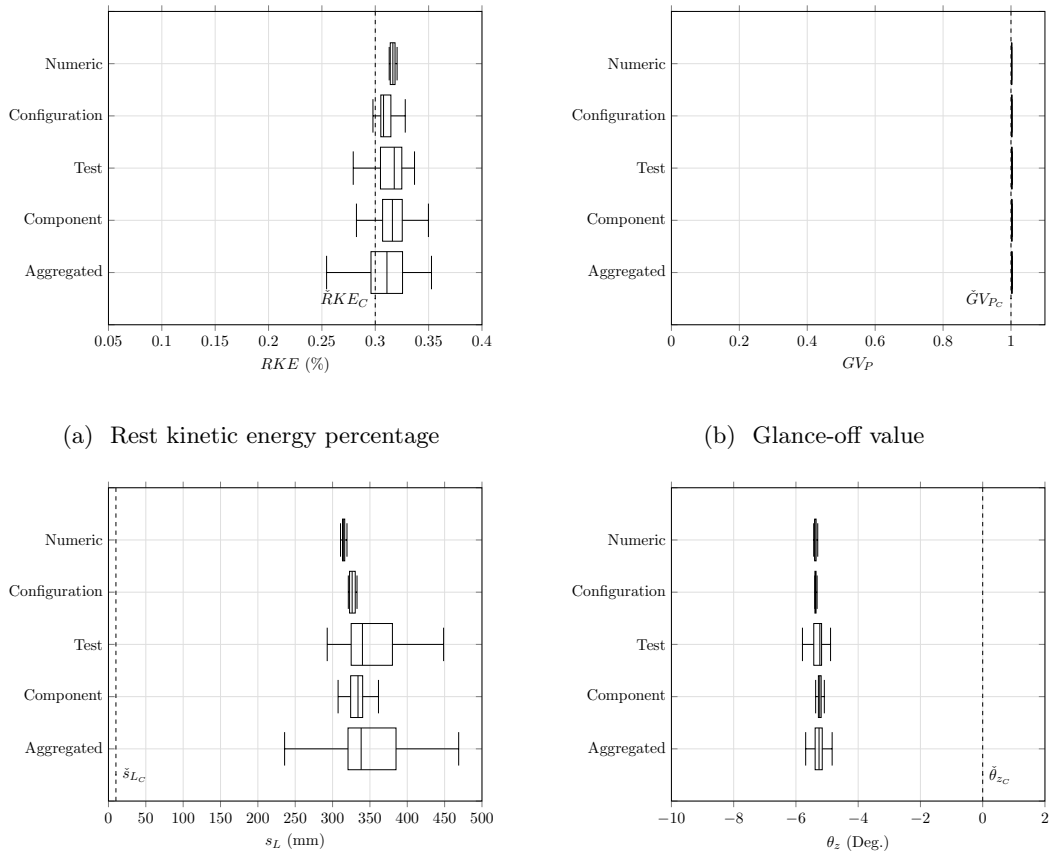

(a) Rest kinetic energy percentage

(b) Glance-off value

(c) Rest deformation length

(d) Total rotation

Figure 8.32 Kinematic parameters boxplot for numerical, component, test and aggregated robustness analysis for RKE_{30}: rest kinetic energy, RKE (a), glance-off value, GV_P (b), rest deformation length, s_L (c), total rotation, θ_z (d))

The assessment on the primary target of achieving a safety distance larger than 30% under all circumstances in context of the uncertainty sources is presented in Figure 8.33.

After the explicit consideration of the numerical aspects of the FE solver, configuration, test conditions, component and aggregated uncertainties the D_{SG} lies within a range of 80% to 90%. This positions the design into the top three vehicles tested by the IIHS with the highest D_{SG}. Moreover, this D_{SG} range is achievable with a variety of vehicle configurations, test conditions, and component properties scatter. With that in mind, the solution-space-based iterative simulation scheme shows through this design exercise not only its potential to indicate a clear design direction with regards to the layout of the structure but is also capable of achieving the vehicle primary and secondary targets in a robust manner.

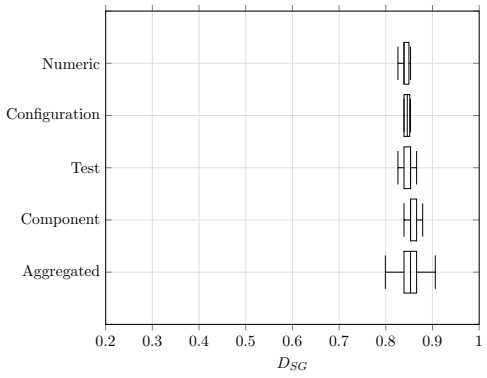

Figure 8.33 Safety distance, D_{SG} for the uncertainty analysis of the RKE_{30} model

Chapter 9

Discussion

The limitations of the methods presented and applied in this work, whose objective was to accelerate the crashworthiness design so that the structural targets are achieved in a robust manner, are presented in this chapter. This summary of critical reflections of the issues identified has the intention to recognize under which circumstances the low-fidelity kinematic model, solution spaces, and robustness assessments result in outcomes other than the expected. This assessment on the effectiveness of the methodology can lead the way to its future improvement needed to overcome the current limitations. An outlook on complementary topics that would also enrich the methodology presented in this work is given at the end of this chapter.

9.1. Characterization and Analysis of the SOF load case

The corner stone of the methodology presented in this work is the extraction of information from a crash test, either virtual or in hardware. The accurate measurement of the accelerations, velocities, rotations, displacements and forces is fundamental for the kinematic analysis. In that regards, the crash event analysis scheme presented in Section 3.1 is clearly sensitive to the input data. On one hand, the accuracy of the analysis performed on the high-speed video footage depends on a constant camera position with a completely perpendicular orientation in its top view that minimizes the parallax errors. Even if the IIHS conducts its testing with the highest standard, the position of the camera and perspective has changed slightly over the years. On the other hand, the trajectory reconstruction by means of the sensor signal analysis also represents its own set of challenges. It can be expected that the precise orientation of the sensor is not available at every single crash test. A sensitivity study, studying the effect of the deviation from the standard orientation of the sensor, could quantify the scatter expected from these measurements. Ideally, both methodologies are combined so that the benefits in accuracy from the usage of the acceleration and rotational velocity signals and

the simplicity in the application of the video analysis help overcome the lack of precise information concerning the sensor initial orientation. An optimization procedure can be set up in order to find the most probable initial orientation of the sensor by minimizing the difference in the trajectory obtained from the video analysis.

9.2. Structural Target and Safety Distance

The data extracted from the IIHS database is evidently dependent on the amount of vehicles tested by the institute. During the time in which the analysis was conducted the COVID-19 pandemic affected the number of vehicles tested by the IIHS in the year 2020. The cluster and correlation analysis shown in Section 3.3 includes the data collected in 2020. However, the addition of new vehicles, specially in context of the electrification of the automotive industry may affect the trends identified and used to derive the kinematic constraints. Additionally, the IIHS has already implemented changes to the assessment protocols of other load-cases. For this reason, if in the future the institute decides to change the assessment procedures and methods to calculate the safety ratings for the Small Overlap load case, a mapping of the new and old schemes is necessary to be able to compare the results and identify and interpret future trends.

9.3. Low-fidelity Physics-based Kinematic Model

Due to the fact that the kinematic model is itself a simplification of a complex multi-physics phenomenon, i.e. the crash event, deviations from the results obtained from a hardware test or FE simulation are expected. One of the issues identified involve the selection of load-path positions. The components in the structure are not idealized springs but three-dimensional and complex geometries. By the selection of the position of the load-path as a single line, the real spatiality of the geometry of the structure is lost. This affects two aspects. First, the point of application of the force is assumed to lie exactly in the load-path position, which in reality is a three-dimensional space. This affects the lever arm and consequently the total rotation of the vehicle. Second, the boundary boxes used to find the projections of the load-paths onto the barrier do not consider that the components in the load-path could move outside the boxes due to the deformations of the structure. This implies that the mapping of the force levels into the load-path may be done to not exactly the same components originally belonging to the load-path. Even if a finer discretization of the load-paths could alleviate the effect of this issue, it loses its potential for practical applications for the design of the structure.

Another issue identified has to do with one of the main assumptions used to construct the kinematic model, namely the assumption of a planar motion in the xy plane. The IIHS has already witnessed some extreme cases where the longitudinal forces and their correspondent lever arms create a large enough moment to cause the vehicle to exhibit a more complex fully three-dimensional motion. One example of this extreme behavior is the Jeep Wrangler 2019 with test number CEN2001. In that same direction, the rigid body assumption only holds if the rest of the car, from the A-Pillar position backwards,

does not present any large deformations. Additionally, the measurement of the rest deformation length is affected directly by the selection of the location of the A-Pillar. The position of the A-Pillar point should coincide with the point where the intrusion measurements are taken, but the A-Pillar construction usually involves a considerably large volume not representable by a single point. Moreover, the kinematic model does not take into account any changes in the relative position of the center of gravity or loss of mass during the crash. Which due to extreme deformations, detachments of components with significant mass can be expected.

The validation procedure presented in Section 7.1 showed that the kinematic model results were in agreement with the kinematics of the reference test. However, even if in the application section a completely different kinematic was studied, a future validation should explicitly include other kinematic modes as well as a wider spectrum of masses and vehicle characteristics so that the limits of the kinematic model are evident. This comparison should also consider the uncertainty of the hardware test measurements mentioned before.

9.4. Solution Space Calculator

The backwards calculation presented in Section 5.1.1 is computationally intensive. A relatively high number of iterations and model evaluations is needed to achieve a useful solution space. The implementation of a parallelization scheme was required in order to maintain the time needed for the solution space calculation to an acceptable range. Also in that regards, not only the model evaluation is costly but also the sample generation can consume time and computational power to reach the minimum acceptable coverage of the design space. Also, the outcome of the calculation is sensitive to the selected discretization of the deformation space and to the selected design bounds. The issues with the discretization become evident in Section 7.2 where the reconstructed RDC did not fully lie inside the solution space. A finer discretization could improve the solution space fulfillment but the computational cost of calculating it becomes unacceptable.

Moreover, even if the exploration phase takes out a significant portion of the unfeasible regions, after a given number of iterations the consolidation phase slows down and the achievement of the higher success rates is often asymptotic and the solution spaces become too small to be useful. Another sensitivity identified involves the mapping of the RDC from the full-vehicle to the load-path level. The mapping is sensitive to the Y_{eq}, which is in turn sensitive concerning the magnitude of the force-levels particularly at the beginning and end of the crash.

9.5. Data Driven Optimal Constraint Identification

The relationships between the vehicle kinematics and the safety distance presented in Section 5.2 hold for the dataset analyzed, which is assumed to be representative of industrial cases. In that sense, a considerable amount of cases that presented a $RKE<30\%$ also received a good safety rating with relatively higher safety distances. This indicates

that a variety of design strategies exist within the industry and that not all vehicles are designed with an efficiency in mind in the sense of maximizing the RKE. Complementary to the study of the relationships between the kinematics and crashworthiness, an analysis that involves the study of the type of structures used in the vehicles, for example the type of suspension system and their effect on crashworthiness results would also help to establish trends and useful correlations.

9.6. Robustness Analysis

The sources of uncertainty presented in Section 6.2 may be complemented by additional variables such as the properties of the contact between the barrier and vehicle surfaces. Concerning the sampling scheme in a high-dimensional problem, the OLHC may not be enough to offer an acceptable coverage of the design space. In the same direction, the probability distribution approximation compared against the target distribution has to have *a priori* information on the expected distribution for it to be meaningful. It can be assumed with a certain degree of certainty that the output distribution resembles the input distribution which is known for this problem statement. Therefore, the error made by assuming a similar output distribution can be considered acceptable. In that sense, the use of the Kolmogorov distance as quantity to characterize the robustness offers the flexibility to compare any *cdf*s even if they are only represented numerically.

The robustness index analysis is a path to the identification of particularly sensitive components. This can be achieved by the time series analysis. The moment the robustness index decays is an indicative of the moment of activation of a component that could use an improvement in the modeling. However, even if the robustness index offers an objective way to compare the behaviors of the output quantities, the limits that define the index are completely dependent on the user input. Therefore, the definition of robustness remains affected by the expected behavior of the model.

9.7. Solution Space-based Iterative Simulation Scheme

The implementation of a SSBISS as presented in Section 6.1 can be expanded to consider the effect of the maximization of the fulfillment of the solution space in other load cases. During the application procedure carried out in Section 8.2, it became evident that the quality of the base model plays a significant role and that the base model should at least fulfill the numeric uncertainty phase requirements. Additionally, when comparing the effect of the different sets of uncertainties, the selected box plot visualization leaves the outliers out. It would be valuable also to study the extreme cases.

The results of the calculation of the solution space shown in Section 8.3 display a set of relatively high forces that were needed to achieve the secondary targets and fulfill the kinematic constraints. The countermeasures implemented to fulfill the solution spaces may affect negatively other load cases due to excessive stiffening of the sub-frame needed to withstand the increased load levels caused by the extension and early contact with the barrier. Other countermeasures involving the topology of the shotgun load-path may

offer a new field of solutions if changes to the BIW are allowed.

9.8. Outlook

The design exercise presented in this work offered the opportunity to integrate countermeasures in an already developed structure in order to improve the robustness and achievement of the primary structural targets. The limitation of using a mature design as a base is of course the lack of flexibility to apply major structural changes. Due to the electrification of the vehicle platforms and the inclusion of new manufacturing technologies in the series production, it is beneficial to establish what is the optimum topology and optimum crash mode to overcome the challenges the automotive industry currently faces. These challenges include the significant increase of mass in the structure due to the use of high voltage batteries to power the electric motors, the added degree of protection that these systems require as well as the definition of the structural role such massive components play in the vehicle platform. Additionally, to exploit the benefits of the communality of the components across the manufacturers lineup, the vehicle structures should be integrated in vehicle platforms that are capable to serve as a base for a variety of vehicle types, including a wide spectrum of masses and proportions.

9.8.1. Optimal Topology

The physical quantities involved in the Small Overlap crash test were identified and analyzed during this work. Consequently and considering the flexibility a new design not limited by the current vehicle architectures offers, the identification of optimal front-structure topologies becomes of special interest. In the case the design strategy is to produce a purely rotational or purely glance-off kinematic behavior the structure should be designed in a consistent matter so that the complete structure delivers the necessary load levels to produce the selected kinematic.

In the case of the rotation mode, the maximization of longitudinal forces across the structure is fundamental for achieving this kinematic mode. Additionally, the maximization of the transversal lever arm to maximize the positive moment around the vertical axis, supports the principles of this kinematic mode. Therefore, the load-paths located outwards in the vehicle should maximize their longitudinal forces. From the perspective of the glance-off kinematic mode, the first principles analysis indicated that similarly to the design exercise presented in this work, the transversal forces should be maximized, while at the same time minimizing the longitudinal component; simultaneously, maximizing the longitudinal lever arm to increase the negative movement that assist reaching a glance-off value of 1. The transversal forces are a function of the contact point of the vehicle relative to the barrier. The transversal forces can only be produced when the load-paths contact the curved surface of the barrier. Taking that into account, the structures that maximize the conditions needed for glance-off are the ones that have contact with the curved section of the barrier early on in the crash and for as much time as possible. Tangential structures to the vehicle trajectory towards the barrier, starting

inwards and moving outwards near the A-Pillar maximize the transversal forces and decrease the longitudinal component at the same time. However, the main contribution of longitudinal forces is in many cases the wheel load-path. In that case, the longitudinal force from this load-path should be minimized either by influencing the wheel kinematic and reducing the failure load of the wheel or by completely taking the wheel out of the load-path by causing a detachment from the suspension. This strategy comes certainly with its own set of challenges when trying to control the often unrestrained nature of the wheel kinematics.

9.8.2. Optimal Kinematic Mode

As it was established in this work, a relationship exists between the vehicle kinematics and its crashworthiness performance in the Small Overlap load case. It was also identified that the deformations in the occupant compartment are dependent on the kinematic parameters and not specifically in the kinematic mode of the vehicle during the test. Meaning that if the structural targets can be achieved by both kinematic modes then, determining the optimal mode for a vehicle with a given set of characteristics is relevant at the early stages of the design. As in any optimization problem, the optimum depends on the constraints and objective function of the problem. Two performance indicators are present in the design of the vehicle structure: robustness and efficiency. As stated in this work, the robustness can be interpreted as the fulfillment of the structural targets under the explicit consideration of the sources of uncertainty. The efficiency can be understood as reaching these targets with the least amount of mass possible. Both indicators can be translated into parameters that can be defined in the kinematic model language, namely the rest kinetic energy for the efficiency and rest deformation length for the robustness. Taking that into consideration, an optimal kinematic mode is entirely dependent on the prioritization of these two often contrary objectives.

9.8.3. Solution Spaces for the Component Level

The deepest level at which the solution spaces were defined in this work is the load-path level. However, the load-path is not the deepest level of structural design; that is in fact the component level. Using the solution space methodology presented in this work to also define the functional properties and its correspondent solution spaces at the component level as function of the properties of the load-path would exploit even further the benefits of independence and parallelization of the design processes. This can be achieved by reinterpreting the components as condensed deformation elements such as beams that have three-dimensional load-carrying capacity properties. For each component in the load-path the sum of their three-dimensional load-carrying capacities should align with the solution space defined at the load-path level. The challenge of this approach is the effective condensation of the components into beam elements and the efficient mapping of load-carrying capacity properties.

Chapter 10

Conclusion

The Small Overlap frontal (SOF) crash test was introduced by the Insurance Institute for Highway Safety in 2012. The front structure design across automobile manufacturers has considerably improved in the last decade reaching an industry average Good structural rating with a safety distance of 30%. This suggests that the strategies to overcome the challenges of the SOF load case are already known. Therefore, the current challenge lies in defining the system, subsystem and component targets to achieve a competitive structural rating in the most efficient way possible, starting in the early design phase. Following the V-diagram of crashworthiness design, this work proposes a structural design strategy for the SOF load case with the objective of defining, decomposing and implementing the design targets at each structural level of the vehicle through a development process. The resulting structural topology, i.e. the way the load-paths are placed within the vehicle frame along with their connections as well as the load-carrying capacities and energy absorption properties, will determine the overall crashworthiness performance of the vehicle. Defining the required force levels for structural components in the early phase improves the outcome of the project in terms of cost, efficiency and performance.

Starting with the available set of basic vehicle properties at the early design phase (mass, center of gravity, rotational inertia, vehicle width, vehicle overhang, and greenhouse proportions), a physics-based low-fidelity model is proposed to estimate the vehicle kinematics. Even though the kinematics of a vehicle subjected to the loads present in a crash is a complex phenomenon, basic physical principles can be applied to understand the influencing factors and their effect on the resulting trajectory of the vehicle. A detailed analysis of the interdependencies between the kinematic response of a vehicle and its crash performance was carried out. Two distinctive kinematic modes are identified: *glance-off* and *deformation* mode. For each mode, specific kinematic variables that correlate with the crash performance are identified. These are used in the design phase together with the kinematic model to assess the resulting SOF load case crashworthiness and to determine the vehicle safety rating. Ensuring the crash performance of the vehicle

from the early phase design requires designing with a kinematic model which is as simple as possible and as complex as necessary to represent the crash event. Such a low-fidelity physics-based model should overcome the lack of detailed vehicle information and instead use it as leverage to further drive the vehicle design process and thus, define the functional properties of the structure, i.e. load-carrying capacities and energy absorption properties.

By using a low-fidelity model that links the vehicle properties and its kinematic response, the resistance-to-deformation characteristics (RDC) are described at the load-path and full-vehicle levels resulting in a well-defined trajectory with a predictable crash performance. Such a forwards calculation is efficient and suitable for the early phase design. However, the inverse problem statement, i.e. determining the RDC that produce a desired kinematic response, is of greater interest in the vehicle design. The backwards calculation of the low-fidelity model also described as the computation of force-displacement solution spaces allowed to efficiently search and find suitable RDC towards a robust achievement of the structural target. The solution space approach finds the set of force-displacement curves that fulfill the given kinematic constraints. This enables the definition of force-level requirements for the load-paths in the structure. Statistically speaking a set of kinematic constraints exists that maximizes the probability of fulfilling the primary structural targets, meaning obtaining a Good rating.

The Solution Space-based Iterative Simulation Scheme (SSBISS) takes the requirements defined in the early phase for each subsystem as objective function and determines the level of violation of the solution space for each design proposal while explicitly considering the relevant sources of uncertainty and the variation they produce. The sources of uncertainty are identified and characterized. The robustness of the design is quantified through the use of a robustness index. The use of the SSBISS decreases the number of output variables with a negative robustness index. Meaning that a design that fulfills the solution space and that considers the sources of uncertainty explicitly in its development achieves a more robust response. The fulfillment of the solution space and subsequently of the kinematic constraints, enables the achievement of not only the secondary kinematic response targets, but also the primary structural targets with the explicit consideration of the sources of uncertainty.

Disclaimer

The results, opinions and conclusions expressed in this work are not necessarily those of Bayerische Motoren Werke Aktiengesellschaft.

Bibliography

Abdollahzadeh G, Faghihmaleki H (2017) Seismic-explosion risk-based robustness index of structures. International Journal of Damage Mechanics 26(4):523–540, DOI 10.1177/1056789516651919

Abramowicz W, Jones N (1984) Dynamic axial crushing of square tubes. International Journal of Impact Engineering 2(2):179–208, DOI 10.1016/0734-743X(84)90005-8

Ambrósio J, Dias J (2007) A road vehicle multibody model for crash simulation based on the plastic hinges approach to structural deformations. International Journal of Crashworthiness 12(1):77–92, DOI 10.1533/ijcr.2006.0171

Andricevic N, Duddeck F, Hiermaier S (2016) A novel approach for the assessment of robustness of vehicle structures under crash. International Journal of Crashworthiness 21(2):89–103, DOI 10.1080/13588265.2015.1125618

Anselma PG, Niutta CB, Mainini L, Belingardi G (2020) Multidisciplinary design optimization for hybrid electric vehicles: component sizing and multi-fidelity frontal crashworthiness. Structural and Multidisciplinary Optimization 62(4):2149–2166, DOI 10.1007/s00158-020-02603-6

Avalle M, Belingardi G, Ibba A, Kayvantash K, Delcroix F (2007) Stochastic crash analysis of vehicle models for sensitivity analysis and optimization. In: The 20th International Technical Conference on the Enhanced Safety of Vehicles (ESV), Lyon, France

Bach J, Langner J, Otten S, Holzapfel M, Sax E (2017) Data-driven development, a complementing approach for automotive systems engineering. In: 2017 IEEE International Systems Engineering Symposium ISSE, Vienna, Austria, DOI 10.1109/syseng.2017.8088295

Bagloee SA, Sarvi M, Wolshon B, Dixit V (2017) Identifying critical disruption scenarios and a global robustness index tailored to real life road networks. Transportation Research Part E: Logistics and Transportation Review 98:60–81, DOI 10.1016/j.tre.2016.12.003

Baker JW, Schubert M, Faber MH (2008) On the assessment of robustness. Structural Safety 30(3):253–267, DOI 10.1016/j.strusafe.2006.11.004

Barley SA, Cripps RJ (1992) Executive-centred system design for CAD applications. Computer-Aided Design 24(5):235–242, DOI 10.1016/0010-4485(92)90076-M

Benson DJ, Hallquist JO, Igarashi M, Shimomaki K, Mizuno M (1986) Application of DYNA3D in large scale crashworthiness calculations. In: Computers in Engineering, Proceedings of the International Computers in Engineering Conference, Lawrence Livermore National Laboratory, Chicago, IL, USA

Bhise V (2017) Automotive Product Development: A Systems Engineering Implementation. CRC Press, Boca Raton, FL, USA

Biondini F, Frangopol DM, Restelli S (2008) On structural robustness, redundancy, and static indeterminacy. In: ASCE / Structures Congress 2008: Crossing Borders, Reston, VA, Canada, pp 1–10, DOI 10.1061/41016(314)237

Blanchard BS, Fabrycky WJ (2011) Systems Engineering and Analysis. Prentice Hall, Upper Saddle River, NJ, USA

Box GEP, Wilson KB (1951) On the experimental attainment of optimum conditions. Journal of the Royal Statistical Society: Series B (Methodological) 13(1):1–38, DOI 10.1111/j.2517-6161.1951.tb00067.x

Brach M, Brach RM (1998) Crush energy and planar impact mechanics for accident reconstruction. SAE Technical Paper 980025 DOI 10.4271/980025

Brach RM, Brach RM, Pongetti K (2014) Analysis of high-speed sideswipe collisions using data from small overlap tests. SAE Int J Trans Safety 2(1):86–99, DOI 10.4271/2014-01-0469

Böttcher CS, Frik S, Gosolits B (2005) 20 years of crash simulation at Opel-experiences for future challenges. In: 4th LS-DYNA Anwenderforum, DYNAmore GmbH, Bamberg, Germany, pp 79–86

Carvalho M, Ambrósio J (2010) Identification of multibody vehicle models for crash analysis using an optimization methodology. Multibody System Dynamics 24(3):325–345, DOI 10.1007/s11044-010-9221-z

Carvalho M, Ambrósio J, Eberhard P (2010) Identification of validated multibody vehicle models for crash analysis using a hybrid optimization procedure. Structural and Multidisciplinary Optimization 44(1):85–97, DOI 10.1007/s00158-010-0590-y

Chen B, Lei F, Chen G, Guan F (2012) A method of simplified modeling based on part influence coefficient for vehicle crash. In: 2012 Third International Conference on Digital Manufacturing & Automation, IEEE, Gulin, China, DOI 10.1109/icdma.2012.17

Chen YL, Huang L, Lu YQ, Deng L, Tan HZ (2016) Assessment of structural robustness under different events according to vulnerability. Journal of Performance of Constructed Facilities 30(5):04016,004, DOI 10.1061/(ASCE)CF.1943-5509.0000854

Cheng Z (2002) Analysis of automobile crash responses using wavelets. SAE Technical Paper 2002-01-0183 DOI 10.4271/2002-01-0183

Cheva W, Yasuki T, Gupta V, Mendis K (1996) Vehicle development for frontal/offset crash using lumped parameter modeling. SAE Technical Paper 960437 DOI 10.4271/960437

Christensen J, Bastien C (2016) Vehicle architectures, structures, and safety requirements. In: Nonlinear Optimization of Vehicle Safety Structures, Elsevier, pp 1–49, DOI 10.1016/b978-0-12-417297-5.00001-8

Cicchino JB (2015) Consumer response to vehicle safety ratings. In: 24th International Technical Conference on the Enhanced Safety of the Vehicles (ESV), Insurance Institute for Highway Safety, Gothenburg, Sweden, 15-0069, pp 1–9

Clough RW (1960) The finite element method in plane stress analysis. In: Proceedings of Second ASCE Conference on Electronic Computation, Pittsburg, PA, USA, 8, pp 345–378

Coulomb CA (1785) Théorie des machines simples, en ayant égard au frottement de leurs parties, et à la roideur des cordages. Memoires de Mathématique et de Physique presentés à l'Académie royale des sciences 10

Courant R (1943) Variational methods for the solution of problems of equilibrium and vibrations. Bulletin of the American Mathematical Society 49, DOI 10.1090/S0002-9904-1943-07818-4

Cox DC, Baybutt P (1981) Methods for uncertainty analysis: A comparative survey. Risk Analysis 1:251–258, DOI 10.1111/j.1539-6924.1981.tb01425.x

Cuevas-Salazar I, Song L (2018) Robustness analysis and identification of relevant structural parameters for the small overlap crash test. In: Automotive CAE Grand Challenge 2018 CARHS, Hanau, Germany

Cuevas-Salazar I, Song L, Fender J, Duddeck F (2017) Methodology for the nonlinear kinematic design of vehicle structures subjected to the small overlap crash test. In: XIV International Conference on Computational Plasticity, Barcelona, Spain

Cuevas-Salazar I, Duddeck F, Song L (2019) Small overlap assessment for early design phases based on vehicle kinematics. International Journal of Crashworthiness 25(1):24–53, DOI 10.1080/13588265.2018.1514689

D'Ambrosio J, Soremekun G (2017) Systems engineering challenges and MBSE opportunities for automotive system design. In: 2017 IEEE International Conference on Systems, Man, and Cybernetics (SMC), Banff, AB, Canada, DOI 10.1109/smc.2017.8122925

Daub M (2020) Optimizing flexibility for component design in systems engineering under epistemic uncertainty. PhD Thesis, Technische Universität München, Munich, Germany

Daub M, Duddeck F (2018) Complex systems design under non-reducible lack-of-knowledge uncertainties. In: Proceedings of the joint ICVRAM ISUMA UNCERTAINTIES conference, Florianopolis, SC, Brazil

Daub M, Duddeck F (2020) A decoupled design approach for complex systems under lack-of-knowledge uncertainty. International Journal of Approximate Reasoning 119:408–420, DOI 10.1016/j.ijar.2020.01.006

Daub M, Duddeck F, Zimmermann M (2020) Optimizing component solution spaces for systems design. Structural and Multidisciplinary Optimization 61(5):2097–2109, DOI 10.1007/s00158-019-02456-8

David R, Joseph H, Marlon F, Ke D (2003) Development of a stochastic approach for vehicle FE models. In: ASME International Mechanical Engineering Congress and Exposition, Washington, DC, USA, vol Transportation: Making Tracks for Tomorrow's Transportation, pp 37–69, DOI 10.1115/IMECE2003-55107

Dehnad K (1988) Quality Control, Robust Design, and the Taguchi Method. Springer US, Pacific Grove, CA, USA, DOI 10.1007/978-1-4684-1472-1

Denavit J, Hartenberg RS (1955) A kinematic notation for lower-pair mechanisms based on matrices. Journal of Applied Mechanics 22(2):215–221, DOI 10.1115/1.4011045

Dias J, Pereira M (2004) Optimization methods for crashworthiness design using multibody models. Computers & Structures 82(17):1371–1380, DOI 10.1016/j.compstruc.2004.03.032

Dong G, Wang D, Zhang J, Huang S (2007) Side structure sensitivity to passenger car crashworthiness during pole side impact. Tsinghua Science and Technology 12(3):290–295, DOI 10.1016/S1007-0214(07)70043-3

Dopker B (1988) Developments in interdisciplinary simulation and design software for mechanical systems. Engineering with Computers 4(1):229–238, DOI 10.1007/BF01213984

Dowlatshahi S (1992) Product design in a concurrent engineering environment: an optimization approach. International Journal of Production Research 30(8):1803–1818, DOI 10.1080/00207549208948123

Duddeck F (2007a) Multidisciplinary optimization of car bodies. Structural and Multidisciplinary Optimization 35(4):375–389, DOI 10.1007/s00158-007-0130-6

Duddeck F (2007b) Survey on robust design and optimisation for crashworthiness. In: Proceedings of the EUROMECH Colloquium 482, Queen Mary University London, London, UK

Duddeck F, Wehrle E (2015) Recent advances on surrogate modeling for robustness assessment of structures with respect to crashworthiness requirements. In: 10th European LS-DYNA Conference 2015, DYNAmore GmbH, Würzburg, Germany

Eichmueller G, Meywerk M (2020) On computer simulation of components for automotive crashworthiness: validation and uncertainty quantification for simple load cases. International Journal of Crashworthiness 25(3):263–275, DOI 10.1080/13588265.2019.1582577

Elkady M, Elmarakbi A (2012) Modelling and analysis of vehicle crash system integrated with different VDCS under high speed impacts. Central European Journal of Engineering 2(4):585–602, DOI 10.2478/s13531-012-0035-z

Elkady M, Elmarakbi A, Crolla D (2011) A numerical study for optimizing vehicle dynamics control systems in offset impacts. SAE Technical Paper 2011-01-0954 DOI 10.4271/2011-01-0954

Elkady M, Elmarakbi A, MacIntyre J (2012a) Enhancement of vehicle safety and improving vehicle yaw behaviour due to offset collision using vehicle dynamics. International Journal of Vehicle Safety 6, DOI 10.1504/IJVS.2012.049011

Elkady M, Elmarakbi A, MacIntyre J (2012b) The influence of a vehicle dynamics control system on the occupant's dynamic response during a vehicle collision. Proceedings of the Institution of Mechanical Engineers, Part D: Journal of Automobile Engineering 226, DOI 10.1177/0954407012445698

Elmarakbi A, Elkady M, MacIntyre J (2013) Numerical analysis of vehicle-to-vehicle impact using vehicle dynamics control systems for collision mitigation. International Journal of Dynamics and Control 1, DOI 10.1007/s40435-013-0017-x

Elmarakbi AM, Zu JW (2005) Crashworthiness improvement of vehicle-to-rigid fixed barrier in full frontal impact using novel vehicle's front-end structures. International Journal of Automotive Technology 6(5):491–499, ISSN: 1229 9138

Erschen S, Duddeck F, Gerdts M, Zimmermann M (2018) On the optimal decomposition of high-dimensional solution spaces of complex systems. ASCE-ASME Journal of Risk and Uncertainty in Engineering Systems 4(2):1–15, DOI 10.1115/1.4037485

Faber MH, Maes MA, Straub D, Baker J (2006) On the Quantification of Robustness of Structures. In: International Conference on Offshore Mechanics and Arctic Engineering, Hamburg, Germany, Volume 3: Safety and Reliability; Materials Technology; Douglas Faulkner Symposium on Reliability and Ultimate Strength of Marine Structures, pp 79–87, DOI 10.1115/OMAE2006-92095

Fang J, Gao Y, Sun G, Zhang Y, Li Q (2014) Crashworthiness design of foam-filled bitubal structures with uncertainty. International Journal of Non-Linear Mechanics 67:120–132, DOI 10.1016/j.ijnonlinmec.2014.08.005

Fang J, Sun G, Qiu N, Kim NH, Li Q (2016) On design optimization for structural crashworthiness and its state of the art. Structural and Multidisciplinary Optimization 55(3):1091–1119, DOI 10.1007/s00158-016-1579-y

Fender J (2014) Solution spaces for vehicle crash design. PhD thesis, Technische Universität München, Munich, Germany

Fender J, Duddeck F, Zimmermann M (2013) On the calibration of simplified vehicle crash models. Structural and Multidisciplinary Optimization 49(3):455–469, DOI 10.1007/s00158-013-0977-7

Fender J, Graff L, Zimmermann M, Harbrecht H (2014) Identifying key parameters for design improvement in high-dimensional systems with uncertainty. Journal of Mechanical Design DOI 136(4):041007,DOI:10.1115/1.4026647

Fender J, Duddeck F, Zimmermann M (2016) Direct computation of solution spaces. Structural and Multidisciplinary Optimization 55(5):1787–1796, DOI 10.1007/s00158-016-1615-y

Fisher G (1998) Model-based systems engineering of automotive systems. In: 17th DASC. AIAA/IEEE/SAE. Digital Avionics Systems Conference, IEEE, Bellevue, WA, USA, DOI 10.1109/dasc.1998.741455

Free JC, Hall JW, Montano CA (1976) Identification of mathematical models from impact data: Application to thoracic impact. SAE Spec Publ SP-142

Friedman J, Ghidella J (2006) Using model-based design for automotive systems engineering - Requirements analysis of the power window example. SAE Technical Paper 2006-01-1217 DOI 10.4271/2006-01-1217

Georgiou G, Zeguer T (2018) On the assessment of the macro-element methodology for full vehicle crashworthiness analysis. International Journal of Crashworthiness 23(3):336–353, DOI 10.1080/13588265.2017.1328723

Ghannam MY, Clark T, Reddy Y, Lee J (2011) A study of crash energy and severity in frontal vehicle-to-vehicle crash tests. SAE Technical Paper 2011-01-0541 DOI 10.4271/2011-01-0541

Graff L (2013) A stochastic algorithm for the identification of solution spaces in high-dimensional design spaces. PhD thesis, University of Basel, Basel, Switzerland

Graff L, Harbrecht H, Zimmermann M (2016) On the computation of solution spaces in high dimensions. Structural and Multidisciplinary Optimization 54(4), DOI 10.1007/s00158-016-1454-x

Gu L, Yang RJ, Li G, Tyan T (2005) Structural optimization for crash pulse. SAE Technical Paper 2005-01-0748 DOI 10.4271/2005-01-0748

Gui C, Bai J, Zuo W (2018) Simplified crashworthiness method of automotive frame for conceptual design. Thin-Walled Structures 131:324–335, DOI 10.1016/j.tws.2018.07.005

Gutermuth A, Jung U, Pitzer M (2013) Komponenten-Berechnungsmodelle von PKW-Karosserien. ATZ-Automobiltechnische Zeitschrift 115(9):722–729

Halgrin J, Haugou G, Markiewicz E, Rota L (2008) Integrated simplified crash modelling approach dedicated to pre-design stage: evaluation on a front car part. International Journal of Vehicle Safety 3(1):91, DOI 10.1504/ijvs.2008.020086

Harbrecht H, Troendle D, Zimmermann M (2019) A sampling-based optimization algorithm for solution spaces with pair-wise-coupled design variables. Structural and Multidisciplinary Optimization 60(2):501–512, DOI 10.1007/s00158-019-02221-x

Harbrecht H, Troendle D, Zimmermann M (2021) Approximating solution spaces as a product of polygons. Structural and Multidisciplinary Optimization 64(4):2225–2242, DOI 10.1007/s00158-021-02979-z

Harwood SM, Barton PI (2017) How to solve a design centering problem. Mathematical Methods of Operations Research 86(1):215–254, DOI 10.1007/s00186-017-0591-3

Hassan MT, Shi MG, Meguid SA (2019) Nonlinear multibody dynamics and finite element modeling of occupant response: part i—rear vehicle collision. International Journal of Mechanics and Materials in Design 15, DOI 10.1007/s10999-019-09449-x

Hegazy S, Rahnejat H, Hussain K (2000) Multi-body dynamics in full-vehicle handling analysis under transient manoeuvre. Vehicle System Dynamics 34, DOI 10.1076/0042-3114(200008)34:1;1-K;FT001

Hershman LL (2001) The US new car assessment program past present and future. In: 17th International Technical Conference on the Enhanced Safety of Vehicles (ESV), U.S. Department of Transportation, Amsterdam, The Netherlands

Hong SJ, Lee DC, Jang JH, Han CS, Hedrick K (2006) Systematic design process for frontal crashworthiness of aluminium-intensive electrical vehicle bodies. Journal of Automobile Engineering 220(12):1667–1678, DOI 10.1243/09544070jauto273

Howard M, Thomas A, Koch W, Watson J, Hardy R (2000) Validation and application of a finite element pedestrian humanoid model for use in pedestrian accident simulations. In: Proceedings of IRCOBI Conference, Montpellier, France, vol 28, pp 101–119

Hrennikoff A (1941) Solution of problems of elasticity by the framework method. Journal of Applied Mechanics 8, DOI 10.1115/1.4009129

Huang M (2002) Vehicle crash mechanics. ASME Applied Mechanics Reviews September 2003 56(5):B68–B69, DOI 10.1115/1.1584416

Hunkeler S, Duddeck F, Rayamajhi M, Zimmer H (2013) Shape optimisation for crashworthiness followed by a robustness analysis with respect to shape variables. Structural and Multidisciplinary Optimization 48(2):367–378, DOI 10.1007/s00158-013-0903-z

Hwang KH, Park GJ (2005) Development of a Robust Design Process Using a New Robustness Index. In: International Design Engineering Technical Conferences and Computers and Information in Engineering Conference, Volume 2: 31st Design Automation Conference, Parts A and B, pp 231–241, DOI 10.1115/DETC2005-84555

INCOSE (2015) INCOSE Systems Engineering Handbook - A Guide for System Life Cycle Processes and Activities. John Wiley & Sons, New York City, NY, USA

Insurance Institute for Highway Safety (2017) IIHS TechData. URL `https://techdata.iihs.org`, (Date accessed: 03.12.2017)

Insurance Institute for Highway Safety (2021) IIHS Small Overlap Frontal Crashworthiness Evaluation Crash Test Protocol (Version VII), URL `https://www.iihs.org/media/ec54a7ea-1a1d-4fb2-8fc3-b2e018db2082/1A5oYw/Ratings/Protocols/current/small_overlap_test_protocol.pdf`, (Date accessed: 01.09.2021)

Ionut RA, Corneliu C, Bogdan T (2017) Mathematical model validated by a crash test for studying the occupant's kinematics and dynamics in a cars' frontal collision. International Journal of Automotive Technology 18, DOI 10.1007/s12239-017-0099-0

Jazar RN (2017) Vehicle Dynamics. Springer International Publishing, Cham, Switzerland, DOI 10.1007/978-3-319-53441-1

Jergeus J (2018) Challenges in introducing cast aluminum in full car crash simulation. In: Automotive CAE Grand Challenge 2018 CARHS, Hanau, Germany

Jonsén P, Isaksson E, Sundin KG, Oldenburg M (2009) Identification of lumped parameter automotive crash models for bumper system development. International Journal of Crashworthiness 14(6):533–541, DOI 10.1080/13588260902837262

Kamal MM (1970) Analysis and simulation of vehicle to barrier impact. SAE Technical Paper. 700414:86–99

Kamariotis A, Antinori G, Papaioannou I, Duddeck F (2019) Mixed aleatory-epistemic uncertainty quantification and sensitivity analysis. In: 17th International Probabilistic Workshop, Edinburgh, UK

Kennedy BM, Sobek DK, Kennedy MN (2014) Reducing rework by applying set-based practices early in the systems engineering process. Systems Engineering 17(3):278–296, DOI 10.1002/sys.21269

Kiefer T, Erb P, Gosolits B, Visinescu R (2004) Simulation of airbag sensing signals using finite element method. In: LS-DYNA User Forum, Bamberg, Germany

Kim C, Arora J (2003a) Nonlinear dynamic system identification for automotive crash using optimization: A review. Structural and Multidisciplinary Optimization 25(1):2–18, DOI 10.1007/s00158-002-0267-2

Kim C, Arora JS (2003b) Development of simplified dynamic models using optimization: Application to crushed tubes. Computer Methods in Applied Mechanics and Engineering 192(16):2073–2097, DOI 10.1016/S0045-7825(03)00242-1

Kim C, Mijar A, Arora J (2001) Development of simplified models for design and optimization of automotive structures for crashworthiness. Structural and Multidisciplinary Optimization 22(4):307–321, DOI 10.1007/pl00013285

Kim DH (2017) Study of an enhanced body of small vehicle in frontal crash test and IIHS small overlap test. SAE Technical Paper 2017-01-1468 DOI 10.4271/2017-01-1468

Kim HS, Kang SY, Lee IH, Park SH, Han DC (1996) Vehicle frontal crashworthiness analysis by simplified structure modeling using nonlinear spring and beam elements. International Journal of Crashworthiness 2(1):107–118, DOI 10.1533/cras.1997.0038

King AI, Chou CC, MacKinder JA (1972) Mathematical model of an airbag for a three-dimensional occupant simulation. SAE Technical Paper 720036 DOI 10.4271/720036

Kirkpatrick S, MacNeill R, Bocchieri R (2003) Development of an LS-DYNA occupant model for use in crash analyses of roadside safety features. In: Transportation Research Board 82nd Annual Meeting 2003, Washington, DC, USA

Kortüm W (1993) Review of multibody computer, codes for vehicle system dynamics. Vehicle System Dynamics 22(1):3–31, DOI 10.1080/00423119308969463

Kossiakoff A, Biemer SM, Seymour SJ, Flanigan DA (2020) Systems Engineering Principles and Practice. John Wiley & Sons, New York City, NY, USA

Kundla M, Schramm D, Zimmermann M, Justen N, Scheirl F, Lindner T, Till F, Jeyakumar JHI (2020) Utilizing artificial neural networks and design solution spaces to cope with the complexity in subframe design. In: 11th International Munich Chassis Symposium 2020, Springer Berlin Heidelberg, Munich, Germany, pp 279–295, DOI 10.1007/978-3-662-63193-5_21

Kuykendall TA (2001) Systems Architecting-Creating & Building Complex Systems, vol 4. Prentice Hall, DOI 10.1002/inst.20014349

Lange V, Fender J, Duddeck F (2018a) Relaxing high-dimensional constraints in the direct solution space method for early phase development. Optimization and Engineering 19(4):887–915, DOI 10.1007/s11081-018-9381-x

Lange V, Fender J, Song L, Duddeck F (2018b) Early phase modeling of frontal impacts for crashworthiness: From lumped mass–spring models to deformation space models. Journal of Automobile Engineering 233(12):3000–3015, DOI 10.1177/0954407018814034

Larsson T (2001) Multibody dynamic simulation in product development. PhD thesis, Luleå University of Technology, Luleå, Sweden

Lee KH, Park GJ (2002) Robust optimization in discrete design space for constrained problems. AIAA Journal 40(4):774–780, DOI 10.2514/2.1712

Lehar M, Zimmermann M (2012) An inexpensive estimate of failure probability for high-dimensional systems with uncertainty. Structural Safety Vol. 36-37:32–38

Lin CH, Gao R, Cheng YP (2001) A stochastic approach for the simulation of an integrated vehicle and occupant model. In: The 17th International Technical Conference on the Enhanced Safety of Vehicles (ESV), Amsterdam, The Netherlands

Liu X, Liang R, Hu Y, Jiang C, Tang X, Bastien C (2021a) Body optimization approach of sedan structure for improving small overlap impact rating. International Journal of Crashworthiness 26(2):182–190, DOI 10.1080/13588265.2019.1701360

Liu X, Liang R, Hu Y, Tang X, Bastien C, Zhang R (2021b) Collaborative optimization of vehicle crashworthiness under frontal impacts based on displacement oriented structure. International Journal of Automotive Technology 22(5):1319–1335, DOI 10.1007/s12239-021-0115-2

Liu Y (2005) Development of simplified models for crashworthiness analysis. PhD thesis, University of Louisville, Louisville, KY, USA, DOI 10.18297/etd/843

Lomario D, De Poli GP, Fattore L, Marczyk J (2007) A Complexity-Based Approach to Robust Design and Structural Assessment of Aero Engine Components. In: ASME Turbo Expo 2007: Power for Land, Sea, and Air, vol 5, pp 1091–1099, DOI 10.1115/GT2007-27205

Lottaz C (2000) Collaborative design using solution spaces. PhD thesis, École polytechnique fédérale de Lausanne, Lausanne, Switzerland, DOI 10.5283/EPUB.44260

Luu NPT, Anh LH (2021) A study on optimal design of longitudinal shape for improving small-overlap performance. In: Lecture Notes in Mechanical Engineering, Springer Singapore, pp 109–128, DOI 10.1007/978-981-15-9893-7_7

Makkonen P (1999) On multi body systems simulation in product design. PhD thesis, Royal Institute of Technology, KTH, Stockholm, Sweden

Mario H, Dietrich W, Gfrerrer A, Lang J (2013) Integrated Computer-Aided Design in Automotive Development. Springer Berlin, Heidelberg, Germany, DOI 10.1007/978-3-642-11940-8

Marler RT, Kim CH, Arora JS (2006) System identification of simplified crash models using multi-objective optimization. Computer Methods in Applied Mechanics and Engineering 195(33-36):4383–4395, DOI 10.1016/j.cma.2005.09.002

Marzbanrad J, Pahlavani M (2011) Calculation of vehicle-lumped model parameters considering occupant deceleration in frontal crash. International Journal of Crashworthiness 16:439–455, DOI 10.1080/13588265.2011.606995

McKenney TA, Kemink LF, Singer DJ (2011) Adapting to changes in design requirements using set-based design. Naval Engineers Journal 123(3):66–77

Meng Y, Pak W, Guleyupoglu B, Koya B, Gayzik FS, Untaroiu CD (2017) A finite element model of a six-year-old child for simulating pedestrian accidents. Accident Analysis and Prevention 98, DOI 10.1016/j.aap.2016.10.002

Mentzer SG, Radwan RA, Hollowell WT (1992) The SISAME methodology for extraction of optimal lumped parameter structural crash models. SAE Technical Paper 920358 DOI 10.4271/920358

Milanese M, Norton J, Piet-Lahanier H, Walter É (eds) (1996) Bounding Approaches to System Identification. Springer US, Boston, MA, USA, DOI 10.1007/978-1-4757-9545-5

Mourelatos ZP, Liang J (2005) A reliability-based robust design methodology. In: SAE World Congress, SAE International, Detroit, MI, USA, DOI 10.4271/2005-01-0811

Mueller BC, Brethwaite AS, Zuby DS, Nolan JM (2014) Structural design strategies for improved small overlap crashworthiness performance. SAE Technical Paper 2014-22-0006 DOI 10.4271/2014-22-0006

Munyazikwiye B, Karimi H, Robbersmyr K (2013) Mathematical modeling of vehicle frontal crash by a double spring-mass-damper model. In: 24th International Conference on Information, Communication and Automation Technologies, ICAT 2013, Sarajevo, Bosnia and Herzegovina, DOI 10.1109/ICAT.2013.6684071

Munyazikwiye B, Karimi H, Robbersmyr K (2017) Application of genetic algorithm on parameter optimization of three vehicle crash scenarios. IFAC-PapersOnLine 50(1):3697–3701, DOI 10.1016/j.ifacol.2017.08.564

Munyazikwiye B, Vysochinskiy D, Khadyko M, Robbersmyr K (2018) Prediction of vehicle crashworthiness parameters using piecewise lumped parameters and finite element models. Designs 2(4):43, DOI 10.3390/designs2040043

Myers RH, Khuri AI, Carter WH (1989) Response surface methodology: 1966–l988. Technometrics 31(2):137–157

National Highway Traffic Safety Administration (2007) Systems Engineering for Intelligent Transportation Systems - An Introduction for Transportation Professionals. FHWAHOP-07-069, Department of Transportation Office of Operations, Washington, DC, USA

Naujoks B, Beume N, Emmerich M (2005) Multi-objective optimisation using s-metric selection: application to three-dimensional solution spaces. In: 2005 IEEE Congress on Evolutionary Computation, vol 2, pp 1282–1289, DOI 10.1109/CEC.2005.1554838

Nguyen LPT (2017) An optimisation approach to choose thickness of three members to improve IIHS small-overlap structural rating. International Journal of Crashworthiness 22(5):518–526, DOI 10.1080/13588265.2017.1281203

Nguyen PTL, Lee JY, Yim HJ, Kim HK, Lee SB, Heo SJ (2015a) Optimal design of vehicle structure for improving small-overlap rating. International Journal of Automotive Technology 16(6):959–965, DOI 10.1007/s12239-015-0098-y

Nguyen PTL, Lee JY, Yim HJ, Lee SB, Heo SJ (2015b) Analysis of vehicle structural performance during small-overlap frontal impact. International Journal of Automotive Technology 16(5):799–805, DOI 10.1007/s12239-015-0081-7

Nikravesh PE (2012) Multibody dynamics formulation. In: Grasping in Robotics, Springer London, pp 57–76, DOI 10.1007/978-1-4471-4664-3_3

Nocedal J, Wright SJ (2006) Numerical Optimization. Springer, New York City, NY, USA

Noorsumar G, Robbersmyr K, Rogovchenko S, Vysochinskiy D (2020) Crash response of a repaired vehicle-influence of welding UHSS members. SAE Technical Paper 2020-01-0197 DOI 10.4271/2020-01-0197

Noorsumar G, Rogovchenko S, Robbersmyr KG, Vysochinskiy D (2021) Mathematical models for assessment of vehicle crashworthiness: a review. International Journal of Crashworthiness 0(0):1–15, DOI 10.1080/13588265.2021.1929760

Numata S, Mizuno K, Ito D, Okumura D, Kinoshita H (2018) Validation of crush energy calculation methods for use in accident reconstructions by finite element analysis. SAE International Journal of Transportation Safety 6, DOI 10.4271/09-06-02-0009

Omar T, Eskandarian A, Bedewi N (1998) Vehicle crash modelling using recurrent neural networks. Mathematical and Computer Modelling 28, DOI 10.1016/S0895-7177(98)00143-5

Pahlavani M, Marzbanrad J (2015) Crashworthiness study of a full vehicle-lumped model using parameters optimisation. International Journal of Crashworthiness 20(6):573–591, DOI 10.1080/13588265.2015.1068910

Pak W, Meng Y, Schap J, Koya B, Gayzik SF, Untaroiu CD (2019) Finite element model of a high-stature male pedestrian for simulating car-to-pedestrian collisions. International Journal of Automotive Technology 20, DOI 10.1007/s12239-019-0042-7

Papaioannou I, Daub M, Drieschner M, Duddeck F, Ehre M, Eichner L, Eigel M, Götz M, Graf W, Grasedyck L, Gruhlke R, Hömberg D, Kaliske M, Moser D, Petryna Y, Straub D (2019) Assessment and design of an engineering structure with polymorphic uncertainty quantification. GAMM-Mitteilungen 42(2):e201900,009, DOI 10.1002/gamm.201900009

Pars LA, Lagrange JL (1966) Mecanique analytique. The Mathematical Gazette 50, DOI 10.2307/3614003

Paz J, Díaz J, Romera L (2020) Analytical and numerical crashworthiness uncertainty quantification of metallic thin-walled energy absorbers. Thin-Walled Structures 157:107,022, DOI 10.1016/j.tws.2020.107022

Percivall GS (1992) Systems engineering in the automotive industry. INCOSE International Symposium 2(1):501–508, DOI 10.1002/j.2334-5837.1992.tb01533.x

Pifko A, Winter R (1981) Theory and application of the finite element analysis to structural crash simulation. In: Noor AK, McComb HG (eds) Computational Methods in Nonlinear Structural and Solid Mechanics, Pergamon, pp 277–285, DOI 10.1016/B978-0-08-027299-3.50036-4

Portal RJF, Dias JMP (2006) Multibody models for vehicle accident reconstruction. In: III European Conference on Computational Mechanics, Springer Netherlands, pp 775–775, DOI 10.1007/1-4020-5370-3_775

Prochowski L, Ziubiński M, Pusty T (2018) Experimental and analytic determining of the characteristics of deformation and side stiffness of a motor car body based on results of side-impact crash tests. In: IOP Conference Series: Materials Science and Engineering, (Online) UK, vol 421, DOI 10.1088/1757-899X/421/3/032025

Putra IPA, Iraeus J, Sato F, Svensson MY, Linder A, Thomson R (2021) Optimization of female head–neck model with active reflexive cervical muscles in low severity rear impact collisions. Annals of Biomedical Engineering 49, DOI 10.1007/s10439-020-02512-1

Qiu N, Gao Y, Fang J, Sun G, Li Q, Kim NH (2018) Crashworthiness optimization with uncertainty from surrogate model and numerical error. Thin-Walled Structures 129:457–472, DOI 10.1016/j.tws.2018.05.002

Rahnejat H (2000) Multi-body dynamics: Historical evolution and application. Proceedings of the Institution of Mechanical Engineers, Part C: Journal of Mechanical Engineering 214, DOI 10.1243/0954406001522886

Ramaswamy K, Radhakrishnan J, Patham B, Savic V (2016) Fast and stable quasi-static bending simulations in ls-dyna: Identification of optimal finite element model parameters. SAE Technical Paper 2016-01-1392 DOI 10.4271/2016-01-1392

Rayamajhi M (2014) Efficient methods for robust shape optimisation for crashworthiness. PhD Thesis, Queen Mary University of London, London, UK

Redhe M (2004) On vehicle crashworthiness design using structural optimization. PhD thesis, Linköpings Universitet, Linköpings, Sweden

Redhe M, Nilsson L (2005) A multipoint version of space mapping optimization applied to vehicle crashworthiness design. Structural and Multidisciplinary Optimization 31(2):134–146, DOI 10.1007/s00158-005-0544-y

Ren Y, Xiang J (2014) Crashworthiness uncertainty analysis of typical civil aircraft based on Box–Behnken method. Chinese Journal of Aeronautics 27(3):550–557, DOI 10.1016/j.cja.2014.04.020

Riekert P, Schunck TE (1940) Zur Fahrmechanik des gummibereiften Kraftfahrzeugs. Ingenieur-Archiv 11(3):210–224, DOI 10.1007/bf02086921

Rocco C, Moreno J, Carrasquero N (2003) Robust design using a hybrid-cellular-evolutionary and interval-arithmetic approach: A reliability application. Reliability Engineering & System Safety 79:149–159, DOI 10.1016/S0951-8320(02)00226-0

Roetzer S, Thoma D, Zimmermann M (2020) Cost optimization of product families using solution spaces. In: 16th International Design Conference Proceedings, Cavtat, Croatia, vol 28, pp 1087–1094, DOI 10.1017/dsd.2020.178

Sandberg S, Lundin M, Näsström M, Lindgren LE, Berglund D (2013) Supporting engineering decisions through contextual, model-oriented communication and knowledge-based engineering in simulation-driven product development: an automotive case study. Journal of Engineering Design 24(1):45–63, DOI 10.1080/09544828.2012.697133

Schäffer M, Sturm R, Friedrich HE (2018) Automated generation of physical surrogate vehicle models for crash optimization. International Journal of Mechanics and Materials in Design 15(1):43–60, DOI 10.1007/s10999-018-9407-8

Schumacher A, Olschinka C (2007) Robust design considering highly nonlinear structural behavior. Structural and Multidisciplinary Optimization volume 35(3):263–272, DOI 10.1007/s00158-007-0193-4

Schäffer M, Sturm R, Friedrich HE (2017) Methodological approach for reducing computational costs of vehicle frontal crashworthiness analysis by using simplified structural modelling. International Journal of Crashworthiness 0(0):1–15, DOI 10.1080/13588265.2017.1389631

Sellgren U (1999) Simulation-driven design – motives, means, and opportunities. PhD thesis, Royal Institute of Technology, KTH, Stockholm, Sweden

Sen X, Yang J, Zhong Z (2013) Research and optimization of crashworthiness in small overlap head-on collision. In: 2013 Fifth International Conference on Measuring Technology and Mechatronics Automation, IEEE, DOI 10.1109/icmtma.2013.214

Shahidi G, Pakzad SN (2013) Time domain response surface model updating for nonlinear structures. In: Structural Health Monitoring 2013: A Roadmap to Intelligent Structures - Proceedings of the 9th International Workshop on Structural Health Monitoring, IWSHM 2013, Stanford, CA, USA

Sharp RS, Goodall JR (1969) A mathematical model for the simulation of vehicle motions. Journal of Engineering Mathematics 3, DOI 10.1007/BF01535170

Shephard MS, Beall MW, O'Bara RM, Webster BE (2004) Toward simulation-based design. Finite Elements in Analysis and Design 40(12):1575–1598, DOI 10.1016/j.finel.2003.11.004, the Fifteenth Annual Robert J. Melosh Competition

Shi L, Yang RJ, Zhu P (2012) A method for selecting surrogate models in crashworthiness optimization. Structural and Multidisciplinary Optimization 46(2):159–170, DOI 10.1007/s00158-012-0760-1

Shi MG, Hassan MT, Meguid SA (2019) Nonlinear multibody dynamics and finite element modeling of occupant response: part ii—frontal and lateral vehicle collisions. International Journal of Mechanics and Materials in Design 15, DOI 10.1007/s10999-019-09450-4

Silva XD, Parera N (2016) Forces involved in small overlap crash. In: European Automotive Congress EAEC-ESFA 2015, Springer Internal Publishing, Bucharest, Romania, pp 105–116

Singh G (2009) Short introduction to finite element method. Norwegian University of Science and Technology, Trondheim, Norway

Sippel H, Marczyk J (2009) Application Strategies of Robust Design & Complexity Management in Engineering. Current Status & Future Trends in Multi-disciplinary Product Development. WOK Kreuzer, Haar

Song L, Fender J, Duddeck F (2015) A semi-analytical approach to identify solution spaces for crashworthiness in vehicle architectures. In: 24th International Technical Conference on the Enhanced Safety of Vehicles (ESV), Gothenburg , Sweden

Song L, Pabst M, Duddeck F, Fender J (2018) A simplified model for barrier–vehicle interaction in a rear crash for early phase development and solution spaces. International Journal of Crashworthiness 23(5):507–520, DOI 10.1080/13588265.2017.1350091

Sousa L, Veríssimo P, Ambrósio J (2008) Development of generic multibody road vehicle models for crashworthiness. Multibody System Dynamics 19, DOI 10.1007/s11044-007-9093-z

Spethmann P, Herstatt C, Thomke SH (2006) The impact of crash simulation on productivity and problem-solving in automotive R&D. Econstor 43

Starossek U, Haberland M (2009) Evaluating measures of structural robustness. In: ASCE / Structures Congress 2009: Crossing Borders, Austin, TX, USA, pp 1–8, DOI 10.1061/41031(341)194

Streilein T, Hillmann J (2002) Stochastische Simulation und Optimierung am Beispiel VW Phaeton. In: VDI-Congress, Wuerzburg, Germany

Sørensen JD (2011) Framework for robustness assessment of timber structures. Engineering Structures 33(11):3087–3092, DOI 10.1016/j.engstruct.2011.02.025, modelling the Performance of Timber Structures

Thomas C (2011) The role of vehicle structure in reducing injuries in small overlap crashes. In: Proceedings of International Automotive Body Congress, International Automotive Body Congress, Troy, MI, USA, pp 105–116

Tomassoni JE (1984) Simulation of a two-car oblique side impact using a simple crash analysis model. SAE Technical Paper 840858 93(4):164–191, DOI 10.4271/840858

Tomazic S, Stancin S (2011) Simultaneous orthogonal rotation angle. Electrotechnical Review 78:7–11

Tran T, Hou S, Han X, Tan W, Nguyen N (2014) Theoretical prediction and crashworthiness optimization of multi-cell triangular tubes. Thin-Walled Structures 82:183–195, DOI 10.1016/j.tws.2014.03.019

Trella TJ, Kanianthra JN (1985) Occupant response sensitivity analyses using a lumped mass model in simulation of car-to-car side impacts. In: 10th International Technical Conference on the Enhanced Safety of Vehicles (ESV), Oxford, UK

Ulrich KT, Eppinger SD (2015) Product Design and Development. Irwin McGraw-Hill, New York City, NY, USA

Usta F, Eren Z, Kurtaran H, Türkmen HS, Kazancı Z, Mecitoglu Z (2018) Crashworthiness optimization of nested and concentric circular tubes using response surface methodology and genetic algorithm. Latin American Journal of Solids and Structures 15, DOI 10.1590/1679-78254385

Vangi D (2020) Vehicle collision dynamics. In: Vangi D (ed) Vehicle Collision Dynamics, Butterworth-Heinemann, p xv, DOI 10.1016/B978-0-12-812750-6.00013-5

Varat MS, Husher SE (2003) Crash pulse modeling for vehicle safety research. Proc 18th International Technical Conference on the Enhanced Safety of Vehicles

Vogt ME, Duddeck F, Wahle M, Zimmermann M (2018) Optimizing tolerance to uncertainty in systems design with early- and late-decision variables. IMA Journal of Management Mathematics 30(3):269–280, DOI 10.1093/imaman/dpy003

Wagstrom L, Kling A, Norin H, Fagerlind H (2013) A methodology for improving structural robustness in frontal car-to-car crash scenarios. International Journal of Crashworthiness 18(4):385–396, DOI 10.1080/13588265.2013.801292

Wall J (2007) Simulation-driven design of complex mechanical and mechatronic systems. PhD thesis, Blekinge Institute of Technology, Blekinge, Sweden

Ward AC, Seering WP (1993) Quantitative inference in a mechanical design compiler. Journal of Mechanical Design 115(1):29–35, DOI 10.1115/1.2919320

Ward AC, Liker JK, Cristiano JJ, Sobek DK (1995) The second Toyota paradox: how delaying decisions can make better cars faster. Sloan management review 36(3):43, URL https://sloanreview.mit.edu/article/the-second-toyota-paradox-how-delaying-decisions\-can-make-better-cars-faster, (Date accessed: 18.08.2016)

Watai A, Nakatsuka S, Kato T, Ujiie Y, Matsuoka Y (2009) Robust Design Method for Diverse Conditions. In: Proceedings of the ASME 2009 International Design Engineering Technical Conferences & Computers and Information in Engineering Conference, San Diego, CA, USA, pp 1131–1138, DOI 10.1115/DETC2009-87108

Weber J (2009) Automotive Development Processes. Springer Berlin Heidelberg, Heidelberg, Germany, DOI 10.1007/978-3-642-01253-2

Wei Z (2017) Analysis, modeling and CAE validation of vehicle crashes using advanced signal processing tools. PhD thesis, Universitet i Agder/University of Agder, Kristiansand, Norway

Wei Z, Krimi HR, Robbersmyr KG (2015) A model of vehicle-fixed barrier frontal crash and its application in the estimation of crash kinematics. In: 24th International Technical Conference on the Enhanced Safety of Vehicles (ESV), Gothenburg, Sweden

Wierzbicki T, Abramowicz W (1983) On the Crushing Mechanics of Thin-Walled Structures. Journal of Applied Mechanics 50(4a):727–734, DOI 10.1115/1.3167137

Will J, Frank T (2008) Rechnerische Robustheitsbewertungen von Strukturcrashlastfaellen bei der Daimler AG. In: 5th Annual Weimar Optimization and Stochastic Days, Weimar, Germany

Will J, Stelzmann U (2008) Robustness evaluation crashworthiness simulation results. In: 6th European LS-DYNA Users Conference, Gothenburg, Sweden

Winner H (2013) Challenges of automotive systems engineering for industry and academia. In: Automotive Systems Engineering, Springer Berlin Heidelberg, pp 3–15, DOI 10.1007/978-3-642-36455-6_1

Woolley RL (2008) Crash pulse modeling of force limiting structures. SAE Technical Paper 2008-01-0175 DOI 10.4271/2008-01-0175

Xueyan Y, Yubin Q, Ying W (2019) Establishment and verification of finite element model of pedestrian head based on accident reconstruction. In: Proceedings - 2019 2nd World Conference on Mechanical Engineering and Intelligent Manufacturing, WCMEIM 2019, Shanghai, China, DOI 10.1109/WCMEIM48965.2019.00151

Yadav S, Pradhan S (2014) Investigations into dynamic response of automobile components during crash simulation. Procedia Engineering 97:1254–1264, DOI 10.1016/j.proeng.2014.12.404

Youn BD, Jung BC, Xi Z, Kim SB, Lee W (2011) A hierarchical framework for statistical model calibration in engineering product development. Computer Methods in Applied Mechanics and Engineering 200(13-16):1421–1431, DOI 10.1016/j.cma.2010.12.012

Yu C, Wang F, Wang B, Li G, Li F (2020) A computational biomechanics human body model coupling finite element and multibody segments for assessment of head/brain injuries in car-to-pedestrian collisions. International Journal of Environmental Research and Public Health 17, DOI 10.3390/ijerph17020492

Zimmermann M, von Hoessle JE (2013) Computing solution spaces for robust design. International Journal for Numerical Methods in Engineering 94(3):290–307, DOI 10.1002/nme.4450

Zuolong W, Reza KH, Gunnar RK (2015) A model of vehicle-fixed barrier frontal crash and its application in the estimation of crash kinematics. In: 24th International Technical Conference on the Enhanced Safety of Vehicles (ESV), Seoul, South Korea

Şenaras AE (2019) Parameter optimization using the surface response technique in automated guided vehicles. Sustainable Engineering Products and Manufacturing Technologies 1(8):187–197, DOI 10.1016/B978-0-12-816564-5.00008-6